

ISSN 1880-8468

Technical Report of  
International Development Engineering

国際開発工学報告

TRIDE-2013-01

February 14, 2013

Abstracts of Master Theses

Presented in February 2013

Department of International Development Engineering,  
Graduate School of Science and Engineering,  
Tokyo Institute of Technology  
<http://www.ide.titech.ac.jp/TR>

## Preface

Master theses of Department of International Development Engineering, Tokyo Institute of Technology were presented successfully on August 3, 2012 and February 14, 2013. This technical report consists of the abstracts of those theses.

**Technical Report of International Development Engineering  
TRIDE-2013-03m**

**Table of Contents**

**(Completing in September 2012)**

**Application of Knowledge Management System in Development Project:**

**A Case of World Heritage Site in Luang Prabang, Lao P.D.R**

..... Tetsuro OKUMURA 1

**Antenna Pattern Reconstruction Using Spherical Harmonics and Its  
Application to Double-Directional Channel Modeling**

..... Yang MIAO 5

**Decomposition of Gas-phase Benzene using Ag/TiO<sub>2</sub> Packed Nonthermal  
Plasma Catalyst Reactor**

..... Christian PANGILINAN 9

**Study of Private Participation Influence on the Efficiency Performance of  
Municipal Water Supply Management in Indonesia**

..... Nirmala HAILINAWATI 13

**Contact-less Heartbeat Detection Method by using Microwave**

..... Yanran LIU 17

**(Completing in March 2013)**

**Numerical Study on Localized Heavy Rain using Latest Urban  
Parameterizations and High-Resolution Sea-surface Temperature**

..... Kumiko NAKANO 21

**The Decomposition of Methyl Orange over Titania Coated Magnetic  
Activated Carbon.**

..... Takuro HARAGUCHI 25

**Selective Catalytic Reduction of Nitrogen Oxides with Propene over Ag/CeO<sub>2</sub>-  
TiO<sub>2</sub> Catalyst**

..... Yang YANG 29

**Estimation of CO<sub>2</sub> Emission from Urban Freight Transport in Khon Kaen,  
Thailand**

..... Shinsuke MOGI 33

<b>Which Factors Influence the Relief Goods Convergence in Humanitarian Logistics?</b>	
.....Tsunenori ANDO	37
<b>Economic Operation of Large-Scale Photovoltaic Power Plants under Uncertainty</b>	
.....Junichirou ISHIO	41
<b>Lifetime Prediction of Concrete Mixed with Seawater against Chloride Attack and Carbonation</b>	
.....Hiroki OHARA	45
<b>Effect of Temperature, Oxygen Concentration and Solution on the Degradation of Paint on Steel in Marine Exposure Tests and Accelerated Test</b>	
.....Yu KAMIYA	49
<b>Synthesis of Zeolites from Lake Sludge as Ammonium Adsorbent Materials</b>	
<b>Estimating CO2 Emissions of an Automobile Company in Global Supply Chain: Case Study of Locational Conditions in Thailand</b>	
.....Yuhki KAWAHARA	53
<b>Microbial Community Analysis of the Methane Fermentation Process Treating Glycerol</b>	
.....Kohei HATTA	57
<b>Moral Hazard Issues Contractor and Subcontractor in Construction Overseas Project</b>	
.....Shotaro FUKAO	61
<b>An Analysis on Consumers' Preferences for the Residential Photovoltaic System Focused on Its Long-Term Operation</b>	
.....Toshiya MORIZUMI	65
<b>Quantitative Analysis of the Atmospheric Boundary Layer Flow Field using Doppler Lidar</b>	
.....Ayako YAGI	69
<b>Application of Virtual Reality(VR) Panorama for Townscape Monitoring in the World Heritage Site of Luang Prabang , Lao P.D.R.</b>	
.....Kenta YOKOI	73
<b>Equilibrium Extraction of Light Rare Earth Metals with PC-88A as Extractant</b>	
.....Naoto YOSHIMURA	77



<b>Optimal Design and Control of a Buck Converter Used for Energy Harvesting</b> .....	Jiawei WANG	81
<b>Preparation of Acidic Activated Carbon from Bagasse Fly Ash</b> .....	Zhaoxia GAN	85
<b>Bioethanol Concentration Process using Solvent Extraction</b> .....	Haihao HU	89
<b>Image Based Real-time Vehicle Classification for ETC</b> .....	Cong GENG	93
<b>Outdoor Experiments on Human Bio-Meteorology at the Hottest City Tajimi Using a New Wearable Measurement System</b> .....	Rui SHI	97
<b>Distributed Video Coding By Selective Line Pruning and Multi-frame based Interpolation</b> .....	Phan Tuan TAI	101
<b>Determinants of Mobile Learning Acceptance in Luang Prabang: Towards World Heritage Site Preservation Awareness Promotion</b> .....	Yew Siang POONG	105

# APPLICATION OF KNOWLEDGE MANAGEMENT SYSTEM IN DEVELOPMENT PROJECT: A CASE OF WORLD HERITAGE SITE IN LUANG PRABANG, LAO P.D.R.

Student Number: 10M18022      Name: Tetsuro OKUMURA      Supervisor: Shinobu YAMAGUCHI  
Jun-ichi TAKADA

開発プロジェクトへの知識管理システムの活用:ラオス人民民主共和国ルアンパバーン世界遺産地域のケース  
奥村 哲郎

本研究は、ラオス・ルアンパバーン世界遺産地域における情報システムに関する重要な知識や情報を継承するための知識管理システムを構築し評価することを目的とする。提案された 3 種類のシステムの中から、クラウドコンピューティングサービスを用いた方法が最適であると判断され試行した。有効性、必要性、持続可能性の側面から評価を行った結果、導入したシステムは知識を継承するのに効果的なツールであることが判明した。同時に、情報が管理共有されることで業務効率が高まることが示唆された。

## 1 Introduction

Information and Communication Technology (ICT) has a dramatic impact on achieving specific social and economic development goals as well as playing a key role in broader national development strategies [1]. However, it is said that 85% of e-government project was partially or completely failed in developing countries due to big gap between design and local situation [2].

Luang Prabang, Lao PDR was inscribed as UNESCO world heritage site in 1995. As a part of tri-partite cooperation among Tokyo Tech, the Department of World Heritage Luang Prabang (DPL) of Lao government and UNESCO, the significant collaboration started with development and operation of a database management system (DBMS) at DPL in 2003 [3].

During the course of its operation, the local team faced the difficulty of updating its database for more than one year in 2010. Field survey identified three aspects which are contributing to the situation: 1) Technical aspect, 2) human resources aspect and 3) external aspect.

## 2 Problem Analysis and Research Objectives

### 2.1 Problem Analysis

The field survey took place between February and March in 2011 to analyze the conditions at local site. As a result, it was identified that the project was facing difficult situation of not being able to succeed project knowledge and skills. Among multiple factors, one of the significant reasons was the high human mobility of the team members, both at local ICT team and Tokyo Tech team.

Since DPL was upgraded to the department from local office in 2009, tasks and duties were expanded. Therefore, due to lack of training time for new team members who joined after 2008, they were experiencing difficulties in getting previously trained skills from experienced members who had been working since the very beginning of the project.

On the other hand, a number of students from Tokyo

Tech have been working with the local ICT team since 2003 have changed over time. Each student had worked on specific tasks reflecting local needs and their own skills. From 2005 to 2008, web log was existed built on Zope. ICT team recorded acquired knowledge and daily activities in the log daily. However, due to broken hard disk drive, all the data were lost. So the project keeps limited information such as web application and several design documents such as database structure diagram. With this incident, a keen need to manage project data in more effective manner came into attention.

According to Gorelick, project knowledge management is “*basically, systematic approach to optimize access appropriate and feasible advice, knowledge, and experience located in somewhere in the organization for individuals or team in organization*”[4]. Milton proposed knowledge management model, and there are two methods of knowledge succession from trained person to beginners [5]. Connection approach succeeds knowledge in direct way. This is the most effective method if succeeding person and succeeded person located at same place on the same time. Collection approach proposes knowledge bank which accumulates explicit knowledge, and collect knowledge from skilled person, then knowledge bank transfer knowledge to beginners. This method is considered as possible solution under high human mobility because it does not require people staying at the same place at the same time.

Reflecting these literature review, to hand over skills and knowledge to new team members both for local ICT team and Tokyo Tech team, appropriate knowledge management system has become urgent requirement to avoid project knowledge and skill from losing.

### 2.2 Research Objectives

This study aims to build and evaluate a system to effectively transfer project knowledge and skills for

heritage management in Luang Prabang, Lao P.D.R. Specifically, the study took three steps: First, local environment and users' needs were carefully analyzed. Second, feasible and sustainable knowledge management system was studied using comparative analysis of several potential methods. Third, usability, effectiveness and sustainability of introduced system were evaluated.

### 3 Methodology

Method to build knowledge management system follows three steps based on the Milton's model [5]: 1) Comparative study for knowledge management system, 2) training of building and using knowledge management system and 3) building of knowledge management system.

#### 3.1 Comparative Study for Knowledge Management System

Field observation and brainstorming with local ICT team identified two preconditions for applying local situation and four local requirements for knowledge management system.

There are three preconditions to be carefully considered for introducing the system: 1) Low speed Internet access, 2) unstable power supply, 3) expected number of users. DPL has ADSL Internet connection which can download up to 1 M bps (bit per second). However, there are around 30 computers sharing the connection. Also, the connection is unstable. Power supply is not stable especially in rainy season from April to October. Because of that, hard disk drives in PC crash two or three times a year. As the number of users for knowledge management system is around 10, the system can be designed for relatively smaller scale.

System requirements were discussed in DPL in October 2011. Following are the four requirements identified to build appropriate knowledge management system.

- 1) Accessibility: Accessibility means that project information and knowledge need to be easily shared between ICT team and Tokyo Tech team members as well as among the internal members of DPL.
- 2) Ability to store various kinds of file formats: Because project information and knowledge were recorded in various kinds of file formats, the system is required to store information in different format. For example, design document for database system was created by Excel format, and teleconference minutes were recorded as text file.
- 3) Data modifiability: Project activities have possibility to be modified according to local needs and functionality of the system after first development. Thus, created contents in the system should be

editable.

- 4) Easy to search contents: It is preferable to have a function to obtain necessary contents easily from hundreds of accumulated information. Also user will be changed as time advances, system are required to obtain necessary contents in simple way for beginners.

Considering two preconditions and four local needs, three knowledge management system solutions were suggested.

- 1) In-house system: Local team members can build their own knowledge management system by utilizing PHP with PostgreSQL. PHP is a script language to build web application. PostgreSQL is a database server. Both are widely used around the world.
- 2) Free and open source software: Free software named MediaWiki, which is a wiki package written in PHP and is originally developed for Wikipedia, has all the required functionalities [6]. *"Wiki is a website that allows the creation and editing of any number of interlinked web pages via a web browser using a simplified markup language or a text editor"* (Wikipedia).
- 3) Cloud computing: Internet services to share the documents, such as Google Drive, Evernote [7] and Dropbox, can also fulfill all the requirements.

As the local team has already been introduced PHP and PostgreSQL for the database development and management [8], they can implement the knowledge management system with the flexibility to match their own needs. In contrast, the technical succession of this system itself in the future is an additional burden to the local team. Considering software development, PHP and PostgreSQL would be possible to update for long term because they has large number of users and developers. Therefore, sustainability of this solution depends on fitting design with local needs.

MediaWiki requires PHP and PostgreSQL, but the team does not need to launch a new server. MediaWiki is equipped with full-text searching functionality. MediaWiki can handle text, graphics and data files, and user can edit the contents easily. Although it is free software, customization to respond to specific local needs is difficult.

Cloud computing does not need any local server. Instead, everything can be accessed via Internet. Among the cloud computing services, software as a service (SaaS) is the most suitable service to the end users. Users can run the application via Web browser and data files are stored on cloud servers. There are free services

that satisfy the requirements. In developed countries, the introduction of cloud computing is massive as they can drastically save the cost for system administration. However, it is not necessarily feasible solution in the project site due to very slow Internet connection. Although, it is considered that this solution is a sustainable way to keep data.

As a result of discussion with local ICT team, Evernote was selected as a knowledge management system. Three reasons were raised for the introduction of Evernote: 1) Easiness to introduce the system, 2) maintenance-free and 3) ability to share contents between Tokyo Tech and local ICT team members.

First, Evernote does not have complicated installation on the server because it has client software for PCs as well as web interface. Users including local ICT team and Tokyo Tech team can concentrate in contents management. Second, Evernote does not require internal administrator to maintain the system. Evernote corp. provide system maintenance and software updates. Third, Evernote enables to share all contents between local ICT team and Tokyo Tech team because contents are stored in the server on the Internet. Synchronization is performed using client software on PC.

### 3.2 Training for Building and Using Knowledge Management System

The next step of introducing Evernote as knowledge management system was the provision of training on the use of client software and method of knowledge management. Seven training components for knowledge management were developed as followings: 1) Installation of Evernote client software; 2) input method for contents; 3) search necessary contents; 4) backup and restore; 5) get previous updating data; 6) clipping web page to Evernote; and 7) practice of inputting materials.

In order to conduct training, relevant knowledge management system manuals were prepared. The training was conducted at ICT center in mid-December in 2011.

### 3.3 Building Knowledge Management System

Past project information was retrieved from hard disks in Tokyo Tech and local ICT team. In total, 355 contents were identified.

Table 1 lists the identified contents. Technical documents mainly include system design documents, training materials, and software operational manual (Fig. 1). Project report was composed of activity report created by students. Presentation to public refers presentation materials shared at local workshop and symposium.

Minutes includes records of regular weekly tele-

Table 1: Identified contents (as of June 2012)

Category	Number of contents
Technical document	133
Project report	44
Presentation to public	88
Minutes	75
Knowledge management instruction	9
Administrative document	5
<b>Total</b>	<b>355</b>

Source: created by author, July 2012

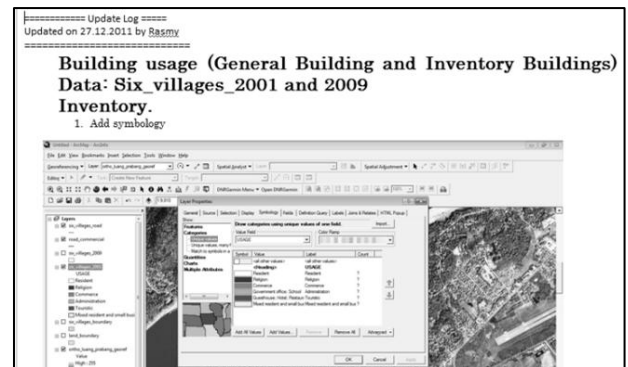


Fig. 1 An example of operational manual

Source: Evernote created by ICT team, 2010

conference between local ICT team and Tokyo Tech team. Knowledge management instruction refers to documents for building and introduction training of knowledge management system. Administrative document includes contents which are not categorized as above such as list of members, useful address list.

Local ICT team members conducted input activity after introductory training. Input activity follows the standard template which require an individual to fill title, author, tag (keyword) for all the contents. Evernote can accept text form, so text files were typed directly. Other file formats were uploaded as an attachment.

## 4 Evaluation Analysis

To evaluate usefulness, effectiveness, and sustainability of introduced knowledge management system using Evernote, two evaluation methods (case trials and interviews) were conducted.

### 4.1 Case Trials

Case trial simulates the situation where users are requested to use knowledge management system to retrieve necessary information. It has two objectives. First, advantages and problems of using Evernote are expected to be identified. Second, users can experience and become familiar with Evernote. Four cases are prepared simulating past activities: 1) Creating map of building usage using ArcGIS, 2) how to transmit GIS skills from experienced member to the beginner, 3)

building environment for database application and 4) fixing bug in PHP script. Ten members, four from local ICT team and six from Tokyo Tech team, participated in case trials from January to April, 2012. Case trials were conducted in pairs and one member observed participant's behavior such as referring manual and having question to other members, and recorded them with time.

The case trials identified three major findings. First, GIS manuals effectively assisted beginners' operation. Further, GIS manual/video can be a supportive tool to explain specific skills and knowledge for both beginners and skilled members. Second, screen shot is useful to cope with language barrier. Users can understand processes in the manual easily with visualization. Additionally, videos are especially useful for beginners to understand operations of software with step-by-step explanations. Third, manuals for PHP application need to cater for different level of users. Members who did not join the application development need specification document to understand basic of the system. Because members involved in the development have already known system's specification, they need only script diagram or log of bug fix to remind system schema.

#### 4.2 Interviews

To supplement case trials analysis, interviews were conducted to participants to obtain their feedbacks on the following three aspects: 1) Usability of the introduced knowledge management system, 2) necessity of the introduced knowledge management system, 3) sustainability of the introduced knowledge management system. In addition, participants were asked to provide their opinion on individual case trials. Interview conducted to all participants of case trials. Interview illustrated three major findings.

1. **Evernote functioned as a tool to avoid knowledge loss:** Evernote provided a platform to accumulate and share knowledge and information between Tokyo Tech and local ICT team. Evernote also contributed to efficient work by reducing frequency of asking help from others.
2. **Evernote cannot fully replace implicit knowledge:** implicit knowledge, such as technical tips or "know-hows" was accumulated through user's experience. Data stored in Evernote are not as intuitive as human experience, but remain as a good source of information repository.
3. **Updating contents in efficient manner is important for sustainable knowledge management:** Updating contents is needed for long-term use of Evernote. This research identified

four principles to record technical documents in Evernote efficiently: 1) table of contents should be created to facilitate overview to each project, 2) high resolution screen shots is recommended to be used, 3) captions should be written in each screen shot to give supplemental explanation, 4) reviewing manual with colleagues is important to check mistake and to promote understandings.

## 5 Conclusions

In the world heritage town of Luang Prabang in Lao P.D.R., various activities using information technology have been introduced since 2003. Valuable knowledge and skills related to heritage management accumulated over time were not successfully shared nor utilized by project members due to high human mobility. To cope with such condition, knowledge management system was introduced following the model proposed by Milton. Evernote was selected as a most feasible method of knowledge management system, reflecting local condition. A total of 355 contents were covered in Evernote, including technical documents, project documents, workshop information as well as local training manuals.

Evaluation of established knowledge management system was carried out using four case trials and interviews for the users. Evaluation analysis revealed that Evernote can serve as a potential tool to avoid knowledge loss. In addition, Evernote was found to effectively function to improve work efficiently. However, it is also important to note that Evernote cannot replace implicit knowledge through experience. Finally, continuous updating of contents was found vital for sustainable knowledge management.

## Acknowledgement

This work was supported by JSPS KAKENHI Grant Number 21404001.

## References

- [1] Digital Opportunity Initiative, "Creating a Development Dynamic; Final report of the Digital Opportunity Initiative," Accenture, Markle Foundation, UNDP, 2001.
- [2] Heeks R. B., "Most eGovernment-for-Development Projects Fail: How Can Risks be Reduced?," iGovernment Working Paper Series, Paper No. 14, IDPM, University of Manchester, 2003.
- [3] Yamaguchi, S. Y., Takada, J., Ooka, N., Kawaguchi, Y., (2006) "Application of Information Communication Technology to Promote Sustainable Development - Case Study: Luang Prabang, Lao PDR," 42nd Congress of International Society of City and Regional Planners (ISOCaRP), Istanbul, Turkey.
- [4] Gorelick, C., April K., and Milton, N., 2004, "Performance Through Learning: Knowledge Management in Practice," Burlington, MA: Butterworth-Heinemann.
- [5] Milton, N., 2009, Project knowledge management, Cincom systems Japan, pp.7-11. (in Japanese)
- [6] Wikipedia, [online] <http://en.wikipedia.org/wiki/Wiki>, (accessed on Oct. 20, 2011)
- [7] Evernote. [online] <http://evernote.com> (accessed on July 2, 2012)
- [8] Okumura, T., Leong, C., Takada, J., and Yamaguchi, S. Y., "Analysis on Sustainability of Free and Open Source Software (FOSS) Application ~Database Management of World Heritage Site of Luang Prabang, Lao P.D.R.~, " JASID 12th spring conference, Tokyo, pp. 137-138.

# Antenna Pattern Reconstruction Using Spherical Harmonics and Its Application to Double-Directional Channel Modelling

Student Number: 10M51605   Name: Yang MIAO   Supervisor: Jun-ichi TAKADA

To characterize antenna, the acquisition of its three-dimensional radiation pattern is very important. Spherical antenna measurement is a practical approach to measure antenna pattern in spherical geometry. However, due to the limitation of measurement range and measurement time, the measured samples may either be incomplete on scanning sphere, or be inadequate in sampling interval; there is a need to extrapolate and interpolate the measured samples. Spherical wave expansion provides a good approach to reconstruct antenna pattern in spherical geometry, and its cut-off (band-limited) property makes it possible to be analysed by the sampling theorem. This research identifies the limitation of pattern reconstruction by conventional algorithm, and proposes a novel approach to virtually deviate the antenna position by the phase shift of measured data. Numerical investigations are conducted to validate the proposed algorithm for both complete and incomplete data.

## 1 Introduction

The major concerns for wireless propagation channels recently are the measurement and modelling of directional properties of channel. The introduction of double-directional channel model enables to evaluate the performances of different antennas in certain propagation environment. To study the double-directional channel, the acquisition of full antenna pattern, the complex polarimetric antenna response in angular domain, is very important.

This thesis focuses on analytic and continuous antenna pattern reconstruction from measured samples. Spherical antenna measurement is a practical approach to measure the pattern of antenna under test (AUT), through scanning over a spherical surface in both azimuthal and elevation dimensions. However, due to the limitation of measurement time, coarse sampling interval is not sufficient, and there is a need to interpolate the measured pattern. On the other hand, due to the limitation of measurement set-up, the scanning may not be conducted on the whole sphere but only on some part of it, therefore the measured samples are incomplete and there is a need to extrapolate the incomplete data.

A review of antenna pattern extrapolation together with interpolation has been done and the related work are generally concluded as the iterative Fourier transform approach [1][2][3], the iterative spherical wave expansion approach [4][5][6], and the equivalent current approach [7][8]. The first two approaches utilize the plane wave representation and the spherical wave representation of antenna radiated field, respectively. While plane wave model has infinite angular resolution regardless of antenna size, the spherical wave model has finite angular resolution determined by antenna size. In this research, spherical wave function is utilized as the tool to reconstruct the antenna pattern.

The main objective of this research is to systematically study the antenna pattern reconstruction for both complete and incomplete spherical measurement by using spherical wave functions, and to investigate the effect of sampling interval and measurement range on the reconstruction accuracy.

## 2 Spherical Wave Expansion Technique

Spherical wave functions (SWF) [9], are homogeneous solutions to vector Helmholtz equation in the spherical coordinates. The radiation pattern outside the minimum sphere of antenna can be expanded into a weighted sum of spherical wave functions, i.e. spherical wave expansion (SWE) [9]:

$$\mathbf{E}(r, \theta, \phi) = k\sqrt{\eta} \sum_{s=1}^2 \sum_{n=1}^N \sum_{m=-n}^n Q_{smn} \mathbf{F}_{smn}(r, \theta, \phi) \quad (1)$$

where:

$m$ : mode indices for  $\phi$  direction

$n$ : mode indices for  $\theta$  direction

$\mathbf{F}_{smn}(r, \theta, \phi)$ : SWF, TE ( $s = 1$ ) and TM ( $s = 2$ ) mode SWF compose of a complete orthogonal set

$Q_{smn}$ : spherical wave coefficient (SWC)

$k\sqrt{\eta}$ : coefficient to ensure the normalization condition that unit SWC corresponds to  $1 \text{ W}^{\frac{1}{2}}$ ,  $k$  is the wavenumber

$N$ : truncation number

The minimum sphere of an antenna is defined as the smallest possible spherical surface, which is centred at the coordinate origin and could enclose the antenna completely. In this thesis, truncation number is determined by the minimum sphere radius  $r_0$  as  $N \geq [kr_0]$ , where the square brackets indicate the largest integer smaller than or equal to  $kr_0$ . The highest spatial frequency for a radiating field is  $1/\lambda$ , according to the sampling theorem, the minimum sampling interval should be  $\lambda/2$ , thus the sampling number is no more than  $[2kr_0]$  per circumference of the minimum sphere. To represent the radiation field, the spherical wave

Continuous flow-type experiments were carried out using a single-stage plasma driven catalysis system.

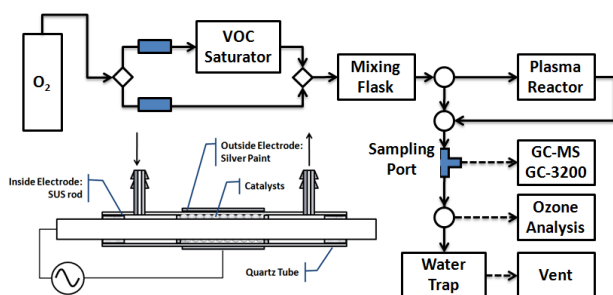


Figure 2. Flow chart of experimental set-up

The nonthermal plasma reactor is made of quartz tube with (OD=15 mm, L=200 mm, t=1 mm). Stainless steel rod with D=9 mm was fixed inside the center of the quartz tube as a high-voltage electrode and silver paint was coated outside the reactor as the ground electrode. The silver paint was coated to make a length of 50 mm around the outside body of the quartz tube to make the effective length of the reactor. Catalysts were placed within the effective length of the reactor and the plasma was generated by passing low-current high-voltage across the electrodes of the reactor.

### 2.3. Activity Experiments

Preliminary experiments involved initial ozone concentration generated by the plasma, effect of plasma on benzene concentration, and effect of the catalyst on ozone concentration. Initial ozone concentration at specified voltages were determined by allowing the feed gas to pass through the plasma reactor without benzene and the catalysts. The effect of plasma on benzene concentration was tested by allowing the pollutant to go through the reactor while the plasma was turned on and testing its concentration afterwards. Finally, the effect of the presence of the catalyst on ozone concentration was tested by placing the catalysts within the plasma region and turning on the plasma then testing the resulting ozone concentration.

Before doing activity tests, the catalysts in the reactor were saturated with gas-phase benzene until adsorption equilibrium was reached. An initial concentration of 200 ppm of benzene was used for the experiments. After adsorption equilibrium, activity tests were performed by varying the applied voltage to the reactor and effluent composition and concentrations were monitored.

### 2.4. Chemical and Electrical Analysis

Benzene concentration and its by products were analyzed by using GC-MS equipped with and Equity-5 column. GC-TCD was used to monitor CO<sub>2</sub> and CO concentration of the effluent gas and a

gas detection tube system was used to monitor ozone concentration. Carbon balance, CO<sub>2</sub> yield and selectivity were calculated as follows:

$$CB = \frac{[CO_2] + [CO] + n[\text{by-products}] + 6[C_6H_6]}{6[C_6H_6]_0} \times 100$$

$$Y_{CO_2}, \% = \frac{[CO_2]}{6([C_6H_6]_0 - [C_6H_6])} \times 100$$

$$S_{CO_2}, \% = \frac{[CO_2]}{[CO_2] + [CO]} \times 100$$

High-voltage supplied to the reactor was generated by connecting the reactor to a neon transformer, (LECIP Co. Ltd., 100-A-15HCS) connected to a volt slider and a 50 Hz, 100 V AC power supply. The applied voltage,  $V$ , was measured with a 1000:1 high-voltage probe (Agilent Technologies, N2771B) and the charge,  $Q$ , was determined by measuring the voltage across a 10 nF capacitor connected in series with the ground line of the reactor. The signals were recorded by an oscilloscope (GW Instek, GDS-1072A-U) by averaging 64 scans. Waveform data obtained from the oscilloscope were processed to produce  $V$ - $Q$  diagrams. The discharge power,  $P_{dis}$ , and the specific input energy, SIE, to the reactor were calculated using the  $V$ - $Q$  Lissajous method. From the  $V$ - $Q$  diagram, the area was calculated corresponding to the electric energy consumed per voltage cycle and then was multiplied to the frequency of the feeding voltage to obtain discharge power. The specific input energy was calculated by dividing the discharge power with the gas flow rate.

### 3. Catalyst Characterization

TG-DTA was performed on the base TiO<sub>2</sub> to determine the effect of temperature on the catalyst. During the calcination step for IP method, depending on the temperature used, the resulting TiO<sub>2</sub> phase may either be anatase, rutile or a mixture of both. Based from the TG-DTA results, only an exotherm for the evaporation of water at ~100°C was present indicating no other physical or chemical transformations occurred on the catalyst. For the IP method, a calcination temperature of 500°C was chosen.

The bulk crystal structure and crystal size of the prepared catalysts were analyzed by XRD (Figure 3). Results show that all prepared catalysts retained its anatase crystal structure with a crystal size of ~20 nm. With increasing Ag loading, the intensity of the anatase peak at  $2\theta = 25^\circ$  slightly decreases. Although silver was deposited on the catalyst, no peaks relating to silver or any of its oxides were detected by XRD due to the small amount of the loaded metal on TiO<sub>2</sub>.

number should be no less than  $[2kr_0]$ , therefore the bandwidth (truncation number) should be at least  $[kr_0]$ ; by increasing the bandwidth, the evanescent components of the field can be retained.

For the application of SWE, generally SWC are unknown; measured field samples at certain sphere are achieved to calculate SWC, once the SWC have been solved, the field can be calculated at anywhere outside the antenna minimum sphere. Generally, there are two approaches to achieve SWC: inner product method and least square solution method.

1) Inner product method:

$$Q_{1mn} = \frac{1}{(h_n^{(2)}(kr))^2} \frac{(-1)^m}{k\sqrt{\eta}} \quad (2)$$

$$\int_{\phi=0}^{2\pi} \int_{\theta=0}^{\pi} [E_{\theta}(r, \theta, \phi) \cdot \mathbf{F}_{1,-m,n}^{(4)}(r, \theta, \phi) \cdot \hat{\theta} + E_{\phi}(r, \theta, \phi) \cdot \mathbf{F}_{1,-m,n}^{(4)}(r, \theta, \phi) \cdot \hat{\phi}] \sin \theta d\theta d\phi$$

$$Q_{2mn} = \frac{1}{\left\{ \frac{1}{kr} \frac{d}{d(kr)} (kr h_n^{(2)}(kr)) \right\}^2 + n(n+1) \left( \frac{h_n^{(2)}(kr)}{kr} \right)^2} \quad (3)$$

$$\frac{(-1)^m}{k\sqrt{\eta}} \int_{\phi=0}^{2\pi} \int_{\theta=0}^{\pi} [E_{\theta}(r, \theta, \phi) \cdot \mathbf{F}_{2,-m,n}^{(4)}(r, \theta, \phi) \cdot \hat{\theta} + E_{\phi}(r, \theta, \phi) \cdot \mathbf{F}_{2,-m,n}^{(4)}(r, \theta, \phi) \cdot \hat{\phi}] \sin \theta d\theta d\phi$$

This method has a strict requirement that the electric field should be given over the whole scanning sphere.

2) Least square solution method:

$$a_{mn} = k\sqrt{\eta} h_n^{(2)}(kr) \frac{1}{\sqrt{2\pi}} \frac{1}{\sqrt{n(n+1)}} \left( -\frac{m}{|m|} \right)^m Q_{1mn} \quad (4)$$

$$b_{mn} = k\sqrt{\eta} \frac{1}{kr} \frac{d}{d(kr)} (kr h_n^{(2)}(kr)) \frac{1}{\sqrt{2\pi}} \frac{1}{\sqrt{n(n+1)}} \left( -\frac{m}{|m|} \right)^m Q_{2mn} \quad (5)$$

$$\begin{pmatrix} a_{11} \\ \vdots \\ a_{mn} \\ \vdots \\ b_{11} \\ \vdots \\ b_{mn} \\ \vdots \end{pmatrix} = (X^H X)^{-1} X^H \begin{pmatrix} E_{\theta}(\theta_1, \phi_1) \sin \theta_1 \\ \vdots \\ E_{\theta}(\theta_{l_1}, \phi_{l_2}) \sin \theta_{l_1} \\ \vdots \\ E_{\phi}(\theta_1, \phi_1) \sin \theta_1 \\ \vdots \\ E_{\phi}(\theta_{l_1}, \phi_{l_2}) \sin \theta_{l_1} \\ \vdots \end{pmatrix} \quad (6)$$

where,

$$X = \begin{pmatrix} \mathbf{X}_A & \mathbf{X}_B \\ -\mathbf{X}_B & \mathbf{X}_A \end{pmatrix} \quad (7)$$

$$\mathbf{X}_A = \begin{pmatrix} \frac{-jm \bar{P}_n^{(m)}(\cos \theta_1)}{\sin \theta_1} e^{-jm\phi_1} \sin \theta_1 \cdots \\ \vdots \\ \frac{-jm \bar{P}_n^{(m)}(\cos \theta_{l_1})}{\sin \theta_{l_1}} e^{-jm\phi_{l_2}} \sin \theta_{l_1} \cdots \\ \vdots \end{pmatrix} \quad (8)$$

$$\mathbf{X}_B = \begin{pmatrix} \frac{d \bar{P}_n^{(m)}(\cos \theta_1)}{d\theta} e^{-jm\phi_1} \sin \theta_1 \cdots \\ \vdots \\ \frac{d \bar{P}_n^{(m)}(\cos \theta_{l_1})}{d\theta} e^{-jm\phi_{l_2}} \sin \theta_{l_1} \cdots \\ \vdots \end{pmatrix} \quad (9)$$

Achievable pseudo-inverse problem for complex matrix must satisfying:

$$\left( \frac{\pi}{\Delta\theta} + 1 \right) \times \left( \frac{2\pi}{\Delta\phi} \right) \geq N(N+2) \quad (10)$$

where  $\Delta\theta$  and  $\Delta\phi$  are the sample interval for  $\theta$  and  $\phi$  dimensions respectively.

### 3 Antenna Pattern Reconstruction for Complete Spherical Measurement

Through complete spherical antenna measurement, complete field samples over the whole scanning sphere are achieved:  $\mathbf{E}(\theta_{l_1}, \phi_{l_2})$ ,  $\theta_{l_1} \in [0 : \Delta\theta : \pi]$ ,  $\phi_{l_2} \in [0 : \Delta\phi : (2\pi - \Delta\phi)]$ . Therefore, the main task for antenna pattern reconstruction should be interpolation. Conventionally, SWC can be calculated from measured complete samples, and interpolation can be conducted with the reconstruction of antenna pattern by SWE.

According to the sampling theorem and the band-limited property of SWE, the sampling number per circumference should be at least twice the truncation number  $2N$ , that is, the sampling interval in measurement should be less than  $\frac{2\pi}{2N}$ . In practical measurement, AUT is not necessarily located in the center of global coordinate. For the same AUT, the minimum sphere radius when it is deviated from coordinate center is obviously bigger than the radius when it is centred, therefore, the required sampling number per circumference (sampling interval) for deviated case should be bigger (smaller) than that of the centred case.

Taken open-ended rectangular waveguide (OERW) as an example of AUT for illustration, the following figure shows the reconstruction error for both deviated case and centred case with the change of sampling number per circumference.

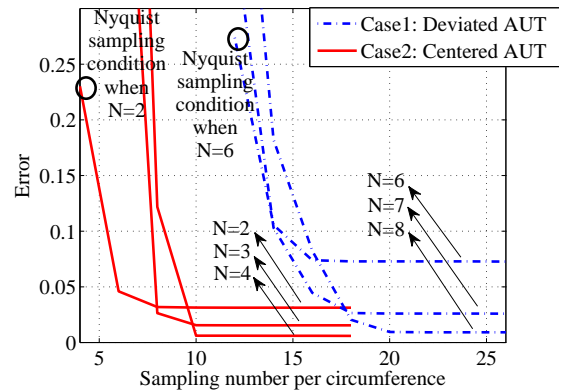


Figure 1: Error of reconstructed pattern by conventional interpolation approach for both deviated AUT and centred AUT



Surface morphologies and active metal dispersion on the catalyst surface was imaged using SEM-EDS. Figure 4 shows the different SEM images of the prepared catalysts and the base  $\text{TiO}_2$  and Figure 5, its Ag metal dispersion. The images show that IP catalysts formed small aggregate structures covering the catalyst surface due to its calcination where as for DP catalysts, did not have these aggregate structures. Digital mapping of Ag on the catalyst surface show that with increasing Ag loading, the Ag density on the surface also increases. DP catalysts showed very good Ag dispersion on the catalyst surface as compared to IP catalysts. This is attributed to the long aging time of 24 h in the IP method, as compared to only 2 h for DPN and 30 mins for DPH. This allowed the silver salt to enter into the pores of the catalyst by capillary forces instead of retaining it on the surface.

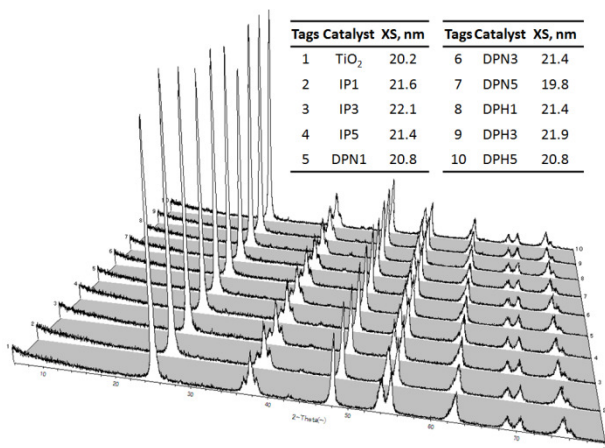


Figure 3. XRD patterns of prepared catalysts

Table 1 shows the characterization results of ICP-AES and  $\text{N}_2$  adsorption by BET method of the prepared catalysts. Actual Ag concentration of Ag/ $\text{TiO}_2$  catalysts were determined using ICP-AES. For IP catalysts, 3% and 5% showed only ~13% difference from the theoretical value but around 45% for the 1% Ag. For DPN catalysts, 21%~23% difference was observed, consistent for all Ag loading amounts. However for DPH catalysts, the difference reached up to 87%~95%. Even after 24h of sample digestion, DPH samples still contained a residue that was not dissolved within the solution. This was not observed from the other preparation methods. It is speculated that this residue contains the silver metal.

Surface area, pore volume and pore diameter of the prepared catalysts were analyzed by BET method using Autosorb 1 (Quantachrome). For IP catalysts, with increasing Ag loading, surface area decreased from 64.95  $\text{m}^2/\text{g}$  of the base  $\text{TiO}_2$  to 49.00  $\text{m}^2/\text{g}$  in the 5% Ag loaded catalyst. The pore diameter increased with Ag loading, 17.30 nm from the base  $\text{TiO}_2$  to 20.88 nm in 5% Ag/ $\text{TiO}_2$ , the total

pore volume slightly decreased from 0.2809  $\text{cm}^3/\text{g}$  to around ~0.2557  $\text{cm}^3/\text{g}$  indicating that the pores might have been blocked by the silver as it went inside the pores of the catalyst. DPN and DPH catalysts showed no significant change in surface area, pore volume and pore diameter.

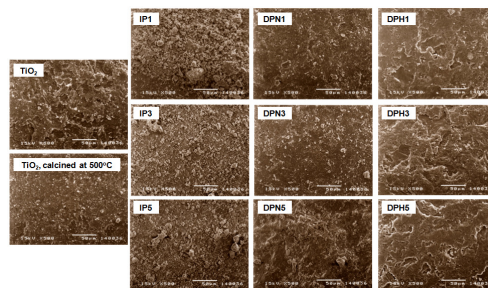


Figure 4. SEM images of Ag/ $\text{TiO}_2$  catalysts

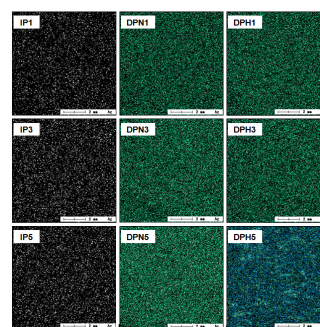


Figure 5. SEM-EDS Ag digital mapping of Ag/ $\text{TiO}_2$  catalysts

Table 1. Summary of ICP-AES and BET results

Catalyst	Theo wt%	Actual wt%	%Diff	Surface Area, $\text{m}^2/\text{g}$	Pore Vol., $\text{cm}^3/\text{g}$	Pore Diameter, nm
$\text{TiO}_2$	-	-	-	64.95	0.2809	17.30
IP1	1.02	0.56	45.19	61.64	0.2700	17.52
IP3	3.04	2.63	13.38	53.54	0.2540	18.98
IP5	5.02	4.34	13.56	49.00	0.2557	20.88
DPN1	1.00	0.77	23.49	64.73	0.2843	17.56
DPN3	3.01	2.34	22.13	64.60	0.2717	16.80
DPN5	5.04	3.93	21.93	63.28	0.2664	16.82
DPH1	1.00	0.12	87.95	65.54	0.2783	17.03
DPH3	3.00	0.15	94.85	65.14	0.2782	17.14
DPH5	5.02	0.24	95.13	64.94	0.2767	17.04

#### 4. Activity Results

The results of the effect of catalysts on ozone concentration are presented in Figure 6. It shows that ozone generation is directly proportional to the applied SIE to the reactor with the initial concentration reaching up to ~1940 ppm at the highest voltage setting. Placing catalysts inside the reactor decreased the discharge gap resulting in the formation of ozone at lower SIE values. A decrease in ozone concentration was also observed due to the catalytic decomposition of ozone to oxygen gas and its reaction with silver or silver oxide to form silver (II) oxide.

# DECOMPOSITION OF GAS-PHASE BENZENE USING Ag/TiO<sub>2</sub> PACKED NONTHERMAL PLASMA CATALYSIS REACTOR

Student Number: 10M51611

Name: Christian PANGILINAN

Supervisor: Hirofumi HINODE

This research describes the decomposition of gas-phase benzene using Ag/TiO<sub>2</sub> catalysts in a plasma driven catalysis system. Ag/TiO<sub>2</sub> catalysts were prepared using three methods: IP, DPN and DPH with varying Ag loading amount and were characterized by TG-DTA, XRD, SEM-EDS, ICP-AES and N<sub>2</sub> adsorption (BET). Benzene decomposition, by-product formation, carbon balance, carbon dioxide yield and selectivity and ozone utilization were used to measure catalytic performance of the prepared catalysts.

## 1. Introduction

Recently, raising environmental awareness and promoting environmental protection is becoming an issue of growing concern as our world is becoming more and more polluted. Industrialization has led to the emission of various substances in our atmosphere that pose significant threat to both human and ecological life.

One major group of these pollutants are volatile organic compounds (VOCs) and the emissions by industrial, commercial and agricultural processes are a major source of air pollution and is a concern for human health and the environment. Depending on their structure and concentration, VOCs together with nitrogen oxides and sulfur containing compounds reacts in a series of complex chemical reactions once released in the troposphere. These leads to the formation of secondary pollutants such as photochemical smog, secondary aerosol and suspended particulate matter and tropospheric ozone, acid deposition, and formation of organosulfuric compounds. Prolonged exposure to these chemicals are detrimental to human health and to the environment. [1-4].

In this research, treatment of gas-phase benzene as a representative VOC with silver on titanium dioxide catalysts using a nonthermal plasma driven catalysis (PDC) system was investigated. Benzene is commonly used in manufacturing processes of materials such as polymers, plastics, resins and adhesives. Improper use and storage of this chemical leads to its vaporization and exposure increases the risk of cancer and other illnesses.

The specific objectives of this research are as follows: (1) preparation of Ag/TiO<sub>2</sub> catalysts using three different methods and characterization of the prepared catalysts, (2) nonthermal plasma reactor system assembly, (3) determination of catalytic activity of the prepared catalysts, and (4) evaluation of catalytic performance through pollutant decomposition, by-product formation, carbon

dioxide and carbon monoxide yield and selectivity, and ozone utilization.

## 2. Methodology

### 2.1. Catalyst Preparation and Characterization

Catalysts were prepared by three methods: impregnation method (IP), deposition-precipitation with NaOH<sup>[5]</sup> (DPN) and deposition-precipitation by H<sub>2</sub>O<sub>2</sub><sup>[6]</sup> (DPH) with varying Ag loading of 1%, 3% and 5% by weight. A summary of the methods is presented in Figure 1. Anatase type TiO<sub>2</sub> was obtained commercially from Sakai Chemical Industry Co., Ltd., Japan and was used as the base catalyst. The catalysts were characterized by TG-DTA, XRD, SEM-EDS, ICP-AES and BET.

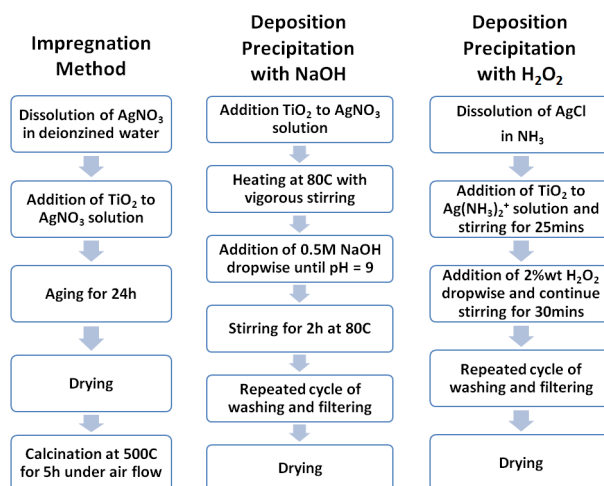


Figure 1. Catalyst preparation methods

Conventional IP method was compared to deposition-precipitation methods to determine the effect of metal dispersion on catalyst performance in PDC system. In the DP methods, slow addition of the precipitating agent facilitates the precipitation of silver on the catalyst surface as compared to aging in IP method.

### 2.2. Experimental Set-up

Figure 2 shows the flow chart of the experimental set-up and the reactor used.

Table 1: OERW simulation environment

Wavelength	27.3mm
Aperture size (a × b)	$0.84\lambda \times 0.37\lambda$
Aperture location	1) deviated case: move along x-axis by $\lambda$ from center (N=6) 2) center-located (N=2)
Observing distance	$45.5\lambda$

It is not difficult to find the following points. Firstly, for each case, the reconstruction accuracy will stay the same with adequate sampling numbers, and the bigger the truncation number is, the higher the reconstruction accuracy will be. Secondly, the Nyquist sampled,  $2N$  points per circumference, is not sufficient to completely reconstruct the pattern;  $2(N+1)$  points per circumference is enough, therefore the sampling interval should be no more than  $\frac{2\pi}{2(N+1)}$ . Thirdly, comparing between both cases when truncated at  $N = [kr_0]$  respectively, the reconstruction accuracy for the deviated AUT case from measured samples with adequate sampling interval is lower than that for the centred case; the required sampling interval for the deviated case is smaller than the centred case. In conclusion, the antenna pattern reconstruction by conventional approach is limited by the AUT location in global coordinate.

## 4 Antenna Pattern Reconstruction for Incomplete Spherical Measurement

Through incomplete spherical antenna measurement, incomplete samples on some part of the scanning sphere are achieved. Here is a typical incomplete measured data set:  $\mathbf{E}(\theta_{l_1}, \phi_{l_2})$ ,  $\theta_{l_1} \in [0 : \Delta\theta : \theta_{scan}]$ ,  $\phi_{l_2} \in [0 : \Delta\phi : (2\pi - \Delta\phi)]$ . The main task for antenna pattern reconstruction of the incomplete measured samples should be extrapolation as well as interpolation.

Conventional iterative SWE algorithm [4] [5] could extrapolate and interpolate the incomplete measured samples:

1. extend samples by zero-padding to cover entire sphere
2. calculate SWC using extrapolated data
3. calculate new field samples by SWE using SWC in step 2
4. updated data in step 3 are replaced by the measured samples within the scanned area

Steps 2 to step 4 are repeated iteratively.

For practical measurement, AUT is not necessarily located in the center of global coordinate system. Considering the deviated and centred OERW in Table 1 again, given absolutely sufficient sampling interval  $\Delta\theta = \Delta\phi = \frac{\pi}{60}$ , the effect of measurement range on reconstruction accuracy for both cases are investigated as in Figure 2.

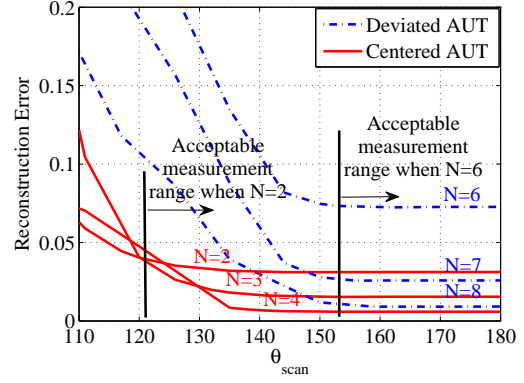


Figure 2: Error of reconstructed pattern with different measurement range for both deviated and centred AUT case

Obviously, the reconstruction accuracy will stay the same with adequate measurement range; for each case, the bigger the truncation number is, the higher the reconstruction accuracy. However, when truncated at  $N = [kr_0]$  respectively, the reconstruction accuracy for deviated case is lower than the reconstruction accuracy for the centred case. According to sampling theorem, the un-measured range on scanning sphere should be less than the biggest allowable sampling interval  $\frac{2\pi}{2(N+1)}$ . Therefore, the measurement range for elevation and azimuthal dimension should be no less than  $\pi(1 - \frac{1}{N+1})$  and  $2\pi(1 - \frac{1}{2(N+1)})$  respectively. Obviously, the bigger the minimum sphere is, the larger the measurement range should be. In conclusion, the reconstruction accuracy and the requirement for measurement range are limited by the AUT minimum sphere, furthermore limited by AUT location in global coordinate of measurement set-up.

## 5 Proposed Algorithm Applying Translational Phase Shift Technique

A novel approach is proposed to virtually transfer the AUT position by the translational phase shift of measured samples, assuming the scanning sphere radius is much bigger than the shifted distance. Through shifting the deviated AUT pattern to coordinate center, the minimum sphere radius will always be minimized; both the requirement for sampling interval and measurement range will be lower, at the same time the reconstruction accuracy will be increased correspondingly. The proposed algorithm guarantees the same requirement of both sampling interval and measurement range for the same AUT, and the antenna pattern reconstruction will not be limited by AUT location any more.

Given the incomplete measured samples distributed as  $0 : \frac{\pi}{6} : \frac{2\pi}{3}$  in  $\theta$  dimension and  $0 : \frac{\pi}{6} : \frac{11\pi}{6}$  in  $\phi$  dimension, for the deviated OERW case in Table 1, Figure 4 and Figure 5 shows the E-plane amplitude of reconstructed pattern by conventional algorithm and proposed algorithm respectively; obviously, the proposed algorithm could well reconstruct the incomplete samples while the conventional algorithm could not.

Catalytic activity was tested on benzene decomposition using PDC treatment. Results (Figure 7) show that DP catalysts were able to fully decompose benzene at low SIE values while IP catalysts were only able to reach ~20% decomposition. The low efficiency of IP catalysts is attributed to the decrease in its surface area from calcination.

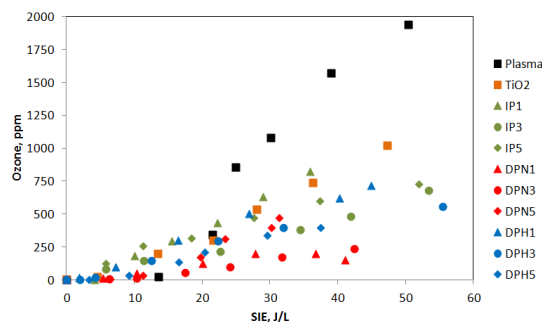


Figure 6. Effect of catalysts on ozone generation

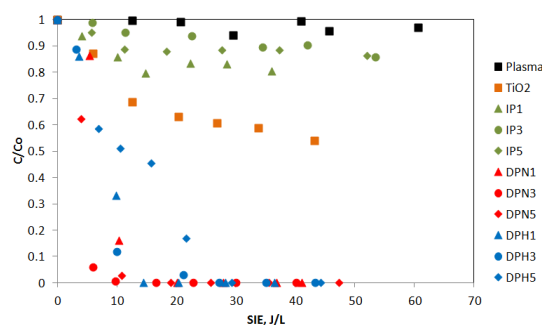


Figure 7. Benzene decomposition

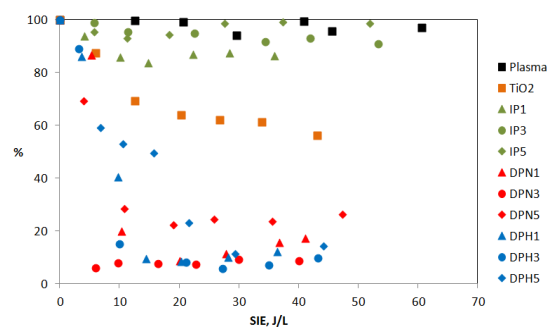


Figure 8. Carbon balance

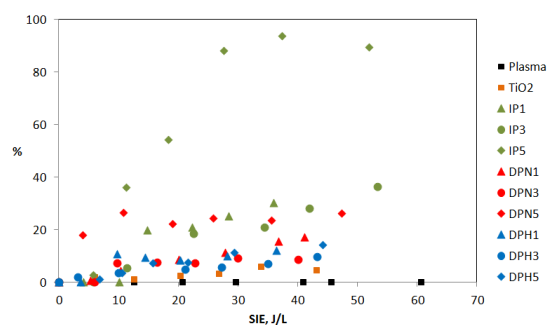


Figure 9. Carbon dioxide yield

Benzene decomposition is not the only factor considered in catalyst performance. GC-MS only detected benzene, oxygen and carbon dioxide with

no other carbon containing compounds in the effluent after treatment giving 100% selectivity to carbon dioxide. Carbon balance (Figure 8) and carbon dioxide yield (Figure 9), however, were not able to reach 100% which indicates the formation of intermediates such as carbon peroxy radicals or plasma polymerization of the pollutant which were deposited on the catalyst surface.

Ozone concentration after the treatment (Figure 10) was also monitored and results show a decrease in ozone concentration (from Figure 6) which indicates a synergetic effect of the system in the decomposition of benzene as well as ozone by PDC, with DPN5 catalyst fully decomposing the ozone produced.

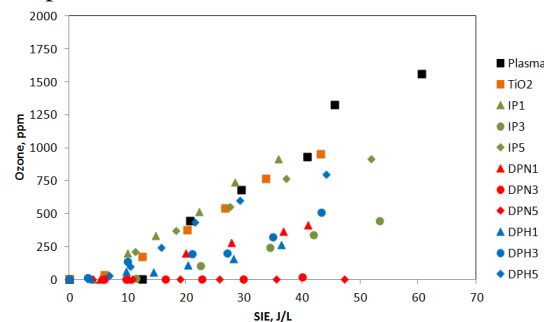


Figure 10. Ozone concentration after PDC treatment

## 5. Conclusions and Future Work

Prepared DP Ag/TiO<sub>2</sub> catalysts were able to fully decompose benzene at low SIE compared to IP catalysts which only reached ~20% with DPN catalysts also able to decompose the ozone generated in the system. Although benzene was fully decomposed, carbon balance and carbon dioxide yield was not able to reach 100%. Further increase in applied SIE is expected to give better results.

Future work includes the following: decomposition kinetics; use of different reactor configurations; use of different types of catalysts; and modification of process parameters such as voltage frequency and background gas.

## References

- [1] Chen, H. L., Lee, H. M., Chen, S. H., Chang, M. B., Yu, S. J., Li, S. N. Environmental Science Technology, 43 (2009) 2216-2227.
- [2] Dewulf, J., Van Durme, J., Leys, C., Van Langenhove, H. Applied Catalysis B: Environmental, 78 (2007) 324-333.
- [3] Whitehead, J. C. Pure Applied Chemistry, 82, 6, (2010) 1329-1336.
- [4] Passant, N.R. Retrieved from <http://pubs.rsc.org>, doi: 10.1039/9781847552310, published October 31, 2007.
- [5] Sandoval, A., Aguilar, A., Louis C., Traverse, A., Zanella, R. Journal of Catalysis 281 (2011) 40-49
- [6] You, X., Chen, F., Zhang, J. Anpo, M. Catalysis Letters, Vol. 102, Nos. 3-4 (2005)



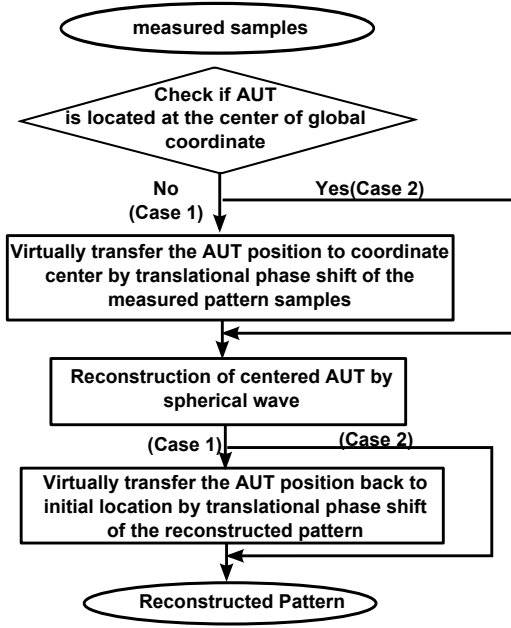


Figure 3: Proposed algorithm for both complete and incomplete spherical measurement

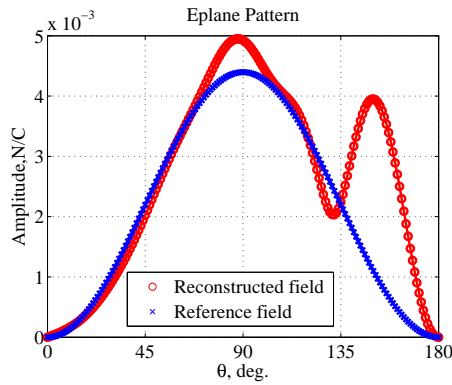


Figure 4: E-plane of reconstructed pattern by conventional algorithm

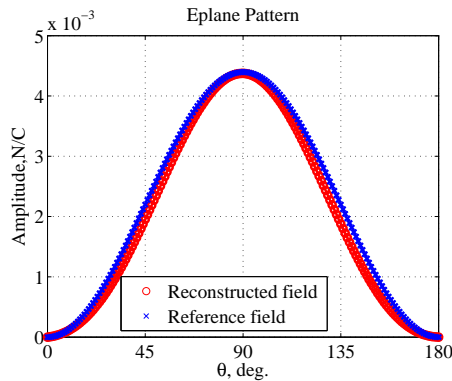


Figure 5: E-plane of reconstructed pattern by proposed algorithm

## 6 Conclusion and Future Work

This research systematically studied the antenna pattern reconstruction for both complete and incomplete spherical measurement, by means of spherical wave functions. The band-limited property of spherical wave expansion make it

possible to be analysed by the sampling theorem, and both sampling interval and measurement range can be decided by the minimum sphere of AUT in global coordinate system. The limitations of pattern reconstruction by conventional algorithms are identified, and algorithms applying translational phase shift are proposed and validated by numerical results for both complete and incomplete measured data.

In the end, the theoretical modelling of double-directional channel by spherical harmonics is studied through the equivalent circuit model, and the antenna complex amplitude can be extracted from the model. Therefore, to evaluate the performance of different antennas in certain propagation environment, the antenna pattern reconstruction is one of the important parts.

In future, channel sounding will be conducted, and channel parameter will be estimated according to the data of both channel sounding and antenna measurement. The double-directional channel modelling by spherical harmonics will be testified by comparison with the plane wave channel model.

## Acknowledgement

This work is supported by "The research and development project for expansion of radio spectrum resources" of the Ministry of Internal Affairs and Communications, Japan.

## References

- [1] R.W. Schafer, R.M. Mersereau, and M.A. Richards, "Constrained iterative restoration algorithm," *Proc. IEEE*, vol.69, pp.432-450, Apr. 1981.
- [2] A. Papoulis, "A new algorithm in spectral analysis and band-limited extrapolation," *IEEE Trans. Circuits Syst.*, vol. CAS-22, pp. 735-742, 1975.
- [3] M.D. Sacchi, T.J. Ulrych, and C.J. Walker, "Interpolation and extrapolation using a high-resolution discrete Fourier transform," *IEEE Trans. Signal Processing*, vol. 46, pp. 31-38, 1998.
- [4] W.Zhang, R.A Kennedy, and T.D. Abhayapala. "Iterative extrapolation algorithm for data reconstruction over sphere", in *Proc. IEEE ICASS 2008*, Las Vegas, Nevada, Mar. 2008, pp.3733-3736.
- [5] E. Martini, S.Maci, and L.J. Foged, "Spherical near field measurement with truncated scan area", in *processing of the European Conference on Antenna and Propagation*, pp.3412-3414, Rome, Italy, April 2004.
- [6] R.C. Wittmann, C. F. Stubenrauch, M.H. Francis, "Using truncated data sets in spherical scanning antenna measurements", *International Journal of Antenna and Propagation Volume 2012*.
- [7] J.R. Perez and J. Basterrechea, "Antenna far-field pattern reconstruction using equivalent currents and genetic algorithms", *Microwave Opt. Technol. Lett.*, vol. 42, no. 1, pp. 21-25, 2004.
- [8] L.J. Foged, L. Scialacqua, F. Saccardi, and F. Mioc, "Comparative investigation of methods to reduce truncation errors in partial spherical near field antenna measurements", *EuCAP 2012*.
- [9] J.E. Hansen, editor. *Spherical Near-Field Antenna Measurement*. London, U.K., Peter Peregrinus, 1988.

# Study of Private Participation Influence on the Efficiency Performance of Municipal Water Supply Management in Indonesia

Student number: 10M51628

Name: Nirmala Hailinawati

Supervisor: Naoya Abe

Increasing demand for safe and affordable water supply to people in developing countries shall be satisfied by good practices of water utilities. In year 2010, 58% of public-managed water utilities in Indonesia were showing low performance in various aspects. Thus, with expectation to turn around this condition, private participation has being initiated and growing diversely in many forms of contract, while also raised doubt of its implementation since several partnerships were performing under agreed target. This study aims to figure out the efficiency performance of municipal water utilities in Indonesia and examines whether the private participation is influencing the overall efficiency performance of water utilities based on the Data Envelopment Analysis.

## 1. Introduction

Increasing demand for safe and affordable water supply has become more and more essential in the developing world. A partnership between public and private entity has become one of alternative choices to answer a vast water demand and to turn around poor performance of publicly managed utilities.

Private participation was introduced in 1990's in Indonesia with the absence of national regulatory framework<sup>[1]</sup>. After more than two decades, while more private participation has been initiated in Indonesia, the pro and counter discussions on it have continued. The existing studies on this subject are mainly utilizing a direct comparison on net achievement of water utility.

This study impartially observes the relative efficiency performance of municipal water utility in Indonesia based on Data Envelopment Analysis (DEA). DEA able to identify "frontier" that is used to evaluate observation representing the performance of all the entities that are to be evaluated<sup>[2]</sup>. The term "efficiency performance" in this study is trying to explain *how efficient a water utility utilizes its available resources (inputs) to obtain an optimal overall performance (outputs)*. This study comprehensively embraced entire performance dimensions: technical, financial, organizational, and service. The objective of this study is divides into two main streamlines: 1) to uncover the efficiency profile of water utility in Indonesia, which include identifying best practices and classifying the group characteristics, and 2) to observe private participation influence on the efficiency performance, which include confirming the difference between water utilities with and without private participation and understanding the ownership structure of water utility with private participation.

## 2. Overview of private participation in water supply sector

### 2.1. Private participation in water supply sector

In early 1990s many governments implemented reform on their water supply and sanitation services, which often included delegating the management of utilities to private operators under various contractual arrangements<sup>[3]</sup>, noticeably in European countries like France and UK.

In developing countries, the initial contracts of private participation in water sector were the concession in Corrientes in Argentina and Buenos Aires in Brazil. These contracts then quickly followed by other

contracts in Latin America, Sub-Saharan Africa, and Asia, with increasing trend until now.

However, several cases of water PPPs contract terminations and failures to reach the targeted performance were noted, such as in Argentina (the country with the largest contract termination), Sub-Saharan countries, and in Malaysia<sup>[3]</sup>. This issue has considerably raising doubts of the PPPs implementation.

### 2.2. Water supply in Indonesia and private participation

The nature of water utilities in Indonesia is publicly managed, generally under municipality government. Performance evaluation released by government shows that until 2010 only around 41.94% of water utilities were performed healthy.

Bear by the Asian financial crisis in 1998, the conditions of most of the public water utilities in Indonesia have deteriorated. The Indonesian government reform after the crisis affected the direction of water supply management. With Law No.22/1999 on Local Autonomy, which transferred some infrastructure function to local government, more private participation on infrastructure sectors were encouraged.

The pro and counter discussions on private participation in water supply management were going on and getting sharper when taking utility's performance as point of view. The issue sparks when highlighted performance of the private sector concessionaires in Jakarta indicates that key original performance targets have been dramatically scaled back<sup>[4]</sup>, and the part privatization of Bali's piped water supply has led to increased inequality and restricted access for the poorest sectors of society<sup>[5]</sup>. Meanwhile, public water utilities still could not come out from unfavorable performance condition, as 58% of water utilities in year 2010 are in less satisfactory and critical condition. In this circumstances, many disputes whether ones' performances are better than others'.

## 3. Efficiency performance of water utility

What most evaluation method widely used by government, regulatory body, and scholars is the direct comparison of water utilities net achievement or comparison with the previous situation. This is a very straightforward method and easy to understand, however this method is letting us to imagine the similar size of water utilities being observed.

The evaluation by DEA approach has started the use frequently these days to assess the efficiency

performance of water utilities, with case study in UK, Italy, Japan, Portugal, and Australia.

### 3.1. Data envelopment analysis (DEA)

DEA is a non-parametric mathematical programming technique to assess the efficiency of homogenous units. The unit under study is called a decision making unit (DMU). The basic concept of DEA is rooted from a common efficiency ratio: output/input unit.

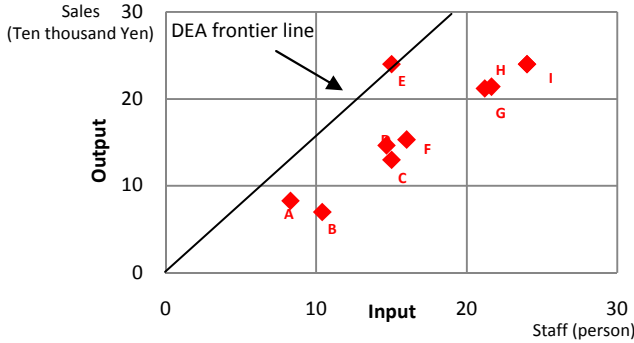


Figure 1. Frontier line where a single input and a single output model is applied

In a single input and a single output model, DMU with the highest slope (output/input) sets the “benchmark” to other DMUs. DEA frontier line designates the performance of the best DMU (point E) and measures the efficiency of other DMUs by deviations from E. Here, we move from the output/input ratio for each DMU to the “ratio of ratios”. Thus, the efficiency scores gained are *relative* within a specific dataset.

In this study, we are employing the basic DEA model namely CCR, input oriented, which named after Charnes, Cooper and Rhodes in 1978. The first step is to determine the weights of input ( $v_i$ ) and output ( $u_r$ ) of  $DMU_k$  ( $k = 1, 2, \dots, n$ ) using linier programming so as to maximize the ratio:

$$\max_{v,u} \theta = \frac{u_1 y_{1k} + u_2 y_{2k} + \dots + u_s y_{sk}}{v_1 x_{1k} + v_2 x_{2k} + \dots + v_m x_{mk}} \quad \dots(\text{eq.1})$$

Subject to:

$$\frac{u_1 y_{1j} + \dots + u_s y_{sj}}{v_1 x_{1j} + \dots + v_m x_{mj}} \leq 1 \quad (j = 1, \dots, n) \quad \dots(\text{eq.2})$$

$$v_1, v_2, \dots, v_m \geq 0 \quad \dots(\text{eq.3})$$

$$u_1, u_2, \dots, u_s \geq 0 \quad \dots(\text{eq.4})$$

The ( $v^*$ ,  $u^*$ ) obtained as an optimal solution for linier programming results in a set of optimal weights for  $DMU_k$ . The ratio scale is evaluated by:

$$\theta^* = \frac{\sum_{r=1}^s u_r^* y_{rk}}{\sum_{i=1}^m v_i^* x_{ik}} \quad \dots(\text{eq.5})$$

$v_i^*$  is the optimal weight for the input item  $i$  and its magnitude expresses how highly the item is evaluated. Similar for  $u_r^*$  which is the optimal weight for output item  $r$ .

Reference set is the efficient DMU which its performance is referred by other inefficient DMU(s). In the case where  $DMU_k$  has  $\theta^* < 1$  (CCR-inefficient), the weights ( $v^*$ ,  $u^*$ ) produces equality between the left and

right hand side (2.) since, otherwise,  $\theta^*$  could be enlarged. Let the set of such  $j \in \{1, \dots, n\}$  be:

$$E'_k = \left\{ j: \sum_{r=1}^s u_r^* y_{rj} = \sum_{i=1}^m v_i^* x_{ij} \right\} \quad \dots(\text{eq.6})$$

### 3.2. Model construction

A model for analysis for this study is constructed by depicted the main activities of water utility in Indonesia. The model concept is trying to embrace *how water production activity explains the distribution and accessibility achievement*. With regard to DEA, we describe three variables as “input” and eight variables as “output”. Table 1 shows the input and output variables and the comparison with the variables used in previous studies. In previous ones, the “production activities” tried to be represented by operating cost, while in this study represented directly by production capacity, production hours, and number of staff. More input and output variables are included in current study with aim to do the evaluation more comprehensive.

Table 1. Variables evaluated as input and output in water utility’s efficiency performance evaluation

No	Variable	Case study: Italy <sup>[6]</sup>	Case study: UK <sup>[7]</sup>	This study: Indonesia
Input				
1	Operating cost	O	O	X
2	Production capacity	X	X	O
3	Production hours	X	X	O
4	Number of staff	X	X	O
Output				
1	Total connection	X	O	O
2	Distribution capacity	O	O	O
3	Pipe length	X	O	X
4	Burst repair cost	X	O	X
5	Coverage area	X	X	O
6	Number of people per connection	X	X	O
7	Service hours	X	X	O
8	Idle capacity rate	X	X	O
9	Non revenue water	X	X	O
10	Average tariff	X	X	O

### 3.3. Datasets

The study evaluates 236 water utilities, treated as DMU, which considered representing around 60% of water utilities in Indonesia. Equal footing based on population size is applied for fair comparison among DMUs. Larger population size means higher responsibility “pressure” and complexity to the municipality government to provide safe water to the people. Population size in Indonesia is very varied and undeniably created huge gap between municipalities (from the population database in this study minimum value is 30,653; median is 326,636; and maximum is 9,583,247). This concern becomes our main consideration to split the database into two groups by one million population threshold: high ( $n_H = 39$ ) and low ( $n_L = 197$ ) populated municipality. Figure 2 shows the standard range of datasets in both groups.

Private participation being reviewed is located in 22 municipalities, in both high and low populated groups, which include 37 contracts. All of the private participation located in the relative urbanized area, compare to other areas in the same province, and have population more than 100 thousand people.

Nine types of contract discusses are: concession, build own operate (BOO), build operate transfer (BOT), managerial contract, rehab operate transfer (ROT), joint venture (JV), leasing contract, rehab upgrade operate transfer (RUOT), and rehab expand operate transfer (REOT).

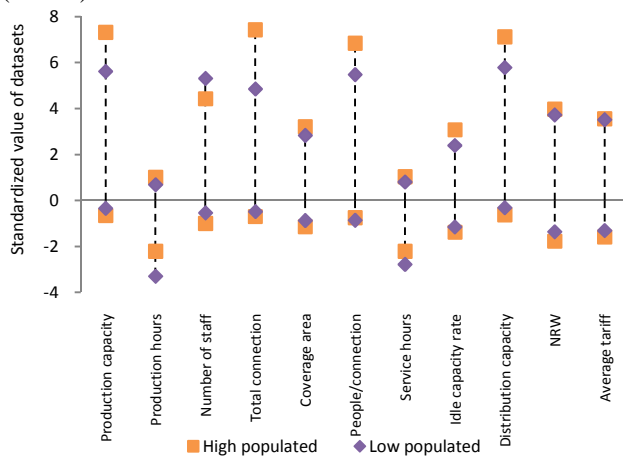


Figure 2. Standard range of datasets (mean = 0)

### 3.4. Relative efficiency performance

Figure 3 shows the summary results of efficiency scores by DEA in high and low populated groups.

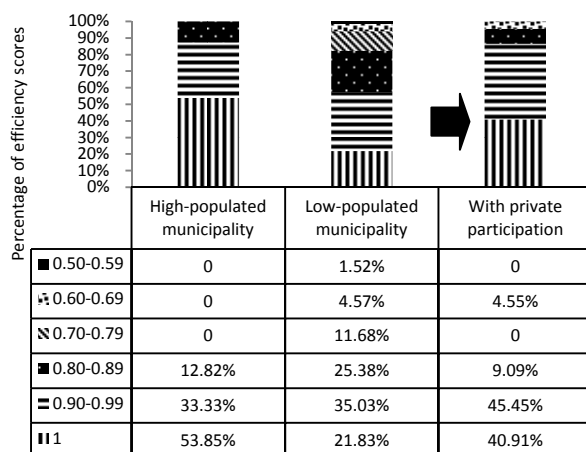


Figure 3. Summary of efficiency scores percentages

From the results we can see that high populated group is having higher magnitude and median of efficiency score. Also, we can infer that low populated group is having a wide range of efficiency performance.

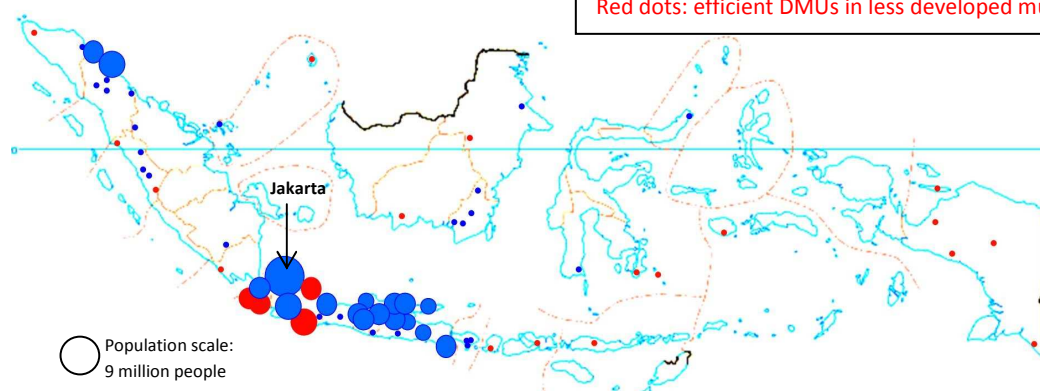


Figure 5. Geographical distribution of best practice water utilities in Indonesia

Further, we identified the efficiency score of “with private participation” water utilities from both high (11 DMUs) and low (11 DMUs) populated groups. In Section 5 we will tests whether private participation does influencing those efficiency scores or not.

## 4. Characteristics of water utility in Indonesia

We identified the characteristics of inefficient and efficient DMUs, in high and low populated municipality, based on its weighted value obtained from DEA. The methodology used is cluster analysis by agglomerative hierarchical clustering with Ward’s algorithm.

For inefficient DMUs we give recommendation to each DMU and identify to which efficient cluster it is projected. Figure 3 is showing the clusters of efficient DMUs in high populated group, and Table 1 is showing one example of recommendation for an inefficient DMU in high populated group.

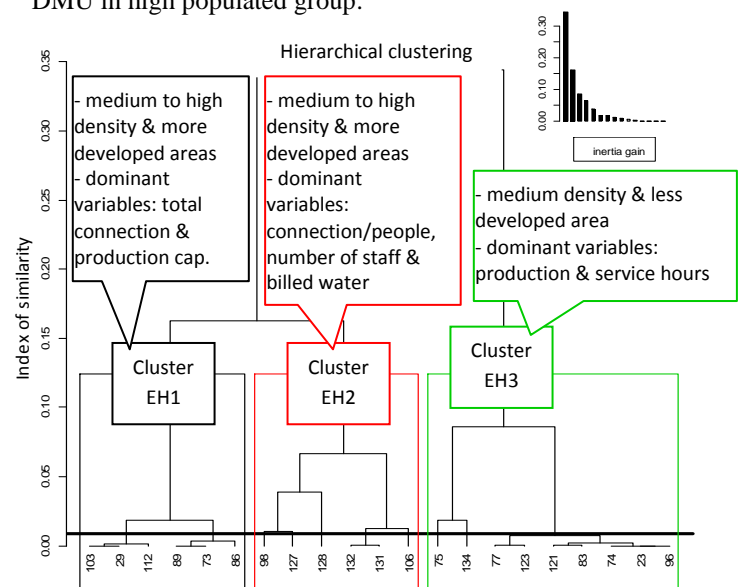


Figure 4. Clusters of efficient DMUs in high populated municipality

Table 2. Suggested input variables changes for DMU #126 of high populated municipality (efficiency score: 0.939, main referred to cluster EH3)

Variables	Unit	Projection	Changes
Production capacity	l/s	900.368	-6.02%
Production hours	Hour	22.556	-6.02%
Number of staff	Person	342.767	-26.29%

Blue dots: efficient DMUs in more developed municipalities  
Red dots: efficient DMUs in less developed municipalities



Besides, we also plotted the efficient DMUs in Indonesia map in Figure 6. From the map, we can conclude that the distribution of best practice water utilities with efficient performance is well-dispersed. It is a good sign that the inefficient water utilities could “learn” from their nearest neighbors, where social and economic condition are assumed as relatively similar, of how they efficiently utilizing available resources.

## 5. Performance different of water utilities with and without private participation

The statistics test conducted to confirm whether there is difference of efficiency performance between water utilities with and without private participation using non-parametric statistical Mann-Whitney U test.

The results from high (Mann-Whitney  $U_H = 145$ ,  $N_{H1} = 11$ ,  $N_{H2} = 28$ ,  $p > 0.05$ ) and low populated (Mann-Whitney  $U_L = 1271$ ,  $N_{L1} = 11$ ,  $N_{L2} = 186$ ,  $z_L = 1.350$ ,  $p > 0.05$ ) groups shows that the distributions of efficiency scores in with and without private participation groups are not significantly different.

Moreover, to be more convinced, we stepped back and do equal footing by density, region, and development status, and repeated the analysis. All of the results confirmed that we fail to reject null hypothesis by 5% significance level, which consistent with the previous finding.

Table 3. Summary of Mann-Whitney statistical test

Footing by	Category	U	$U_{crit}$	p-value	z ( $z_{crit}=1.96$ )	Remarks
Population	high	145	90	0.759		Fail to reject Ho
	low	1271	-	0.175	1.350	Fail to reject Ho
Density	high	247	-	0.433	0.773	Fail to reject Ho
	middle	288	-	0.927	0.087	Fail to reject Ho
	low	74	-	0.869	0.152	Fail to reject Ho
Region	west	893	-	0.103	1.603	Fail to reject Ho
	central	106	-	0.697	0.354	Fail to reject Ho
	east	14	1	0.695		Fail to reject Ho
Development status	more developed	1217	-	0.120	1.524	Fail to reject Ho
	less developed	65.5	-	0.821	0.219	Fail to reject Ho

## 6. Ownership structure of water utilities with private participation

The private participation is letting a private ownership to some extends. A majority shareholder is somehow dominating the direction of management. Given the results in Section 5, we would like to see the majority ownership profile of private participation in water utility in Indonesia. Here, we summarize the ownership percentage of local-private partners, foreign-private partners, and government for each type of contract.

From the results we can infer that foreign private shares is found higher in concession, JV, leasing contract, REOT, ROT and RUOT type of contract. Those types of contract are mainly involved in water treatment plant (WTP) operational and all operational activities that delegated to private partner. While, local private share is found higher in BOO and BOT type of contract, which involved WTP and distribution network to supply residential and industrial areas. In other hand, though having shares in some contracts, government has never

become majority shareholder in the contracts analyzed in this study

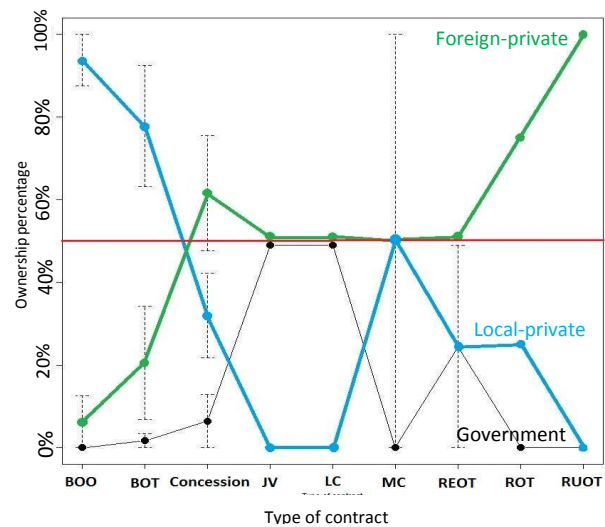


Figure 6. Plot of means and standard error of government, local-private, and foreign-private share for each type of contract

## 7. Conclusion

This study confirmed following results: 1) water utilities in high populated municipality is tend to perform more efficient than the ones in low populated municipality; 2) 53.85% and 21.83% of water utilities in high and low populated municipality, respectively, are showing an efficient performance. Also, geographical distribution of best practice water utilities is well-dispersed in Indonesia; 3) clusters of inefficient and efficient water utilities, along with their characteristics have been identified in this study; 4) efficiency performance of with and without private participation are not statistically different; and 5) foreign private shares is majority in concession, JV, leasing contract, REOT, ROT and RUOT, while local private shares is majority in BOO and BOT type of contract, in other hand, the government has never become majority shareholder.

## References

- [1] National Working Group of the Water Dialogues Indonesia (WDI), 2009, *Final Technical Report*, IDRC
- [2] Cooper, W. H., et al., 2006, *Introduction to Data Envelopment Analysis and its uses*, Springer
- [3] Marin, P., 2009, *Public-Private Partnership for Urban Water Utilities*, The World Bank Report
- [4] Bakker, K., 2007, *Trickle down? Private sector participation and the pro-poor water supply debate in Jakarta, Indonesia*, Geoforum 38 (2007) 855-868
- [5] Cole, S., 2012, *A political ecology of water equity and tourism: a case study from Bali*, Annals of Tourism Research, Vol.39, No.2, pp. 1221-1241
- [6] Romano, G., and Guerrini, A., 2011, *Measuring and comparing the efficiency of water utility companies: a data envelopment analysis approach*, Journal of Utilities Policy, 19, 202-209
- [7] Thanassoulis, E., 2000, *The use of data envelopment analysis in the regulation of UK water utilities: water distribution*, European Journal of Operational Research, 126, 436-453

# Contact-less Heartbeat Detection Method by using Microwave

Student ID : 10M51634 Name : Yanran LIU Supervisor : Jun-ichi TAKADA

## マイクロ波を用いた非接触心拍検出方法

劉 妍然

本論文では、マイクロ波を用いた、心拍の変動の検出に関する実験結果を報告する。心拍変動の変化は居眠り状態のひとつ重要なサインとなる。マイクロ波の透過係数の振幅または位相の変化によって、心臓の動きを直接とらえて、電波変化を検知することから、人体や車体の大きな振動にも耐性があると考えられる。4名の被験者に対して、周波数、偏波、アンテナ位置、アンテナ距離などをパラメータとして、従来法である透過係数の測定による検出法と比較を行った。その結果、提案法がより安定して心拍を検出できることを示すとともに、より確実に検出できる条件を明らかにした。

### I. INTRODUCTION

Nowadays, the demand for contact-less heartbeat detection has increased, especially for sleepiness detection in vehicles. Driver's sleepiness is one of the most dangerous causes for the traffic accidents which may end with fatal death. Several techniques to prevent driver from falling asleep at the wheel have been developed. One well known approach is using imaging sensors to count eye blinks while driving [1]. However, it is necessary to predict sleepiness early before drivers show signs of sleepiness so that preventing steps can be applied before accident is almost inevitable. We focused on heartbeat because the change of the pattern of heartbeat is a significant sign of sleep. It is influenced by posture, state of mind, surrounding temperature and so on [2]. But except for mental condition, if other factors are almost constant during driving, sleepiness becomes the major factor. Therefore, detecting the change of the pattern of heartbeat is very useful for preventing traffic accidents.

Heart Rate Variability (HRV) is a physiological phenomenon where the time interval between heartbeats varies. It is measured by the beat-to-beat variation of heart rate. The level of sleepiness can be estimated from the decrease in heart rate and the increase in high frequency component of heartbeat intervals [3]. Therefore, as long as we obtain the heartbeat interval in time domain, sleepiness can be judged.

The activity of heartbeat can be recorded by using electrocardiogram (ECG). It needs electrodes attached to the surface of skin and records ECG wave by an external device. Since measurement is done in a long term, extra mental stress may be applied to the driver. So sleepiness is difficult to evaluate accurately. Microwave radiation, however, can be transmitted to other dielectric medium, and information inside the body can be obtained from transmissive wave. Using this characteristic, heartbeat can be measured without the mental stress of the driver due to the attachment of

oximeter sensor. Therefore, we proposed a contact-less heartbeat detection method by using microwave. The sleepiness detection system using this method is very simple and low cost, so it can be used widely.

Doppler radar has been considered for the detection of heartbeat [4]. It can be used to measure the chest displacement due to heartbeat and respiration by the reflected signal. The variation of displacement due to respiration is between 4 and 12 mm, and the chest displacement caused by heartbeat alone is between 0.2 and 0.5 mm [5]. Heart Rate Variability (HRV) can be extracted from temporal variation of the phase of the reflection signal. But the detection is quite difficult when the motion of the body exceeds the order of the wavelength [6]. Another approach is using ultra-wideband (UWB) pulse radar. It can detect the small motion of the body surface and also is robust to the large motion of the body [7]. However, the use of microwave UWB is prohibited in the vehicle in Japan, while quasi millimeter wave UWB has the potential interference as it is used for inter-vehicular radar [8].

### II. MEASUREMENT

#### *Chest Cross sectional view*

Principle of the proposed method is to detect the change of the permittivity in biological tissues including heartbeat, arterial pulsation, and breathing. These motions are almost concentrated in the thorax, but also some include the abdomen. Figure 1 shows the chest cross sectional view. Two thirds of the heart is at the left of the body center. Heart drives blood into the arteries and the size of heart changes. So the motion caused can be detected at the skin surface. When each ventricle contracts, the heart ejects a surge of blood into the aorta, leading to pressure wave through the body [9]. Therefore, this motion does not occur at the same time as the chest wall motion due to the heartbeat. The delay from the chest to the pulse points could cause some

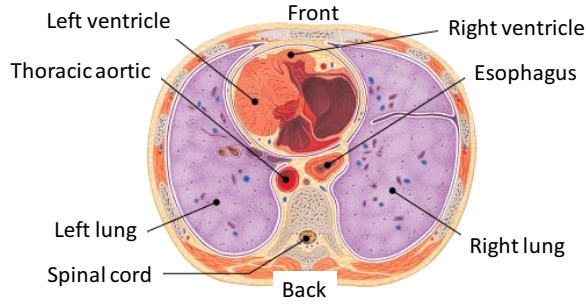


Fig. 1. Chest cross sectional view

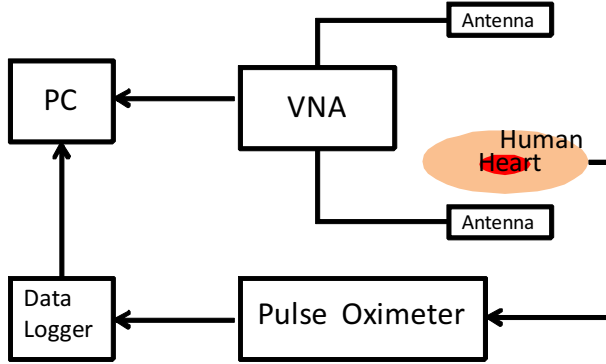


Fig. 2. Measurement setup

spreading in time of the signal during the measurement. The lungs are located in cavities on either side of the heart. In the measurement using microwave, transmission wave through body measures the permittivity of heart, aorta and lungs. As a comparison, measurements are also done using the reflection wave. Reflection wave in front of body mainly measures the motion of heart, and at back mainly measures the motion of lungs.

#### Measurement setup

To demonstrate the feasibility of heartbeat detection by microwave, Measurement are performed by using a vector network analyzer (VNA) and two antennas at 950 MHz and 10.5 GHz. Fig.2 shows the schematic experimental setup. VNA measures full 2-port  $S$ -matrix to compare the detection performances between transmission and reflection properties. One antenna is set in front as well as back side of the body. Two male and two female specimen were examined to check the gender dependency. Moreover, a pulse oximeter measures the pulse of blood flow of the specimen as reference for comparison. The VNA measurement and the oximeter measurement are done at same time.

Fig. 3 shows the locations of transmitter and receiver antennas. We assumed that the possible locations of the sensors are in the back of the seat for one side, seat belt, steering wheel or instrument panel for the other side in vehicle. The front antenna was connected to Port 1. The separation between body and front  $d_f$  is varied from 3 to 100 cm. The horizontal offset at driver's front  $s_f$  is varied from 0 to  $-6.5$  cm ('-' means left side distance from body

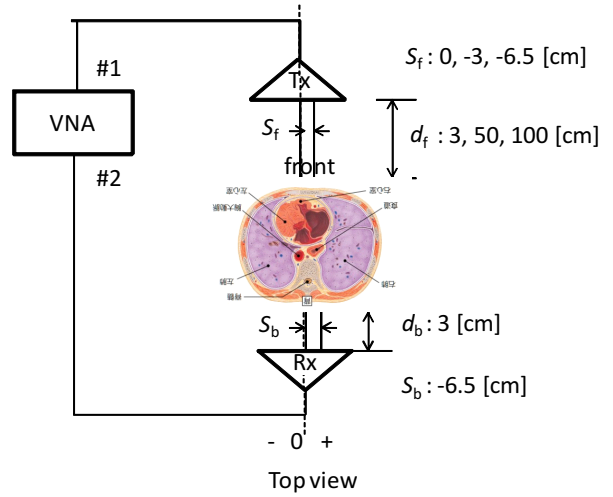


Fig. 3. Antenna locations

TABLE I  
MEASUREMENT SPECIFICATIONS

Equipment	VNA (Agilent) Data logger (NI USB-6221BNC) Pulse Oximeter
Frequency	950 MHz, 10.5 GHz
Car speed	0 m/s
Specimen	Body 1 (female), Body 2 (male) Body 3 (female), Body 4 (male)
Vector Network Analyzer:	
No. of points	1200
Sweep time	60 s
Sample rate	20 Hz
Pulse Oximeter:	
No. of points	60000
Sweep time	60 s
Sample rate	1000 Hz
Antenna polarization:	
950 MHz	Horizontal, Circular
10.5 GHz	Horizontal, Vertical
Antenna location:	
$d_f$	3 / 50 / 100 [cm]
$d_b$	3 [cm]
$s_f$	0 / -3 / -6.5 [cm]
$s_b$	-6.5 [cm]

center). The back antenna was connected to Port 2, and the separation between body and back  $d_b$  is 3 cm. The horizontal offset at driver's back  $s_b$  is  $-6.5$  cm. In the next section, the performance of heartbeat detection will be investigated in terms of these antenna locations and also the most suitable locations for the sensors will be determined. The measurement specifications are shown in Table 1.

### III. SIGNAL PROCESSING

#### HRV Extraction

To extract HRV, detect the peaks of signal takes an important role because an irregularity of heart beat can be determined through heartbeat interval. heartbeat interval has the largest amplitude among. Since we have the measurement data from VNA, and the pulse oximeter data as reference, the

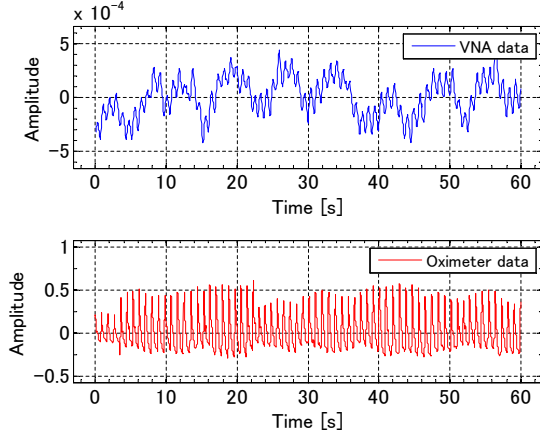


Fig. 4. Raw data: VNA and oximeter

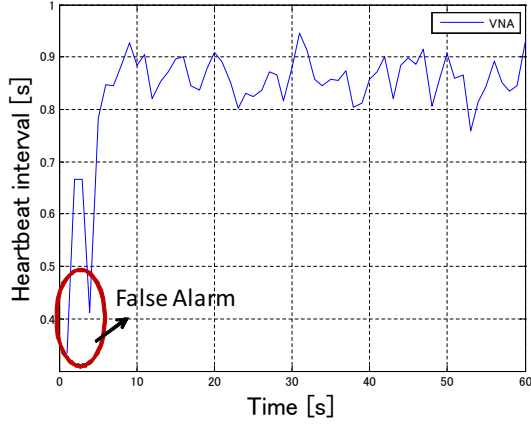


Fig. 5. Heartbeat interval (VNA data)

signal processing is divided into two steps. The first step is to determine whether heartbeat can be detected using the proposed method. The next step is to estimate the detection error.

Fig. 4 shows an example of raw data at 950 MHz. In the VNA data, it includes the information of heartbeat, respiration and noise. The oximeter data includes the pulse wave of specimen. According to the previous study, the peak among 1 ~ 2 Hz in frequency domain is the component of heartbeat. Therefore, band pass filter is applied for all data. Pass band frequency is chosen to be 1 ~ 2 Hz.

The sampling rate of VNA data is 20 Hz, for oximeter data it is 1000 Hz. Before detecting the peaks, VNA data are interpolated to the same sampling rate as oximeter data. The time difference between two consecutive peaks corresponds to the heartbeat interval.

Fig. 5 shows the heartbeat interval extracted from VNA data. Since the normal heart rate is from 60 to 120 bpm, the threshold of false alarm is determined within 0.5 s ~ 1.0 s. If heartbeat interval out of this range is detected, false alarm occurs and the value is changed to the average of heartbeat intervals so that it will not affect the detection.

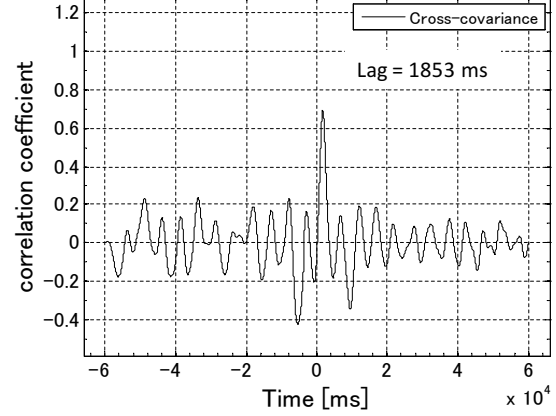


Fig. 6. Time lag between VNA data and oximeter data

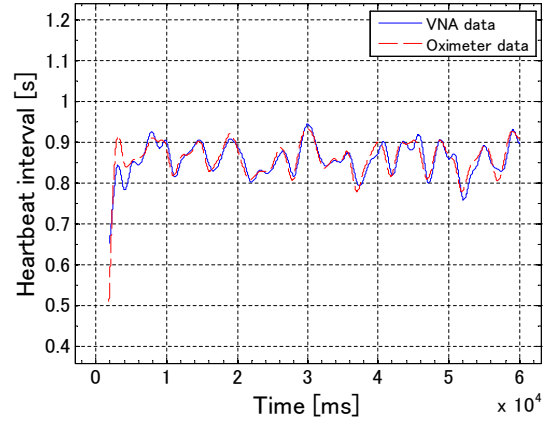


Fig. 7. synchronized Heartbeat interval data

As explained above, the oximeter data does not occur synchronized with VNA data. There is a time lag exist. To obtain the time lag between these two data, correlation coefficient is calculated and defined by:

$$C_{XY}(n) = \frac{E[(X_{p+n} - \mu_X)(Y_p - \mu_Y)]}{\sqrt{E[(X_{p+n} - \mu_X)^2]E[(Y_p - \mu_Y)^2]}} \quad (1)$$

where  $X$  and  $Y$  are heartbeat intervals of VNA data and oximeter data,  $\mu_X$  and  $\mu_Y$  are the mean values of  $X$  and  $Y$ . Before calculating, heartbeat intervals are resampled to millisecond unit to improve the accuracy. Therefore, here  $p = 1, 2, \dots, 60000$ ,  $C_{XY}(n)$  obtained the interdependence of  $X$  and  $Y$  by observing these two variables at times  $n$  milliseconds apart. Fig. 6 shows the result of correlation coefficient. For this case, the time lag is 1853 ms.

Fig. 7 shows the synchronized heartbeat intervals after shifting lag time. The solid line is VNA data, and the dashed line is oximeter data. If the difference time between two data is less than five percent of oximeter data, we assume that heartbeat is detected. Otherwise, heartbeat is misdetected. Miss detection rate is calculated for evaluation. For the data which heartbeat is detected successful, root-mean-square

error (RMSE) is used to estimate the detection error and defined as follow:

$$\text{RMSE} = \sqrt{E[(R_{\text{VNA}}(i) - R_{\text{oxi}}(i))^2]} \quad (2)$$

where  $R_{\text{VNA}}$  is heartbeat interval of VNA data, and  $R_{\text{oxi}}$  is heartbeat interval of oximeter data.

#### IV. RESULTS

By calculating RMSE and misdetection rate of extracted heartbeat intervals, frequency dependency, microwave type, antenna conditions, and signal feature are evaluated. We can observe that the detection performance at 950 MHz is much better than 10.5 GHz. Misdetection rate at 950 MHz is about 18 %, but more than 80 % heartbeat detection is failed at 10.5 GHz. Since the mechanism of proposed method is to measure the permittivity of heart, the electrical characteristics of biological tissue and cells have the frequency dependence. Permittivity decreases as the frequency increases. Therefore, heartbeat could be detected better at lower frequency.

The permittivity of heart, aorta, and lungs are measured using the transmission type of microwave. Reflection wave is also measured as comparison. As expected, from the raw data waveform, the displacement of heartbeat and respiration can be observed clearly from the transmission wave, but very difficult seen from reflection at back. Misdetection rate of transmission wave is smaller than reflection in front.

The orientation of the antenna influences to the heartbeat detection performance. At same measurement condition, we can observed that there is a very big difference depend on antenna polarization. Heartbeat could be detected only using horizontally polarized wave. From the results at different antenna positions, heartbeat could be detected best when  $d_f$  is 3 cm and  $s_f$  is  $-6.5$  cm. Therefore, antennas can be installed in the seatbelt at left side of driver in vehicle.

Moreover, the VNA data is complex number. From the results, phase component shows better detection performance than amplitude component. Using the best measurement condition above, Fig. 8 shows the results of heartbeat interval of four specimens. Because microwave measured the transmission through body, gender dependency is not seen obviously. But individual deference exists. Cardiac arrhythmia is found from specimen Body 2.

Therefore, the results can be summarized as follow:

- Heartbeat could be detected using phase component utilizing transmission property of microwave at 950 MHz.
- The orientation of the antenna influences to the heartbeat detection performance. Horizontal polarization showed better performance.
- Antenna should be placed at left side of body.
- Closer the sensor located to the body, the better heartbeat detected.
- Gender dependency was not observed using transmission wave, but individual patterns varied. Detection results are influenced by the health condition.

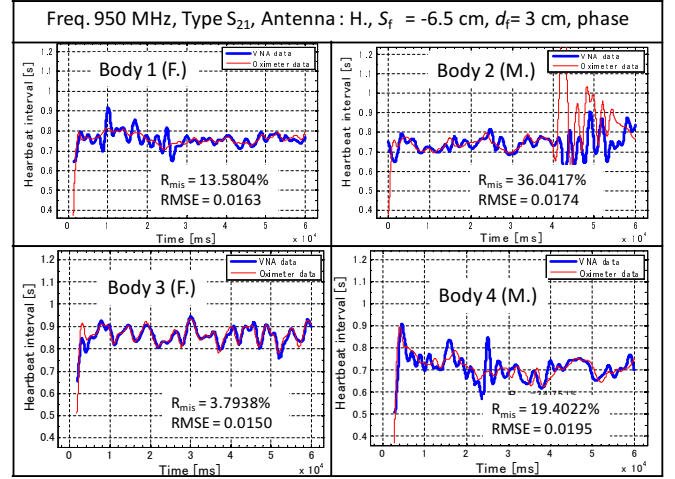


Fig. 8. Sample dependency

#### V. CONCLUSION

A new contact-less heartbeat detection method by using microwave was proposed in order to detect the sleepiness of drivers. Measurements were performed with different antenna positions at 950 MHz and 10.5 GHz. Heartbeat intervals are extracted from  $S$ -parameters measured by VNA and compared to the waveform measured by pulse oximeter.

For healthy specimens, extracted heartbeat intervals of proposed method are matched well with the oximeter data. 87.7 % of heartbeats are detected successfully. Since the level of sleepiness can be judged from the change of the pattern of heartbeat. It is expected that this study is very useful to predict driver from falling asleep while driving and reduce traffic accidents.

#### REFERENCES

- [1] S. Furugori, Y. Miura, N. Yoshizawa and C. Iname, "Analysis of Driver's Behavioral Change for a Long Term Driving," *JSAE Annual Congress*, no. 55-02, pp. 1-4, 2002.
- [2] M. Yanagidaira and M. Yasushi, "Method for Predicting Drowsiness," *PIONEER R&D*, Vol. 17, no. 1, 2007.
- [3] M. Yasushi and M. Yanagidaira, "Estimating Sleepiness during Expressway Driving," *J. Int. Soc. Life Inf. Sci.*, vol.21, no.2, pp.442-448, 2003.
- [4] D. Obeid, S. Sadek, G. Zaharia, and G. E. Zein, "Non-contact Heartbeat Detection at 2.4, 5.8 and 60 GHz: A Comparative Study," *Microwave Opt. Technol. Lett.*, vol. 51, no. 3, pp. 666-669, 2009.
- [5] G. Ramachandran and M. Singh, "Three-dimensional reconstruction of cardiac displacement patterns on the chest wall during the P, QRS, and T-segments of the ECG by laser speckle interferometry," *Med. Bio. Eng. Comput.*, vol. 27, no. 5, pp. 525-530, 1989.
- [6] H. J. Kim, K. H. Kim, Y. S. Hong and J. J. Choi, "Measurement of human heartbeat and respiration signals using phase detection radar," *Review of Scientific Instruments*, vol. 78, no. 10 pp. 104703-104703-3, 2007.
- [7] E. M. Staderini, "UWB radars in medicine," *IEEE Aerosp. Electron. Syst. Mag.*, vol. 17, no. 1, pp. 13-18, 2002.
- [8] Japan Ministry of Internal Affairs and Communications website. Available : <http://www.tele.soumu.go.jp/j/adm/freq/search/share/index.htm>
- [9] A. Owen, "Effect of increasing age on diastolic motion of the left ventricular atrioventricular plane in normal subjects," *International Journal of Cardiology*, vol. 19, no. 1, pp. 203-212, 1998.



# NUMERICAL STUDY ON LOCALIZED HEAVY RAIN USING LATEST URBAN PARAMETERIZATIONS AND HIGH-RESOLUTION SEA-SURFACE TEMPERATURE

Student Number: 10M18128    Name: Kumiko NAKANO    Supervisor : Manabu KANDA

高精度の都市地表面パラメータ・海表面温度を導入した都市型集中豪雨シミュレーション

仲野 久美子

高解像度の海表面温度（SST）と東京都心の詳細な修正粗度・運動量粗度・熱粗度を含む最新の都市パラメータを導入した「NEW」と、都市影響を考慮しない「OLD」の条件を設定し、メソ気象モデルWRFを用いた都市型豪雨シミュレーションを行い解析値の比較を行った。その結果、主に以下の事が明らかになった。①NEWの条件における都市上空での雨の強化と実況降雨の再現性の向上、②都市域の熱・水蒸気の滞留と、それに伴う海風侵入の影響による豪雨発生メカニズム、③東京都心の詳細な運動量・熱粗度による都心上空の風速場の再現性の向上

## 1. Introduction

Urban localized heavy rainfall (LHR) has become a serious issue especially during summer in the Tokyo metropolitan area. Although it has been still difficult to predict LHR due to the uncertainties of weather forecasting, urbanization is suspected to be one of the key factors to generate LHR. In the previous researches, urban effects on LHR have been studied using Weather Research and Forecasting (WRF) model, where some urban characters were parameterized, i.e. anthropogenic heat and moisture emission (AHE・AME) and urban canopy model (UCM) incorporating actual displacement height ( $d$ ) of Tokyo [1]. UCM, coupled with WRF, is a model used to calculate fluxes from each building facet by assuming uniform and infinitely-long street canyons. Although these parameters improved the reproductivity of LHR, they remain to be insufficient in terms of representing aerodynamic parameters of realistic building configurations and sea surface temperature. The former problems are summarized as follows;

1. Previous researches considered only actual  $d$  and treated the actual roughness length of momentum and heat ( $z_0$  and  $z_T$ ) constant, for urban areas.  $z_0$  and  $z_T$  are important parameters for drag effect of buildings.
2. The  $d$  was calculated from old-fashioned Macdonald's equation with building GIS information.
3. The area of  $d$  was previously available only within Tokyo. By default, UCM assigns constant surface roughness parameters in all urban areas. Kanda et al.[2] showed that Macdonald's equation largely underestimated  $d$  and  $z_0$  from highly detailed large eddy simulations (LES) incorporated with real urban morphologies of Tokyo.

Secondly, the representation of the sea surface temperature (SST) is also important factor for LHR occurrence in terms of

the surface boundary condition since the weather of Kanto region tends to be influenced by SST [3]. Therefore, the urban-sea interaction in Kanto region should be taken into account more carefully by improving the boundary condition.

In this research, to evaluate the urban effect on LHR with more detailed parameterizations, high special-resolution SST and aerodynamic parameters considering actual urban geometries of expanded area were incorporated into WRF for the better representation of the urban area and the sea character.

## 2. Improvement of parameters for WRF

$d$  and  $z_0$  were calculated with a new parameterization obtained from LES [2], using average building height ( $H_{ave}$ ), maximum building height ( $H_{max}$ ), height variance ( $\sigma_H$ ), plane ( $\lambda_p$ ) and frontal area indices ( $\lambda_f$ ), estimated from real urban morphologies of Kanto region. Those parameters with 1-km resolution in Tokyo were calculated with building GIS information with 1-m. resolution provided by CADCENTER and those of the other areas of Kanto region were estimated by incorporating four datasets: Google Maps, the Advanced Spaceborne Thermal Emission and Reflection Radiometer Global Digital Elevation Map of Ministry of Economy, Trade, and Industry of Japan and NASA, and a free high resolution digital elevation model and land use data from the Geospatial Information Authority of Japan. The previous  $d$  values by Shimoju et al. [1] calculated from McDonald's equation are much lower in Tokyo (Fig. 2-1): maximum difference is 50-m. Also, roughness length for heat ( $z_T$ ) was estimated in UCM by eq. (1)[4],

$$\ln\left(\frac{z_0}{z_T}\right) = \kappa B^{-1} = (1.2 - 0.9\lambda_v^{0.29})Re^{*0.25} - 2.0 \quad (1)$$

where  $Re^* (= u^*z_0/\nu)$  is roughness Reynolds number and  $\lambda_v$  is plane area vegetation ratio.  $u^*$  is the friction velocity and  $\nu$  is the molecular diffusivity of air ( $=1.46 \times 10^{-5} (\text{m}^2\text{s}^{-1})$ ).

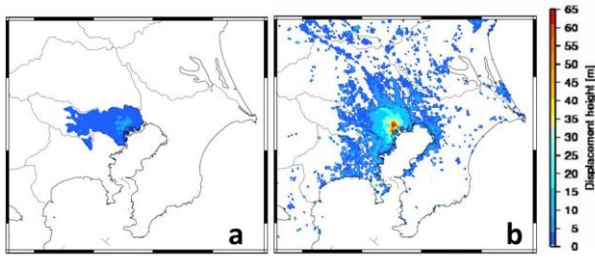


Fig.2-1 Displacement height (a: previous one , b: new one)

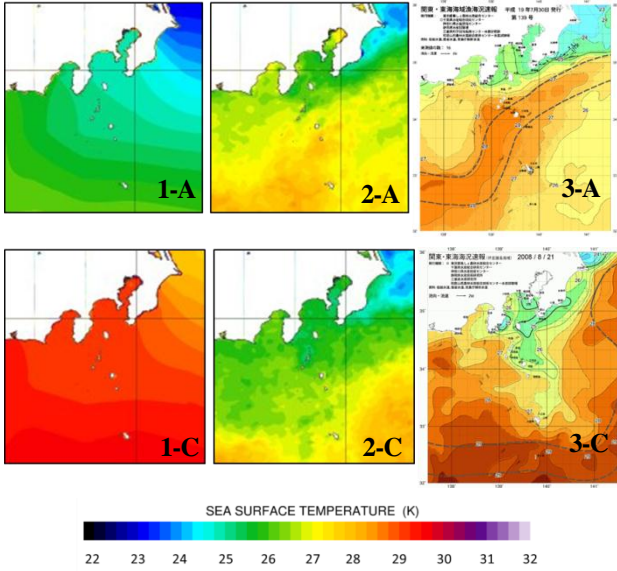


Fig. 2-2 Spatial distribution of SST at 13:00 of  
(A)29<sup>th</sup> July 2007 and (C)21<sup>st</sup> August 2008.

1,2 and 3 :TSK, MODIS SST, Observation respectively.

Sea Surface Temperature (SST) acquired from NASA Moderate Resolution Imaging Spectroradiometer (MODIS) was prepared for the simulation using monthly day and night time SST data linearly interpolated to the desired simulation date with 4-km resolution which is a significant improvement from the 25-km SST resolution commonly used for WRF models, named TSK. MODIS SST agrees well with the observed SST provided by the agricultural institute of Kanagawa (Fig. 2-2). Also, this figure shows that TSK overestimates actual SST. Maximum differences between MODIS SST and TSK range from 3 to 4 deg C during daytime.

### 3. Simulation Date and Cases

In order to investigate urban effects on LHR, the MODIS SST and the latest urban parameterizations, including AHE • AME and the new aerodynamic parameters of Kanto region, were applied to WRF using the improved UCM. Three analysis dates, 29<sup>th</sup> of July 2007, 16<sup>th</sup> and 21<sup>st</sup> of August 2008, were selected for the simulations, where an intense localized heavy rain occurred by the urban effect [1]. The simulation results were compared with those without MODIS SST and the urban parameterizations, named OLD (Table 3-1).

Table 3-1 Simulation cases

Name	SST	UCM	AHE • AME	$d, Z_0, Z_T$
OLD	TSK	NO	NO	Const.
NEW	MODIS	YES	YES	New parameterization
OLD+SST	MODIS	NO	NO	Const.
STANDARD	MODIS	YES	YES	Const.

Table 3-2 Additional cases for OLD and NEW

Name	IBC	Spin-up time
NCEP	NCEP	1 day
NCEP_1w		1 week
ECMWF	ECMWF	1 day
ECMWF_1w		1 week
JMA	JMA	1 day
JMA_1w		1 week

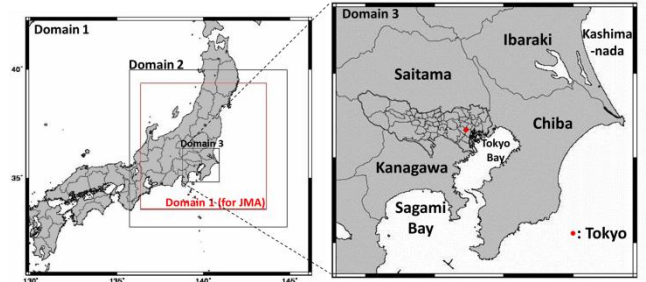


Fig. 4-1 Computational domains

Table 4-1 Grid Information of each domain (for NCEP and ECMWF)

Domain	Grid number	Grid size
Domain1	62×56×58	30 km
Domain2	171×171×58	6 km
Domain3	201×181×58	1.2km

Table 4-2 Grid Information of each domain (for JMA)

Domain	Grid number	Grid size
Domain1	171×171×58	4.8km
Domain2	201×181×58	1.2 km

To increase reliability of results, each day has six different setting of two kinds of spin-up period, one day or seven days, and three types of initial boundary conditions (IBC): Global Final Analyses from National Center for Atmospheric Research (NCEP), Global Atmospheric Reanalysis Interim by European Centre for Medium-Range Weather Forecasts (ECMWF) and Meso Scale Model Grid Point Value of Japan Meteorological Agency (JMA) (Table 3-2). Furthermore, sensitivity analysis for SST and the aerodynamic parameters was also conducted by incorporating MODIS SST into OLD\_NCEP and changing the new aerodynamic parameters of NEW\_NCEP to constant value in urban areas (Table 3-1).

### 4. Numerical settings

Simulation was conducted with three nests when using IBC of NCEP and ECMWF, and with two nests in case of using that of JMA (Fig.4-1). All of the smallest domains have the same grid size, 1.2-km. To validate the model, rainfall data from radar (AMESH) are also shown.



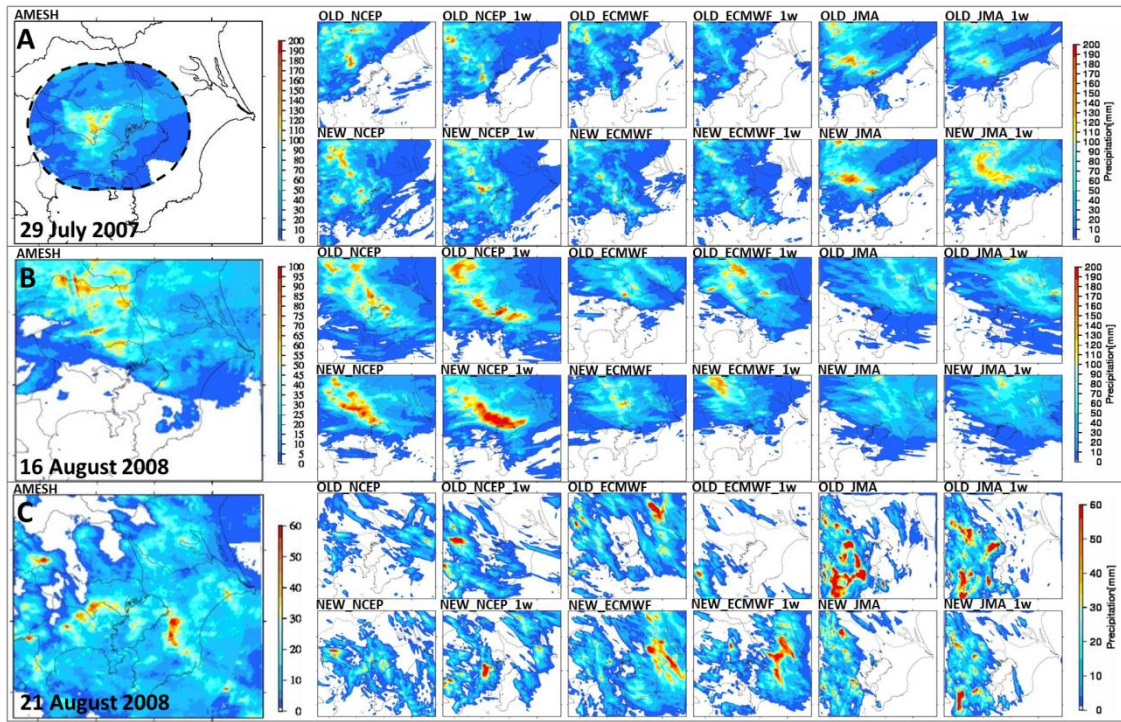


**Fig.4-1** Spatial distribution of total rainfall of AMESH and simulations from 12:00 to 24:00 of each analysis date  
(The area bounded by broken lines is the radar's coverage for 2007)

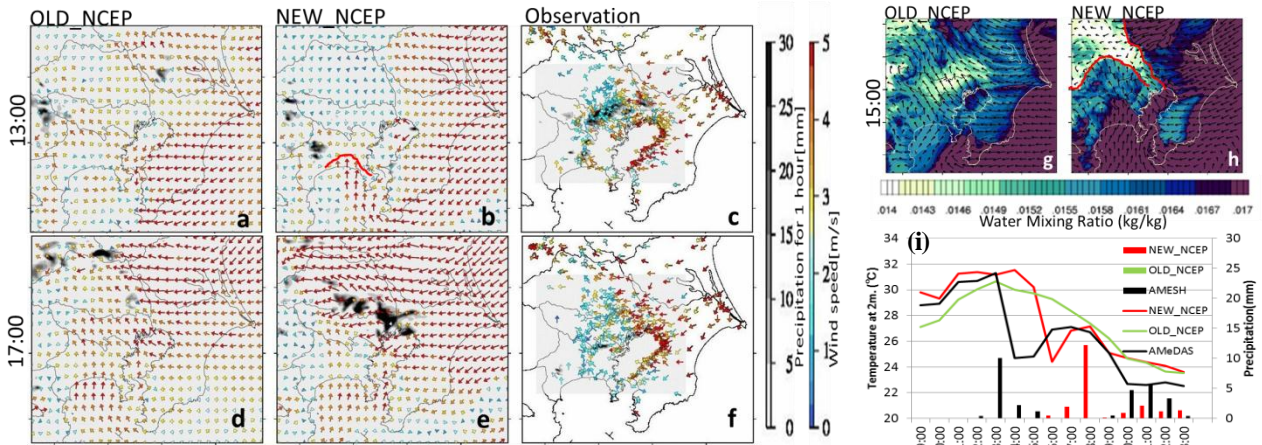


**Fig. 4-2** Results of OLD\_NCEP and NEW\_NCEP in 29 July 2007 comparing with observation. (a)~(f): 25-m. wind velocity and hourly precipitation snapshots at 13:00 and 17:00 JST, (g), (h): 1<sup>st</sup> atmospheric level water mixing ratio at 15:0 JST, (i): Time-series of 2-m. temperature and hourly precipitation AMeDAS and AMESH observation

## 4. Results

### a) Precipitation

**Fig 4-1** shows the total amount of rainfall from 12:00 to 24:00. NEW is likely to increase rainfall around Tokyo (**Fig 4-1**). Especially with IBC of NCEP, spatial distribution of rainfall agrees well with that of AMESH in all of the analysis dates although the amount of rainfall in the simulation is overestimated in the case of 16<sup>th</sup> August 2008. However, in 21 August 2008, the cases of NEW which used IBC of JMA did not show increase of rainfall around city. Potential temperature at the first level ( $T_a$ ) also tended to be lower than observation in using IBC of JMA for all analysis dates (not shown). This

means that IBC of JMA has low accuracy and IBC has a significant impact on the accuracy of LHR simulation.

### b) Mechanism of LHR

The mechanism of LHR can be represented well when using IBC of NCEP. In 29<sup>th</sup> July 2007, strong convergence occurred over the city by the sea breeze from Sagami bay and Kashima-nada. Water vapor advected by sea breeze increased rainfall around Tokyo in NEW, not simulated in OLD (**Fig.4-2g,h**). Even though onset of rain is delayed by around 4 hours in all cases of NEW (**Fig 4-2a-f**), NEW realized more accurate rainfall than OLD. Temperature of NEW above Tokyo becomes higher than that of OLD and close to observation(**Fig4-2i**) This improvement of NEW



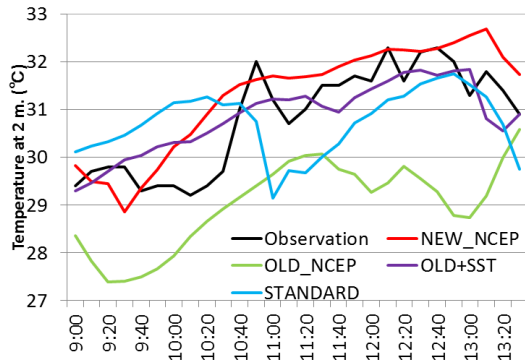


Fig.5-1 Temperature at 2m. above Nerima in 29 July 2007

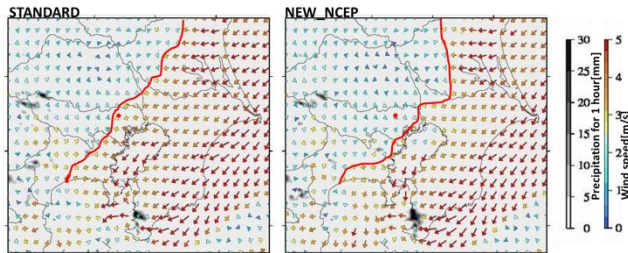


Fig.5-2 Wind velocity at 25m. at 11:00 in 29 July 2007  
(Red point : Nerima, Red line; drawn where sea breeze speed becomes less than 2.5m/s )

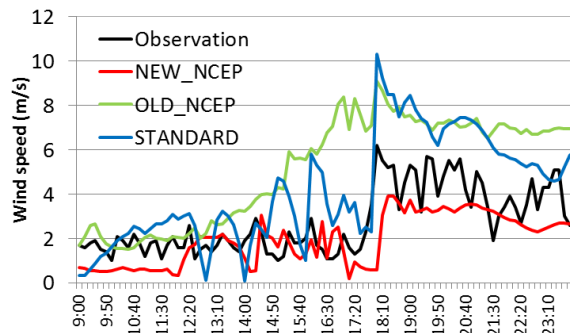


Fig.5-3 Wind velocity at 25m. above Tokyo in 21 August 2008 (per 10 min.)

made temperature gap between the sea and the land larger thereby enhancing seabreeze penetration noon. The penetration of sea breeze can obviously be found around Sagami bay(Fig 4-2b).

## 5. Sensitivity Analysis

### a) SST

The impact of MODIS SST can be seen in the temperature distribution. With MODIS SST, spatial distribution of temperature improved (not shown). Especially default SST caused under/overestimation of air temperature over the land depending on its bias; underestimated SST in 29 July 2007 caused lower  $T_a$  or overestimated one of 21<sup>st</sup> August 2008 contributed to higher  $T_a$ . Fig.5-1 shows that the 2-m temperature of OLD\_NCEP of 29<sup>th</sup> July 2007 keeps lower than that of OLD+SST above Nerima in the morning because of the underestimation of default SST of OLD\_NCEP.

### b) Aerodynamic parameter ( $d$ , $z_0$ , $z_T$ )

NEW\_NCEP largely its simulated wind velocity and temperature from STANDARD. New roughness length of city delayed seabreeze from Kashima-nada especially above Tokyo. Fig.5-2 shows that the north-easterly seabreeze whose wind speed is more than 2.5m/s at 25m height from ground is delayed when entering Tokyo in NEW\_NCEP whereas one of STANDARD keeps its speed while passing over Tokyo. This means that new roughness length significantly drags wind speed over city. Fig.5-3 shows that 25-m wind speed of Tokyo of NEW\_NCEP agrees better with observation than that of STANDARD which is overestimated in 21 August 2008. This drag of wind over city can be found in all analysis dates. Furthermore, the new roughness length also has an impact to stagnate heat and moisture, which increase temperature and rainfall in city. Fig.5-1 shows that 2-m temperature of Nerima of NEW\_NCEP keeps higher than that of STANDARD from 11:00 to 13:00 of 29 July 2007 because of the stagnation of heat of NEW\_NCEP.

## 6. Conclusion

The conclusions of this study are summarized as follows:

- Results, applying the new urban parameterization, tended to realize a more accurate simulation of localized heavy rainfall and also simulate more rainfall in city than those without it.
- Big improvement of temperature of Kanto region could be found by the change of SST especially when previous SST was too overestimated or underestimated.
- The new aerodynamic parameter delayed sea breeze and increased the stagnation of heat and water vapor around city because the new roughness length worked as the drag of urban geometry for wind velocity.

## References

- [1] Shimoju R., M. Nakayoshi, and M. Kanda, (2010). Case analyses of localized heavy rain in kanto considering urban parameters. *Annual Journal of Hydraulic Engineering*., JSCE, 54., pp.349-354. (in Japanese)
- [2] Kanda, M. et al: New Aerodynamic Parameterization for Real Urban Surfaces derived from LES. *Proceedings of the 8th international conference for urban climate*, 118, 2012.
- [3] Oda, R. et al. : Impact of the actual sea surface temperature of Tokyo bay of urban air temperature. *Annual Journal of Hydraulic Engineering*., JSCE, 52., pp.283-288, 2008. (in Japanese)
- [4] Kawai, T et al.: Evaluation of the Simple Urban Energy Balance Model Using Selected Data from 1-yr Flux Observations at Two Cities.Preview, *Journal of Applied Meteorology and Cimatology*, Vol 8, No4, 693-715, 2009

## 磁性 TiO<sub>2</sub>/AC 光触媒による染料の分解

原口拓郎

本研究では、2つの異なる粒子径の活性炭担持酸化チタン光触媒と磁性 TiO<sub>2</sub>/AC 光触媒を調製し、メチルオレンジの分解に対する触媒活性を評価した。活性炭担持酸化チタン光触媒では、酸化チタンと活性炭の割合が 66 : 33 かつ大きい粒子径の触媒が再利用後も酸化チタンより高活性を示した。磁性 TiO<sub>2</sub>/AC 光触媒は活性炭担持酸化チタン光触媒よりも活性が下がり、また粒子径の小さい触媒の方が触媒活性低下が大きいことが分かった。

### 1 Introduction

Titania photocatalytic oxidation offers potentially a facile and cheap method for removing organic pollutants from wastewaters. Typically, a photocatalytic reaction is conducted in a suspension of submicrometer-sized titania. However, removing such fine particles from large volumes of water involves further expense [1]. To solve this problem, Beydoun et al prepared titania coated magnetic particles that can be easily separated and collected by magnet [1]. However, photocatalytic activity was reduced significantly due to the phenomenon of photodissolution. Ao et al prepared Titania coated magnetic activated carbon (TMAC) which exhibit high photocatalytic activity and magnetic property [2]. It is also reported that the property of Activated Carbon (AC) strongly affect the photocatalytic activity of catalyst [3].

In this study, TMAC with different particle size of AC were developed for treatment of dye pollutant (Methyl Orange, MO) in water. The effect of AC particle size on photocatalytic activity and magnetic property were evaluated.

### 2 Experimental

#### 2.1 Catalyst preparation

The preparations of TAC (Titania coated AC) and TMAC was shown in Fig1. Firstly, magnetic activated carbon (MAC) was prepared using two types of AC with two sizes (50 - 125 $\mu$ m and 125 - 425 $\mu$ m). Each AC was modified by HNO<sub>3</sub> and mixed with solution containing iron nitrate. MAC containing Fe was prepared after 3 hours calcinations at 750 $^{\circ}$ C in N<sub>2</sub> condition. Secondly, Titania sol was prepared by TTIP (Titanium Tetra isopropoxide), glacial acetic acid and water with molar ratio of 1:10:350. The weight ratio of TiO<sub>2</sub> and AC is shown in Table 1. TTIP was hydrolyzed using glacial acetic acid at 0 $^{\circ}$ C. Water was added to this solution dropwise under vigorous stirring for 1hour, subsequently the solution was ultrasonicated for 30 minutes and stirred further 5 hours.

Thirdly, TMAC or TAC was prepared by adding MAC or AC into titania sol. Then, the solution was ultrasonicated for 30 min and placed in an oven maintained at 70 $^{\circ}$ C for 12 hours for aging process. The resulting gel was then dried at 100 $^{\circ}$ C and calcined in a furnace at 500  $^{\circ}$ C for 5 hours.

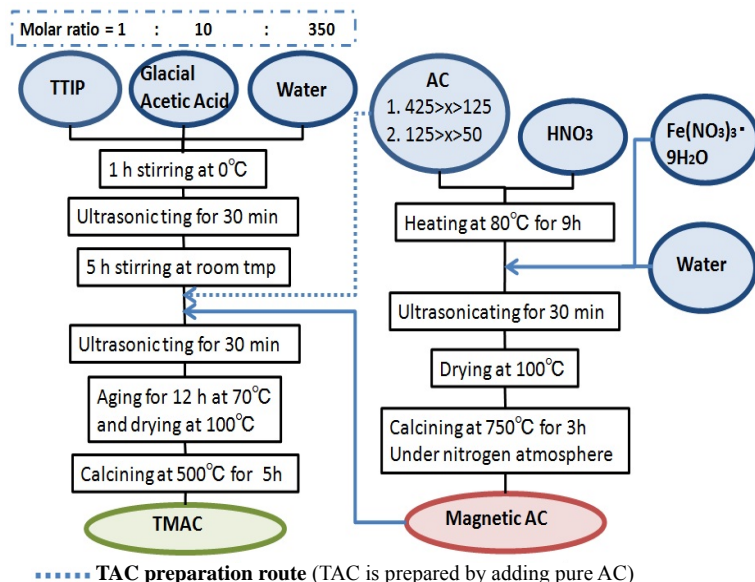


Figure 1 Sample preparation of TAC and TMAC

Table 1 Identification of photocatalyst

		Size of AC	
		Big size 125-425 $\mu$ m	Small size 50-125 $\mu$ m
Weight ratio (TiO <sub>2</sub> : AC) of TAC and TMAC	50 : 50	TAC5B TAC5B1, TAC5B2	TAC5S TAC5B1, TAC5B2
	66 : 33	TAC6B TAC6B1, TAC6B2	TAC6S TAC5B1, TAC5B2
	75 : 25	TAC7B TAC7B1, TAC7B2	TAC7S TAC5B1, TAC5B2

## 2.2 Photocatalytic activity test

For photocatalytic activity test, 100W ultraviolet lamp (with a wavelength from 250-600 nm) covered by a Pyrex glass sleeve was placed at the center of the reactor. Before UV irradiation, 0.25 g sample was added into 900 ml solution containing 50 ppm of Methyl Orange and the mixture was maintained in dark condition for 7 hours to reach adsorption equilibrium. After that, the UV irradiation was carried out, and sampling (5 ml) was done at regular intervals of 1 hour for analysis by UV-vis spectrometry. Recycling of used sample of TAC was also carried out to observe the change in photocatalytic activity after use. Reused sample was by collected new catalyst through filtration and drying after photocatalytic activity test.

## 3. Catalyst characterization

### 3.1 XRD

XRD patterns of TMAC6B and TMAC5S were presented in Fig. 2. TMAC6B showed anatase phase of  $\text{TiO}_2$ , magnetite phase of iron oxide and composite oxide of Ti and Fe (Ilmenite), while TMAC5S showed not only anatase, magnetite and Ilmenite but also composite oxide of Ti and Fe (Pseudobrookite).

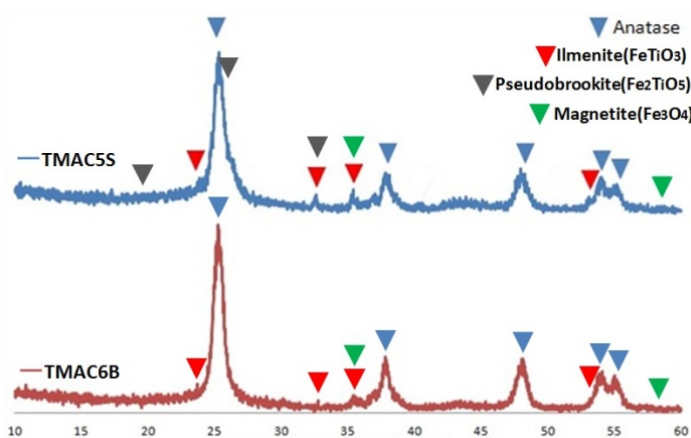


Figure 2 XRD patterns of TMAC6B and TMAC5S

### 3.2 Surface area measurements

Table 2 shows the results of surface area measurements of AC, TAC and TMAC by BET method. As mass ratio of Titania increased, surface area decreased. This is probably due to blockage of AC pores by titania[4]. The decrease of surface area of TMAC could be attributed to the blockage of AC pores by magnetite [5].

Table 2 Surface area of samples with different particle size

	AC	TAC5	TAC6	TAC7	TMAC
Big size ( $\text{m}^2/\text{g}$ )	991.4	545.3	439.2	306.4	351.3
Small size ( $\text{m}^2/\text{g}$ )	1032	818.5	449.9	368.8	521.6

### 3.3 SEM-EDS

The SEM images of TMAC6B and TMAC5S were shown in Fig. 3. Small particles of Titania could be observed. The EDS was shown in Fig4 indicated a heterogeneous distribution of Fe and Ti on the surface of AC. On the other hand, TMAC5S showed a uniform distribution of Fe and Ti.

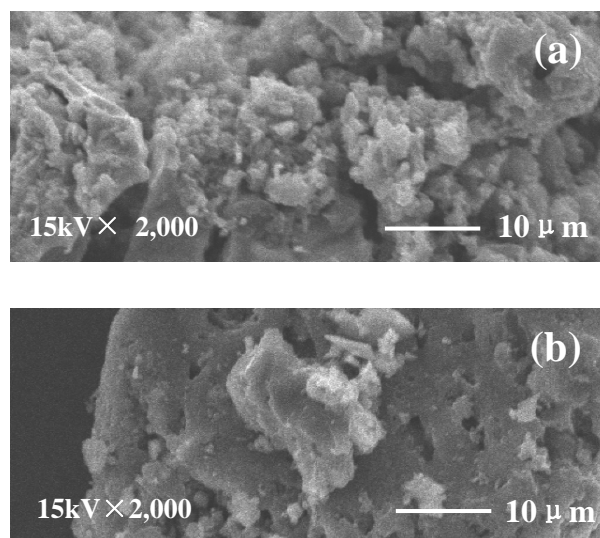


Figure.3 SEM images of (a)TMAC6B and (b)TMAC5S

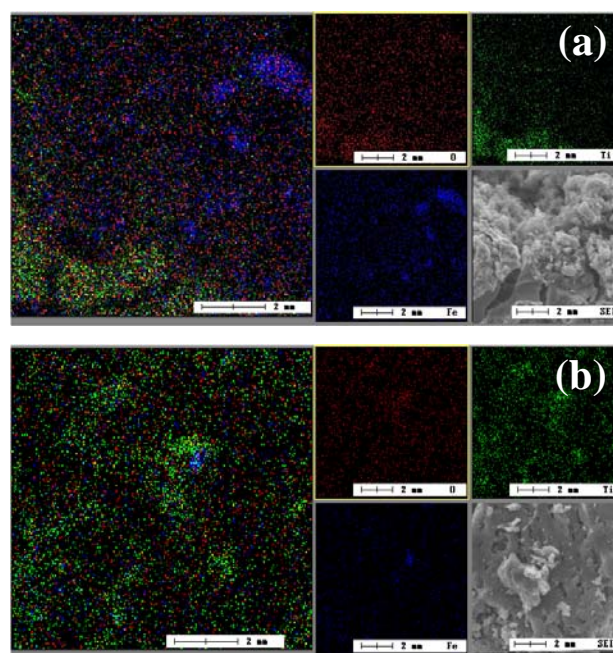


Figure 4 EDS results of (a) TMAC6B and (b) TMAC5S



## 4. Results and discussion

### 4.1 Photocatalytic activity of TAC.

The result of photocatalytic activity of new sample of TAC (TAC1) and reused sample of TAC(TAC2) were shown in Fig 5 and Table 3. The photocatalytic activity of TiO<sub>2</sub> was also measured for comparison. Here, the photocatalytic activity of small size of TAC1 (TACS1) was much higher than big size of TAC1 (TACB1) and TiO<sub>2</sub>. However, TACS2 showed significant drop in photocatalytic activity compared to TACB2. The drop in photocatalytic activity could be attributed to the detachment of TiO<sub>2</sub> from TACS during the photocatalytic activity test and/or the covering of TACS by the byproducts from MO photodegradation. On the other hand, TAC6B showed comparable performance to pure TiO<sub>2</sub> although the amount of TiO<sub>2</sub> was only about 2/3 of pure one. And this sample also showed insignificant dropped in photocatalytic activity after reuse. Previous study explained about the synergy effect between TiO<sub>2</sub> and AC which improves the photocatalytic activity of the composite material [3].

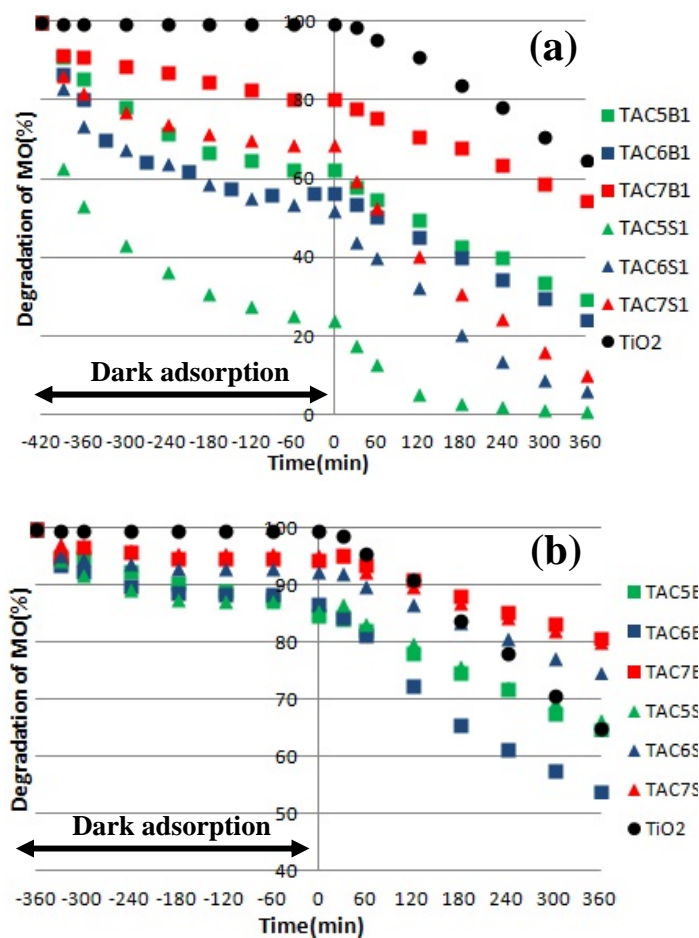


Fig.5 photocatalytic activity of (a) TAC1 and (b) TAC2

Table.3 Degradation of amount of MO by TAC and TiO<sub>2</sub>

	75 : 25		66 : 33		50 : 50		TiO <sub>2</sub>
	Big	Small	Big	Small	Big	Small	
	TAC7B	TAC7S	TAC6B	TAC6S	TAC5B	TAC5S	
New catalyst	26%	58%	32%	46%	33%	23.4%	35%
Reused catalyst	14%	15%	34%	18%	22%	21%	-
Decrease	46%	74%	-6%	61%	33%	10%	-

### 4.2 Photocatalytic activity of TMAC

The result of photocatalytic activity test of TMAC was shown in Fig. 6 and Table 4. TMAC showed a very low photocatalytic activity compared to TAC. Moreover, photocatalytic activity of TMAC5S is much lower than that of TMAC6B. This low activity could be attributed to heat treatment and photodissolution during UV irradiation.

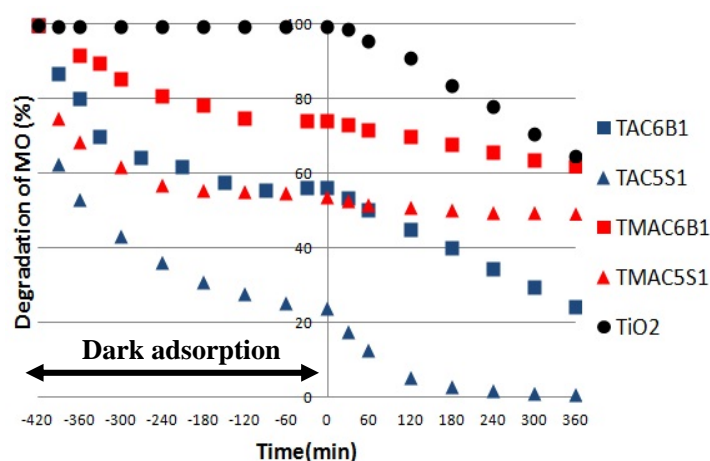


Figure.6 Photocatalytic activity of TMAC

Table.4 Degradation of amount of MO by TAC and TMAC

	Big size	Small size
TAC	32.0%	23.4%
TMAC	12.2%	4.6%
Decrease	61.9%	80.3%

#### 4.2.1 Heat treatment

Three causalities can be considered concerning the decrease in photocatalytic activity of TMAC, the phase transformation of TiO<sub>2</sub> from anatase to rutile [7], Formation of Pseudobrookite, Fe<sub>2</sub>TiO<sub>5</sub> [7], and the diffusion of Fe ions into the layer of TiO<sub>2</sub> coated on the surface of AC[8]. The first issue of phase transformation could be removed since XRD analysis show no rutile phase. For the second issue, TMAC5S showed phase of

Fe<sub>2</sub>TiO<sub>5</sub> that could act as recombination site for electron and hole, thus reducing the photocatalytic activity of the catalyst. For the third issue, Beydoun et al[1] showed that Fe diffused into TiO<sub>2</sub> during the heat treatment could also act as recombination site for electron and hole. It is possible that the second and the third causalities mentioned above caused the decrease in photocatalytic activity of TMAC.

#### 4.2.2 Photodissolution

Photodissolution of Fe in titanium/iron oxides system during UV irradiation has been reported in previous study [1]. This phenomenon occurs due to electronic interactions between TiO<sub>2</sub> coating and iron oxide where the photogenerated electrons in TiO<sub>2</sub> phase are transferred into iron oxide phase. This causes the formation of Fe ions that could migrate to the solution through the pores of TiO<sub>2</sub> coating. However, in this study, ICP-AES analysis of Fe ions after UV irradiation showed no Fe element detected meaning that photodissolution of Fe did not occur in the system. This could be explained from the preparation procedure where in this study, firstly, the iron oxide introduced into the AC before coating by TiO<sub>2</sub>, while in the previous study, the TiO<sub>2</sub> was coated directly on iron oxide core [1]. The interaction between TiO<sub>2</sub> and iron oxide in this study is thought to be minimal.

#### 4.3 Magnetic property of TMAC

XRD analysis result showed magnetite phase in TMAC. The test of magnetic property was carried out by applying commercial neodymium magnet on the samples and weighting the amount left (not attached to the magnet). The result is showed in Table 5. Magnetic force of TMACB was stronger than that of TMACS. The formation of Fe<sub>2</sub>TiO<sub>5</sub> reduced the amount of magnetite phase in TMACS, thus decreasing the magnetic force of TMACS.

Table.5 Comparison test of magnetic force

	Big size (g)	Small size (g)
MAC	0.22	0.197
TMAC	0.1	0.063
Decrease	54.5%	68.0%

#### 5. Conclusions

TAC and TMAC were successfully prepared. All prepared catalysts showed photocatalytic activity toward MO degradation under UV irradiation.

The photocatalytic activity of TAC decreased after reused. Especially, decrease of photocatalytic activity of TACS is higher than that of TACB. The decrease of photocatalytic activity could be attributed to the detachment of TiO<sub>2</sub> from TACS during the photocatalytic activity test and/or the covering of TACS by the byproducts from MO photodegradation.

The decrease of TMACS photocatalytic activity could be attributed to the formation of composite oxide of Ti and Fe, and the diffusion of Fe into TiO<sub>2</sub> during heat treatment

All prepared catalysts showed magnetic property due to the presence of magnetite phase in them.

#### 6. Future plans

In order to develop TMAC as a practice photocatalyst, additional researches are needed to increase photocatalytic activity of TMAC. The two ways of enhance photocatalytic activity could be considered. The first way is to develop a method that calcinations temperature is decreased until diffusion of Fe ions can be inhibited and anatase phase of TiO<sub>2</sub> is prepared. The second way is to introduce of an intermediate passive SiO<sub>2</sub> layer between the titanium dioxide phase and Activated Carbon inhibited the direct contact.

#### 7. References

- [1] D. Beydoun, J. Phys. Chem, B 104 (2000) 4387–4396.
- [2] Y. Ao et al, Separation and Purification Technology , 61 (2008) 436–441
- [3] J. Matos et al, Applied Catalysis B: Environmental , 18 (1998) 281-291
- [4] X. Wang et al, Journal of Hazardous Materials, 169 (2009) 1061 – 1067
- [5] J. Araña et al, Applied Catalysis B: Environmental, 44 (2003) 161–172
- [6] Y. Ao et al, C A R B O N, 4 6 ( 2 0 0 8 ) 5 9 6 – 6 0 3
- [7] F.X. Ye et al, Materials Science and Engineering B,148 (2008) 154–16
- [8] Jimmy C et al, Environmental Science and Technology, VOL. 37. NO. 10, 2003 /

# Selective Catalytic Reduction of Nitrogen Oxides with Propene over Ag/CeO<sub>2</sub>-TiO<sub>2</sub> Catalyst

Student Number: 10M18298 Name: Yang YANG Supervisor: Hirofumi HINODE

プロペンを還元剤とした Ag/CeO<sub>2</sub>-TiO<sub>2</sub> 触媒による NO 選択還元

楊 洋

本研究では、過剰酸素存在下でプロピレンを還元剤とする NO 選択還元 (HC-SCR) を目的とした触媒の開発を行った。Ag/CeO<sub>2</sub>-TiO<sub>2</sub> 触媒を用い、焼成温度、Ag 担持量、C<sub>3</sub>H<sub>6</sub> 濃度影響及び酸素有無影響を検討した。550℃は最適な焼成温度であり、この温度で焼成した 3wt%Ag/CeO<sub>2</sub>-TiO<sub>2</sub> 触媒が最大活性を示し、400℃で約 63%の NO 分解が達成できた。また、HC-SCR において C<sub>3</sub>H<sub>6</sub> と酸素の存在は不可欠であることを確認した。

## 1 Introduction

Air pollution by nitrogen oxides (NO<sub>x</sub>) emitted from mobile and stationary sources is one of serious environmental problems to be solved because NO<sub>x</sub> contribute to the formation of acid rain and photochemical smog, global warming, depletion of ozone layer.

Nowadays, three-way catalysts (TWC) are generally used to reduce NO<sub>x</sub> in automobiles. This method can reduce NO<sub>x</sub> with high efficiency at specific air to fuel (A/F) ratio. Recently, lean-burn gasoline or diesel engines have highly attracted attention due to their fuel efficiency. However, the presence of excess O<sub>2</sub> in exhaust gas from these engines suppresses NO reduction activity. Therefore, catalyst that can efficiently convert NO to N<sub>2</sub> in the presence of O<sub>2</sub> is desirable. Among several applicable methods, selective catalytic reduction with hydrocarbons (HC-SCR) contained in the exhaust is currently the most studied technology for NO reduction.

Ceria (CeO<sub>2</sub>) is an important rare earth oxide and has been widely investigated in the automotive exhaust purification related to oxygen storage and release catalysis. A remarkable property of CeO<sub>2</sub> is the number of

effective redox Ce<sup>4+</sup>/Ce<sup>3+</sup> sites and their ability to exchange oxygen[1]. The presence of ceria enhanced the oxidation of NO to NO<sub>2</sub>, thereby increasing the activity of NO reduction[2]. In our laboratory, activity of various TiO<sub>2</sub> support metal catalysts had been investigated[3-5]. In reaction mechanism suggested, NO reduction possibly occurred via the formation of NO<sub>2</sub>. Some studies also reported the role of CeO<sub>2</sub>-TiO<sub>2</sub> mixed oxide which has a high surface area in enhancing the oxidation of NO to NO<sub>2</sub>[2,6]. On the other hand, silver plays an important role as the active species and enhance the catalytic activity of Ag/TiO<sub>2</sub>-ZrO<sub>2</sub> in HC-SCR of NO using C<sub>3</sub>H<sub>6</sub>[7].

Therefore, in this study, the unique properties of CeO<sub>2</sub>-TiO<sub>2</sub> support and the activity of Ag were combined to develop a CeO<sub>2</sub>-TiO<sub>2</sub> supported Ag catalyst effective for HC-SCR of NO using C<sub>3</sub>H<sub>6</sub> in the presence of O<sub>2</sub>. The effects of calcination temperature, Ag loading levels, C<sub>3</sub>H<sub>6</sub> concentrations and oxygen presence on catalytic activity of prepared catalysts have been investigated.

## 2 Experimental

### 2.1 Materials

CeO<sub>2</sub>-TiO<sub>2</sub> catalysts were prepared by co-precipitation method using TiO<sub>2</sub> precursor of [(CH<sub>3</sub>)<sub>2</sub>CHO]<sub>4</sub>Ti (Wako) and CeO<sub>2</sub> precursor of Ce(NO<sub>3</sub>)<sub>3</sub> · 6H<sub>2</sub>O (Wako) with the same molar ratio for Ce and Ti. Firstly, Ce(NO<sub>3</sub>)<sub>3</sub> · 6H<sub>2</sub>O was dissolved in 35ml of deionized water with continuous stirring and the pH was maintained between 0.5-1.0 by addition of HNO<sub>3</sub>. Then [(CH<sub>3</sub>)<sub>2</sub>CHO]<sub>4</sub>Ti was added to the solution and the pH was adjusted to between 9-11 by addition of NH<sub>3</sub> solution. The resulting mixture was filtered, dried at 100°C for 8hours and calcined at 550°C for 4hours under air flow.

Ag/CeO<sub>2</sub>-TiO<sub>2</sub> catalysts were prepared by impregnation method. Firstly, Ag precursor of AgNO<sub>3</sub> (Wako) was dissolved in 50ml of deionized water and mixed with CeO<sub>2</sub>-TiO<sub>2</sub>. Then the mixture was stirred at room temperature for 12hours and dried at 80°C for 12hours and calcined at 400, 550, 700 or 800°C for 4 hours under air flow. Using this method, Ag/CeO<sub>2</sub>-TiO<sub>2</sub> catalysts with Ag loading of 0.5, 1, 2, 3, 5wt% were prepared.

All catalysts were pelletized, crushed, and sieved to 0.71-1.00 mm prior to catalytic activity test.

### 2.2 Catalytic Activity Test

The catalytic activity test was carried out with a fixed-bed flow reactor by passing a reactant gas containing 1500ppm of NO, 10% of O<sub>2</sub>, 1500ppm of C<sub>3</sub>H<sub>6</sub>, and helium as balance gas. 1.0 g of catalyst was used with a corresponding space velocity of 13000 h<sup>-1</sup> and a total gas flow rate of about 4 ml/s. The temperature was changed stepwise from 150°C

to 550°C.

NO and NO<sub>2</sub> concentration were analyzed by NO<sub>x</sub> analyzer (Shimadzu, NOA-7000). N<sub>2</sub>O and CO<sub>2</sub> were analyzed by gas chromatographs (GC-323W for N<sub>2</sub>O; GC-390 for CO<sub>2</sub>). Catalysts were characterized by TG-DTA, XRD, N<sub>2</sub> adsorption (BET method) and SEM-EDS.

## 3 Results and Discussion

### 3.1 Characterization of Prepared Catalysts

Figure 1 shows the XRD patterns of 3wt%Ag/CeO<sub>2</sub>-TiO<sub>2</sub> catalysts with different calcination temperature. Ag metal phase was confirmed at calcinations temperature higher than 550°C. Starting from 700°C, the rutile phase of TiO<sub>2</sub> was observed indicating the phase transformation of TiO<sub>2</sub> from anatase to rutile.

Figure 2 shows the XRD patterns of

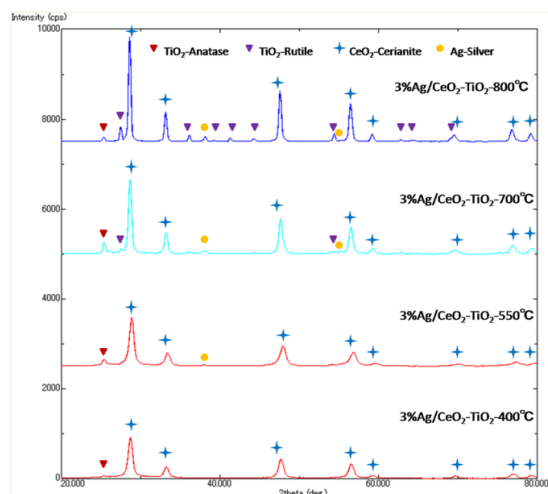


Figure 1 XRD patterns of 3wt%Ag/CeO<sub>2</sub>-TiO<sub>2</sub> catalyst with different calcination temperature.

Ag/CeO<sub>2</sub>-TiO<sub>2</sub> catalysts with different Ag loading levels. Ag phase was confirmed in all catalysts prepared. Ag loading of more than 3wt% showed an effect on TiO<sub>2</sub> phase formed. At 5wt% of Ag loading level, both anatase and brookite phase of TiO<sub>2</sub> were observed.

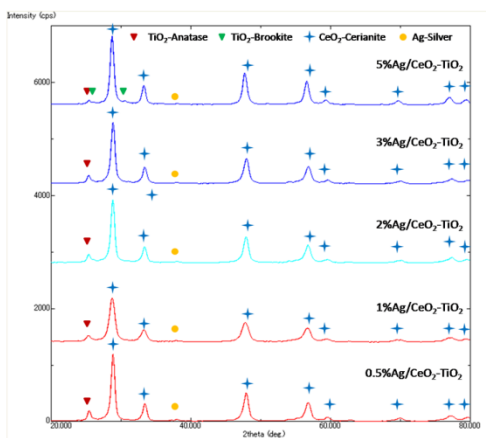


Figure2 XRD patterns of Ag/CeO<sub>2</sub>-TiO<sub>2</sub> catalyst with different Ag loading levels.

Table 1 shows the specific surface area of several samples. It can be seen that high calcination temperature could significantly decreased the surface area of the catalysts. It was generally known that due to the sintering effect on particles, bigger particles with lower surface area will be formed at high calcination temperature.

Table 1 BET results of several catalysts.

Catalysts	Specific Surface Area[m <sup>2</sup> /g]
Pure TiO <sub>2</sub>	27.04
Pure CeO <sub>2</sub>	71.19
CeO <sub>2</sub> -TiO <sub>2</sub>	105.7
3%Ag/CeO <sub>2</sub> -TiO <sub>2</sub> (400)	93.66
3%Ag/CeO <sub>2</sub> -TiO <sub>2</sub> (550)	31.14
3%Ag/CeO <sub>2</sub> -TiO <sub>2</sub> (700)	9.83
3%Ag/CeO <sub>2</sub> -TiO <sub>2</sub> (800)	6.96

### 3.2 The Effect of Calcination Temperature

Figure 3 shows the conversion of NO to N<sub>2</sub> over 3wt%Ag/CeO<sub>2</sub>-TiO<sub>2</sub> catalysts with different calcination temperature (400,550,700,800°C). The catalyst calcined at 550 °C showed the maximum activity. This result together with the XRD patterns suggested that calcination temperature of 400°C was not enough to provide the catalyst with catalytically active phase of Ag metal. On the other hand, the decrease of activity on catalysts prepared at calcination temperature higher than 700°C could be attributed to the

decrease of specific surface area and the reduction in anatase phase of TiO<sub>2</sub>. To confirm the latter possibility, the comparison between the catalytic activity of anatase and rutile phase of TiO<sub>2</sub> in Ag/CeO<sub>2</sub>-TiO<sub>2</sub> catalyst is necessary. One previous study reported that the dispersion of active sites was better in anatase phase than rutile phase leading to a better catalytic activity[8].

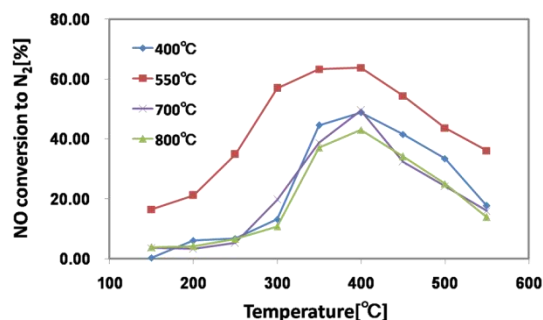


Figure 3 Catalytic activity of 3wt%Ag/CeO<sub>2</sub>-TiO<sub>2</sub> catalyst for the reduction of NO to N<sub>2</sub> using C<sub>3</sub>H<sub>6</sub> with different calcination temperature.

### 3.3 The Effect of Ag Loading Levels

Figure 4 shows the conversion of NO to N<sub>2</sub> over Ag/CeO<sub>2</sub>-TiO<sub>2</sub> catalysts with different Ag loading levels (0.5, 1, 2, 3, 5 wt%). Ag loading level of 1wt% led to an improved activity of the catalyst. Previous study proposed a reaction mechanism where Ag promotes the conversion of NO to N<sub>2</sub> through the reaction of isocyanate (-NCO) species with NO<sub>2</sub> on Ag active sites[7]. However, Ag loading level higher than 3wt% showed a decrease in the activity of the catalysts. This could be attributed to the formation of brookite phase of TiO<sub>2</sub> which reduced the amount of anatase phase of TiO<sub>2</sub>. Again, the comparison of activity of anatase and brookite phase of TiO<sub>2</sub> in Ag/CeO<sub>2</sub>-TiO<sub>2</sub> catalyst is necessary to confirm this.



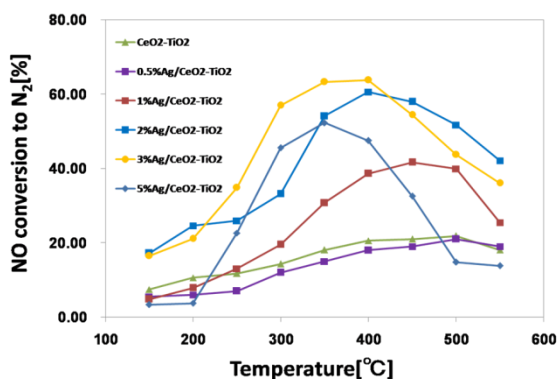


Figure 4 Catalytic activity of Ag/CeO<sub>2</sub>-TiO<sub>2</sub> catalyst for the reduction of NO to N<sub>2</sub> using C<sub>3</sub>H<sub>6</sub> with different Ag loading levels.

### 3.4 The Effect of C<sub>3</sub>H<sub>6</sub> Concentrations

Figure 5 shows the conversion of NO to N<sub>2</sub> over 3wt%Ag/CeO<sub>2</sub>-TiO<sub>2</sub> catalyst with different C<sub>3</sub>H<sub>6</sub> concentrations (0, 500, 1000, 1500 ppm). Without C<sub>3</sub>H<sub>6</sub> (0 ppm), NO could not be decomposed. When C<sub>3</sub>H<sub>6</sub> was added to the system, there was a significant increase in NO conversion to N<sub>2</sub>, while the conversion of NO to NO<sub>2</sub> decreased (data not shown). These confirmed the role of C<sub>3</sub>H<sub>6</sub> as reducing agent in HC-SCR of NO and that NO<sub>2</sub> was one of the intermediates during NO conversion to N<sub>2</sub>.

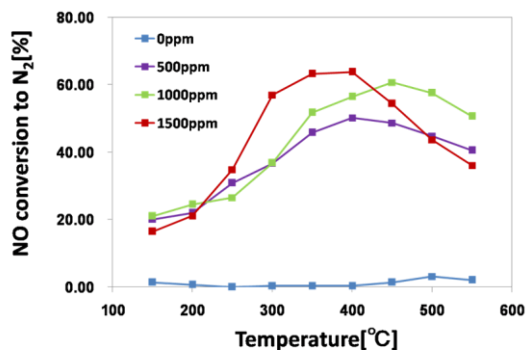


Figure 5 Catalytic activity of 3wt%Ag/CeO<sub>2</sub>-TiO<sub>2</sub> catalyst for the reduction of NO to N<sub>2</sub> using different C<sub>3</sub>H<sub>6</sub> concentrations.

### 3.5 The Effect of O<sub>2</sub> Presence

Figure 6 shows the conversion of NO to N<sub>2</sub> over 3wt%Ag/CeO<sub>2</sub>-TiO<sub>2</sub> catalyst with 10%O<sub>2</sub> or without O<sub>2</sub>. In the presence of O<sub>2</sub>, NO decomposition activity shifted to lower temperature range compared to that without O<sub>2</sub>. This shows that the presence of O<sub>2</sub> could improve the activity of prepared catalyst on HC-SCR of NO.

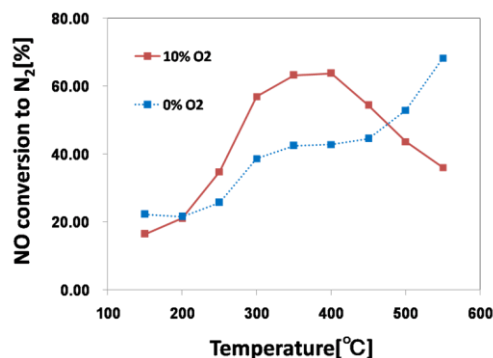


Figure 6 Catalytic activity of 3wt%Ag/CeO<sub>2</sub>-TiO<sub>2</sub> catalyst for the reduction of NO to N<sub>2</sub> using C<sub>3</sub>H<sub>6</sub> with O<sub>2</sub> or without O<sub>2</sub>.

## 4 Conclusions

Ag/CeO<sub>2</sub>-TiO<sub>2</sub> catalyst active for selective catalytic reduction of NO using C<sub>3</sub>H<sub>6</sub> was successfully prepared in this study.

The catalyst calcined at 550°C showed the highest activity (maximum NO conversion to N<sub>2</sub> 63% at 400 °C). Calcination temperature affected several factors determining the activity of catalyst, the specific surface area of catalyst, the type of TiO<sub>2</sub> phase and the amount of Ag metal formed in the catalyst.

Catalyst with Ag loading level of 3wt% showed the highest activity (maximum NO conversion to N<sub>2</sub> 63% at 400°C). Ag loading up to a certain amount enhanced the catalytic activity. However, a high Ag loading level could lead to formation of TiO<sub>2</sub> phase that could decrease the activity.

C<sub>3</sub>H<sub>6</sub> role as reducing agent and the importance of O<sub>2</sub> presence in HC-SCR of NO has been confirmed.

## References

- [1] Proceedings of the 11<sup>th</sup> ECERS Conference, Krakow, 2009
- [2] R.Q.Long,R.T.Yang Appl.Catal.B 27 (2000) 87-95
- [3] J.Mitadera; Master Thesis, Tokyo Institute of Technology (2003)
- [4] H. Kawai; Master Thesis, Tokyo Institute of Technology (2004)
- [5] C.Tang; Master Thesis, Tokyo Institute of Technology (2006)
- [6] Journal of Hazardous Materials 174(2010) 734-739
- [7] Catalysis Today 42(1998) 127-135
- [8] M.Makii; Master Thesis, Tokyo Institute of Technology (2008)

# ESTIMATION OF CO<sub>2</sub> EMISSION FROM URBAN FREIGHT TRANSPORT IN KHON KAEN, THAILAND

Student Number: 10M18217 Name: Shinsuke Mogi

Supervisor: Shinya HANAOKA

## タイ国コンケン市における都市内物流部門からの CO<sub>2</sub> 排出量推定

茂木慎祐

本論文では、タイ国コンケン市を対象に、都市内物流部門からの CO<sub>2</sub> 排出量を推定した。現地で物流調査を実施し、現状維持、公共交通整備に伴う駅周辺商業地域発展、大型貨物車通行規制、電気ピックアップ普及という 4 つのシナリオで、2012 年から 2050 年まで走行貨物車による CO<sub>2</sub> 排出量の将来推定を行った。その結果、公共交通整備に伴う駅周辺商業地域発展及び電気ピックアップ普及を組み合わせた場合、最も CO<sub>2</sub> 排出量抑制効果があることを示した。

## 1. Introduction

It is imperative to reduce CO<sub>2</sub> emission from transport sector in terms of global warming. However, due to increasing motorization rate in cities of developing countries, it is difficult to reduce CO<sub>2</sub> emission by around 20 to 50 percent with general CO<sub>2</sub> cut policies. Therefore, Low-Carbon Asia Research Project, which is funded by the Ministry of the Environment, Japan, aims at identifying policy roadmaps including land use policy toward a 2050 vision of low carbon society in Asia. However, many cities in developing countries have no existing data on logistics so that they face difficulties to make effective CO<sub>2</sub> reduction policy on logistics. Consequently, it is necessary to estimate CO<sub>2</sub> emission from urban trucks in order to assess physical distribution policies in cities of developing countries.

Research objectives are as follows.

- 1) To estimate truck trip origin-destination (OD) at a base year of 2012 by conducting an interview survey in Khon Kaen
- 2) To compare 2050 estimated CO<sub>2</sub> emission from urban trucks between four scenarios: 1) Business-as-usual (BAU), 2) Transit-oriented development (TOD), 3) Heavy truck ban and 4) Electric vehicle pickup dissemination (i.e. EV pickup)

Transit-oriented development (TOD) is an approach to city development with public transportation focusing on land use around stations of the public transportation. In this research, TOD is applied to both passenger and freight transport sectors, so TOD also indicates that a public transport network is constructed on truck routes and more offices are condensed near the stations.

## 2. Research Methodology

### 2.1 Selection of Study Area

The study area is an urban area of Mueang Khon Kaen District in Khon Kaen province, Thailand (hereinafter referred to as “Khon Kaen”). Since Khon Kaen is located on Greater Mekong

Subregion’s East West Corridor, Khon Kaen is planned to develop traffic and transportation system. In fact, Khon Kaen has a plan to construct 5 lines of bus rapid transport (BRT) by 2022.

### 2.2 Selection of Methodology

Four-step model is a general method applied to forecast traffic volume in road network. In this research, the first two steps of four-step model are applied to estimate truck OD. The whole estimation steps are shown in Figure1.

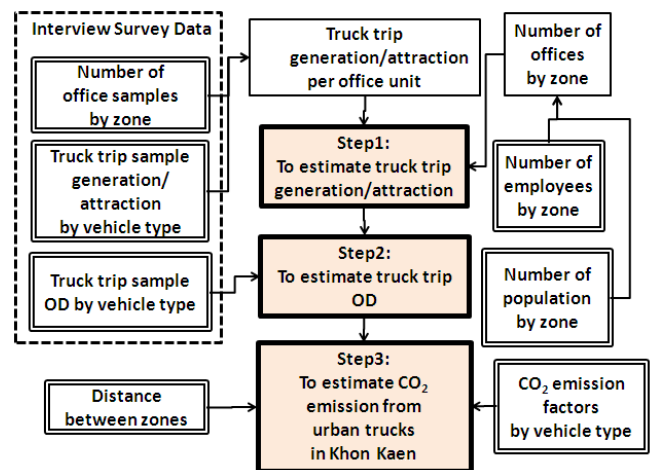


Figure1. Flowchart to estimate CO<sub>2</sub> emission

#### 2.2.1 Zoning of the study area

Khon Kaen is divided into 45 zones, while outside of it is divided into 5 zones, totally 50 zones (See Figure2).

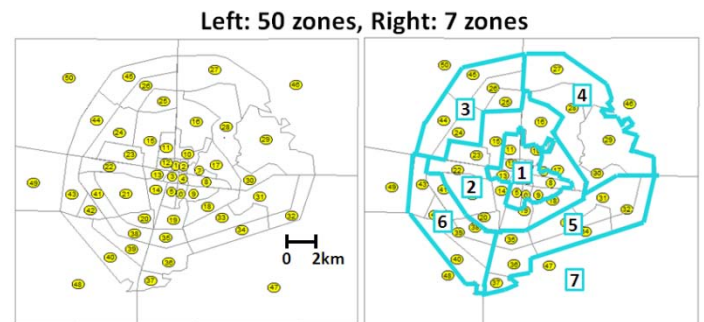


Figure2. Zoning map of Khon Kaen

### 2.2.2 Estimation of truck trip generation/attraction

Truck trip generation (i.e.  $G$ ) and attraction (i.e.  $A$ ) are estimated in equation (1).

$$\begin{aligned} G &= \alpha_g N_o, & A &= \alpha_a N_o \\ &= \frac{t_g}{n_o} N_o, & &= \frac{t_a}{n_o} N_o \end{aligned} \quad (1)$$

Here, trip generation/attraction per office unit:  $\alpha_g, \alpha_a$ , the number of offices by zone:  $N_o$ , the number of office samples by zone:  $n_o$ , truck trip sample generation/attraction:  $t_g, t_a$

The number of offices by zone (i.e.  $N_o$ ) in equation (1) is estimated with a regression model equation (2) which has two independent variables: the number of employees (i.e.  $N_e$ ) and population (i.e.  $N_p$ ).

$$N_o = \beta_0 + \beta_1 N_e + \beta_2 N_p \quad (2)$$

In addition, truck trip production (i.e.  $T$ ) is set up by equation (3) as control total of the amount of truck trips in Khon Kaen.

$$\begin{aligned} T &= \frac{a_e N_e^T}{2n_e} \\ &= \frac{t_g + t_a}{2n_e} N_e^T \end{aligned} \quad (3)$$

Here, truck trip production per employee:  $a_e$ , the total number of employees in Khon Kaen:  $N_e^T$ , the number of employee samples:  $n_e$ , truck trip sample generation/attraction:  $t_g, t_a$

### 2.2.3 Estimation of truck trip OD

Frater method is used to estimate truck trip OD by vehicle type based on truck trip sample OD and estimated truck trip generation/attraction in 2012. However, since the truck trip sample OD has the value of 0 at many cells, 50-zone sample OD matrices are consolidated into 7-zone sample OD matrices at first by following 7 zones in Figure2. After estimation, truck trips in 7-zone OD matrices are divided into each cell of 50-zone OD matrices by using the number of employees by zone.

### 2.3 Scenario Setting

Based on a concept of TOD, Khon Kaen is planned to open 5 BRT lines by 2022. Therefore, newly commercial area is expected to develop near BRT stations. TOD scenario means that the number of offices near BRT stations increases year by year while those far from the stations decrease year by year.

Table1 indicates that in 2012 more than half of the total truck trips in Khon Kaen are 6 and 10 wheel truck trips (heavy truck trips), even if Khon Kaen is an urban area. Therefore, Heavy truck ban may be effective in terms of CO<sub>2</sub> reduction from

urban trucks. Heavy truck ban scenario has two major setups: the first one is that the number of pickup trips increases at much higher rate than one of 6 and 10 wheel trips year by year. The second one is that the distribution of truck trips in 2050 becomes the same as the distribution of registered trucks in Bangkok Metropolitan Region in 2002 when heavy trucks with 10 wheels or more had been restricted to entry and park within the Middle Ring Road.

Since pickup trips are largest of three in 2012 (See Table1), EV pickups are expected to be used in the future. EV pickup scenario means that newly registered EV pickups increase every year among the total newly registered pickups in Khon Kaen.

Table1. Distribution of trips by vehicle types

Vehicle type	All scenarios in 2012	Heavy truck ban scenario in 2050
Pickup	7,280 (44%)	177,634 (93.5%)
6 wheel truck	5,380 (32%)	7,133 (3.8%)
10 wheel truck	3,991 (24%)	5,212 (2.7%)
Total	16,651 (100%)	189,979 (100%)

## 3. Data Collection

### 3.1 Outputs of interview survey

This interview survey has the two outputs: 1) truck trip sample generation/attraction per office unit and 2) truck trip sample OD.

### 3.2 Steps of the interview survey

A surveyor visits a target office and conduct interview to a shopkeeper of the office. Totally 24 surveyors and 3 directors worked on the survey for 15 days (i.e. from 16 to 30 November 2012).

### 3.3 Survey items

Survey items used to this research are showed in Table2. When an interviewee answers to vehicle type, he or she selects one of four vehicle types: pickup truck, 6 wheel truck, 10 wheel truck and more than 10 wheel truck.

Table2. Survey items of Interview Survey

Outline of office	Incoming truck	Outgoing truck
1. Name	1. Vehicle type	1. Vehicle type
2. Address	2. Frequency per week	2. Frequency per week
3. Zone no.	3. Location of incoming truck	3. Location of outgoing truck
4. Business type		
5. No. of employees		

## 4. Results and Discussion

### 4.1 Results

#### 4.1.1 Analysis on survey data

As the result of the survey, the number of effective office samples is 127 (i.e. 8.26% of the total number of offices in Khon Kaen) and 330 truck trip effective samples. In the interview survey, office samples in each zone were collected, but some zones had 0 effective office samples as shown in Figure3.

Since the number of more than 10 wheel truck trip samples is only 4 of the total number of truck trip samples of 330, this truck trip's sample OD matrix cannot be used to estimate trip OD matrix in 2012 with Frater method. Thus, a more than 10 wheel truck is not considered when estimating truck trip generation/attraction in 2012.

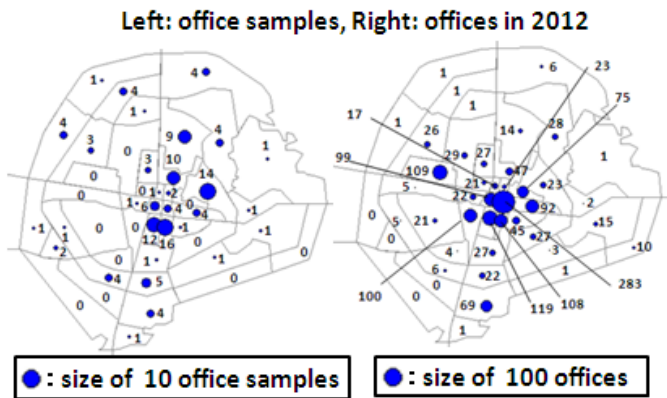


Figure3. Location distribution of offices in 2012

#### 4.1.2 Truck trip generation/attraction and OD in 2012

Figure4 illustrates where truck trip samples and estimated truck trips in 2012 are generated. Truck trip sample generation tends to be high when office samples are located in suburb of Khon Kaen and have greater than or equal to 50 employees. However, it cannot not be judged whether the truck trip sample generation reflects realistic situation on logistics in Khon Kaen because commercial area and residential area exist in the same zone in Khon Kaen. Therefore, when truck trip generation in 2012 is estimated, it is assumed that the number of offices by zone is proportional to the number of truck trips by zone.

Figure5 shows that truck trip sample OD from/to outside and suburb of Khon Kaen is relatively large, when office samples are located in suburb and have greater than or equal to 50 employees. The fact that there are more empty lots in suburb than in center of Khon Kaen may lead to build offices which have large number of employees.

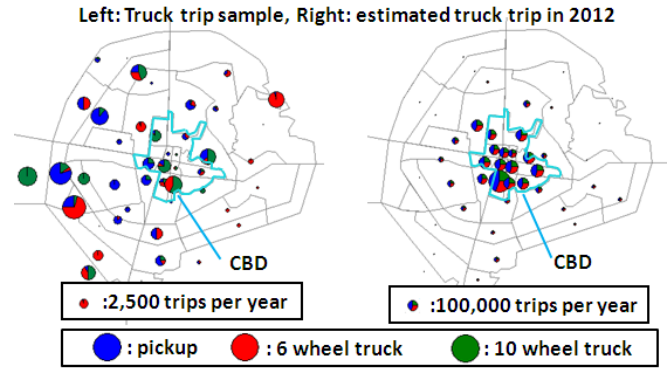


Figure4. Location distribution of truck trip generation in 2012

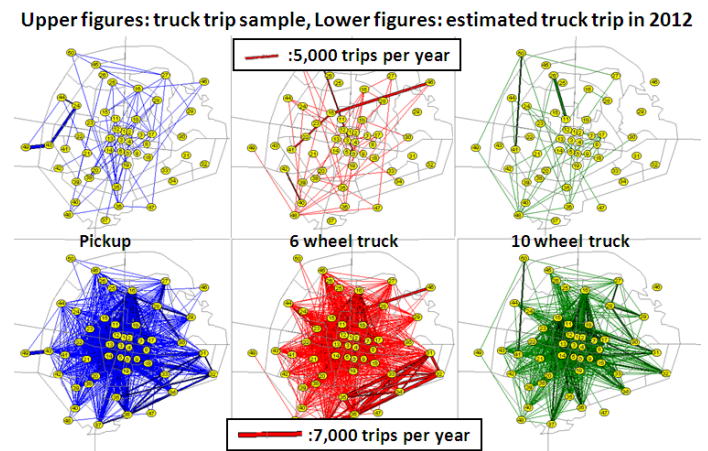


Figure5. Truck trip OD in 2012

#### 4.1.3 2050 estimated truck trip generation/attraction

TOD scenario indicates that the number of offices near BRT stations increase while those far from the stations decrease. Ito et al. (2011) represents population distribution as an urban structure to minimize CO<sub>2</sub> emission from passenger transport in Khon Kaen in 2022. Since such the population distribution is used in the TOD scenario, more offices are located near BRT lines in 2050 as shown in Figure6. Additionally, Figure7 shows the same trend in case of truck trip generation at the year of 2050.

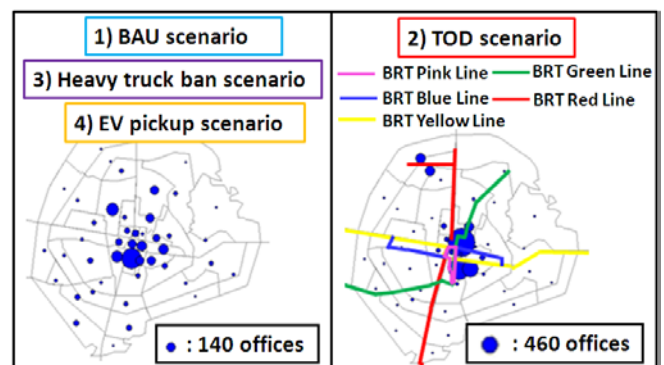


Figure6. Location distribution of offices in 2050



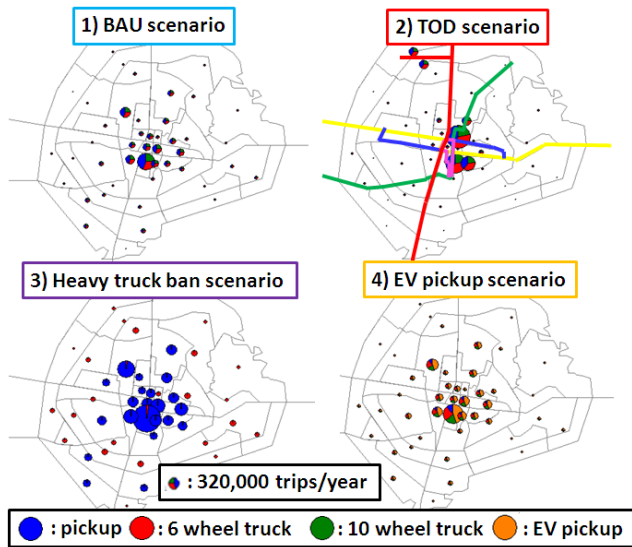


Figure7. Location distribution of truck trip generation in 2050

## 4.2 Discussion

Estimated results from 2012 to 2050 in not only 4 scenarios but also combined TOD and EV pickup scenario are shown in Figure8 and Figure9.

### 4.2.1 Comparison of 2050 estimated vehicle-kilometers

Compared with in BAU scenario, 2050 estimated vehicle-kilometers in TOD scenario are reduced by 27 percent (See Figure 8). This is because more truck trip OD has shorter distance between zones since more truck trip generation is concentrated near the BRT stations.

Heavy truck ban and EV pickup scenario increase 2050 estimated vehicle kilometers by 155 and 27 percent compared with BAU scenario. This is because 4 and 6 pickup trips are generated when a 6 and a10 wheel truck trip are converted, and 2 EV pickup trips are generated when a pickup trip is converted. Trip conversion ratios are decided based on ratios between payloads of 2 different vehicles.

### 4.2.2 Comparison of 2050 estimated CO<sub>2</sub> emissions

Figure9 shows that 2050 CO<sub>2</sub> emission in TOD scenario is reduced by 26 percent compared with in BAU scenario due to the huge reduction of 2050 vehicle kilometers.

Heavy truck ban scenario increases 2050 CO<sub>2</sub> emission by 64 percent compared with BAU scenario due to huge growth in 2050 vehicle kilometers.

EV pickup scenario reduces 2050 CO<sub>2</sub> emission by 6

percent compared with BAU scenario, because the estimated CO<sub>2</sub> emission is influenced by downward trend of CO<sub>2</sub> emission from power sector in Thailand Power Development Plan.

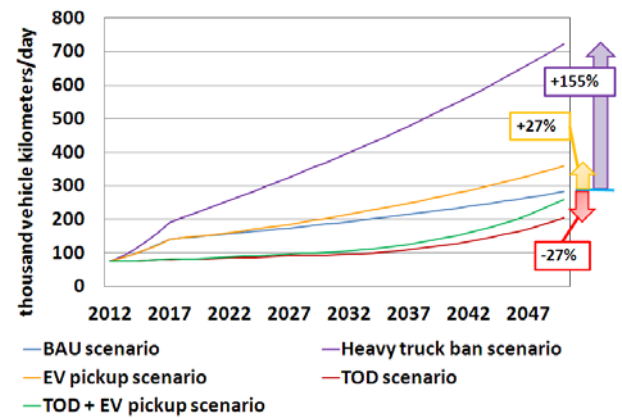


Figure8. Comparison of estimated vehicle-kilometers toward 2050

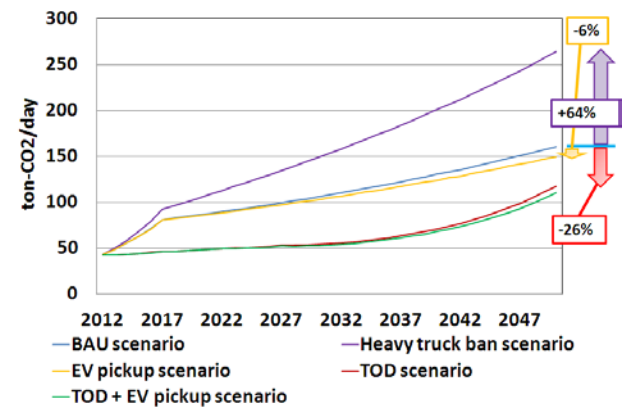


Figure9. Comparison of estimated CO<sub>2</sub> emission toward 2050

## 5. Conclusions

Based on the interview survey, characteristics of truck trip generation/attraction in Khon Kaen are clarified. For example, heavy trucks easily enter Khon Kaen and truck flow from/to outside and suburb of Khon Kaen is relatively large.

As the result of comparison between 4 scenarios, TOD has big impact on reducing 2050 CO<sub>2</sub> emission. Heavy truck ban has big impact on increasing 2050 CO<sub>2</sub> emission. EV pickup dissemination has small impact on reducing 2050 CO<sub>2</sub> emission. Consequently, combined TOD in freight transport and EV pickup dissemination is the most effective for CO<sub>2</sub> reduction.

## References

- 1) Y. Ito et al. (2011): Study on the Model for Developing the Urban Structure to Minimize CO<sub>2</sub> Emission –Case of Khon Kaen City, Thailand–, Master Thesis at Nihon University (in Japanese)

# Which factors influence the relief goods convergence in humanitarian logistics?

Student Number: 11M18019 Name: Tsunenori ANDO Supervisor: Shinya HANAOKA

## 人道援助ロジスティクスにおける物資滞留問題の解析

安藤 恒徳

東日本大震災のような大規模災害時には、被災者支援を目的とした人道援助ロジスティクスが必要であり、支援物資輸送はその中心に位置づけられる。しかし、過去の災害も含め、集積所における物資の滞留が問題点として指摘されてきた。そこで本研究では、東日本大震災を対象に物資滞留に影響を与える要因を明らかにした。また、支援物資輸送の滞留現象を再現するシミュレーションモデルを構築し、物資滞留発生現象の主要因を解明した。

## 1. INTRODUCTION

In recent years, natural disasters, such as an earthquake, a flood, and a typhoon, are increasing globally as shown in Fig.1. When the earthquake and tsunami in the coast of Sumatra that occurred in 2004, that supplies the necessary support to victims have not received enough is actualized, is globally recognized as "Logistics is a concern issue". Since then, the need to build appropriate humanitarian logistics (HL) has been pointed out in many places.

In the Haiti earthquake in 2010, although the support goods from each country had arrived to the large-scale warehouse, even the disaster victim of the end was not prudent and it exposed insufficient logistics management. In addition, due to the frequent occurrence of large-scale natural disasters, there is a growing interest in the HL also in international organizations. The World Food Program (WFP) manages United Nations Humanitarian Response Depot (UNHRD), which owns 40 vessels, 60 airplanes, and 5,000 trucks directly, and is carrying out HL itself.

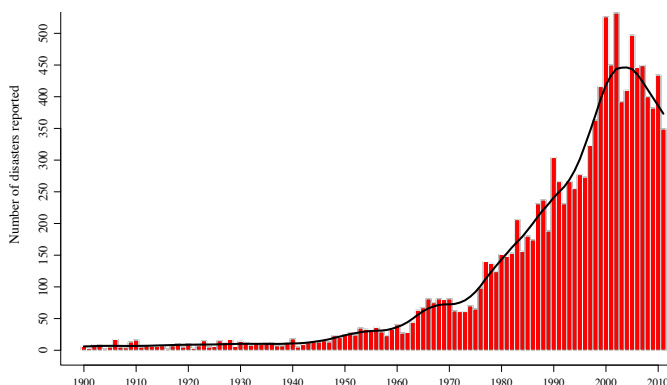


Fig.1. Natural disasters reported 1975-2011

Source: EM-DAT

Relief goods convergence is a big issue of

humanitarian logistics, and it is often observed in the Tohoku Earthquake. Fig.2 shows the amount of inventories in warehouse. It turns out that volume of inventories was dramatically increasing on 16 March, but after that there were few amounts of goods leaving the warehouse and many goods remained as stock. This is a phenomenon of goods convergence.

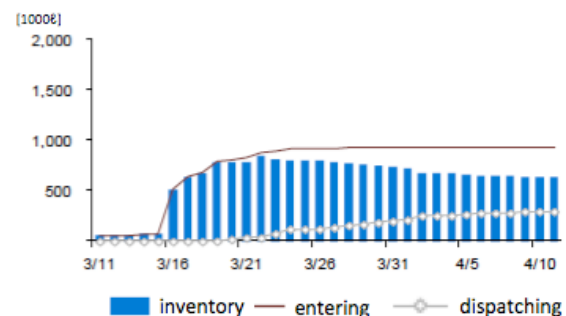


Fig.2. Amount of relief supplies[water] in Miyagi 1st warehouse Source: NRI[1]

For solving this problem, this study proposes to build a simple model to express relief goods convergence in humanitarian logistics based on the Asymmetric Simple Exclusion Process (ASEP). The objectives of this study are summarized as the following:

- To identify the causes of relief goods convergence.
- To build humanitarian logistics flow model.
- To analyze the simulate results.

## 2. IDENTIFYING CAUSES OF RELIEF GOODS CONVERGENCE

Several reports describes the problem of relief goods convergence of Tohoku Earthquake [2][3] Based on these report, there are six causes for this problem, as follows:

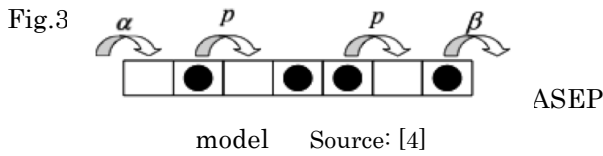
- Operation by inexperienced officers
- Unregulated and uncontrolled operation

- iii.) Lack of warehouse facilities
- iv.) The difficulty in sharing information
- v.) Frequent demand change
- vi.) Many suppliers

This study focuses on the problems of vi.) many suppliers. Other causes are not subjects of this study because they are possible for solving by standardization of the operation method and technological development.

### 3. ASEP MODEL

ASEP is a non-equilibrium statistical mechanics model, called the one-dimensional asymmetric simple exclusion process. ASEP is referred to as an open system that the system as shown in Fig.3. Particles are inserted into the line with the inflow probability  $\alpha$  and move to next box in probability  $p$ . After that, they removed at the end with the outflow probability  $\beta$ .



ASEP model is used to represent traffic stream. ASEP figured out principle of traffic congestion and proposed a solution. And, it was applied the results to improvement of production efficiency in plant by considering products as cars. So, this model can represent relief goods convergence in humanitarian logistics in a similar way.

Minemura, et al[4] developed a simple model of a production plant based on the ASEP and simulate the dependence of the lead time  $T$  on the lot size  $r$ . Then, they derived an analytical description of the simulation results based on exact results for the single-species ASEP. Furthermore, they determined the optimum lot size and investigate dependence of it on several parameters used in the simulations. A production plant is in general characterized by a complex network structure where many processes join and diverge each other. In order to simplify things, they first consider a one-dimensional model with a strictly linear structure (Fig.4).

## 4. MODEL DEVELOPMENT

### 4.1 Concept of Humanitarian logistics

Collected relief goods are loaded in trucks and other means of transport in distribution point.

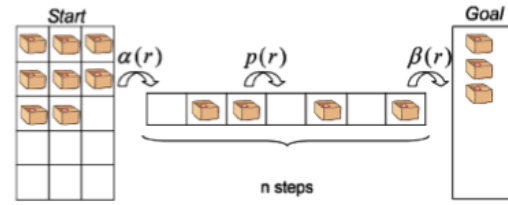


Fig.4. Production plant model Source:[4]

After that, they are transported to 1st warehouse placed in the prefecture. In 1st warehouse, the unloaded relief goods are sorted for 2nd warehouse placed in the municipality and transported to 2nd warehouse. In 2nd warehouse, the unloaded relief goods are again sorted for shelter and transported to shelter. This flow is used as a reference to make a model.

### 4.2 Modeling humanitarian logistics by ASEP

Humanitarian logistics flow is generally characterized by a complex network structure where many processes join and diverge each other. In order to simplify things, we consider a one-dimensional model with a strictly linear structure as shown in Fig.5. Let us assume that humanitarian logistics delivers  $N$  relief goods. The  $N$  relief goods move downstream to the shelters. Relief goods leave DP by the supply probability  $S_p$ , and move a transportation cell by the transportation probability  $T_p$ , and in this cell, the concept of ASEP is used. In a warehouse cell, there is no effect of ASEP. So two or more goods can put into one cell by the input volume probability  $I_p$ , and come out of here by Output volume probability  $O_p$ .

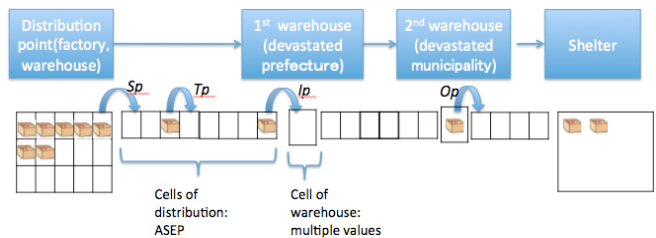


Fig.5. Humanitarian logistics model

#### (1) Setting the cell

Some cells in this model are two of the cells and cell transport depot. First, a transportation cell expresses the process of transportation and the number of cells expresses the length of the time concerning the transportation. Moreover, a warehouse cell expresses a warehouse and the

number of balls that are in this cell is in stock.

#### (2) Setting the transition probability function

Input and output volume probabilities are estimated from the actual data. And transport probability and supply probability are given arbitrarily.

#### (3) Setting the time

Let the concept of the time in this model be the number of times of calculation of a simulation. Calculation times are when the probability calculation was performed in all spheres located on the cell. And it considers that this one calculation is 1 hour, and regards it as one day in 24 hours.

#### (4) Simulation calculation

Simulation is performed 10 times. Java is used for the calculation of the simulation.

## 5. SIMULATION

### 5.1 Aggregate calculation of actual data

Aggregate calculation of database received from Tohoku University Logistics Research Group shows entering and dispatching goods are conducted randomly. This can be regarded as Poisson process with random transport by many suppliers.

### 5.2 Parameter estimation of $I_p$ and $O_p$

Estimate Input volume probability and output volume probability of the Poisson distribution from the actual data. It is calculated as the following equation (1):

$$\Pr(X = k) = e^{-\lambda} (\lambda t)^k / k! \quad (1)$$

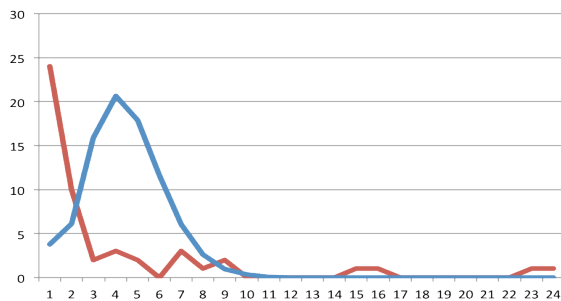


Fig.6. Estimation result

Fig.6 shows expected frequency from estimation result (blue line) and observed frequency of database (red line) of water in Iwate prefecture. X-axis shows the number of occurrences  $k$  and y-axis shows the probability of it.

### 5.3 Simulation conditions

The simulation using Humanitarian logistics model and estimated Input volume probability and Output volume probability is performed. The performed simulations are four cases of Iwate water, Miyagi water, Iwate clothing, and Miyagi clothing. As a virtual value, the number of goods, the number of cells, etc. see volume of inventories and a lead time how change from change of probability. The parameters used in the simulations are summarized in Table1.

Table.1 Simulation condition

Target : Water in Iwate prefecture	
Times of simulation	10 times
Total goods	$N = 50$
Supply probability	$S_p = 100\%$
Transport probability	$T_p = 100\%$
Input volume probability	$I_p = \text{Poisson distribution } \lambda = 2.86$
Output volume probability	$O_p = \text{Poisson distribution } \lambda = 0.91$

### 5.4 Results

Fig.7 shows simulation result of water in Iwate prefecture to follow Poisson distribution based on Table.1. These graphs are the change of entering (left) and dispatching (right). The horizontal axis shows date and the vertical axis shows number of goods.

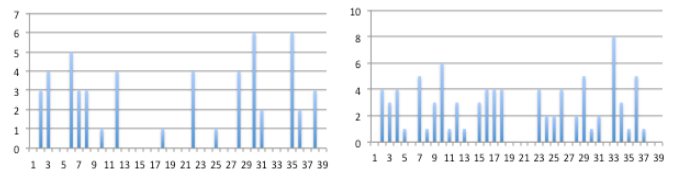


Fig.7 Simulation result

There are 3 patterns of change of inventory volume of water in Iwate prefecture as shown in Fig 8, 9 and 10 .

- (1) Happening the goods convergence (Fig.8): There are more than 5 days that more than 12 inventory volume. 12 is the max dispatching in a day.
- (2) Maintaining inventories (Fig.9): There is no goods convergence and out of inventory.
- (3) Out of inventory (Fig.10): There is a day that out of inventory.

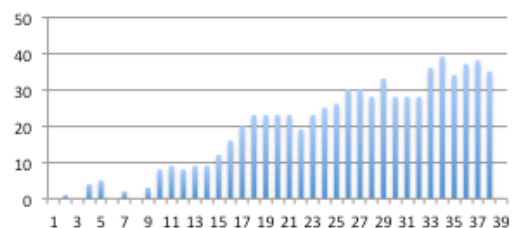


Fig.8 Happening the goods convergence



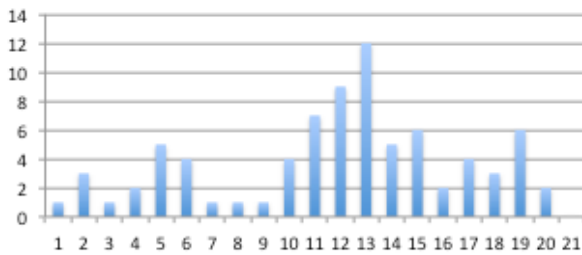


Fig.9 Maintaining inventories

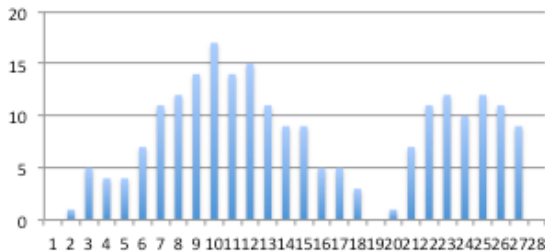


Fig.10 Out of inventory

Table.2 Simulation results

Target : Water in Iwate prefecture	
Input volume probability	Ip = Poisson distribution $\lambda = 2.86$
Output volume probability	Op = Poisson distribution $\lambda = 0.91$
<b>Result</b>	
(1) Goods convergence	5 times
(2) Maintaining inventories	4 times
(3) Out of inventory	1 time
Target : Water in Miyagi prefecture	
Input volume probability	Ip = Poisson distribution $\lambda = 1.85$
Output volume probability	Op = Poisson distribution $\lambda = 0.55$
<b>Result</b>	
(1) Goods convergence	7 times
(2) Maintaining inventories	3 times
Target : Clothes in Iwate prefecture	
Input volume probability	Ip = Poisson distribution $\lambda = 2.94$
Output volume probability	Op = Poisson distribution $\lambda = 2.80$
<b>Result</b>	
(1) Goods convergence	9 times
(2) Maintaining inventories	1 times
Target : Clothes in Miyagi prefecture	
Input volume probability	Ip = Poisson distribution $\lambda = 3.78$
Output volume probability	Op = Poisson distribution $\lambda = 0.28$
<b>Result</b>	
(1) Goods convergence	10 times
(2) Maintaining inventories	0 times

Table 2 shows results of all cases. As a result, the goods convergence can be shown in all cases. The goods convergence is demonstrated due to many suppliers as actual date.

## 5.5 Discussion

Simulation results of change of inventory volume expressed relief goods convergence. For controlling input volume, the other simulation supposing controlled logistics was performed by using fixed Input volume probability (Table.3). Target of this simulation is the clothes of Iwate Prefecture. The result of this simulation shows that it is able to maintain less inventory volume as shown in Fig.11. The goods convergence is able

to be reduced sharply. It can be said that it is an effective measures to perform controlled logistics for the goods convergence in humanitarian logistics from this result.

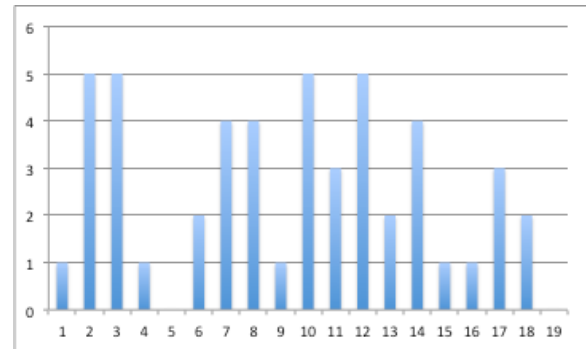


Fig.11 Change of inventory

Table.3 Improvement result

Target : Clothes in Iwate prefecture	
Input volume probability	Ip = 15%(arbitrary)
Output volume probability	Op = Poisson distribution $\lambda = 2.80$
<b>Result</b>	
(1) Goods convergence	1 time
(2) Maintaining inventories	9 times

## 6. CONCLUSION

This paper showed the 6 causes of the goods convergence identified by literature review. In Humanitarian logistics model using ASEP with estimating parameters regarded Poisson process, the goods convergence was expressed and uncontrolled logistics due to many suppliers is identified the cause of the goods convergence. The results show that there is a high possibility that goods may be stuck in the warehouse due to random transporting by many suppliers.

## Reference

- [1]野村総合研究所: 経済産業省委託調査報告書 平成23年度サプライチェーンを支える高度な物流システムの構築事業災害時等における緊急支援物資供給の効率化事業報告書,2012.
- [2]桑原雅夫, 和田健太郎:東日本大震災における緊急支援物資ロジスティクス定量的評価:一次集積所における搬入/搬出記録の分析, 第45回土木計画研究発表会, 2012.
- [3]峯猛:東日本大震災における救援物資供給停滞の発生とその要因, 物流問題研究, No.56,pp16-21,2011
- [4]Takumi Minemura, Katsuhiro Nishinari, and Andreas Schadschneider: Productivity Enhancement through Lot Size Optimization, Cellular Automata Lecture Notes in Computer Science Volume 6350, 2010, pp 593-599

# Economic Operation of Large-Scale Photovoltaic power Plants under Uncertainty

Student number: 11M18031

Name: Junichirou Ishio

Supervisor: Naoya Abe

不確実性を考慮した大規模太陽光発電システムの経済的運用に関する研究

石尾 淳一郎

本研究では、大規模太陽光発電システム（大規模 PV システム）の効率的な維持管理計画を策定するうえで必要となる基礎的要件を明らかにすることを目的とし、構成機器の劣化・故障の動態の分析、動的計画法による PV モジュールとパワーコンディショナ（PC）の交換計画の最適化、以上から想定される維持管理計画の経済性の評価・分析を行った。その結果、モジュールや PC の交換は経済的に効率的ではないことが明らかとなった。

## 1. Introduction

Following the introduction of Feed-in Tariffs (FIT) for large scale commercial photovoltaic (PV) power plants (mega-solar plants), the number of such plant has been substantially increasing in Japan. In order to gain revenue from their plant, operators need to keep the high level of output from the systems during the project. To accomplish this point, the operators have to manage the uncertainties related to failure occurrence. The failures occur at random but random operation and maintenance (O&M) are not so efficient. Well-designed plans for good O&M are necessary for the PV system operators.

## 2. Objectives

1. To simulate the dynamics of time-related deterioration of PV modules, the failure occurrence of power conditioners, and the dynamics of output change of large scale PV systems.
2. To clarify the basic characteristics of well-designed O&M plans which maximize the profit from large-scale PV system.

## 3. Output decline of a mega-solar plant

To simulate the dynamics of large-scale PV system, we simulated the time-related PV module deterioration by considering four types of failure modes, and failure occurrence of power conditioner (PC). We also considered the mismatch losses in PV arrays.

### 3.1. The dynamics of power decline of a PV module

First, we tried to determine the amount of annual output from a pristine PV module. Japanese Industrial Standards (JIS C 8907, 2005) gives the definition to estimate the output of it.

The output depends on nominal battery capacity, quantity of solar radiation, and power losses caused by various factors. We postulated the use of a 200Wp mono crystalline silicon module in Tokyo. It is facing south and the angle of elevation is 30°. Then the amount of annual output from a pristine PV module is given by:

$$E_p = H \times K \times P \times 365 \div I \quad (\text{eq. 1})$$

where,  $E_p$  is the amount of annual output from a module (kWh/year),  $H$  is the amount of solar radiation on the panel per a day in Tokyo (3.74 kWh/m<sup>2</sup>/day),  $K$  is the factors of losses (74%), [ $K$  is composed of loss by heat (15%), loss in PC (6%), and loss of circuit (7%)],  $P$  is the nominal PV capacity (200Wp), 365 is the number of days in a year and,  $I$  is the general solar irradiance (1kW/ m<sup>2</sup>). The resulting amount of annual output from a pristine PV module in Tokyo is 202kWh. This number was then used to simulate the time-related deterioration of PV modules. In this research, we considered four types of failure modes and simulated their occurrence and progress on PV modules.

### 3.1 Output simulation from a PV module

A number of reports on the cause of PV module degradation (i.e., Kato 2010, Ferrara 2012) were studied, but we adopted the report “Mean Time Before Failure of Photovoltaic modules” by Realini (2003). Realini reported not only the factors which cause degradation but also their numerical information such as the frequency of occurrence in 10kW PV modules and the output decline of 21 years old PV modules. We focused on four degradation failures modes what Realini depicted in the report, i.e., “Yellowing”, “Delamination”, “Hot spot”, and “Terminal oxidation”. In this research, these four factors’

probability of occurrence, probability of progress, and effect to the output decline were considered. The function of time-related dynamics of a PV module output is expressed as:

$$P(t) = E_p \times \{1 - DR_y(t)\} \times \{1 - DR_d(t)\} \times \{1 - DR_h(t)\} \times \{1 - DR_t(t)\} \quad (\text{eq. 2})$$

where,  $P(t)$  is the annual amount of output from a module at year  $t$  (kWh),  $P_{max}$  is the annual amount of output of initial year of the project (202 kWh), and  $DR$  is the degradation rate. Each four failure occurs by following each failure occurrence probability. To get the probabilities, we calculated the reliability of a PV module against these failures. The reliability is given by equation (eq. 3) (Fukui 2008).

$$R(t) = \frac{n(t)}{N} \quad (\text{eq. 3})$$

$R(t)$  is the reliability of PV module at year  $t$ ,  $n(t)$  is the number of active items at year  $t$  (“active” means “never failed”) and,  $N$  is the number of total items in the targeting systems. According to Realini (2003) and Hasegawa (2011), who analyzed Realini’s data by FTA (Fault Tree Analysis), for 21 years old PV modules, the reliability against yellowing: 2.4%, delamination: 9.0%, hot spot: 75.1%, terminal oxidation: 56.6%. De Lia (2003) demonstrated that, the degradation rate of a PV module is fixed. Therefore we assumed that the probability of every failure occurrence follow the exponential distribution because the failure rate is independent from time if we assume exponential distribution (eq. 4).

$$h(t) = \lambda \quad (\lambda: \text{fixed}) \quad (\text{eq. 4})$$

Then the reliability function  $R(t)$  is expressed by eq. 5.

$$R(t) = \exp\left(-\int_0^t \lambda dt\right) = \exp(-\lambda t) \quad (\text{eq. 5})$$

Subsequently the failure occurrence probability is given by eq. 6.

$$\lambda = -\frac{\ln R(t)}{t} \quad (\text{eq. 6})$$

We can calculate the failure occurrence probability of each failure mode by eq. 6 and the data given by Realini. The failure occurrence probabilities are: yellowing:  $\lambda_y=0.178$ , delamination:  $\lambda_d=0.115$ , hot spot:  $\lambda_h=0.014$ , terminal oxidation:  $\lambda_t=0.027$ . These factors remain constant through time.

Once these failures occur, they progress by following certain progress probability and make the module worse. Hasegawa (2011) calculated these progress probability and how much the each failure progress decrease the output from a module by attaching FTA and ETA to the data of Realini (2003).

In this research, we adopted the result from Hasegawa and we simulated the time-related dynamics of a PV module output. In the simulation, we generated random numbers which follow normal distribution and conducted a Bernoulli trial by attaching the failure occurrence probabilities as thresholds.

Figure 1 shows the time-related dynamics of a PV module degradation caused by four types of degradation failure modes. And the result is the average of 1,000 trials of Monte-Carlo simulation. The blue

line shows the effect of yellowing, the green line is delamination, the red line is hot spot, and the sky blue line shows the effect of terminal oxidation. We multiplied the effects by the four failures and got Figure 2 as a result of the dynamics simulation of a PV module output (1,000 trials). The average degradation rate was 0.8%/year and it was almost constant (Fig. 3). This result is similar to the result of Jordan (2011) given by real field observation.

Figure 4 shows the distribution of PV module output at year 20. The distribution is bimodal. The mean output is 171.7kWh/year, the median output is 178.6kWh/year and the standard deviation of the distribution is 14.8.

### 3.2 Output from a PV array

One of the characteristics of large-scale PV systems is that the output from the system is not equal to the amount of output from all PV modules in the system. The reasons are the mismatch losses in PV arrays and the failure of PCs. We discuss the mismatch losses here.

In the general PV systems, PV modules are connected in series and parallel to adjust the output (current and voltage) for use, and the group of PV modules are called “PV array”. The actual number of PV modules in a PV array is about 10 to 50. However the output dispersion of each module causes mismatch losses in PV arrays. The lower output modules become the bottleneck of an array and the output from an array is limited by the low output modules even if the other modules are keeping high performance. The loss is generally called mismatch loss. The loss depends on each module’s I-V curve and the circuit structure of an array but we assumed that “The output from an array” = “the lowest output of a module in an array” times “the number of modules in an array” to simplify the simulation model.

### 3.3 Failure of power conditioners

As we mentioned, we need to consider the state of PC when we simulate the output from PV systems. Because of the function as an AC/DC converter, once PC fails the output (AC) from the system will

become 0 substantially.

Kato (2010) investigated 483 residential PV systems and checked the records of their components’ trouble and failure histories. As a result, Kato clarified that 101 PC experienced failures and some of them are replaced in 12 years operation. Many of them failed in early years of their operation. We used Kato’s data to simulate PC failure occurrence. The state of PC is defined as two patterns “normal” or “fail”. We gave a failure occurrence probability as a threshold to conduct Bernoulli trial. To consider the characteristics of PC failure, we renewed the threshold every year.

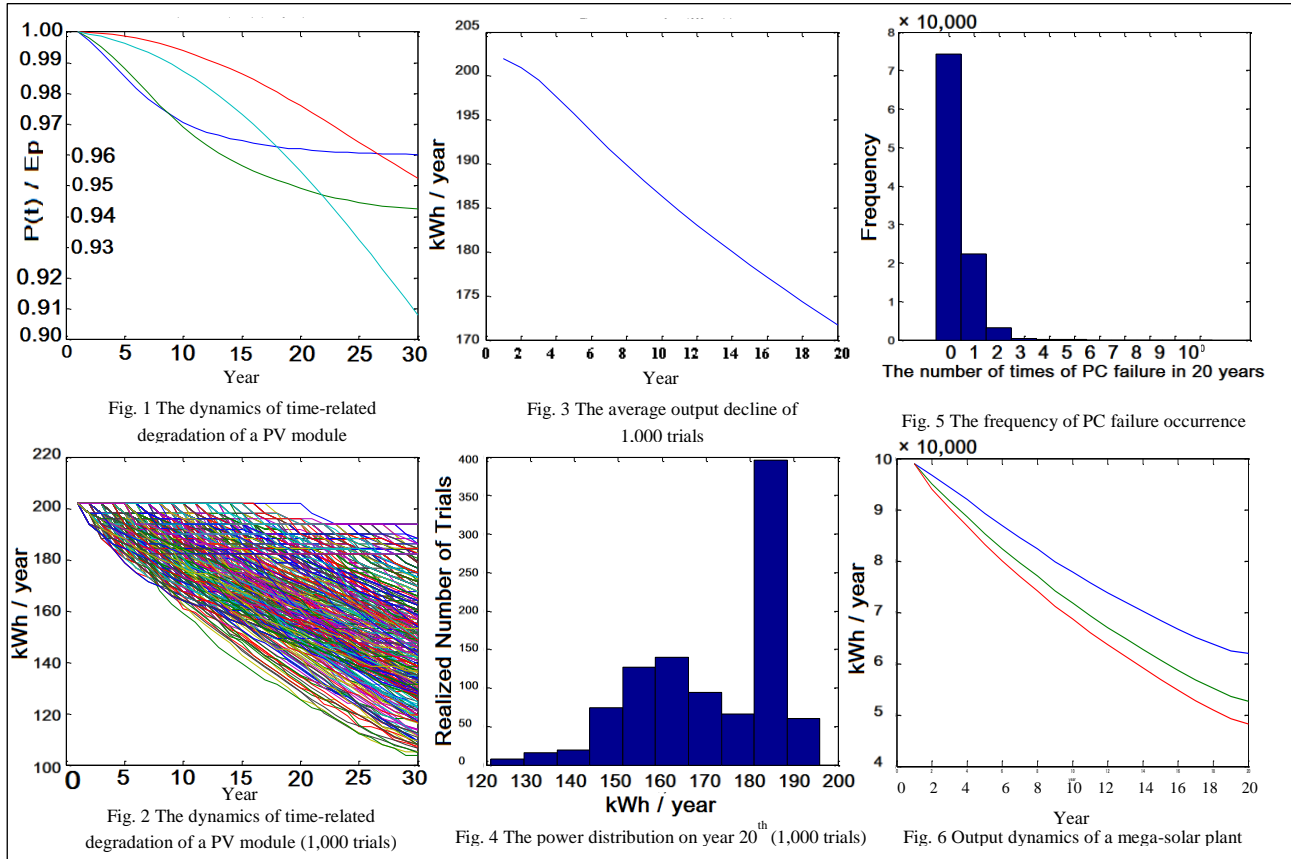
To get the PC failure occurrence probability, we assumed the time-related dynamics of probability follows exponential distribution. Also we assumed the percentage of failed PC in 483 PCs as a PC failure occurrence probability and the total number of failure experienced PCs by year 12 follows the probability density function of an exponential distribution  $F(\tau)$  to get probability distribution function, we considered the probability distribution function as a function of failure occurrence probability at year  $t$ . Figure 5 shows the result of failure occurrence simulation of PC. We simulated 10,000 PCs operations in 20 years. 2,141 PCs failed in the simulation but the PCs which experienced two or more failures were only about 3% of all. The results about the percentages are similar to Kato’s actual investigations. However Kato considered PC only for residential use because of data deficiency about the large scale PCs for commercial use.

### 3.4 The output from a mega-solar

To clarify the time-related output dynamics of large-scale PV systems, we considered the degradation of one module, the effect of mismatch losses in arrays, and PC failure occurrence.

Based on these considerations, we simulated the output from 1MW large-scale PV power plant. We assumed 5 PCs whose maximum capacity are 200kW and each of them are controlling the output from 1,000 PV modules.

The result is shown on Fig. 6. The blue line shows the result of no mismatch losses case. The green line shows the result of a case that one



array is constructed by 10 modules. The red line shows the result of a case that one array is constructed by 50 modules. Through this simulation we clarified that the effect of failure occurrence and mismatch loss because the output from a degraded PV system goes down to 48% ~ 62% of initial output in 20 years if the operators did not take O&M actions.

#### 4. Dynamic programming

The frequent treatment for the components keeps the performance of a mega-solar high but too frequent treatment increase the operational cost of the mega-solar project. To maximize the profit from the mega-solar project, the operators have to develop the plan which balances the revenue and O&M cost. To clarify the basic characteristics of the optimal O&M plan, we applied dynamic programming. In short, dynamic programming is the method to find the discrete action variables which maximized or minimized the target function with considering the option of actions of the discrete states changed by the action.

Let's consider the maximizing program of  $f(x_1, \dots, x_n)$  (eq. 7). A matrix of state variables  $x_i$  a set of countable discrete values  $\{a_1, \dots, a_N\}$ . Then we try to find the optimal set of  $x_i$  which maximizes  $f(x_1, \dots, x_n)$ . If we consider choosing  $x_i$  as making decision, this problem can be recognized as a multistage decision problem (eq. 8). Through the process of eq. 9 to 12, we can consider  $f(x_1, \dots, x_n)$  as a maximization of  $f_n(x_n)$ . If we assume  $x_n^*$  as a set of numbers which maximize  $f_n(x_n)$ ,  $x_{n-1}$  is decided by the function  $x_{n-1}^* = \hat{x}_{n-1}(x_n^*)$ . And we can decide the optimal  $x_1$  which follows  $x_1^* = \hat{x}_1(x_2^*)$  with repeating backward the same processes. The way to find the optimal set of state variables by this way is called backward recursion. We apply backward recursion to solve the optimization problems.

In this research, to find the best replacement plan which maximizes the profit from the system, we assume certain action variables, state transition functions, reward function, and Bellman equation. We solved the Bellman equations by backward recursion.

$$J = f(x_1, \dots, x_n) \rightarrow \max \quad (\text{eq. 7})$$

$$J = f_1(x_1) + h_1(x_1, x_2) + \dots + h_{n-1}(x_{n-1}, x_n) \rightarrow \max \quad (\text{eq. 8})$$

$$f_2(x_2) = \max_{x_1} [f_1(x_1) + h_1(x_1, x_2)] \quad (\text{eq. 9})$$

$$J = f_2(x_2) + h_2(x_2, x_3) + \dots + h_{n-1}(x_{n-1}, x_n) \rightarrow \max \quad (\text{eq. 10})$$

$$f_n(x_n) = \max_{x_{n-1}} [f_{n-1}(x_{n-1}) + h_{n-1}(x_{n-1}, x_n)] \quad (\text{eq. 11})$$

$$J = f_n(x_n) \rightarrow \max \quad (\text{eq. 12})$$

#### 4.1 A PV module replacement

We optimized the PV module replacement plan by using dynamic programming. We assumed 20 years as the project duration and assumed 100,000 yen as a replacement cost of one PV module (200Wp). The revenue function of a PV module is given by equation 13. The action variables for operators are shown on eq. 14. The state transition function is eq. 15. The reward function is eq. 16. The Bellman equation is eq. 17.

$$p(a) = 42 \times \{202 \times (1 - 0.008)^{a-1}\} \quad (\text{eq. 13})$$

$$x \in \{\text{keep, replace}\} \quad (\text{eq. 14})$$

$$g(a, x) = \begin{cases} a+1, & x = \text{keep} \\ 1, & x = \text{replace} \end{cases} \quad (\text{eq. 15})$$

$$f(a, x) = \begin{cases} 42 \times \{202 \times (1 - 0.008)^{a-1}\} & x = \text{keep} \\ -91516, & x = \text{replace} \end{cases} \quad (\text{eq. 16})$$

$$V(a) = \max \{484 \times 0.992^{a-1} + 0.9V(a+1), -91516 + 0.9V(1)\} \quad (\text{eq. 17})$$

We solved the Bellman equation by backward recursion, and got the optimal set of action variables and state transition function which maximize the profit from a PV module operation. Figure 7 shows the optimal state path of a module operation. The vertical axis means the age of the module and the horizontal axis means the year of the project. The age of a PV module is increasing monotonously. It means that no replacement is the best choice which maximizes the profit of a PV module operation.

The opportunity loss caused by conducting no replacement is far smaller than the replacement, it indicates that the degradation rate of PV module is small, or the replacement cost is too high to replace a module. To know the relation of the replacement cost and the decision of replacement, we calculated the maximum costs of replacement that allow operators to replace a module (Fig. 8). The result shows that the replacement cost per a module should be lower than 1,1440yen to allow the operators to replace the degraded module.

#### 4.2 A Power conditioner replacement

We can apply dynamic programming only if the reward function is known, so we cannot apply the method to the case of PC replacement because the occurrence of PC failure is stochastic and sporadic. In contrast to PV modules failures, PC failures are easy to find because of the function of PCs and their failure occurrence frequency is relatively low. According to the result shown by Fig. 5, 70% of PCs never fail in 20 years operation and the PCs fail over two times is only 2% of all PCs in use. So we assumed that PCs fail once in 20 years operation and aimed to give the information for making decision whether or not to replace PCs after they fail. The patterns of failure occurrence are only 20.

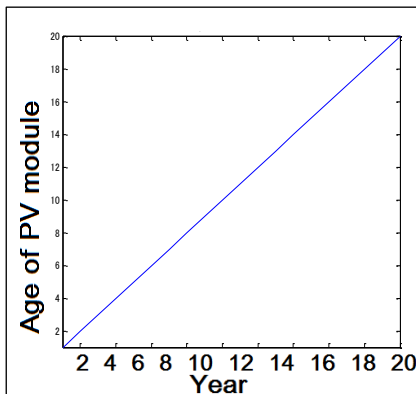


Fig. 7 Optimal state path of a PV module

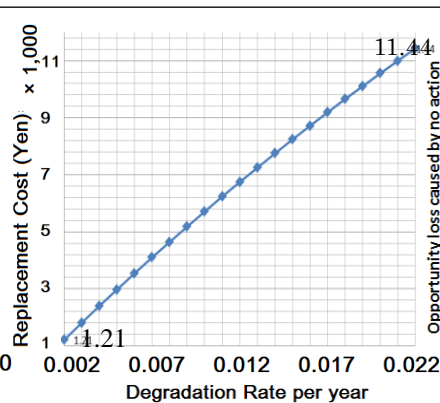


Fig. 8 A module degradation and replacement cost

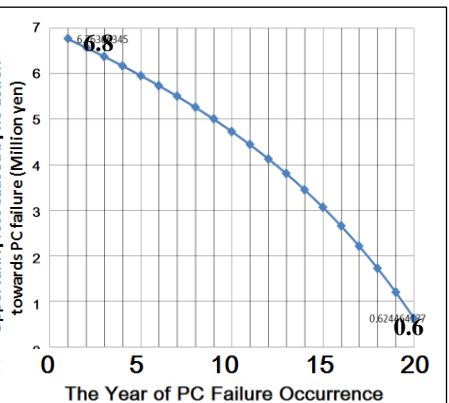


Fig. 9 Opportunity loss caused by no action

So we calculated the opportunity loss of no replacement for each pattern.

We assumed the capacity of PC is 200kW, one PC is controlling 1,000 modules, the array is constructed by 10 modules.  $S_{pc}(a)$  is the state of PC on age  $a$ . If the PC fails  $S_{pc}(a)$  becomes 0. Then the system output is eq. 18.

$$P_{system}(a) = \left[ \sum_{j=1}^{100} \left\{ 10 \times \min_{i \in \{1,2,\dots,10\}} (P_{modulej,i}(a)) \right\} \right] \times S_{pc}(a) \quad (\text{eq.18})$$

We calculated the opportunity loss and the result is shown on the Figure 9. If the replacement cost is higher than the opportunity loss of no replacement, it is more profitable for the operators not to replace the failed PC. If the replacement cost is lower than the opportunity loss, the replacement becomes more profitable. The highest opportunity loss was 6.76 million yen at year 1. The actual replacement cost of large scale PC (200kW) is about 10 million yen (GS Yuasa, telephone survey, 2012.12.26) so it is better for the operators not to replace but to maintain to prevent failures with paying maintenance cost lower than the values of curve on Figure 9.

## 5. The Evaluation of mega-solar projects

We assumed some O&M plans with considering the results by section 4 and evaluated their economic efficiency by calculating NPV of mega-solar plant project under each O&M plan. We assumed 1MW mega-solar plant project and the actual number of its cost and revenue are given by the report from the National Policy Unit of Japan (コスト等検証委員会 2011) (Table 1).

To calculate NPV for each O&M patterns, we need to know the cash flow of the project. According to the numbers on table 1, we simulated the cash flow in case the operators don't conduct any O&M actions (Fig. 10). High initial cost, the revenue decline because of degradation of the components, and scrapping cost on the last year of operation are shown in the figure. We calculated NPV of the project for each O&M pattern and summarized the result on Table 2 but we assumed 5% as a discount rate here.

We assumed 7 patterns of O&M. To validate the result of section 4.1 we assumed no replacement for modules and replacement case conducting module replacement with referring the preventive exchange thresholds (80%, 75%, 70%). To validate the result of section 4.2, we assumed O&M pattern 1, 5, and 7.

According to the results shown on table 2, The O&M patterns which don't replace PV module were more efficient, and not to do any treatment to PC causes similar effect on NPV to pay 4.8 million yen for PC maintenance every year.

However the every pattern of NPV was negative. It is mainly caused by high construction cost so even if the operators manage well the mega-solar plant, the profitability of the project is still low. To improve the profitability, not only O&M but also construction cost should be improved.

## 6. Conclusion

For the first objective, we simulated the time-related dynamics of PV module output and the failure occurrence of power conditioner. With considering the influence of mismatch loss, we simulated the dynamics of the output from a mega-solar (Fig.6). If the operators don't conduct O&M actions, the output from a mega-solar declines to 48% ~ 62% in 20 years.

For the second objective, we clarified that no actions toward degrading PV modules is economical choice for the operators. And maintenances for PCs may be the more efficient action than the full replacement of them because the opportunity loss caused by no replacement of a PC is lower than the replacement cost.

Table 1 Parameters of mega-solar cost (1MW)

Cost	Capital cost 0.473 B yen	Construction cost	System price (350,000 yen/kW)
		• 1MW • 25,000m <sup>2</sup> (0.38 B yen)	Land price (100yen/m <sup>2</sup> )
			Voltage up (15 M yen)
			Line price (12 M yen)
			Real estate tax (370M yen/year)
		Scrapping cost of facilities (19 M yen)	
	Operating cost	Maintenance cost (replacement cost)	
		Other costs (7.25 M yen/ year)	
Revenue	Sales of electricity (42yen/kWh)		

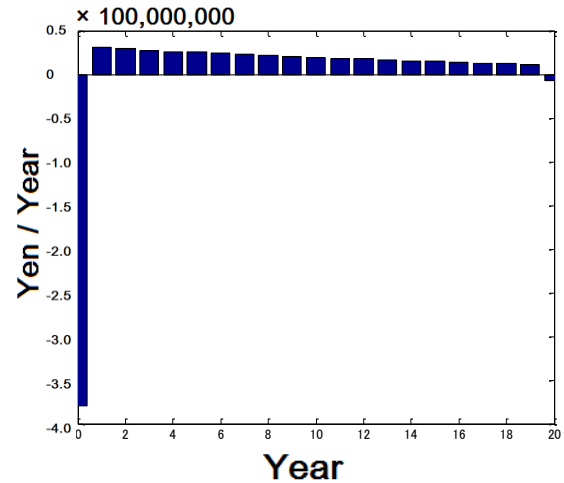


Fig. 10 Cash flow of mega-solar operation (No action case)

Table 2 NPV on each maintenance pattern

	PC	PV module	Rank of profitability
1	No action	No action	3 (NPV:-0.123 B¥)
2		Preventive replacement (80%)	7 (-0.132)
3		Preventive replacement (75%)	6 (-0.126)
4		Preventive replacement (70%)	3 (-0.123)
5	Maintenance	No action	1 (-0.064)
6	0.1Myen/year	Preventive replacement (75%)	2 (-0.065)
7	Maintenance 4.8Myen/year	No action	3 (-0.12)

## Reference

- [1] 加藤和彦, 太陽光発電システムの不具合事例ファイル, 日刊工業新聞社, 2010 年
- [2] Claudio Ferrara and Daniel Philipp, Why Do PV Modules Fail?, 2012, Energy Procedia 15
- [3] Ayumu Hasegawa, et al., Evaluation of Reliability Considering Degradation and sudden Failure of Photovoltaic Module, 2011
- [4] Antonella Realini, Mean Time Before Failure of Photovoltaic modules, 2003, Final report BBW 99.0579
- [5] 福井泰好, 入門 信頼性工学, 2006, 森北出版株式会社
- [6] Francesco De Lia, Salvatore Castello Luigi Abenante, Efficiency degradation of c-silicon photovoltaic modules after 22-year continuous field exposure, 2003, 3<sup>rd</sup> World Conference on Photovoltaic Energy Conversion
- [7] D. C. Jordan, S. R. Kurtz, Photovoltaic Degradation Rates – an Analytical review, 2011, DOI: 10.1002/pip. 1182
- [8] M. Vazquez, Photovoltaic Module Reliability Model Based on Field Degradation Studies, 2008, Wiley InterScience DOI: 10.1002/pip.825
- [9] 大友政吉, 太陽光発電システムにおける経年モジュールの影響評価と信頼性モデルの検討, 2011
- [10] 国家戦略室 コスト検証委員会, コスト等検証委員会報告書, 2011



# Lifetime Prediction of Concrete Mixed with Seawater against Chloride Attack and Carbonation

Student Number: 11M18054

Name: Hiroki OHARA

Supervisor: Nobuaki OTSUKI

塩害および中性化における海水練りコンクリートの寿命予測

小原 弘毅

本論文では、将来的な淡水不足から、練混ぜ水に海水を使用したコンクリートの物質透過性や内部鋼材の腐食挙動を明らかにし、塩害および中性化に対する寿命（潜伏期および進展期）を定量的に評価した。その結果、塩害環境下の潜伏期は、練混ぜ水として海水を用いた場合の方が淡水の場合より短くなった。しかしながら、進展期は前者の方が長くなり、両者を足し合わせた寿命は同程度となった。特に置換率 55% の高炉セメントを用いた場合、両者の差は最も小さくなり、寿命は約 40 年となった。一方、中性化環境下の寿命は練混ぜ水が与える影響は小さく、セメント種類による影響が大きいことが分かった。

## 1. Introduction

World Meteorological Organization (WMO) reports that two-third of world population is going to suffer from water shortage until 2025. At that time, it is necessary to use seawater as concrete material. However, seawater usages as concrete material have not been investigated enough. So considering this background, to use seawater as concrete material, objectives of this thesis are set as below;

1. To clarify material properties and corrosion behavior of concrete mixed with seawater
2. To predict quantitative lifetime of concrete mixed with seawater against chloride attack and carbonation

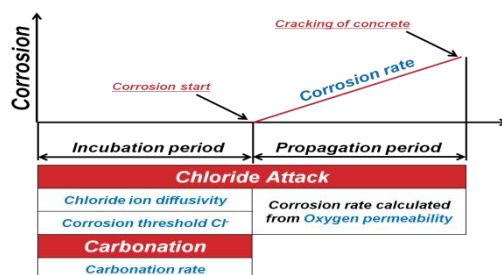


Fig.1 Lifetime

In this research, lifetime of concrete is classified as shown in figure 1. To predict these lifetime, material properties and corrosion behavior such as chloride ion diffusivity, corrosion threshold chloride ion contents, carbonation rate for incubation period, and oxygen permeability for propagation period are investigated.

## 2. Materials property of concrete mixed with seawater

### 2.1 Specimens

In this thesis, two types of specimen are used. First one is concrete to clarify chloride ion

diffusivity, and carbonation rate for chapter 2. The mix proportion have 2 parameters of mixing water (freshwater, seawater), 2 parameters of Water cement ratio (0.5, 0.7), and 4 parameters of BFS (Blast Furnace Slag: By-product from steel industry) replacement ratio (0(Ordinary Portland Cement), 40, 55, 70%). Totally, 16 patterns of concrete are prepared. Additionally, unit water content is 171kg/m<sup>3</sup> (W/C: 0.5), and 174 kg/m<sup>3</sup> (W/C: 0.7). Initial chloride content in concrete induced by seawater is about 3.0kg/m<sup>3</sup>. And s/a is 42% (W/C: 0.5), and 46 % (W/C: 0.7). Target slump and air content are 8±4 cm, and 3±2%. Curing condition is in moist air. Additionally, OPC have been cured for 5 days, and BFS have been done for 7days. Second one is mortar with embedded steel to clarify oxygen permeability and corrosion behavior for Chapter 2 and 3. The mortar specimen embedded steel (φ 13×100mm), mix proportions are similar to concrete. But in case of mortar, curing condition is submerged condition in those mixing water for 7 days. And S/C is equal to 2.0.

### 2.2 Chloride ion diffusivity coefficient

To clarify chloride ion diffusivity, concrete specimen which has been exposed in artificial seawater for 4 months is used. The way to evaluation is conform to Japan Society of Civil Engineers (JSCE)-G 572-2010. And the equation is used Fick's diffusion equation as shown equation 1.

$$\partial c / \partial t = D \nabla^2 c \quad \text{Eq.1}$$

(c: amount of chloride content (kg/m<sup>3</sup>), t: exposure time (year), D: chloride ion diffusivity (cm<sup>2</sup>/year))

As shown in figure 2, chloride ion diffusivity of concrete mixed with seawater is lower than that mixed with freshwater. It might be that initial chloride content induced by seawater as concrete material decreases chloride ion concentration difference between concrete and exposed seawater. Additionally, chloride ion diffusivity is decreased with increasing of slag replacement ratio.

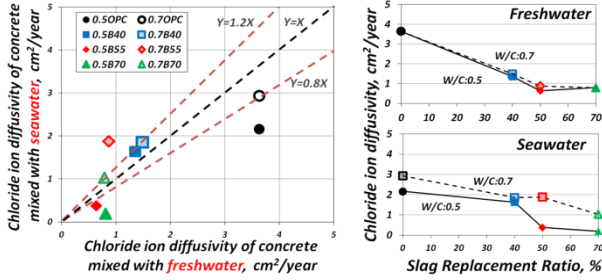


Fig. 2 Chloride ion diffusivity

### 2.3 Carbonation rate coefficient

To clarify carbonation rate coefficient using concrete specimen, the evaluation method is conform to JIS A 1153. The result is shown in figure 3.

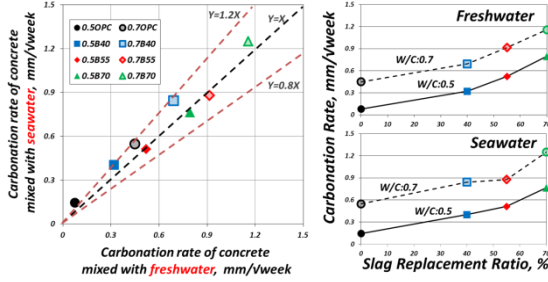


Fig. 3 Carbonation rate coefficient under air

As can be seen, the difference between freshwater and seawater as concrete material is small. So the effect of seawater is very low. However, using BFS the carbonation rate is increased with increasing of replacement ratio. Because high BFS replaced cement have low pH in its cement matrix.

### 2.4 Oxygen permeability

To clarify oxygen permeability, limit current density obtained from cathodic polarization curve with mortar specimen is substituted in equation 2.

$$\partial Q / \partial t = -i_{lim} / nF \quad \text{Eq.2}$$

( $\partial Q / \partial t$ : Oxygen permeability (mol · cm²/sec),  $i_{lim}$ : limit current density (A/cm²),  $n$ : atomic value (=4),  $F$ : Faraday constant (96500c/mol)).

The result is shown in figure 4. As a result, The figure indicate that the difference between freshwater and seawater as concrete material is small for OPC, while BFS cement mortar mixed with seawater have lower oxygen

permeability than that mixed with freshwater. Additionally, this value is decreased with increasing of BFS replacement ratio, because BFS have reduction ability on oxygen supplies.

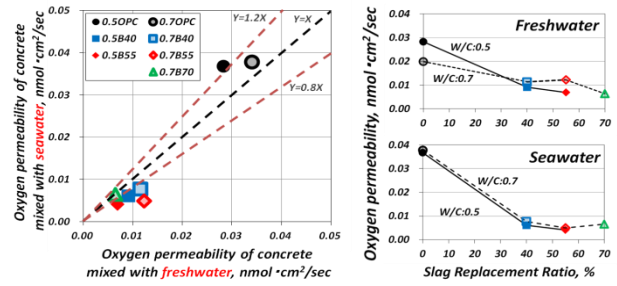


Fig.4 Oxygen permeability

## 3. Corrosion behavior

In this chapter, corrosion behaviors which are corrosion current density and corrosion threshold chloride ion content are investigated.

### 3.1 Corrosion current density

To clarify corrosion threshold chloride ion content, time-dependent change of corrosion current density is needed. This value can illustrate a phenomenon of corrosion. For understanding corrosion current density, AC-impedance method is used. The specimen which is mortar embedded reinforcement is also exposed to 50°C and 3%NaCl spray zone after 7 days submerged curing. The result is shown in figure 5 using W/C=0.5 specimen. And, this figure have red dashed line at 0.2  $\mu\text{A}/\text{cm}^2$ , this is the corrosion threshold current density defined by International Federation for Structural Concrete (FIB). As shown in figure 5, if corrosion current density is higher than this value, embedded steel is corroded.

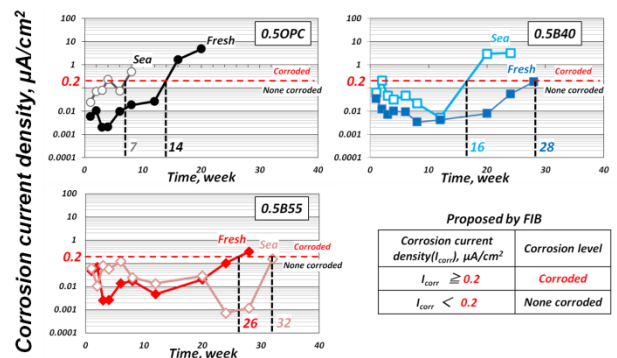


Fig.5 Time dependent of Corrosion current density (In case of W/C=0.5)

The result in figure 5 shows, as can be seen, the duration to reach corrosion threshold current density is steadily increased with increasing of BFS replacement because of decreasing of chloride ion diffusivity. Besides, in case of OPC and BFS 40% replaced pattern, duration of the mortar mixed with seawater to

reach corrosion threshold current density is shorter than that mixed with freshwater, because initial chloride content induced by seawater as concrete material decrease the duration to reach corrosion threshold chloride ion content. On the other hand, BFS55% replaced mortar mixed with seawater has almost same resistance against corrosion than that mixed with freshwater because of long duration to reach corrosion threshold current density and its chloride ion diffusivity are lower than that mixed with freshwater.

### 3.2 Corrosion threshold chloride ion content

In this section, using specimens which reached corrosion threshold current density detected by AC-impedance method in section 3.1, corrosion threshold chloride ion contents are determined. The evaluation method is conformed to JCI-SC45. The result is shown in figure 6. Additionally, the result of chloride ion contents analyzed from mortar specimen is converted into chloride ion content in concrete.

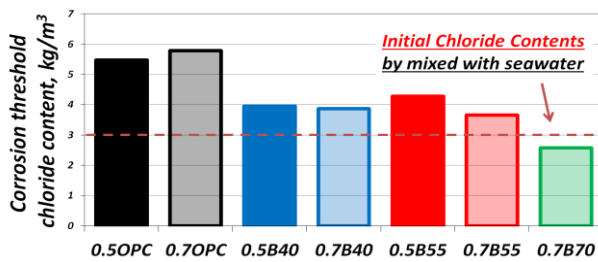


**Fig. 6** Corrosion threshold chloride ion content

As it can be seen, BFS pattern have lower corrosion threshold chloride ion content than OPC pattern. It is highly possible that  $Cl^-/OH^-$  (In general, when the value rises above 0.6, corrosion start.) is increased with increasing of BFS replacement ratio. Because high BFS replaced cement have low pH. Additionally, the value of BFS 70 % replacement (in case of  $W/C=0.7$ ) is less than initial chloride contents (dashed horizontal line shown in figure.6) induced by concrete mixed with seawater. It means BFS 70% replaced concrete mixed with seawater induce corrosion at the initial stage. As a result, in case of OPC pattern, corrosion threshold chloride content is about 5 to 6kg/m<sup>3</sup> and in cases of BFS pattern, the value is about 3 to 4 kg/m<sup>3</sup>.

## 4 Lifetime prediction

### 4.1 Duration of incubation period against chloride attack

To clarify this period, chloride ion diffusivity and corrosion threshold chloride ion content are used. As illustrated in figure 7, all mix proportions of concrete mixed with seawater

has shorter incubation period than that mixed with freshwater. Because seawater as concrete material induces initial chloride content, the duration to reach corrosion threshold chloride ion content is shortened. So, only considering incubation period, concrete mixed with seawater is difficult to use.

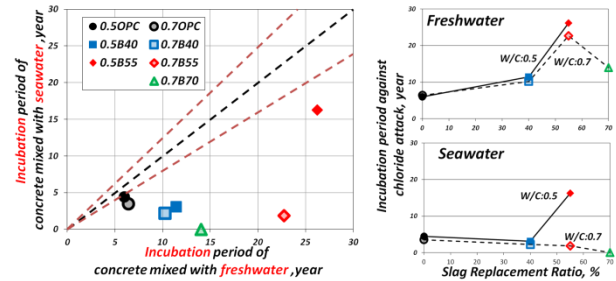


**Fig. 7** Duration of incubation period against chloride attack (In case of 70mm cover depth)

### 4.2 Duration of incubation period against carbonation

To clarify this period, carbonation rate coefficient obtained from section 2.3 is used. The result is shown in figure 8 and table 1.

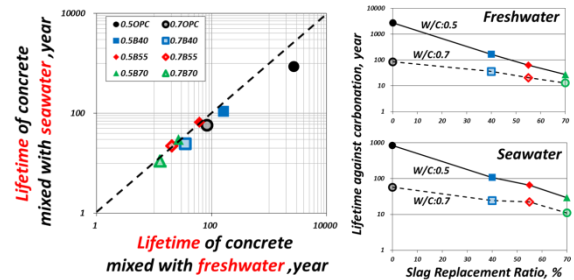


**Fig. 8** Duration of incubation period against carbonation (In case of 30mm cover depth)

From this result, the difference between lifetime of concrete mixed with seawater and freshwater is so small. But lifetime against carbonation is decreased with increasing of slag replacement ratio. Because high BFS replaced concrete have low pH. Thus the effect of seawater on lifetime against carbonation is low, but high BFS concrete can not apply to severe carbonation condition. Additionally, OPC concrete is better than BFS as shown table 1.

### 4.3 Duration of propagation period against chloride attack

To clarify propagation period, amount of corrosion product proposed by Yokozeki<sup>1)</sup> and corrosion rate during propagation period which is calculated by oxygen permeability obtained from section 2.4, and the relationship<sup>2)</sup> between oxygen permeability and corrosion rate are needed. Then, using calculated corrosion rate from oxygen permeability and amount of corrosion product around reinforcement during propagation period (The value is about 54mg/cm<sup>2</sup> in case of 70mm cover depth and  $\phi$

13mm of carbon steel), duration of propagation period is predicted as figure 9. From this result, concrete mixed with seawater have longer duration than that mixed with freshwater, because of its low corrosion rate during this period. Particularly, 55% BFS replaced concrete (0.5B55) mixed with seawater has longer duration than other type of concrete mixed with freshwater as shown in table 1.

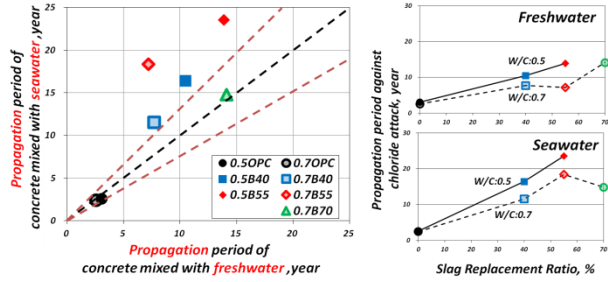


**Fig. 9** Duration of propagation period against chloride attack (In case of 70mm cover depth)

#### 4.4 Lifetime including incubation and propagation against chloride attack

Using results of section 4.1 and 4.3, in this section, lifetime included incubation and propagation is investigated as figure 10, and table 1.

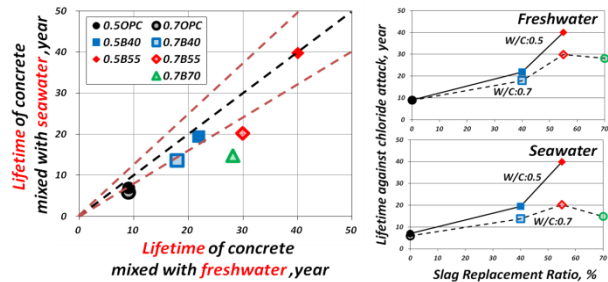


**Fig. 10** Duration of Lifetime against chloride attack (70mm cover depth)

From this result, only considering incubation period, concrete mixed with seawater is difficult to use. But considering incubation and propagation as lifetime, concrete mixed with seawater is slightly shorter than that mixed with freshwater. Especially, the difference between BFS 55% concrete (0.5B55) mixed with seawater and freshwater is minimum value. And the lifetime of concrete mixed with seawater is 40 years. This is enough long to use practically as shown table 1.

**Table 1** Comparison of average incubation and propagation period depending on mixing water

Deterioration factor	Mixing water	Incubation period				Propagation period				Lifetime(Total)			
		Year			Best mix	Year			Best mix	Year			Best mix
		Ave.	Max.	Min.		Ave.	Max.	Min.		Ave.	Max.	Min.	
Chloride Attack	Fresh	Ave.	Max.	26.2	0.5B55	Ave.	Max.	14.1	0.5B55	Ave.	Max.	40.1	0.5B55
		13.8	Min.	6.0		8.4	Min.	2.5		22.3	Min.	8.9	
	Sea	Ave.	Max.	16.3	0.5B55	Ave.	Max.	23.5		Ave.	Max.	39.9	0.5B55
		4.5	Min.	0.0		12.8	Min.	2.4		17.3	Min.	5.9	
Carbonation	Fresh	Ave.	Max.	2759.0	0.5OPC					Ave.	Max.	2759.0	0.5OPC
		396.3	Min.	12.9						396.3	Min.	12.9	
	Sea	Ave.	Max.	842.7	0.5OPC					Ave.	Max.	842.7	0.5OPC
		145.2	Min.	11.0						145.2	Min.	11.0	

## 5 Conclusions

In this thesis, the effects of seawater on material properties and corrosion behavior have been clarified. And using these results quantitative lifetime of concrete mixed with seawater also has been investigated. From this investigation, conclusions are obtained as follows;

1. Chloride ion diffusivity of concrete mixed with seawater is lower than that mixed with freshwater. In case of carbonation rate, the difference of value between concrete mixed with seawater and freshwater is small. In case of oxygen permeability, using OPC the difference of value between freshwater and seawater as concrete material is small, but using BFS the value of concrete mixed with seawater is lower than that mixed with freshwater.
2. In the case of chloride attack, the duration of concrete mixed with seawater is almost same duration as that mixed with freshwater. Especially, in case of BFS 55%, the difference is smallest. And the duration is 40 years.  
In the case of carbonation, the difference of lifetime between concrete mixed with freshwater and seawater is so small. But using BFS, regardless of mixing water, the resistance against carbonation is too low.

## References

- 1) K. Yokozeki et al., (1997). "A Rational Model to Predict Service Life of RC Structures in Marine Environment", Forth CANMET/ACI International Conference on Durability of Concrete 1
- 2) S. Maruyama, (2004), "Influence of Temperature and Cement on Corrosion Rate of Steel Bar under Carbonation", Master thesis of Tokyo Institute of Technology (in Japanese)



# Effect of temperature, oxygen concentration and solution on the degradation of paint on steel in marine exposure tests and accelerated test

Student Number : 11M18077    Name : Yu KAMIYA    Supervisor : Nobuaki OTSUKI

促進試験と海洋曝露試験における塗装鋼板の劣化に及ぼす温度、酸素濃度、溶液の影響

神谷 悠

長期に亘る塗装鋼材の劣化過程を把握することは従来からの課題であり、関連した曝露実験も行われてきたが、その詳細な劣化過程は不明確である。また、試験期間を短縮するための促進試験も提案されているが、温度や酸素、溶液種類等の条件が劣化進行に及ぼす影響は明らかではない。そこで、本論文では屋外曝露試験および既往の実曝露実験から、海中上部での塗装の劣化過程を明らかにした。また、促進試験と屋外曝露試験から塗装に膨れが生じる期間の促進倍率を算定した。さらに個々の促進条件が塗装の劣化進行速度に及ぼす影響を明らかにし、実環境での塗装に膨れが生じる期間を推定した。

## 1.Introduction

Recently the importance of maintenance to actual structures increases. Many offshore structures consist of paint coated steel for protection against corrosion. In these cases, it is important to estimate the life time of these structures for maintenance. While exposure tests have been conducted in actual environment, it is insufficient to clarify deterioration process of paint and still needs more data. In addition, to shorten the long-term process of deterioration of paint on steel, accelerated test have also been conducted. However, conditions for acceleration were determined by knowledge or experience in many cases. And the effect of each condition to the deterioration of paint is not quantitatively evaluated yet. When paint deterioration process is estimated, two types of corrosion should be considered. These are microcell corrosion and macrocell corrosion distinguished by the distance of anode and cathode. And deterioration process and rate also depends on the environment.

From above background, the objectives of this research were shown as follows; (1) to clarify the paint deterioration process and period considering macrocell corrosion in submerged zone. (2) to evaluate quantitatively effects of temperature, solution type, paint thickness, paint type and dissolved oxygen by accelerated test and its magnification.(3) to estimate the deterioration period in actual environment by magnification.

## 2. Clarification of deterioration process and period

### 2.1 Summary of the previous test [1]

Exposure test had been conducted in actual environment in Miyako Island, Okinawa prefecture. Paint coated steel pipe were settled

through seabed, submerged zone, tidal zone and splash zone. Test was conducted for 20years. And observation was conducted at 1, 12 and 20 years. Steel pipe was coated with Tar epoxy(800  $\mu$  m). In submerged zone, blister and ripping appeared by 12 years. After 20years exposure, serious degradation occurred in submerged zone. Many defects and corroded areas were observed. Some corrosion progressed deeply, vertically (Fig.1). These penetrated 4.5mm of steel thickness. It seems the effect of macrocell corrosion.

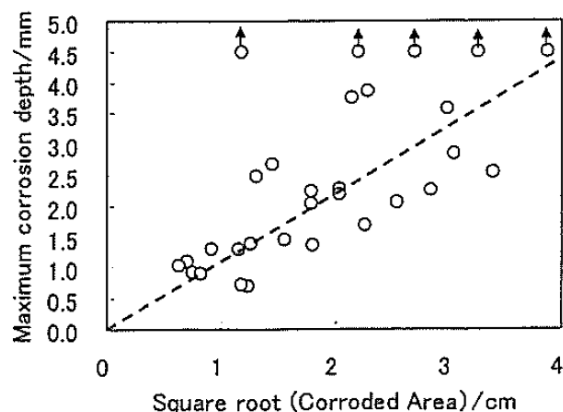


Fig.1 Relation between square root of corroded area and maximum corrosion depth for submerged zone

### 2.2 Exposure test in artificial water tank with seawater

To clarify deterioration process and deterioration period of paint on steel especially for submerged zone more precisely, outside exposure test was conducted. Test site was Futtsu city, Chiba Prefecture.

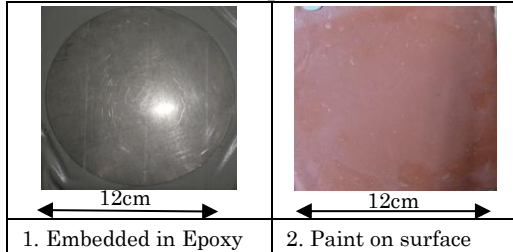
#### (1) Experimental procedure

Specimens were exposed in artificial water tank with natural sea water. Water level changed every 6hours between low water level and high water level. Water temperature was



about 20°C and Dissolved oxygen was about 5.0mg/L. Specimens were settled directly in atmosphere, tidal zone, and submerged zone. Phthalic resin paint was applied in this test. Paint thickness was 150µm. States of specimen are shown in Table.1. Test duration was 11months.

Table.1 specimen



## (2) Visual observation

Visual observation was conducted every month during test period. After the test, paint was peeled and observation of steel surface was conducted. In atmosphere, remarkable transform did not been observed by the end of the test. In tidal zone, rust appeared at 5months, ripping occurred at 8months, then paint tore completely at 9months. In submerged zone, rust appeared at 3months, blister appeared at 5months then ripping occurred at 10months. Secular change of appearance in submerged zone is shown Fig.2. After the exposure test, remarkable transform did not been observed on steel surface in atmosphere. In tidal zone, steel surface was totally corroded because of steel surface appearance by paint tearing. In submerged zone, pitting under the defect (rust) and black rust were observed. Defect on paint and pitting under the defect are shown Fig.3. It seems the initiation of deep, vertical corrosion.

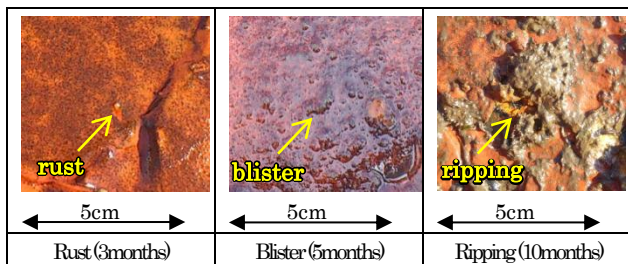


Fig.2 Secular change of appearance in upper underwater

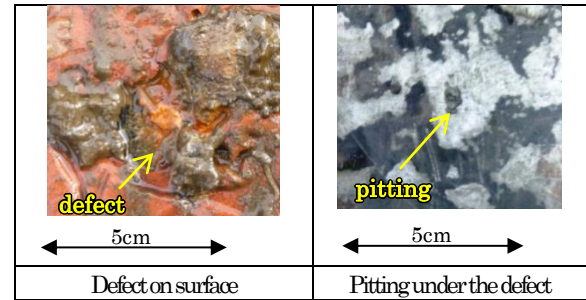


Fig.3 Defect on paint and pitting under the defect

## 2.3. Summary of accelerated tests

### (1) Experimental procedure

This test followed the form proposed by JSCE[3] assuming submerged zone. As accelerated conditions, 1)temperature 2)solution type 3)paint thickness 4) paint type 5) dissolved oxygen (air contact)were selected. Tested combinations of these conditions and duration before blistered are shown in Table.2. Dissolved oxygen was measured by air contact. It means air bubbles hit the paint 1)directly or 2)indirectly. When it was direct, dissolved oxygen was 5.1mg/L, it was indirect, dissolved oxygen was 4.1mg/L at 50°C.

### (2) Visual observation

Visual observation was conducted. From the observation, it was confirmed that each specimen followed the deterioration process that of outside exposure test. That is firstly, rust appeared on surface then, blister generated. Only on one specimen in condition 4) which had 225 µ m paint thickness, rust and blister occurred simultaneously. It seems the effect of thickness. In other words, it needed longer time to rust achieving the surface because the paint was thick. After peeling paint, pitting was also observed under the defect on condition 3) same as outside exposure test.

### (3) Effect of macrocell corrosion

pH inside blister was measured. It was 10~12 at tar epoxy paint. That was alkalized. It was considered by accumulation of hydroxide ions in blister caused by macrocell corrosion current. That is, macrocell corrosion was formed then, blister became cathodic part and defect became anodic part.

Table.2 Tested conditions and duration in accelerated test

	1)Temperature	2)Solution	3)Paint thickness	4)Paint type	5)Dissolved oxygen	Duration
1)	50°C	NaCl3%	150 µ m	OA	5.1mg/L	9days
2)	50°C	NaCl3%	150 µ m	OA	4.1mg/L	11days
3)	50°C	NaCl3%	100 µ m	OA	5.1mg/L	7days
4)	50°C	NaCl3%	225 µ m	OA	5.1mg/L	21days
5)	50°C	Artificial seawater	150 µ m	OA	5.1mg/L	27days
6)	50°C	NaCl3%	150 µ m	TE	5.1mg/L	50-70days

## 2.4 Proposal of paint deterioration process

From the two exposure tests, accelerated test and Funke's model [2] deterioration process in submerged zone which differs corrosion rate and distribution could be proposed as follows;

Step.1 is initiation stage of deterioration. Corrosion occurs under weak paint point and rust is formed. Then, macrocell corrosion cell is formed. Defect part becomes anode and certain paint coated parts turn cathode. (Fig.2.1)

Step.2 is propagation stage. Blister is formed on paint by accumulation of hydroxide ions on cathodic area. And macrocell corrosion current increases. Defect areas progresses in horizontal and vertical direction against the painted surface. (Fig.2.2)

Step.3 is acceleration stage. Blister breaks and it turns into ripping. That is, new defect. And macrocell corrosion distribution changes that leads new blister generation. (Fig.2.3)

From the clarification of deterioration, the duration before blistered was applied as the deterioration period.

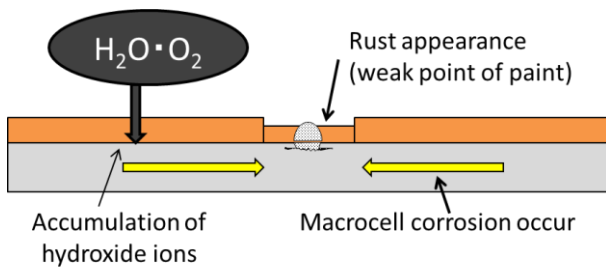


Fig.2.1 Step.1 initiation stage

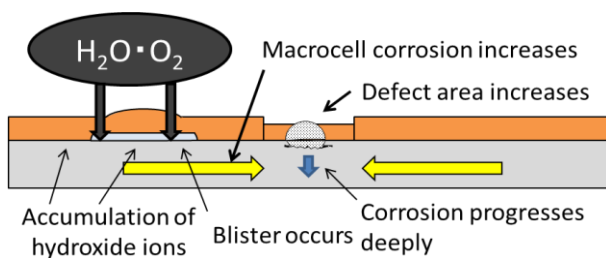


Fig.2.2 Step.2 propagation stage

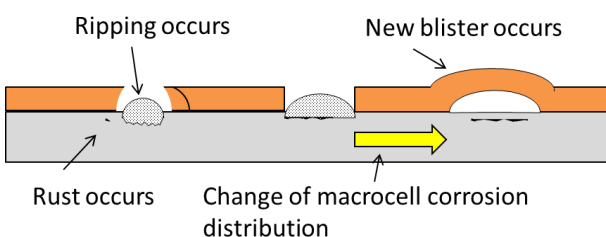


Fig.2.3 step.3 Acceleration stage

## 3. Evaluation of quantitative effects on accelerated conditions and magnification

### 3.1 Evaluation of accelerated conditions

The effect of each accelerated condition was quantitatively evaluated by comparing the duration before blistered in different conditions of accelerated test

#### (1) Effect of temperature

In general, reaction velocity depends on temperature. And it follows Arrhenius' equation. Therefore, the apparent activation energy was calculated with the other experimental results in the group. Its value approached to the activation energy of oxygen diffusion (11kcal/mol). So it seems oxygen diffusion dominated the reaction in this process. Therefore, accelerated coefficient by temperature was estimated by equation.1. It was 5.8times. This value was relatively close to measured one.

$$\frac{V_{T_2}}{V_{T_1}} = \exp \left[ \frac{\Delta E_a}{R} \left( \frac{1}{T_1} - \frac{1}{T_2} \right) \right] \quad (1)$$

Where;  $V_{T_n}$ =corrosion current density ( $\mu\text{A}/\text{cm}^2$ ) at temperature  $T_n$ ,  $\Delta E_a$ = activation energy (cal/mol),  $R$ =gas constant= $1.99$  (cal/K/mol) ,  $T$ =kelvin(K)

#### (2) Effect of solution

When artificial seawater solution was replaced by NaCl3%, duration accelerated 3times by comparing accelerated test condition1) and 5). It seems  $\text{Ca}^{2+}$  and  $\text{Mg}^{2+}$  in seawater prevented chemical reaction more than  $\text{Na}^+$ .

#### (3) Effect of paint thickness

It was confirmed that while paint thickness increased, contribution to the sum of resistance was slight. And it seems that paint thickness divided by duration would get smaller. Therefore, from accelerated test condition1), 3) and 4), logarithm approximation was applied. It was shown in equation.2.

$$Y = 17.264 \ln(X) - 74.171 \quad (2)$$

Where;  $Y$ = duration,  $X$ = paint thickness

#### (4) Effect of paint type

Tar epoxy paint was approximately 6.7 times stronger than Phthalic resin paint by comparing condition1) and 6). In this study, this value was applied as the effect of paint type.

#### (5) Effect of dissolved oxygen

When dissolved oxygen increased 1.24times (4.1mg/L to 5.1mg/L), duration accelerated 1.22times by comparing conditions 1) and 2). From the result of the effect of temperature, the relation between corrosion rate (duration

Table 3 Magnification of each and total factors and comparison of estimated and actual value of the duration of incubation periods

Factors	Conditions for setting each magnification or duration	Laboratory	Futtsu (Outside exposure)		Miyako <sup>1)</sup> (In situ exposure)	
		Lab data	Site Data	Magnification	Site Data	Magnification
Temperature	$\frac{V_1}{V_2} = \exp\left(\frac{\Delta E_a}{R} \left(\frac{1}{T_2} - \frac{1}{T_1}\right)\right)$	50°C (T <sub>2</sub> )	20°C (T <sub>1</sub> )	×5.8	26°C (T <sub>1</sub> )	×4.0
Solution	3%NaCl: ×1.0, Seawater: ×3.0	NaCl3%	Seawater	×3.0	Seawater	×3.0
Paint thickness	$\frac{Y_1}{Y_2} = \frac{17.26\ln(X_1) - 74.17}{17.26\ln(X_2) - 74.17}$ Y:duration, X:Thickness	150μm (X <sub>2</sub> )	150μm (X <sub>1</sub> )	×1.0	800μm (X <sub>1</sub> )	×4.6
Paint type	Phthalic: ×1.0, Tar epoxy: ×6.7	Phthalic	Phthalic	×1.0	Tar epoxy	×6.7
Dissolved oxygen	$\frac{Y_1}{Y_2} = \frac{-2X_1 + 19.2}{-2X_2 + 19.2}$ Y:duration, X: Dissolved oxygen	5.1mg/L	5.0mg/L	×1.0	6.4mg/L	×0.7
Total Magnification	Multiply all magnification	×1	×17		×259	
Estimated duration	Multiply total magnification from 9days	/	153days(=9days×17)		6.6years(=9×258/365)	
Actual duration	From observation		150days		Several years (1~12years)	

before blistered) and dissolved oxygen had a proportional relation. Therefore, the relation between duration and dissolved oxygen could be described as follows;

$$Y = -2X + 19.2 \quad (3)$$

Where; Y= duration, X= dissolved oxygen

### 3.2 Magnification for exposure test in Futtsu

Duration before blistered on exposure test in Futtsu was 6.7times extended compared to the accelerated test condition 1). Estimation process was as follows;

1) Effect of temperature was estimated by 3.1(1). Equation.1 was applied and duration was 5.8times extended compare to acceleration test, condition 1). 2) Effect of solution was estimated by 3.1(2). Duration was 3times extended 3) Paint thickness was same as acceleration test. 4) Paint type was same as acceleration test. 5) Effect of dissolved oxygen was quite small. Therefore, total magnification was 17times.

### 3.3 Magnification for exposure test in Miyako

Duration before blistered on exposure test in Miyako Island was 258times extended compared to accelerated test. And estimation process was same as 3.2. Temperature and dissolved oxygen were approximate values.

1) Effect of temperature was estimated to 4.0times. 2) Effect of solution was estimated to 3times. 3) Effect of paint thickness was estimated to 4.6times. 4) Effect of paint type was estimated to by 4.1(4). And duration was extended about 6.7times 5) Effect of dissolved oxygen was estimated by 4.1(5). Duration was

shortened 0.7times. Therefore, total magnification was 259times.

### 4. Estimation of the duration before blistered

Duration before blistered was estimated by multiplying actual duration of accelerated test condition 1) and total magnification.

So, estimated durations were 153days in Futtsu and about 6.6years in Miyako Island. These values were appropriated with actual duration in exposure tests. Therefore, duration in actual environments could be estimated.

### 5. Conclusions

(1) Deterioration process considering the effect of macrocell corrosion was clarified from the appearance of paint deterioration.

(2) Effects of temperature, solution, oxygen concentration, paint thickness and paint type were quantitatively evaluated. Magnifications of acceleration of each factor from accelerated test to two exposure tests were evaluated.

(3) Duration before blistered (Deterioration period) in actual environments could be estimated by accelerated tests.

### References

- [1] Masahiro YAMAMOTO et al., “Durability of organic coat steel exposed in the marine environment for 20years”, Materials and Environments, Vol.55, 239-244 (2006)
- [2] Funke, W., Ind. Eng. Chem. Prod. Res. Dev., 17 [1], 50-53 (1978)
- [3] Japan society of civil engineers., “Guideline for evaluation of durability and load carrying performance of steel structures in the marine environment” (2009)

# Estimating CO<sub>2</sub> emissions of an automobile company in global supply chain

## : Case study of locational conditions in Thailand

Student Number: 11M18090 Name: Yuhki KAWAHARA Supervisor: Shinya HANAOKA

タイ製造業の立地条件を考慮したグローバルサプライチェーンにおけるCO<sub>2</sub>排出量算定

川原 優輝

本研究では、タイの日系自動車メーカーの一台あたりの生産におけるCO<sub>2</sub>排出量を、グローバルサプライチェーンを考慮して算定した。排出量算定にあたり、今後の自動車市場の動向や企業の立地条件を考慮して2030年の自動車市場を対象としたシナリオを作成した。この結果から、市場に近い場所で生産することが、環境的にも経済的にも有益であり、輸送距離と生産場所の電力源によってCO<sub>2</sub>排出量が大きく異なることが明らかになった。

## 1. Introduction

### 1-1. Background

CO<sub>2</sub> emissions reduction is one of the biggest issues in the world; logistics sector also has same issue. Spreading with the globalization of industry, we should consider a comprehensive way of CO<sub>2</sub> emissions reduction in a global supply chain.

A number of Japanese manufacturing companies, which are active in Asia, reconsider of the plant location or establishment of the new plant due to recent situations such as insurgency, disaster and wage increase. Additionally, free cross-border movement between people, goods, capital and information is even more accelerated by AEC. Especially automobile is a very broad base industry; generally speaking, one automobile needs about 20 or 30 thousands parts. Therefore, automobile manufactures have enormous economic influence. Most automobile manufacturers have assembly plants in Thailand. Fig.1 shows that productivity of automobile industry in Thailand is the fifth in Asia and exportation of automobile is over 50%.

The flood in Thailand charged a heavy toll on Japanese companies in 2011. Moreover, because of wage increase, some companies are considering plants relocation.

Some researchers have already studied CO<sub>2</sub> emissions of inclusive supply chain. Their studies mostly focus on primary products<sup>[1][2]</sup>. However, there are a few studies on

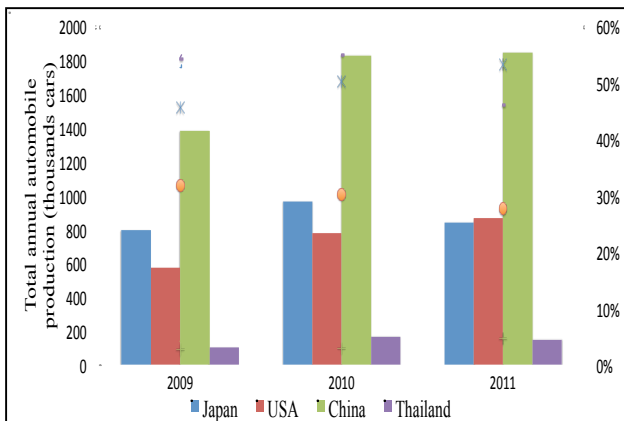


Fig.1 Automobile production and export ratio

comprehensive supply chain and transportation, regarding manufacturing industry<sup>[3]</sup>.

### 1-2. Objectives of the Study

The objectives of this study are the following.

- (1) Estimate total CO<sub>2</sub> emissions within inclusive global supply chain and total production per one vehicle to focus on one Japanese automobile company (company A).
- (2) Estimate the change of CO<sub>2</sub> emissions per one vehicle on scenarios, which consider automobile market and locational conditions in 2030.

According to environmental report of company A, they already figured out their portion of CO<sub>2</sub> emissions. Fig.2, pink area is company A and red line is this research area.

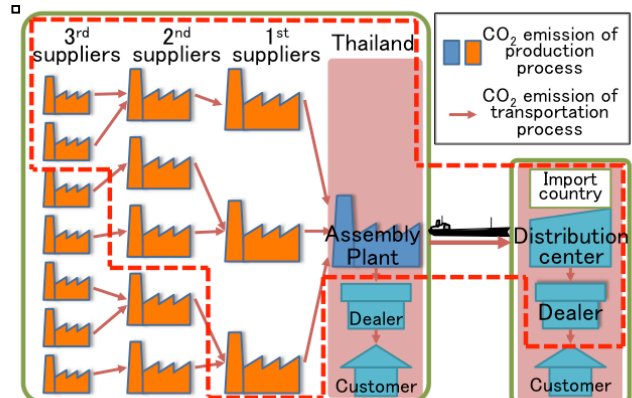


Fig. 2 Research area (red line)

## 2. Methodology

### 2-1. Data

This study mainly uses two types of data. One is to estimate CO<sub>2</sub> emissions per one vehicle. Second is to build the scenarios to project the plant locations and the automobile market in 2030.

#### 2-1-1. Data for Calculation of CO<sub>2</sub> emissions

Estimation of CO<sub>2</sub> emissions needs distance data, weight of parts data, emission factors and input energy of electricity to make parts. Distance data, which is distance of supplier to supplier and suppliers and company A, is calculated by Google Maps. Distance of overseas is from



calculation tool<sup>5)</sup>. Weight of parts and electricity of making parts are also from JLCA database. Emission factors are from calculation tool<sup>[4]</sup>. Tab.1 and Tab.2 are this research target.

Tab.1 Target parts and suppliers

	Number of parts	Number of suppliers
Transportation	75+(engine, body)	88
Production	31	31

Tab.2 Specification of target automobile

Type	Pickup truck 4WD M/T 4 door
Weight [kg]	1,825
Dimension [mm]	5,135 x 1,835 x 1,860
Displacement [cc]	2,494
Engine weight [kg]	207

## 2-1-2. Data for Scenario Building

Building scenario data is based on GDP, car ownership, investment cost. Investment cost is from open source by JETRO.

## 2-2. Estimation Method

### 2-2-1. Transportation Process

Calculation of this study is divided to transportation process and production process. Land transportation is calculated by improved tonnage method. Maritime transportation is calculated by tonnage method. These calculations are calculated by estimation tool form PRILT<sup>[4]</sup>. Calculation equations are the following.

$$E_t = \frac{W_t \times d_{ij} \times C \times 1/1000 \times H \times F \times 44/12}{u} \quad (1)$$

$$E_m = \frac{W \times d_{lm} \times F_t \times 1/1,000,000}{q} \quad (2)$$

Where:

$E_t$  is CO<sub>2</sub> emission of transportation on the truck (t-CO<sub>2</sub>).

$E_m$  is CO<sub>2</sub> emission of maritime transportation (t-CO<sub>2</sub>).

$W_t$  and  $W$  are total parts weight and total vehicles weight.  $d$  is distance (km).

$C$  is fuel usage basic unit (l/tkm).

$H$  is heat generation per unit (GL/kl).

$F$  is emission coefficient (t-C/GL)

$F_t$  is emission factor (t-CO<sub>2</sub>/tkm).

$u$  is number of unit and  $q$  is number of vehicles.

### 2-2-2. Production Process

CO<sub>2</sub> emissions from suppliers are calculated by using JLCA database. CO<sub>2</sub> emissions from assembly plant are from environmental report of company A and emission factor. Equations for calculation are the following.

$$E_p = \sum_n g_n f / 1,000,000 \quad (3)$$

$$E_a = g f / 1,000,000 \quad (4)$$

Where:

$E_p$  is CO<sub>2</sub> emissions of production process on suppliers (t-CO<sub>2</sub>).

$E_a$  is CO<sub>2</sub> emissions of production process on assembly plant (t-CO<sub>2</sub>).

$g_n$  and  $g$  are electricity usage (kWh).

$F$  is emission factor (g-CO<sub>2</sub>/kWh).

## 3. Results

### 3-1. Present Plant Location

Fig.3 presents plant locations of suppliers and location of company A. Large portion of suppliers located around seaside area. Fig.3 also illustrates the flood impact area which if denoted by blue color.

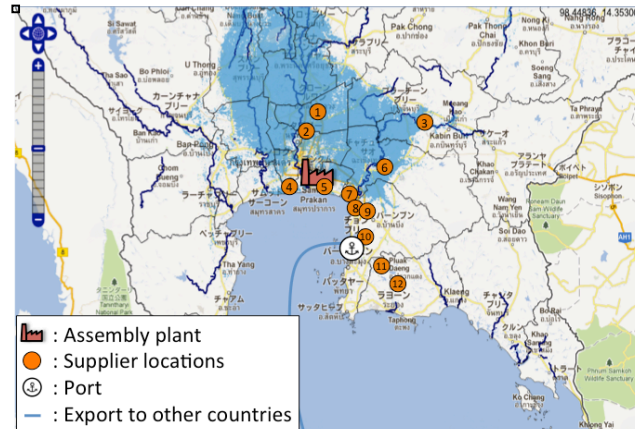


Fig. 3 Present plant locations

### 3-2. Scenario Building

Before the scenario building, this study needs to consider the tendency of company A behavior. This study

Tab.3 Comparison of investment cost

	Thailand	Malaysia	Indonesia	Vietnam	Cambodia	Myanmar
Labor wage	\$286/month	\$344/month	\$209/month	\$130 /month	\$82/month	\$68/month
Total wages	\$15,444,000	\$18,576,000	\$11,286,000	\$7,020,000	\$4,428,000	\$3,672,000
Total annually land cost	\$1,731,053	\$1,491,033	\$3,168,555	\$1,309,200	\$956,589	\$1,335,384
Total electricity cost	\$10,581	\$9,006	\$5,978	\$4,633	\$16,291	\$8,968
Total water rate cost	\$191,861	\$331,038	\$657,097	\$187,031	\$172,169	\$422,019
<b>Total cost</b>	<b>\$17,377,495</b>	<b>\$20,407,077</b>	<b>\$15,117,630</b>	<b>\$8,520,864</b>	<b>\$5,573,049</b>	<b>\$5,438,370</b>



builds 4 scenarios according to investment cost and automobile market.

### 3-2-1. Impact of flood in Thailand

The total amount of suffering the flood created in Thailand is 1.4trillion dollars which was estimated by World Bank. This flood affected 800 companies, including 450 Japanese companies. Some companies that produce parts to company A were included among 450. Therefore, company A was affected by flood impact indirectly.

### 3-2-2. Projection of Automobile Market

This study built 4 scenarios based on the projection study of the automobile market<sup>[5]</sup>. According to this projection, relationship between car ownership and GDP is illustrated in Fig.4.

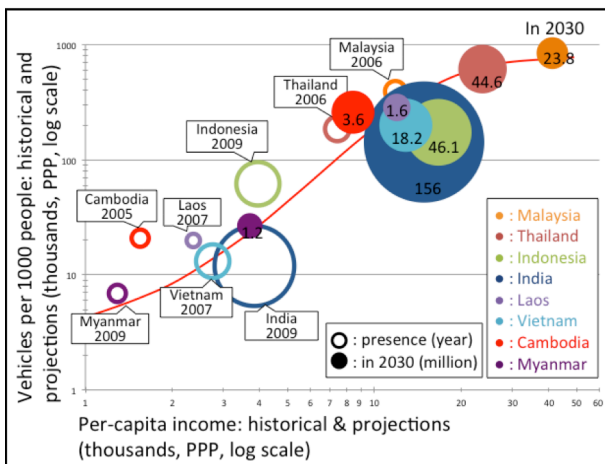


Fig.4 Projection of automobile market in 2030

### 3-2-3. Comparison of Investment

This study compiled investment cost and compared with some countries around Thailand. The result from Table3 suggests that Cambodia and

Myanmar have a good advantage of investment cost especially labor wage. Consequently, Cambodia and Myanmar were decided to build scenarios.

### 3-3. Estimation Results

Tab.4 indicates scenario purpose, plant locations, and target market of each scenario. Fig 5 shows this research scenarios.

#### 3-3-1. East Region Scenario

Purpose of this scenario is to avoid the flood risk. In this scenario, some countries and company A which have flood risk are relocated to east region. From the result of estimation, transportation CO<sub>2</sub> emissions of supplier was reduced because of shortens distance.

#### 3-3-2. Cambodia Production Base Scenario

This scenario aims to Vietnam market. In this scenario, company A establishes its new assembly plant in Phnom Penh. All transportation process is used by truck and carrier car.

From result of this scenario, CO<sub>2</sub> emissions of suppliers were increases by five times compare to present case.

CO<sub>2</sub> emissions of production process were decreased because CO<sub>2</sub> emissions factor in Cambodia is higher than Thailand one.

#### 3-3-3. Myanmar Portion of Suppliers Relocation Scenario

This scenario, some suppliers which have flood risk are relocated to Dawei in Myanmar. This scenario has two purposes. One is to avoid flood effect and the other is to compare the CO<sub>2</sub> emissions if some suppliers change their plant location.

In transportation process, CO<sub>2</sub> emissions of supplier

Tab.4 Target parts and suppliers

Scenario Name	Purpose	Assembly Plant	Suppliers Plant	Market
(1)East Region Scenario	Disaster countermeasure type	Thailand	Thailand	ASEAN
(2)Cambodia Production Base Scenario	Market adapted	Cambodia (Phnom Penh)	Thailand	Vietnam, Cambodia
(3)Myanmar Portion of suppliers Relocation Scenario	Disaster countermeasure type	Thailand	Myanmar (Dawei), Thailand	ASEAN
(4)Myanmar Production Base Scenario	Market adapted	Myanmar (Dawei)	Thailand	India

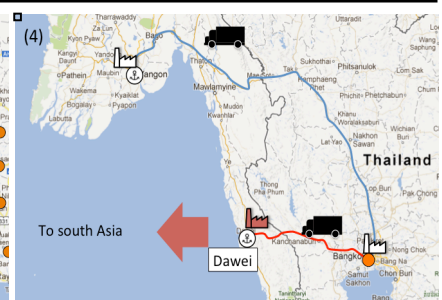
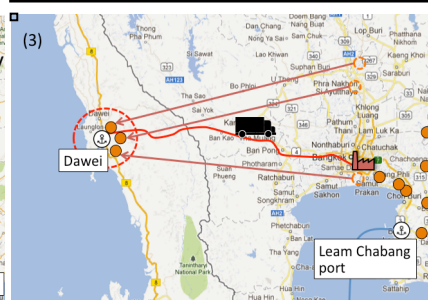
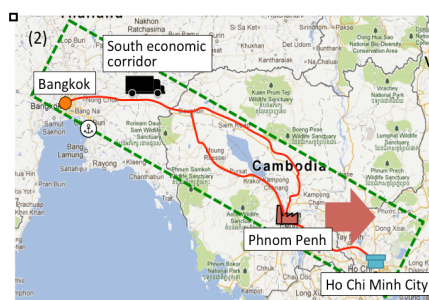
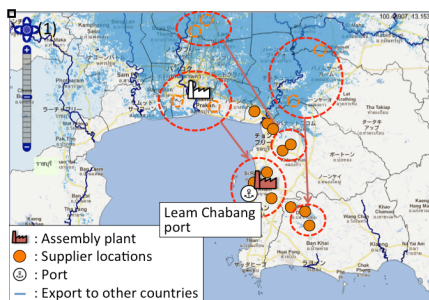


Fig.5 Scenarios

increased due to extended distance.

In production process, CO<sub>2</sub> emissions were decreased because CO<sub>2</sub> emission factor in Myanmar is lower than Thailand.

### 3-3-4. Myanmar Production Base Scenario

This scenario aims to automobile market in India. This scenario establishes a new assembly plant at Dawei in Myanmar.

CO<sub>2</sub> emissions of supplier's transportation were increased, but CO<sub>2</sub> emissions on maritime transportation were decreased. Total CO<sub>2</sub> emissions of transportation was decreased.

CO<sub>2</sub> emission factor is lower than Thailand. Therefore, CO<sub>2</sub> emissions of production process were decreased. Total CO<sub>2</sub> emissions were reduced by approximately 34% compared to present case.

## 4. Conclusions and Discussion

This study focused on one automobile company and estimated inclusive global supply chain CO<sub>2</sub> emissions and clarifies the change of CO<sub>2</sub> emissions result from these comparisons.

In the case of transportation process, CO<sub>2</sub> emissions of suppliers are not effective for whole emissions. In maritime generated a quite little CO<sub>2</sub> emissions, which accounts of the majority of total CO<sub>2</sub> emissions. This result was not only long because of distance but also automobile transport ship issue. It is likely that containership is available to carry much more freights than car carrier.

Regarding to the production process, amount of CO<sub>2</sub>

emissions depends on the electrical resource. When referring from Fig.6 about comparison of transportation cost<sup>[6]</sup> in Myanmar base scenario,. However, Cambodia base scenario indicated that production process of CO<sub>2</sub> emissions depended on country electricity issue. Therefore, manufactures should consider their plants locations where is beneficial plant location for environment and economic.

Efforts of companies and researchers will trigger of innovation of the new technology to develop new eco-friendly automobile. However, if they cannot reduce emissions on the supply chain, they would not be able to reduce CO<sub>2</sub> emissions in automobile industries.

## References

- [1] Christophe Rizet et al.: Assessing carbon footprint and energy efficiency in competing supply chains: Review – Case studies and benchmarking, Transportation Research D17, pp.293-300, 2012.
- [2] Brendan O'Donnell et al.: The relative contribution of transportation to supply chain greenhouse gas emissions: A case study of American wheat, Transportation Research D14, pp.487-492, 2009.
- [3] Ki-Hoo Lee: Integrating carbon footprint into supply chain management: the case of Hyundai Motor Company (HMC) in the automobile industry, Journal of Cleaner Production 19, pp.1216-1223, 2011.
- [4] 国土交通政策研究所：物流から生じる CO<sub>2</sub> 排出量に関する手引き, 2012.
- [5] Joyce Dargay et al.:Vehicle Ownership and Income Growth, Worldwide: 1960-2030, The Energy Journal Vol. 28, pp. 143-170, 2007.
- [6] JETRO: ASEAN Logistics Network Map 2nd Edition, JETRO, 2009.



Fig.6 CO<sub>2</sub> emissions results (S: Supplier, A: Assembly Plant, D: Distributor)

# MICROBIAL COMMUNITY ANALYSIS OF THE METHANE FERMENTATION PROCESS TREATING GLYCEROL

Student Number: 11M18120 Name: Kohei Hatta Supervisor: Kiyohiko Nakasaki

グリセリンを原料としたメタン発酵プロセスにおける微生物叢の解析

八田 恒平

効率的なメタン発酵を可能にするためには、処理しようとしている基質に適したグラニュールを生成することが重要である。以前より、グリセリンを基質としたメタン発酵は効率化が困難であることが知られていた。本研究では食品工場の廃水処理過程で生成したグラニュールを 104 日間かけて馴致することで、2.5 gCOD/L/d の高負荷グリセリンの処理が可能な微生物群集を得ることに成功した。また、馴致にともなってグラニュール中の微生物叢が変化し、これまでに主要な構成微生物としては知られていなかった属の細菌が優勢になることを分子生物学的手法を用いて明らかにした。

## 1 Introduction

Extensive researches have been carried out worldwide to address the environmental problems associated with the depletion of fossil fuels, and the emission of greenhouse gases that contribute to the global climate change. Above all, biodiesel fuel (BDF) is in spotlight and has been produced at industrial scale in the world through base-catalyzed transesterification of vegetable oil, animal fats and waste oil. The increase of BDF production brings about the massive by-product of waste glycerol that is usually incinerated.

One of the solutions to treat this waste glycerol is methane fermentation from glycerol. The methane fermentation is conducted as the anaerobic digestion of the organic wastewater by the variety of microorganisms. Besides the production of the methane, the advantages of the methane fermentation include energy savings, generation of low quantities of sludge and excellent waste stabilization. The methane fermentation process occurs with different groups of bacteria in four steps of reaction: hydrolysis, acidogenesis, acetogenesis, and methanogenesis.

Several research groups have focused on the possibility of anaerobic treatment of glycerol recently and most of these studies have aimed at using the glycerol as a co-substrate for processing of other substrates like pig manure etc. However, BDF plants are not always constructed near the methane fermentation reactor treating other kinds of substrate. Hence, the anaerobic processing of glycerol as a single substrate should be established.

Generally, the start-up of methane fermentation needs acclimation period to propagate adequate

microbial community for each kind of substrate. Many microorganisms are able to metabolize glycerol in the presence of external electron acceptors (respiratory metabolism), however, few are able to metabolize glycerol in the absence of electron acceptors [1]. Therefore, the start-up of methane fermentation from glycerol requires long time for those few kinds of microorganisms, whose specific growth rate is low, to grow up to the concentration that can show the decomposition activity against glycerol.

In this study, the microbial community on the acclimation process was analyzed to find the microorganisms that can decompose glycerol.

## 2 Materials & methods

### 2.1 Acclimation of granule to glycerol using semi-continuous stirred tank reactor (semi-CSTR)

The microbial community in the granule obtained from a food factory was acclimated to glycerol. Fig. 1 shows the schematic diagram of the experimental set-up. The 300 mL of seed granule was inoculated to 2.7 L of water in the sterilized reactor. A carbon source mixture designated as GAL consisted of 5 g of glucose, 2.5 g sodium acetate and 2.08 g lactic acid per liter of distilled water was prepared and the mixture of glycerol and GAL was used as substrate.

Six kinds of the glycerol-GAL mixture designated as S, G0, G25, G50, G75 and G100 were prepared by changing the mixing ratio as shown in Table 1. These substrates were supplied in a stepwise manner: 0-1 days with 100% GAL

(substrate S), 2-21 days with 100% GAL (substrate G0), 22-37 days with 75% GAL and 25% glycerol (substrate G25), 38-49 days with 50% GAL 50% glycerol (substrate G50), 50-61 days with 25% GAL 75% glycerol (substrate G75), and 62-104 days with 100% glycerol (substrate G100). Other inorganic substances were prepared according to the paper of Ghangrekar et al. [2]. Every day, 750 mL of substrate was fed to the reactor after draining 750 mL of supernatant. The reactor was fed with constant organic loading rate (OLR), i.e., 2.5 gCOD/L/d. The pH in the reactor was kept at 7.5 by the addition of 0.1M NaOH solution every day. The reactor was kept at 39°C and stirred at 100 rpm except the feeding period.

The samples withdrawn at adequate time interval were subjected to the analyses of pH, Oxidation-reduction Potential (ORP), concentrations of Volatile fatty acids (VFAs) and lactic acid, PCR-DGGE and DNA sequencing of 16s rRNA gene fragment. The gas samples were analyzed by GC-MS.

Table 1 Compositions of the substrates

Organic components	Concentrations (mmol/L)					
	S	G0	G25	G50	G75	G100
Glycerol	0	0	12.7	25.5	38.2	50.9
Glucose	13.9	27.8	20.8	13.9	6.9	0
Acetic acid	15.2	30.5	22.9	15.2	7.6	0
Lactic acid	8.5	16.9	12.7	8.5	4.2	0

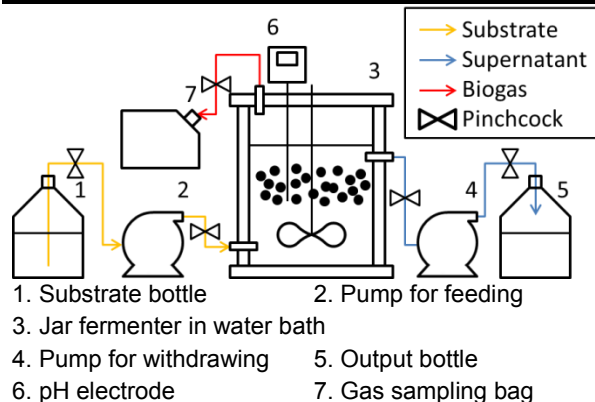


Fig. 1 Semi-CSTR set-up

## 2.2 Chemical analyses

The pH and the ORP of the supernatant withdrawn from Runs A and B were measured with electrodes (PH-3P, Mettler Toledo, Tokyo, Japan).

The concentration of VFAs (acetic acid, propionic acid, butyric acid and iso-butyric acid) and lactic acid was measured with a HPLC system (JASCO, Tokyo, Japan) with a Shodex Sugar SH1011 column (Showa Denko K.K., Tokyo, Japan) and a refractive index detector (Hitach, Tokyo, Japan). Mobile phase was 5 mM H<sub>2</sub>SO<sub>4</sub>, flow rate was 0.9 ml/min and the temperature in the

column oven was set at 40°C.

Methane and carbon dioxide quantities were determined by gas chromatography-mass spectrometry (GC-MS). A GC (GC-17A, Shimadzu, Kyoto, Japan) was equipped with a 25m×0.25mm ID CP-Porabond-Q fused silica column, film thickness 5 mm (Chrompack, Varian Deutschland GmbH, Darmstadt). Helium was used as carrier gas (head pressure 7 kPa). 0.5 ml of gas samples were injected in split mode (split ratio: 90, injector temperature: 50°C, column oven temperature: 40°C).

## 2.3 Microbial community analyses

The granules samples were taken from the granule sampling pipe that has 250 mm height from the bottom on day 17, 19, 28, 37, 45, 49, 55, 61, 67, 77 and 84 in fermentation period of the reactor. A DNA extraction kit, ISOIL for Beads Beating (Nippon Gene Co., Ltd., Toyama, Japan), was used for the extraction of DNA from the granules samples. Samples weighing 0.3 g (wet weight) were directly put into a tube in the beads beating kit. About 950 µL of the Lysis solution BB and 50 µL of the Lysis solution 20S were added to the tube, which was then bead-beaten vigorously for 45 s at a rate of 5500 rpm on a bead-beater (Micro Smash MS-100; Tomy Medico, Ltd., Tokyo, Japan). After incubation at 65°C for 1 h, the samples were centrifuged at 11,000 rpm for 1 min at room temperature by using a microcentrifuge (MX-105 High Speed Refrigerated Micro Centrifuge; Tomy Tech INC., Tokyo, Japan). The wash solution and 70% ethanol containing ethachinmate were used to wash and purify the DNA pellet, which was then vacuum-dried for 20 min. The DNA pellet was then dissolved in TE solution (Tris-HCl, 10 mM; EDTA, 1 mM; pH 8.0).

PCR amplification was conducted with TaKaRa Ex Taq Hot Start Version (Takara Bio INC., Shiga, Japan) using TaKaRa PCR Thermal Cycler Dice (TP600, Takara Bio INC., Shiga, Japan). The primers were as follows: 357F, 5-CGC CCG CCG CGC GCG GCG GGC GGG GCG GGG GCA CGG GGG GCC TAC GGG AGG CAG CAG-3, and 517R, 5-ATT ACC GCG GCT GCT GG-3 [3]. The PCR program was set for initial denaturation at 94°C for 7 min, followed by 35 cycles of 60-s denaturation at 94°C and 60-s annealing at 65°C (first 7 cycles), then at 60°C (second 7 cycles), and finally at 55°C (last 21 cycles). Each annealing step was followed by a 120-s extension except for the final extension (at 72°C for 10 min). For Archaea, the nested PCR amplification was applied. In the



first step, primers PRA46f and PREA1100r were used in order to achieve the 1,072bp fragment, the PCR product from the first step were diluted and used as a template to produce the 179 bp fragment by using PARC340f and PARC519r primers [4].

DGGE was performed using the Dcode DGGE Complete System (BioRad Laboratories, CA, USA). Prior to loading onto 10% (w/v) polyacrylamide gel in 1x TAE buffer (40 mM Tris-acetate; pH 7.4; 20 mM acetate, 1 mM Na<sub>2</sub> EDTA) with a denaturing gradient ranging from 30% to 60%, the PCR products were mixed with an equal volume of 2x gel loading dye (10 mM Tris-HCl (pH 8.0), 20 mM EDTA (pH 8.0), 0.05% (w/v) bromophenol blue, and 70% glycerol). The “100% denaturant” corresponded to 7 M urea and 40% (w/v) deionized formamide. Electrophoresis was undertaken at a constant voltage of 200 V at 60°C. After 3.5 h of electrophoresis, the gels were stained with 1x TAE buffer and ethidium bromide for 30 min, and then rinsed with distilled water before imaging using a UV illuminator (Epi-Light UV FA500; AISIN, Saitama, Japan).

Using the DGGE image as a reference, the bands of interest were excised from the gel on a Dual Intensity Ultraviolet Transilluminator (Model TDS-20; UVP, CA, USA). The extracted bands were then re-amplified and subjected to cloning by using the TOPO TA Cloning Kit (Invitrogen, Carlsbad, CA, USA) in order to purify the DNA bands. Sequencing reactions for the purified DNA bands were carried out with a BigDye Terminator v3.1 Cycle Sequencing Kit (Applied Biosystems, CA, USA), while sequencing was performed using an ABI PRISM 310 Genetic Analyzer (Applied Biosystems, CA, USA). The results of sequencing were compared to the sequences of the 16S rRNA genes available in the databases (DDBJ, EMBL and GenBank) and the affiliation including the relative strains of the sequences were determined using sequence match analysis in the ribosomal database project II (RDP-II) data and analysis services.

### 3 Results & discussion

Fig. 2 shows the courses of biogas production rate during the granule acclimation to glycerol. From the start-up to around Day 14, the concentration of methane was low suggesting that the microorganisms had not adapted to the new substrate. After the day 14, the production rate of methane was stable at around 0.065 mol/d except the day just after the change of the glycerol ratio in the substrate.

VFAs are intermediates produced during the

anaerobic digestion. Firstly, the bacterial group hydrolyses and produces acetic acid through VFAs. Then, acetic acid are further digested to methane by archaea. Under the conditions of stable methane fermentation, VFAs are consumed and then converted to methane immediately after they are produced; therefore VFAs concentration in the reactor is kept at low level in the liquid sample. Acetic acid, propionic acid, butyric acid, and iso-butyric acid were the common acidogenic products in this experiment. Among them, Acetic acid and propionic acid were the first and second most abundant intermediates and their low concentrations were significant and demonstrated the performance of the reactor.

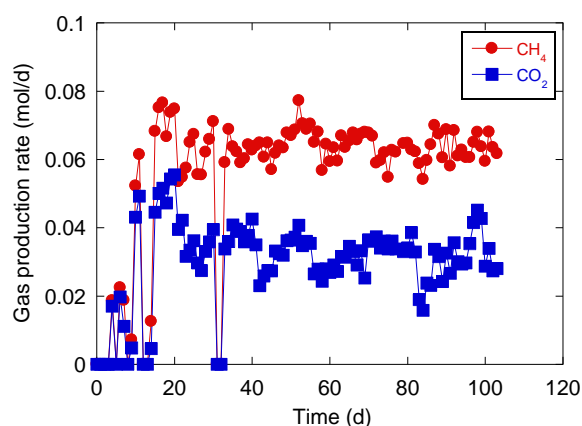


Fig. 2 The courses of biogas production rate during the granule acclimation to glycerol

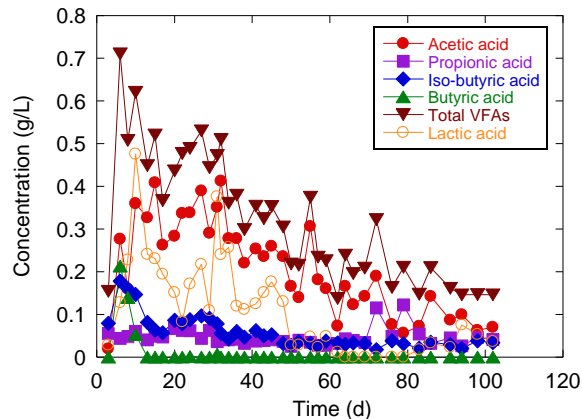


Fig. 3 The courses of VFAs and lactic acid concentration in the supernatant

The VFAs concentration in the liquid sample is shown in Fig. 3. After the start of the experiment, other easily degradable compounds than glycerol, such as sodium acetate and lactic acid are included in the substrate thus the VFAs concentration in the reactor become rather high. Afterward, VFAs were getting decrease when glycerol was gradually increased in synthetic wastewater component. From day 61 of the operation period, the reactor was fed



by 100% glycerol as carbon source; the VFA concentration was lower than 0.2 g/L and stable until the end of the experiment. This indicated that the activity of the microorganisms in the granular sludge was kept at high level. These results indicate that the balance of acinogenesis and methanogenesis was achieved.

The low pH has the adverse effects on the performance of anaerobic processes. This phenomenon was explained by that the methanogens tend to lose their activities under the low pH conditions. The pH value between 6.4 and 7.8 is considered necessary to maintain high performance of the methane fermentation.

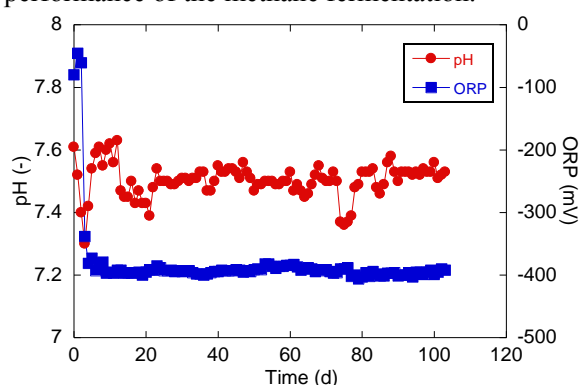


Fig 4 Change of pH and ORP during the operational period

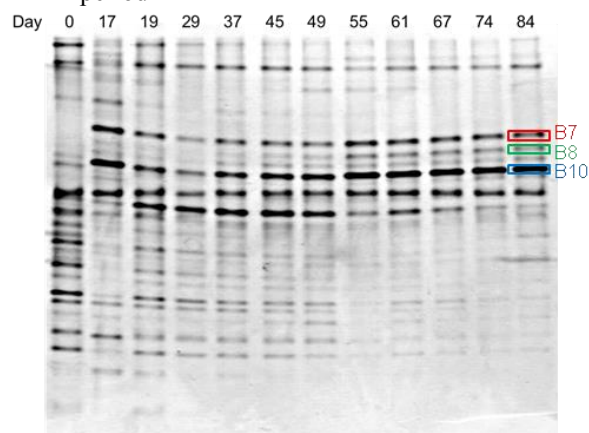


Fig. 5 The DGGE fingerprints of bacteria in the sample from acclimation process of granule to glycerol

Fig. 4 illustrates the time courses of pH and oxidation-reduction potential (ORP) during the acclimation process of the granular sludge. At the early stage, pH value slightly fluctuated from 7.3 to 7.6. Afterward, it was maintained at around 7.5 to achieve the good performance of anaerobic digestion. The ORP indicates whether the reaction condition is kept at the aerobic or the anaerobic. A negative value of ORP represents anaerobic condition and ORP < -200 mV is good condition for

methane fermentation. At the beginning of the methane fermentation, the initial ORP value was -80 mV and then it decreased rapidly to -400 mV. It meant the anaerobic condition was retained in the whole of the acclimation process.

Fig. 5 shows the DGGE fingerprints of bacteria in the samples from acclimation process of granule to glycerol. At the early stage of acclimation, various kinds of bacteria were detected in the reactor. Then, the bacteria that correspond to the band number B7, B8 and B10 became dominant in the later stage of the acclimation process. The differences between DNA sequences corresponding to these three bands were only 1 or 2 bp. No previous studies show that this genus becomes dominant in the methane fermentation from glycerol. Previously, it was reported that this genus can convert glycerol to 1,3-propanediol (main product), lactic acid, acetic acid, and formic acid. The result that 3 strains that correspond to Band B7, B8 and B10 became dominant in our acclimation process supports the hypothesis that these 3 strains that correspond to Band B7, B8 and B10 in the granule decomposed glycerol efficiently.

The results of DGGE fingerprints and DNA sequencing of 16s rRNA gene fragment of archaea confirmed that a strains that correspond to Band A8 and A13 became dominant in the Archaeal microbial community (data not shown). These genera are often observed in the granule sample from the methane fermentation process. Therefore it was suggested that these genera produced methane in this experiment.

## 4 Conclusions

In the acclimation process of granule to glycerol, the stable production rate of methane, low concentrations of VFAs and lactic acid in supernatant and characteristic microbial community were observed, which indicated the successful production of the acclimated granule that have the ability to treat 2.5 gCOD/L/d of glycerol.

It was revealed that 3 strains that correspond to Band B7, B8 and B10 become the dominant in the acclimated granule by the molecular biological analysis.

## References

- [1] Yazdani SS. et al., Curr. Opin. Biotechnol., **18**, 213-9 (2007)
- [2] Ghangrekar MM. et al., Water Res., **39**, 1123-33 (2005)
- [3] Muyzer G. et al., Appl. Environ. Microbiol., **59**, 695-700 (1993)
- [4] Keyser M. et al., Syst. Appl. Microbiol., **29**, 77-84 (2006)

# Moral hazard issues contractor and subcontractor in construction overseas project

Student Number: 11M18137

Name: Shotaro FUKAO

Supervisor: Shinya HANAOKA, Keisuke MATSUKAWA,

## 契約理論から見た海外プロジェクトにおけるプライムコントラクターとサブコントラクターの関係性

深尾 翔太郎

本研究では、海外プロジェクトにおける日系建設会社と現地サブコントラクターとの間で起こるモラルハザード発生メカニズムを契約理論の観点からモラルハザードモデルとして定式化し、分析する。日系建設会社の立場から、現地サブコントラクターとの間で発生するモラルハザードを抑制し、プロジェクトを効率良く進めるために望ましい問題対応スキームに関して理論的アプローチを試みる。そして、今後海外進出を試みる製造業や建設業の意思決定支援に資することを目的とする。

### 1. Introduction

#### 1-1. Background

These days, the fact that construction industries and manufacturing is encountering many challenges is gotten attention since domestic new business is different from foreign new business in terms of various conditions in especially developing country. One of those challenges is moral hazard which occurs with local subcontractor in new construction project Japanese construction and manufacturing industries<sup>[1]</sup>

Some researchers have already studied regarding how occur overseas conflicts. They actually conducted questionnaire and interview survey but their solution of survey result is descriptive and isn't used contract theory. Furthermore, study concern about construction industries by using contract theory is conducted but contract theory model isn't based on actual condition through questionnaire and interview survey.

#### 1-2. Objective

This study of objectives is the following.

- Examine relationship between contractor and subcontractor through questionnaire and interview survey.
- The contract schemes for moral hazard between Japanese Construction Company and subcontractor in the developing countries are formulated in the form of a moral hazard model, whereby the moral hazard issues caused by subcontractor are investigated. Furthermore, the optimal compliant moral hazards issues enhance the project efficiency, are theoretically investigated.

### 2. Research Design

#### 2-1. Research Method

In this research, questionnaire and interview survey is conducted to Japanese Construction Company A who is familiar with overseas construction project firstly to comprehend actual condition of conflict in overseas construction project (Fig.1). Furthermore, verification survey is conducted to confirm the case treating is as to whether occur frequently or not. After survey, narrowing frequent case to many cases and describing theoretically.

Build a model based on a scenario of using a moral hazard model of contract theory was build based on specific conflict in overseas. (Fig2)

#### 2-2. What is Moral Hazard?

By the way, what is moral hazard? **Moral hazard** can be present any time two parties come into agreement with one another. Each party in a contract may have the opportunity to gain from acting contrary to the principles laid out by the agreement.

	Conflict that occurred during Cost Estimation stage and its solution	Conflict during Designing stage and its solution	Conflict during Construction stage and its solution
Time Management A problem concerning Time			
Cost Management A problem concerning Cost			
Quality Management A problem concerning Quality			
Communication Management A problem concerning Communication			

Fig1: Questionnaire for Company A and B

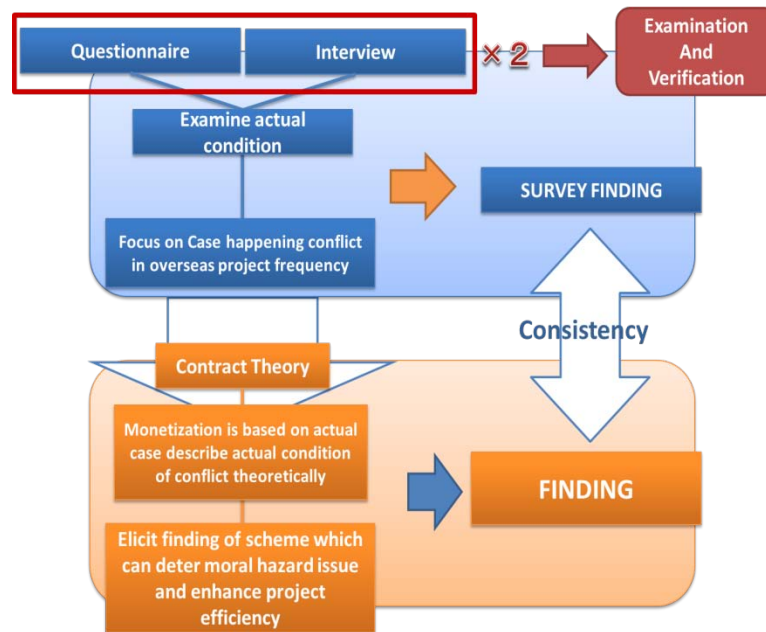


Fig.2 Framework of this research

### 3. Results

#### 3-1. Questionnaire and Interview survey result

Questionnaire is distributed to 28 employee of company A. and interview survey was conducted and these survey results as following Fig3. Fig3 shows the number of conflict in each stakeholder. As following Fig3, it is found that the biggest number of conflict is between contractor and subcontractor.

Therefore, this result can be assumed that conflict between contractor and subcontractor is happened frequently in overseas construction project. It is found that these conflicts

are case of preventing efficiency.

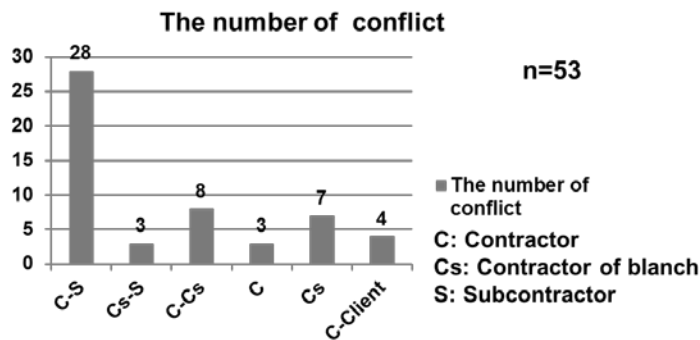


**Fig3. The number of conflict between each stakeholder in overseas projects for Company A**

### 3-2. Verification survey result

This verification survey also was conducted as questionnaire and interview survey. Furthermore, this survey result is Fig4. Conflict between contractor and subcontractor in each stakeholder is the most frequency in overseas project.

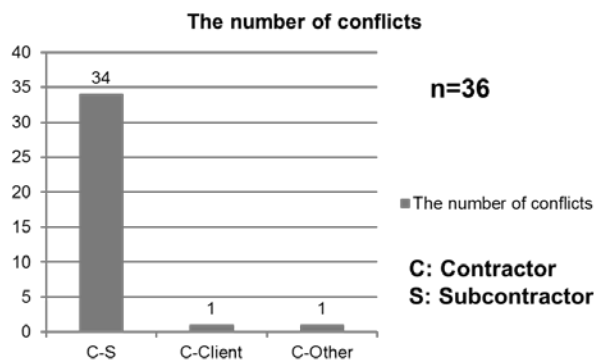


**Fig4. The number of conflict between each stakeholder in overseas projects for Company B**

### 3-3. Narrowing the all case to typical case in overseas

From the above survey, many moral hazard cases were extracted. It can be assumed that one of these research objectives is achieved through above survey. Next, moral hazard cases are narrowed to clarify what can moral hazard cases occur the highest frequency.

Then introduce the case of moral hazard that obtained by previous surveys after narrowing.

### 3-4. introduction narrowed typical 9 cases and classification

**A** : Contractor often proposes contract of incentive payment to subcontractor. If subcontractor can submit product earlier than due date, subcontractor can get incentive fee from contractor. Incentive bonus depends on how early the submission can be made. But if subcontractor can't submit by due date (at behind due date), subcontractor has to pay penalty fee. This way of the contract usually gives incentive in keeping due date of subcontractor.

**B** : Subcontractor sometimes doesn't acknowledge their mistake despite they didn't make an effort and can't meet due date. It blames other company for the mistake.

It means that Subcontractor tries to cheat to avoid penalty fee.

**C** : Schedule had been behind since subcontractors hasn't skill enough for piling block. It occurred because subcontractor had cheated real skill at accepting contract with contractor.

**D** : Due to lack of subcontractor's skills, schedule had been

behind. When contractor and subcontractor executed contract, subcontractor concealed real spec to get job.

**E** : Subcontractor wouldn't make the deadline for contractor but they already got all payment from contractor. Therefore, they got done with work in spite of they hadn't confirmed check enough. After that, contractor found a mistake about certain parts from subcontractor but Contractor had to modify them due to pay all money to Subcontractor already from contractor.

**F** : Case of that subcontractor submit product, since subcontractor was pursued due date, although subcontractor hasn't prepared yet, subcontractor reported as fake that I am ready for Vendor FAT (Factory Acceptance Test, shipping confirmation examination of attendance at proceeding by clients). But since preparation for Vendor FAT wasn't finished yet, subcontractor couldn't pass this examination by clients. Then contractor had to start again.

**G** : Ladder which is for Air Fin Cooler wasn't made as required. Ladder is not importance compare other parts. That's why Subcontractor designed it without asking Contractor.

**H** : Workers of subcontractor often dare to happen strike intentionally since they don't want to work. They take a holiday.

**I** : Worker of subcontractor sometimes dare to jump off from high height with no scaffold since they want to solarium (payment for pain and suffering) .

**J** : Welder of subcontractor make fake welding product which apparently can be seen as a completed product.

**K** : The number of trip by hauler of earth and sand is at gate during construction stage. Hauler sometimes tries to cheat the number of trip by giving extra money to a worker at the gate.

**L** : In hot site, ice provider sometimes try to cheat the number of how many times they provided an ice by putting ice at outside (it means that they dare to make ice melt)

**M** : Worker of subcontractor sometimes do sabotage to stay more at site during test session. They tried to get allowance at site.

Next, classify the case **A~M** as each case is caused by subcontractor(company) or (worker) and where each case is caused country overseas project experience not enough or country overseas project experience enough (Fig5). From Fig5, Case A can be assumed as that case can occur the highest frequency because case A can occur at everywhere and can be caused by both subcontractor company and worker. Case B~G would be happened all over the world except Japan and these can be said general case in overseas. Therefore, from framework of case, the most general case is case A, B and these would be used as model case and proceed theoretically analysis. But case C~G is same as case B in many point, these case can be described generally by using case B. Finally case A and B is decided as representative case

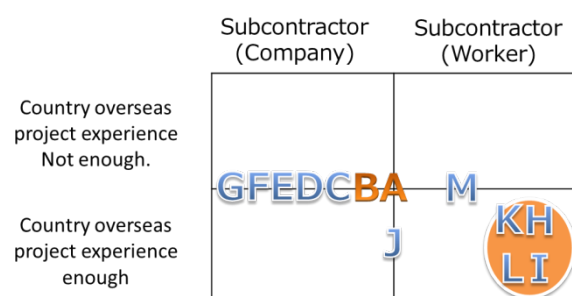


**Fig5: Framework of case**

## 4. Formulation

### 4-1. Model Overview

Build a model based on case A and B.

Incentive contract is the contract which subcontractor gets bonus depending on how early the submission can be made (The faster they submit, the more bonuses they get.) If subcontractor submits before the deadline, contractor also has benefit in terms of time and cost because time can be used for other work and time can link cost.

In case of subcontractor not meeting the deadline, it insists that there are other reasons for delay such as other subcontractor's delay. Subcontractor tries to avoid penalty by behaving like this.

In case of it, contractor claims subcontractor to pay penalty. Payoff of subcontractors by the incentive contract is also the following three.

- I. They submit earlier than due date and get bonus
- II. They make due date just in time and get reward as contracted
- III. They try to submit earlier than due date but they can't do it furthermore they can't submit by due date. Then they probably was forced pay penalty fee.

Moral hazard is caused by subcontractor shifting blame and will not occur if both get a maximum the payoff.

### 4-2. Parameter Distribution

Fig6 shows the game tree of game in extensive form. Payoff  $\pi^P, \pi^A$  is contractor and subcontractor respectively.

Game tree is proceeded as order below

1. Subcontractor chooses as to whether accept contract or not. If not game will be end (node a)
2. Contractor chooses effort level  $a_i (i = H, L)$ . If they choose  $a_H$  and contract type is incentive. If case of  $a_L$  contract is normal. (no incentive) (node b)
3. In this move, subcontractor choose make an effort as  $e_H$  or not make an effort as  $e_L$  and if its choice is in incentive, proceed node c2, and also if its choice in no incentive as well, then proceed c1. In case of that not make an effort, subcontractor can't meet due date, and then if it is in incentive, proceed e3. And if it is in no incentive, proceed e1. (node c1, c2)
4. This move is nature. Subcontractor can be successes by probability  $q$  in incentive and will get reward  $R$  and incentive bonus. If subcontractor is fail with probability  $1-q$ , subcontractor has still chance as probability  $r$  to submit product. In no incentive, subcontractor submit with probability  $p$  by due date and can get reward as contracted (node d1, d2, d3)
5. In case of that subcontractor doesn't make an effort or is fail, they certainly try to shift blame to avoid paying penalty. At the same time, contractor have to make an effort to force them to pay with effort level  $\omega_i (i = H, L)$  (node 1~e4)
6. In case of that in 5, contractor choose make an effort, success probability for forcing them to pay penalty with  $t_1, t_2, t_3, t_4$  (node f1~f4)

### 4-3. Subcontractor's Payoff (Expectation value)

In case of that no incentive ( $a_i = a_L$ ) and receiving confirmation ( $K_i = K_H$ )

$$\begin{aligned}\pi_L^A(a_L)(e'_L)(K_H) &= (1 - t_1)R + t_1(R - P) = R - t_1P \\ \pi_L^A(a_L)(e'_H)(K_H) &= R - \psi' - (1 - p)t_2P\end{aligned}$$

In case of that no incentive ( $a_i = a_L$ ) and no confirmation ( $K_i = K_L$ )

$$\begin{aligned}\pi_L^A(a_L)(e'_L)(K_L) &= R \\ \pi_L^A(a_L)(e'_H)(K_L) &= R - \psi' \\ R &> R - \psi'\end{aligned}$$

$$\pi_L^A(a_L)(e'_L)(K_L) > \pi_L^A(a_L)(e'_H)(K_L)$$

In case of that no confirmation, subcontractor had better to not make an effort to get more payoff.

**Incentive compatibility condition**

(Condition of that subcontractor makes an effort for making on time)

$$\begin{aligned}\pi_L^A(a_L)(e'_H) - \pi_L^A(a_L)(e'_L) \\ = \{R - \psi' - (1 - p)t_2P\} - \{(R - t_1P)\} \geq 0 \\ \psi' \leq \{(t_1 - t_2) + pt_2\}P \dots \dots \dots ①\end{aligned}$$

In case of that incentive ( $a_i = a_H$ ) and receiving confirmation ( $K_i = K_H$ )

$$\begin{aligned}\pi_H^A(a_H)(e_L)(K_H) &= (1 - t_3)R + t_3(R - P) = R - t_3P \\ \pi_H^A(a_H)(e_H)(K_H) &= R - \psi + qF - (1 - q)(1 - r)t_4P\end{aligned}$$

In case of that no incentive ( $a_i = a_H$ ) and no confirmation ( $K_i = K_L$ )

$$\begin{aligned}C2e_L: \pi_H^A(a_H)(e_L)(K_L) &= R \\ C2e_H: \pi_H^A(a_H)(e_H)(K_L) &= R - \psi \\ R &> R - \psi\end{aligned}$$

$$\pi_H^A(a_H)(e_L)(K_L) > \pi_H^A(a_H)(e_H)(K_L)$$

In case of that no confirmation, subcontractor had better to not make an effort to get more payoff.

**Incentive compatibility condition**

(Condition of that subcontractor makes an effort for making on time)

$$\begin{aligned}\pi_H^A(a_H)(e_H) - \pi_H^A(a_H)(e_L) \\ = \{R - \psi + qF - (1 - q)(1 - r)t_4P - (R - t_3P)\} \geq 0 \\ \psi \leq qF + \{(t_3 - t_4) + (q + r - qr)\}P \dots \dots \dots ②\end{aligned}$$

### Optimal Strategy

Subcontractor generally has no choice in contract type. Therefore, all they can do is follow contractor's decision of contract type. Function ① and ② is result of making an effort. That's why subcontractor should make an effort for meeting due date if subcontractor want to get profit more.

### 4-3. Contractor's Payoff (Expectation value)

At node t1~t4, as to whether Contractor should collect from subcontractor or not. Case of that subcontractor cannot make due date is most of same. Therefore, t1 is used as representative case.

**In case of that making an effort for collecting**

$$\pi_L^P(a_L)(e'_L)(K_H) = W - h - \omega + t_1P \dots \dots \dots (*)$$

**In case of that not making an effort for collecting**

$$\pi_L^P(a_L)(e'_L)(K_H) = W - h \dots \dots \dots (**)$$

$$(*) - (**) = (W - h - \omega + t_1P) - (W - h) = t_1P - \omega > 0$$

Then contractor should make an effort to collect as this condition. Next, for being easy to build function, no consider confirmation (remove node e below). At this same time, contractor don't know whether subcontractor make an effort or not. Therefore, if contract is incentive, subcontractor make an effort with  $d$  and if no incentive, probability is  $d'$  (Fig7)

**In case of no incentive, contractor's payoff**

$$\begin{aligned}\pi_L^P(a_L) &= (1 - d')(W - h) + d'\{(1 - p)(W - h) + pW\} \\ &= W - h + d'ph \dots \dots \dots (A)\end{aligned}$$

**In case of incentive, contractor's payoff**

$$\begin{aligned}\pi_H^P(a_H) \\ = (1 - d)(W - h - \varphi) \\ + d[(1 - q)\{(1 - r)(W - h - \varphi) + r(W - \varphi)\} \\ + q(W + E - F - \varphi)]\end{aligned}$$



# FORMULATION

## SHOW CASE A,B AS USING GAME TREE

W: Reward for success of Contractor from Client  
R: Reward for success of Subcontractor from Contractor  
F: Incentive bonus  
P: Penalty fee  
E: Utility thanks to finishing work earlier  
h: Suffer a loss from behind due date  
p,q,r: Probability of Success.  
 $t_1, t_2, t_3, t_4$ : Probability of Success that contractor establish FID of subcontractor and force them to pay penalty

Effect level

$$F(a) = \begin{cases} \varphi & (a = a_H) \\ 0 & (a = a_L) \end{cases}$$

$$L(e) = \begin{cases} \psi & (e = e_H) \\ 0 & (e = e_L) \end{cases}$$

$$L'(e) = \begin{cases} \psi' & (e' = e'_H) \\ 0 & (e' = e'_L) \end{cases}$$

$$Q(k) = \begin{cases} \omega & (k = k_H) \\ 0 & (k = k_L) \end{cases}$$

$\Pi^P$  contractor's pay off  
 $\Pi^A$  Subcontractor's pay off

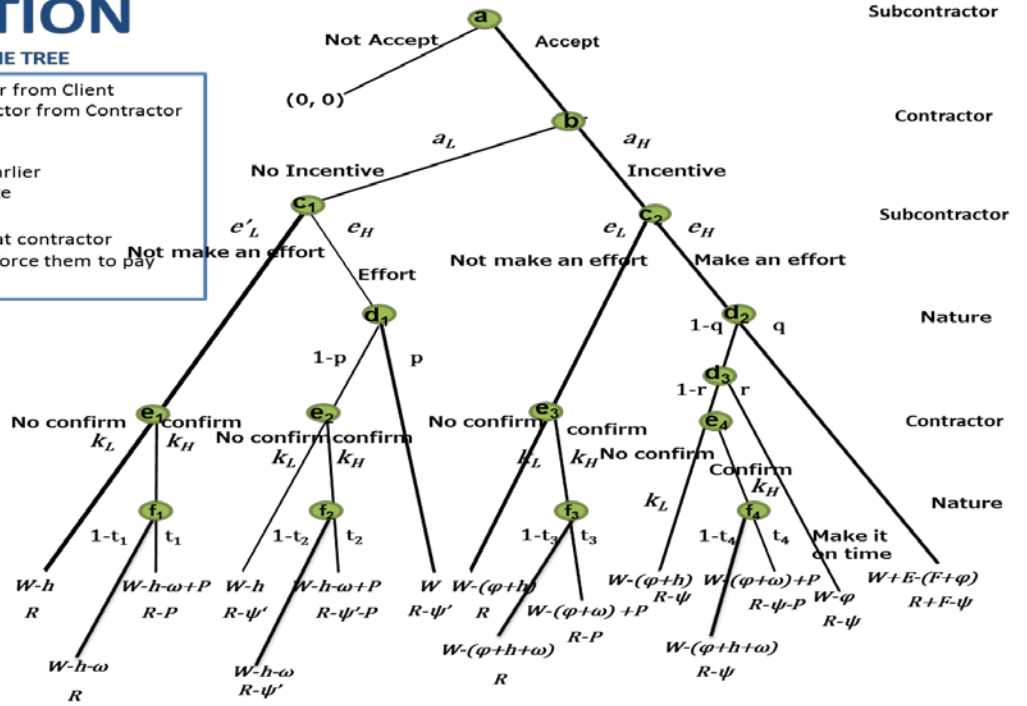


Fig6: Fundamental model of game tree

$$= W - \varphi - (1 - d)h + d\{-(1 - q)(1 - r)h + q(E - F)\}$$

$$= W - \varphi - h\{1 - (q + r - qr)d\} + dq(E - F) \dots \dots (B)$$

### Optimal Strategy

Which incentive and no incentive contract would be better for subcontractor?

$(B) - (A) = \Pi_H^P(a_H) - \Pi_L^P(a_L) > 0$ , Incentive contract is better than no incentive

$$= W - \varphi - h\{1 - (q + r - qr)d\} + dq(E - F) - (W - h + d'ph) > 0$$

$$dqE + \{(q + r - qr)d - pd'\}h - \varphi > dqF$$

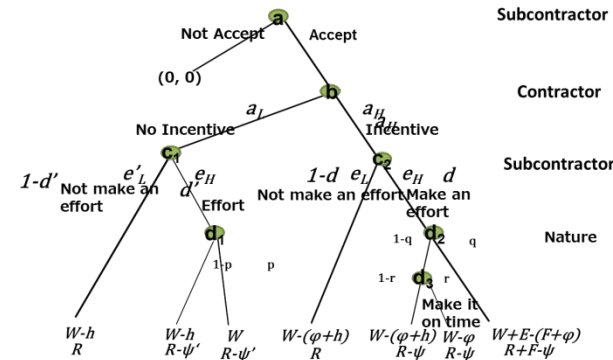


Fig7: In case of no action for collecting penalty

Thus, Contractor should propose Incentive contract to subcontractor. Furthermore, it is found that subcontractor certainly make an effort to meet due date from ① and ②.  $d$  and  $d'$  can be  $d=d'=1$ . Therefore,

$$qE + \{q + (1 - q)r - p\}h - \varphi > qF \dots \dots \dots ③$$

At this time, condition of subcontractor's optimal payoff in incentive contract is

$$\psi \leq qF + \{(t_3 - t_4) + (q + r - qr)\}P \dots \dots \dots ②$$

From ②, ③ we can get

$$\psi \leq qF \leq qE + h\{-p + q + (1 - q)r\} - \varphi \dots \dots \dots ④$$

(But, member of P can be ignored since effect as against function ② is small).

④ is important to get maximum utility each other.

### Interpretation ④

- If F is small, incentive contract can be easy to be adopted for contractor

- If E is big (ahead of schedule is big), incentive contract can be easy to be adopted for contractor
- If h is big (suffer a loss from delay), incentive contract can be easy to be adopted for contractor
- If p is big (even in no incentive, when probability of that subcontractor can meet due date is big)  $q + (1 - q)r - p$  would be small. It means that contract type would be chosen no incentive.

## 5. Conclusion

This study focused on 2 research which one is survey and other is contract theory. Survey's and model's finding as follow

- ✓ In advance, contractor has prepared contingency and man-hour to deal with some risk which can occur simultaneously.
- ✓ From model, some finding as follow
  - ✧ If contractor save incentive bonus as small, utility of contractor will be higher.
  - ✧ If ahead of schedule thanks to subcontractor is big, utility of contractor will be higher.
  - ✧ If suffer a loss from delay is big, contractor must give incentive to subcontractor as submitting earlier.
  - ✧ If probability of that subcontractor can meet due date is big, it means that contract type would be no incentive.

## 6. References

- [1] 山本明男: 日系建設会社のグローバル戦略ーリスクマネジメントから見た事例研究, 2007
- [2] 石磊・小林潔司: 建設契約におけるダブルモラルハザード, 2010
- [3] Joel S.Demski et al.: Resolving double moral hazard problems with buyout agreements, 1991
- [4] Russel Cooper et al.: Product Warranties and Double Moral Hazard, 1985



# An Analysis on Consumers' Preferences for the Residential Photovoltaic System Focused on Its Long-Term Operation

Student Number: 11M18150

Name: Toshiya MORIZUMI

Supervisor: Naoya ABE

## 住宅用太陽光発電システムの長期運用に着目した消費者選好の分析

森住 俊哉

本研究では、普及が進むにつれ近年増加している住宅用太陽光発電システム（以下、住宅用 PV）に係わる消費者トラブルの改善、また消費者に対する故障や保守管理に関する適切な情報提供の重要性とこれらの情報が住宅用 PV の購買行動に与える影響を明らかにすることを目的しアンケート調査を行った。同調査によるデータを分析し、住宅用 PV の保守管理制度に対して高い消費者選好を持つ消費者群の特徴を情報収集の観点から明らかにした。分析結果を基に、消費者が保守管理の重要性を認知し購買意思決定を下すために必要な情報提供の在り方を提言した。

### 1. Introduction

In recent years, electricity output from photovoltaic (PV) systems has been increasing considerably. Specifically, residential PV systems have made a particularly large impact in the Japanese PV market. However, as the number of residential PV system installations increases, the number of consumer problems with PV systems also rises (Figure 1). Consumer problems with PV systems are of great concern because they not only impose financial risks on consumers but also prevent the PV market from developing soundly. Based on this development, Cabinet Office, Japan (2012) proposed solutions from three perspectives: law enforcement, the importance of the quality of maintenance services, and adequate information provision.

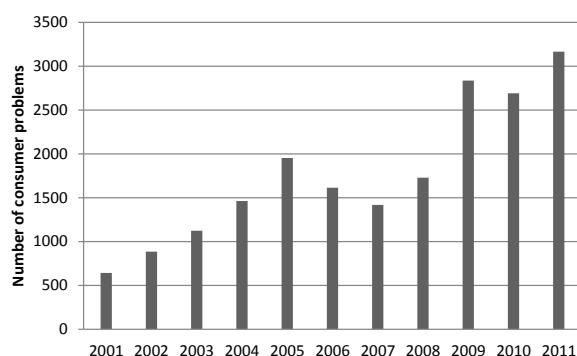


Figure 1. Changes in the number of consumer problems with PV systems (2001–2011)  
Source: Cabinet Office, Japan (2012)

Under this proposal, Cabinet Office, Japan (2012) indicated the importance of the quality of maintenance services for PV systems. An increase in the quality of user support (e.g., warranty and maintenance services) is expected to reduce purchasers' financial risks (Shinp et al., 1982). According to the survey by Kato (2010), approximately 35% of residential PV systems experience some problems within 10 years of installation. In spite of this fact, the importance of user support for PV systems has not been

recognized among policymakers. For example, a report by the Ministry of Economic, Trade, and Industry (METI), Japan (2009a) on the expected initial cost recovery period of residential PV systems under the feed-in tariff, effective from 2012, did not include the aspect of additional costs for user support.

Changes in consumers' behavior in gathering information could be one of the key tools to provide adequate information on PV systems. METI (2009b) surveyed the status of consumers' behavior in gathering product information. The survey results showed that word-of-mouth communications (WOMCs) significantly influence consumers' purchase decisions. In the case of residential PV systems, consumers' behavior in gathering information including WOMCs has become more multifaceted. If consumers' behavior in gathering information on PV systems influences their purchasing decisions, then differences in gathering approaches could affect their preferences for selected attributes of residential PV systems, such as price and performance.

### 2. Objectives

This study suggests solutions to the problems of information provision and the quality of maintenance services proposed by Cabinet Office, Japan (2012). To reduce consumers' financial risks when purchasing PV systems, adequate information provision should not only improve consumer problems with such systems but also make consumers recognize the importance of the quality of maintenance services for their long-term operation. Hence, this study aims to:

- 1) Study the relationship between consumers' preferences for residential PV systems and consumers' behavior in gathering information on such systems through data analysis.
- 2) Assess the proposal by Cabinet Office, Japan (2012) and propose more effective solutions related to information provision on PV systems.

### 3. Data collection

This study conducted an online survey to collect data on consumers' behavior in gathering information on PV systems and their preferences for residential PV systems. Tables 1 and 2 show the summary and content of this survey, respectively.

Table 1. Summary of the online survey

Survey term	3 Oct, 2012~5 Oct, 2012
Respondents	Consumers who are planning to install residential PV systems within 3 years
Sample size	N=291

Table 2. Content of the online survey

Data	Definition
Demographic characteristics	Age, households' income, occupation, education etc.
Behavior for gathering information on PV systems	1) Information sources which respondents use or trust 2) Contents of information which respondents use or trust
Stated preference	Choice-based experiments on residential PV systems

Choice-based experiments (shown in Table 2) are generally used to collect stated preference data for products. In experiments, the researcher provides a number of choice sets to respondents and asks them to choose the most desirable option in each set. Choice sets are constructed from certain profiles including attributes such as price and product quality. This study assumed that cost, benefit, and warranty and maintenance services affect consumers' decisions when purchasing PV systems. In this survey, six attributes with two or four alternatives were defined as the components of profiles (Table 3).

Table 3. List of attributes and alternatives

Attributes	Alternative1	Alternative2	Alternative3	Alternative4
Price	1.8 million JPY	2 million JPY	2.2 million JPY	2.4 million JPY
Initial cost recovery period	7 years	10 years	13 years	16 years
Peripheral warranty period	10 years	15 years		
Module performance warranty period	10 years	15 years	20 years	25 years
Application fee for peripheral warranty	free	10,000 JPY	20,000 JPY	30,000 JPY
Maintenance service (10 years)	none	Periodic check 30,000JPY	Monitoring service free	Monitoring service 30,000JPY

Choice experiment design is concerned with creating choice sets in an efficient way. Applying a full factorial design would generate too many choice sets, which would be cumbersome for respondents to answer. In the case of the design shown in Table 3, the total number of combinations would be 2,048. Therefore, an orthogonal design was adopted by this study to

decrease the number of profiles and to effectively observe consumers' preferences for all alternatives in each attribute. In total, the 32 profiles generated by applying such an orthogonal design were divided into eight choice sets randomly. Table 4 presents an example of the choice sets used in this survey. Four options were then chosen from the 32 profiles and one no-choice option. The no-choice option in choice sets is applied to avoid the overestimation of consumers' preferences (Vermeulen et al., 2008).

Table 4. Example of choice sets

*Q: Which one of the following options would you choose if you were purchasing a residential PV system?*

	Option1	Option2	Option3	Option4	Option5
Price	1.8 million JPY	2 million JPY	1.8 million JPY	2.2 million JPY	
Initial cost recovery period	16 years	10 years	10years	17years	
Peripheral warranty period	10 years	15 years	15 years	10 years	
Module performance warranty period	15 years	25 years	20 years	25 years	
Application fee for peripheral warranty	free	10,000 JPY	free	free	
Maintenance service (10 years)	Periodic check 30,000JPY	Periodic check 30,000JPY	none	Monitoring service 30,000JPY	
Choice	<input type="checkbox"/>	<input type="checkbox"/>	<input type="checkbox"/>	<input type="checkbox"/>	<input type="checkbox"/>

### 4. Data analysis

This study applied the latent class (LC) model to estimate the relationship between consumers' preferences for PV systems and their behavior in gathering information on such systems. First, the methodology of standard conjoint analysis is explained. It is assumed that respondents choose options that possess the combination of attributes that would provide them with the highest level of utility. (Eq. 1) represents the utility level attained from option (i) for individual (n):

$$U_{ni} = \mathbf{X}_{ni}\boldsymbol{\beta}' + \varepsilon_{ni} \quad (\text{Eq. 1})$$

$\mathbf{X}_{ni}$  is the vector of observed attributes with conformable parameter  $\boldsymbol{\beta}'$ , while the error term  $\varepsilon_{ij}$  is unobservable and assumed to follow a Gumbel distribution. The probability that individual (n) chooses option (i) is represented in (Eq. 2):

$$P_{ni} = \frac{\exp(\mathbf{X}_{ni}\boldsymbol{\beta}')}{\sum_i \exp(\mathbf{X}_{ni}\boldsymbol{\beta}')} \quad (\text{Eq. 2})$$

This model estimates  $\boldsymbol{\beta}'$ , which maximizes the log-likelihood function (Eq. 3):

$$\ln L = \sum_n \sum_i d_{ni} \ln P_{ni} \quad (\text{Eq. 3})$$

$d_{ni}$  is the choice result whether individual (n) chooses option (i) or not.

However, it is known that heterogeneity among individuals' preferences makes them difficult to examine in traditional conjoint models. The LC model overcomes this issue by assuming that the population consists of latent classes (Z) and that

the unobserved heterogeneity among individuals can be estimated by these classes through estimating a parameter vector in the membership function (Eq. 4):

$$M_{nz} = \mathbf{W}_n \lambda'_z + \zeta_{nz} \quad (\text{Eq. 4})$$

$\mathbf{W}_n$  is the vector of the characteristics of individuals with conformable parameter  $\lambda'_z$  and  $\zeta_{nz}$  is the unobservable error term. The probability that individual (n) resides in the latent class (z) is

$$\pi_{nz} = \frac{\exp(\mathbf{W}_n \lambda'_z)}{\sum_z \exp(\mathbf{W}_n \lambda'_z)} \quad (\text{Eq. 5})$$

By combining the choice equation (Eq. 2) with the membership equation (Eq. 5), the probability that individual (n) chooses option (i) under the assumption of heterogeneity among individuals is

$$P_{ni} = \sum_c P_{|ni|z} \pi_{nz} \quad (\text{Eq. 6})$$

$$= \sum_z \left[ \frac{\exp(\mathbf{X}_{ni} \beta'_z)}{\sum_i \exp(\mathbf{X}_{ni} \beta'_z)} \right] \times \left[ \frac{\exp(\mathbf{W}_n \lambda'_z)}{\sum_z \exp(\mathbf{W}_n \lambda'_z)} \right]$$

The marginal willingness to pay (MWTP) is used to compare consumers' preferences for each attribute. MWTP is calculated as (Eq. 7)

$$MWTP = - \frac{\beta_z}{\beta_{cz}} \quad (\text{Eq. 7})$$

$\beta_{cz}$  is the estimated parameter of cost in class (z) and  $\beta_z$  is the estimated parameter of attributes except price. The goal of the LC model is to estimate both the MWTP and a vector of parameter  $\lambda_z$  in the membership function.

Table 5. Description of the variables used in the LC model

Variable	Description
<b>Dependent variable</b>	
Chosen	1 if the option is chosen, 0 otherwise
<b>Variables in utility function</b>	
Price	Total price [million JPY] (Price+Application fee for peripheral warranty)
Initial	Initial cost recovery period [year]
Peripheral	Peripheral warranty period [year]
Module	Module performance warranty period [year]
Dum_Periodic	1 if the maintenance service is "Periodic check", 0 otherwise
Dum_Monitor_free	1 if the maintenance service is "Monitoring service (free)", 0 otherwise
Dum_Monitor_paid	1 if the maintenance service is "Monitoring service (30,000JPY)", 0 otherwise
ASC	1 if the option is "no-choice option", 0 otherwise
<b>Variables in membership function 1: Experiences on gathering information</b>	
Dum_Basic	1 if a respondent has collected information about price, performance of PV systems, 0 otherwise
Dum_Governmental	1 if a respondent has collected information about governmental supports for PV systems, 0 otherwise
<b>Variables in membership function 2: Trustworthy information sources</b>	
Dum_e-WOM	1 if a respondent trusts information from e-WOMCs, 0 otherwise
Dum_WOM	1 if a respondent trusts information from WOMCs, 0 otherwise
<b>Variables in membership function 3: Trustworthy contents of information</b>	
Dum_Governmental	1 if a respondent trusts information about governmental supports for PV systems, 0 otherwise
Dum_Actual	1 if a respondent trusts information about actual PV power generation or yield from PV systems, 0 otherwise

## 5. Results

The variables are described in Table 5, while Table 6 shows the results of the LC model. This study classified respondents into three groups based on the heterogeneity of their preferences for residential PV systems. This result shows that approximately 29% of respondents (class 2) have the highest preferences for initial cost recovery period, module performance warranty period, and maintenance service among all respondents. This means that they would like to recover the initial

Table 6. Results of the LC model (N=291)

	Class1		Class2		Class3	
Marginal Willingness to pay (MY: million JPY)						
	MWTP	t-value	MWTP	t-value	MWTP	t-value
Initial [MY/year]	-0.027***	-3.083	-0.296***	-4.363	-0.105	-0.729
Peripheral [MY/year]	0.028***	2.700	0.021	1.387	0.010	0.301
Module [MY/year]	0.022***	4.470	0.040***	3.391	0.013	0.355
Dum_Periodic [MY]	0.305***	4.191	0.550***	2.813	0.180	0.565
Dum_Monitor_free [MY]	0.820***	8.232	0.795***	3.498	0.825	0.838
Dum_Monitor_paid [MY]	0.438***	5.316	0.660***	3.025	0.221	0.516
ASC [MY]	-3.679***	-8.868	-4.344***	-5.917	-1.019	-0.816
Membership function 1: Experiences on gathering information						
	lamda	t-value	lamda	t-value	Base outcome	
Const	0.156	0.474	-0.579	-1.439		
Dum_Basic	1.188***	3.014	0.936**	2.077		
Dum_Governmental	0.234	0.633	0.713*	1.683		
Membership function 2: Trustworthy information sources						
	lamda	t-value	lamda	t-value	Base outcome	
Const	1.048***	5.158	0.178	0.735		
Dum_e-WOM	0.061	0.158	0.942**	2.230		
Dum_WOM	0.585	1.220	0.249	0.457		
Membership function 3: Trustworthy conents of information						
	lamda	t-value	lamda	t-value	Base outcome	
Const	0.920***	4.865	0.093	0.409		
Dum_Governmental	0.695	1.611	1.250***	2.737		
Dum_Actual	1.312	1.225	1.580	1.441		
Class share	54%		29%		17%	

\*\*\*, \*\*, and \* represent statistical significance at the 1%, 5%, and 10% levels, respectively.

cost in a shorter period and that they attach importance to high-quality user support compared with other respondents.

In addition, the LC model estimated consumers' characteristics that may influence the heterogeneity of their preferences for PV systems. The LC model defined class 3 as the base outcome. Therefore, the parameters of the membership functions for classes 1 and 2 are different from that of class 3. This study adopted three datasets, as shown in Table 6. The results are explained as follows.

First, it is observed that consumers who gather information more positively have higher preferences for initial cost recovery and user support than others. The parameters of membership function 1 show that respondents in class 1 tend to gather basic information such as price and system performance, while respondents in class 2 tend to gather both basic information and information on governmental support such as subsidies.

Second, there is a probability that consumers who trust interactive communication with PV users are categorized into class 2. The result of membership function 2 shows that the dummy variable *e-WOM* in class 2 is statistically significant at the 5% level. Information from PV users includes information about their actual PV power generation and actual yields from their systems. This finding implies that respondents in class 2 like to gather more reliable information related to initial cost recovery through e-WOMCs, namely communication with PV users on the Internet.

The probability that consumers who have higher preferences for initial cost recovery and user support would like to gather more reliable information is also observed through another membership function. Membership function 3 (Table 6) was constructed with a dataset about the information content respondents trust the most. The estimated parameter was not statistically significant; however, respondents who attach importance to information on actual PV power generation and yield from PV systems in addition to information on governmental support would be classified under class 2.

## 6. Conclusions

### 1) Conclusion: Objective 1

The LC model expressed the relationship between consumers' preferences for PV systems and their behavior in gathering information on such systems. Consumers who have higher preferences for initial cost recovery and user support have the characteristic of gathering information more positively and attach importance to information sources and content that include more reliable information related to

initial cost recovery.

### 2) Conclusion: Objective 2

Cabinet Office, Japan (2012) proposed that it is important for both consumers and the PV market to provide more understandable and accessible information on PV systems. The results of the LC model support this proposal. If information on PV systems, especially that related to initial cost recovery, was more understandable and accessible for consumers, consumers would attach a higher importance of these information to the long-term operation of PV systems.

### 3) Further study

The proposal by Cabinet Office, Japan (2012) presented a future research avenue for the provision of information on consumers' profitability. In recent years, services for the estimation of PV power generation have been provided to consumers by a number of PV manufacturers. However, as mentioned in the proposal by Cabinet Office, Japan (2012), improvements in estimation accuracy are necessary to provide more reliable information on consumers' profitability. This study has demonstrated that more reliable information on consumers' profitability is also necessary for the long-term operation of PV systems; the assessment of the accuracy of output estimation could thus be further studied. Another research direction could be the re-examination of the calculation of the initial cost recovery period conducted by METI (2009a). As mentioned in the introduction to this paper, the existing calculation does not include the additional cost for user support. To provide more reliable information on consumers' profitability, policymakers should propose more realistic calculation results to consumers.

## References

- Cabinet Office, Japan, 2012, Proposal for consumer troubles on residential photovoltaic systems (in Japanese)
- Kato, 2010, Collection of instances related to troubles on photovoltaic systems, Nikkou Kogyo Shinbunsha (in Japanese)
- METI, Japan, 2009a, Report on feed-in-tariff for photovoltaic systems (in Japanese)
- METI, Japan, 2009b, Survey on the consumers' purchasing behavior after Lehman shock (in Japanese)
- Shimp et al., 1982, Warranty and other extrinsic cue effects on consumers' risk perceptions, *Journal of Marketing*, Vol. 39, No. 2, pp. 36-43
- Vermeulen, Goos and Vandebroek, 2008, Models and optimal designs for conjoint choice experiments including a no-choice option, *International Journal of Research in Marketing*, Vol. 25, pp. 94-103

# Quantitative analysis of the atmospheric boundary layer flow field using Doppler lidar

Student Number: 11M18166      Name: Ayako Yagi      Supervisor: Manabu Kanda

## ドップラーライダーを用いた大気境界層流れ場の定量的解析手法の提案

八木綾子

本論文では、ドップラーライダーにより観測された視線方向風速分布から、都市上空の流れ場を定量的に解析する手法を提案する。各方位角の視線方向風速分布において算出した自己相関係数から流れ場の代表的な長さスケールを抽出した。算出した代表長さは、支配的な構造の特徴、及びその日変化を捉えていた。

### 1 Introduction

Local heavy rainfall and air pollution are atmospheric environmental problems which have strongly influenced our daily life. These problems are strongly coupled with momentum and scalar transport process within the atmospheric boundary layer (ABL). Hence, the understanding of flow field within the ABL is important to solve or mitigate the atmospheric environmental problems.

It is commonly known that flow structure within the ABL configure some characteristic patterns. Woodcock [1] suggested that there are two types of flow structure within the ABL from observation of Herring Gull flight above the sea: i.e. linear structure (LS) and random structure (RS). Grossman [2] estimated the spatial width of the flow structure based on the spectra of vertical velocity observed above the sea.

Doppler lidar is the latest remote sensing system which has been used to analyze ABL flow field in recent years. Doppler lidar beams near infrared laser ( $1.54\mu\text{m}$ ) and receive the backscatter reflected from aerosols floating in the atmosphere. Then, radial wind velocity can be measured by detecting the Doppler shift of the backscatter. Doppler lidar measurements have already made some achievements in the ABL research. Fujiyoshi [3] has observed streaky structure and thermal structure within a field observation in Sapporo. Iwai [4] has detected the two-dimensional wind velocity distribution using Doppler lidar observation and the width of convective rolls from frequency analysis of vertical velocity observed by airplane observation. Oda [5] calculated the width of streaky structure from two-point correlation coefficient of

radial velocity distribution observed by Doppler lidar. These researches contributed to understanding ABL flow field.

Although some researches have shown the span-wise width of streaky pattern of ABL flow, their stream-wise scale was not precisely examined. A considerable reason is because a range of usual Doppler lidar observation is not enough to capture the full scale of stream-wise length of streaky structures. Another reason is from a difficulty in the physical interpretation of the calculated stream-wise length because of the meandering of streaky pattern. The first reason is entirely follow the Doppler lidar equipment. The second reason could be solved by adjusting the estimation procedure, which is a part of the aims of this study.

In addition, most of the previous researches have focused on the streaky pattern and the other patterns are still not well examined since they are much less frequently observed compared to the streaky structure during their limited observation periods.

In this research, a method is proposed to estimate stream-wise representative length and span-wise representative length. This method was applied not only to streaky pattern but also to other flow patterns. Special aspects of this research area as follows: (1) Stream-wise length scale is examined together with the span-wise length scale. (2) This method was applied to whole datasets obtained for two weeks. Based on this analysis, structures of various flow patterns (not only streaky pattern) were analyzed quantitatively and comprehensively.



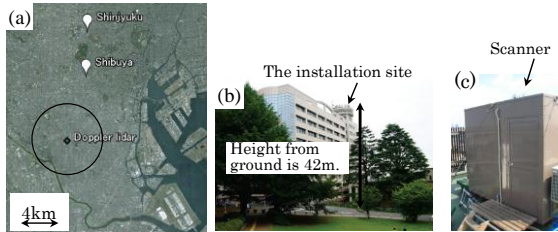
## 2 Overview of Doppler lidar

Table.1 shows specifications of Doppler lidar used for this research. The measurement range in radial direction is from 325 m to 4275 m which is resolved each 50 m. This Doppler lidar is installed on the roof top of West 8<sup>th</sup> building in Tokyo institute of technology (sea level altitude is 78 m, height from ground is 42 m cf. Fig.1). It has operated since August 2011. The measurement area is represented by residential urban area. Outside the measurement area, metropolitans, e.g. Shinjuku and Shibuya, spread in the north east. Such a long term observation in urban area has never been conducted so far.

The measurement was operated by Plane Position Indicator (PPI) scan. In PPI scan, scanner turns round with constant elevation. In this research, elevation angle was set 0°. This means that scanner turns round parallel to the sea surface and the horizontal radial velocity distribution was measured.

**Table.1: Specifics of Doppler lidar**

Range resolution	50 m
Minimum/Maximum range	325 m/4275 m
Range bin number	80
Scan speed	3.0 degree s <sup>-1</sup>



**Fig.1: Observation site**

(a) Observation area of Doppler lidar, (b) Location of Doppler lidar, (c) The scanner of Doppler lidar.

## 3 Analytical basis

Representative length scale of flow patterns are estimated in the following procedures (cf. Fig.2).

(1) Autocorrelation coefficient  $R(\tau)$  was calculated from measured radial wind velocity distribution on each azimuth using eq. (4.1).

$$R(az, \tau) = \frac{\sqrt{\sum_{i=1}^k (V_r(az, r_i) - \bar{V}_r(az, \tau))(V_r(az, r_i + \tau) - \bar{V}_r(az, \tau))}}{\sqrt{\sum_{i=1}^k (V_r(az, r_i) - \bar{V}_r(az, \tau))^2} \sqrt{\sum_{i=1}^k (V_r(az, r_i + \tau) - \bar{V}_r(az, \tau))^2}} \quad (4.1)$$

$$0 < \tau < \tau_{max}, r_k = 1500m, \tau_{max} = 2450m$$

Where,  $R$  is autocorrelation coefficient,  $V_r$  is radial velocity,  $az$  is azimuth angle,  $r$  is radial distance,  $\tau$  is phase lag,  $r_k$  is integral interval. Over bar indicates spatial mean in radial direction. The value of  $r_k$  was decided empirically with considering the precision of autocorrelation coefficient and limitation of observation area. The resolution of  $\tau$  is 50 m, which is the same as the resolution of Doppler lidar.

(2) Integral length  $S$  was calculated by integrating the autocorrelation coefficients in radial direction on each azimuth by eq.(4.2).

$$S(az) = \int_0^{\tau_0} R(\tau) d\tau \quad (4.2)$$

$$R(\tau_0) = 0$$

In this research,  $R(\tau_0) = 0$  was set as indication of correlation.

(3) Two representative lengths, i.e.  $S_{\sigma min}(az_{min})$  and  $S_{\sigma max}(az_{max})$ , were determined among the integral length distribution in azimuth.  $S_{\sigma max}$  represents the longest integral length through azimuth, which implies the stream-wise length scale, and  $S_{\sigma min}$  is the shortest and has a meaning of span-wise length scale. For the determination of these characteristic scales, data during one hour are used in which 10 scans of the data were included.  $S_{\sigma max}$  is determined at the azimuth where variance of  $S$  among 10 scans of data is largest since meandering of structure makes the variance largest in stream-wise direction.  $S_{\sigma min}$  is determined at the azimuth where variance of  $S$  is minimum since variance of  $S$  is less affected by meandering in the span-wise direction.

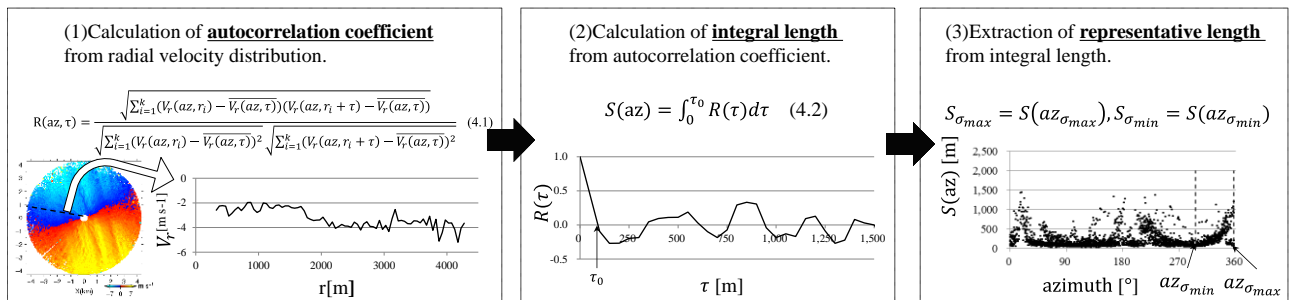


**Fig.2: Flow of analysis procedure**

## 4 Results

### 4.1 Comparison of integral lengths between streak and fishnet cases.

Fig. 3 shows integral length through azimuth. In Fig.3, left figures show radial velocity in which red (blue) means positive (negative) radial velocity toward the observation point. The right figures in Fig.3 show the integral lengths where the dotted lines and dot-dash lines show the span-wise and stream-wise direction, respectively. These wind directions were estimated from Velocity Azimuth Display (VAD) method.

Fig.3 (a) and (b) distinguish the streak and fishnet events respectively. Streak event has the streaky wind velocity pattern along stream-wise direction. Fishnet event is cell-like patterns and isotropic horizontally. As in the Fig.3, the integral length of streak event tends to be longer in stream-wise and to be shorter in span-wise direction. In a fishnet case, the integral length distribution was almost isotropic in azimuth. Therefore, the present method could properly distinguish the two kinds of event adequately.

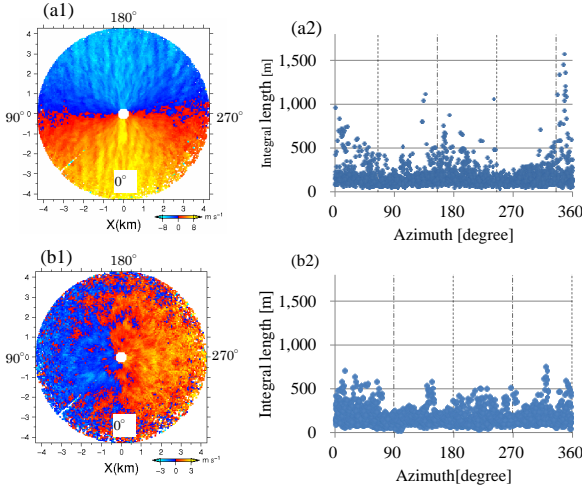


**Fig.3: Comparison integral length of streak case with fishnet case**

### 4.2 The daily change of representative lengths

The representative lengths ( $S_{\sigma min}$  and  $S_{\sigma max}$ ) were calculated in a typical day. The radial velocity pattern used for this analysis was shown in Fig.4. In the night time, streak structure was dominant and the structure was gradually transformed to fishnet pattern with approaching 12:00.

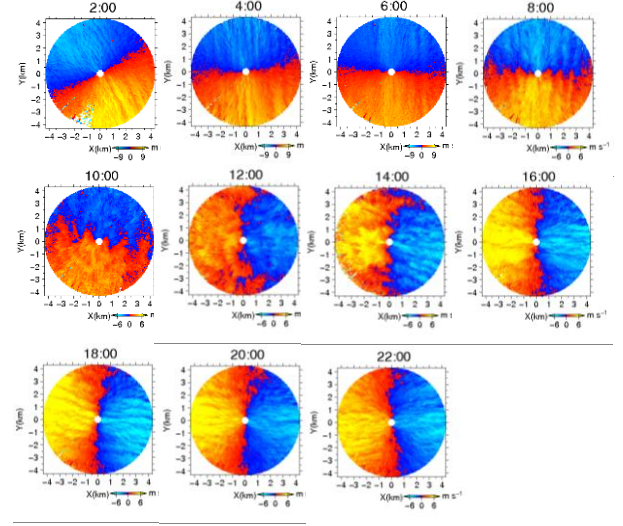


**Fig.4: The daily change of radial velocity distribution**

Fig.5 shows the estimated representative lengths ( $S_{\sigma min}(az_{min})$  and  $S_{\sigma max}(az_{max})$ ). The axis at the right side is for  $S_{\sigma min}$ , and that of left side is for  $S_{\sigma max}$ . The figure shows that  $S_{\sigma max}$  is longer in the night time, and  $S_{\sigma min}$  is getting longer with approaching noon. Fig.6 shows the extracted azimuth ( $az_{min}$  and  $az_{max}$ ) and stream-wise and span-wise estimated from VAD method.  $az_{min}$  ( $az_{max}$ ) is almost identical to stream-wise (span-wise) direction. Therefore the estimated representative lengths seem to correctly reflect the stream wise and span wise.

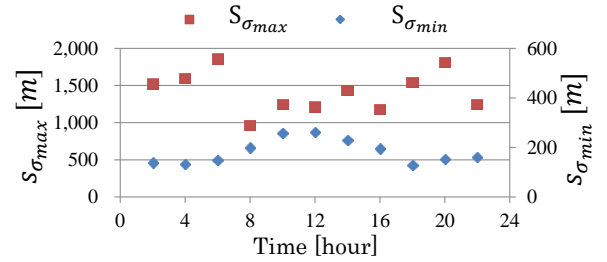


**Fig.5: The daily change of representative length**

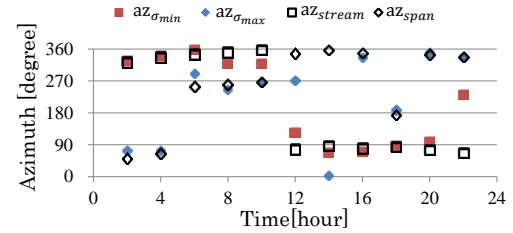


**Fig.6: Comparison  $az_{min}$  and  $az_{max}$  with stream direction calculated by VAD method**

### 4.3 Relationship of representative length with atmospheric stability

Validity of the integral lengths was evaluated in the previous sections. Those integral lengths were used as the index of flow structure in this section.

Fig.7 shows the correlation diagram of atmospheric stability ( $z/L$ ) with aspect ratio of stream- and span-wise lengths ( $S_{\sigma max}/S_{\sigma min}$ ). The analysis was conducted for the datasets obtained in 2012/10/1-2012/10/13 in which 170 cases are included. Figs.7a, b show the unstable ( $z/L > 0$ ) and stable ( $z/L < 0$ ) cases respectively. Atmospheric stability was observed using a sonic-anemometer which was installed within a measurement area of the Doppler lidar. Colors of plots in Fig. 7 correspond to the flow patterns which were visually classified into 6 groups; “Streak”, “No streak”, “Mixed”, “Fishnet”, “Front” and “The others”. In this classification, Mixed is a medium flow pattern between Streak and Fishnet.

In the unstable case, aspect ratio ( $S_{\sigma max}/S_{\sigma min}$ ) tends to decrease with increasing  $z/L$ . The plots of Streak are distributed at relatively large aspect ratio, and it followed by Mixed and Fishnet. This order in the aspect ratio is consistent with the visually classification as Streak is more elongated and fishnet is more round. In the stable case, the aspect ratio looks less sensitive to  $z/L$ .

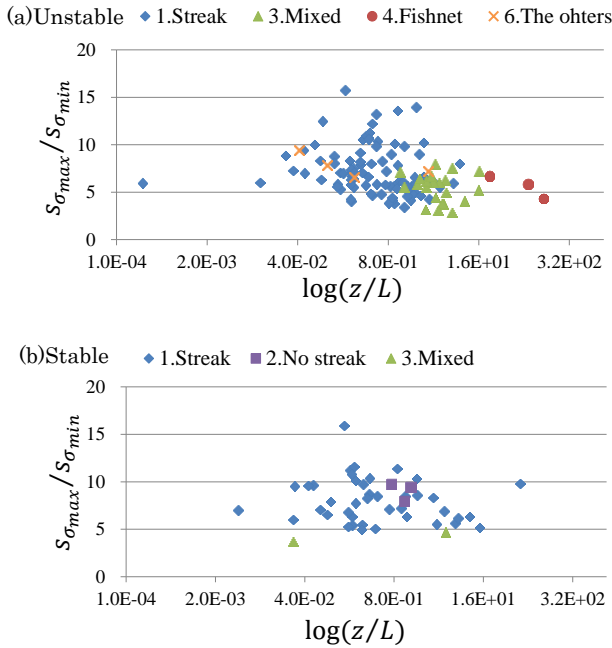


**Fig.7: Relationship atmospheric stability with aspect ratio of representative length**

(a) Unstable case, (b) Stable case.

## 5 Conclusions

Doppler lidar measurements have been mainly used for only qualitative analysis of ABL flow. The method proposed in this paper allows quantitative analysis of ABL flow. The following findings were obtained.

- 1) Representative lengths of flow pattern were determined using radial velocity distribution measured by Doppler lidar.
- 2) Integral length distribution through azimuth showed a reasonable tendency for streak structures and fishnet structures.
- 3) Diurnal variation of representative lengths corresponds to that of the flow pattern.
- 4) The aspect ratio of representative lengths decreases as the atmospheric stability ( $z/L$ ) increases in unstable case. The same tendency cannot be seen in the stable case.

## References

- [1] Woodcock, A. H.: 1975, Thermals Over the Sea and Gull Flight Behavior, Boundary-Layer Meteorol. 9, 63-68.
- [2] Grossman, R L. 1982: An analysis of vertical velocity spectra obtained in the BOMEX fair-weather, trade-wind boundary layer., Bound Layer Meteor., 23, 323-357.
- [3] Y. Fujiyoshi, K. Yamashita, C. Fujiwara: Visualization of Streaks, Thermals and Waves in the Atmospheric Boundary Layer, Journal of Visualization, Volume 9, Issue 4, p 359, 2006.
- [4] Hironori Iwai, Shoken Ishii, Nobumitsu Tsunematsu, Kohei Mizutani, Yasuhiro Murayama, Toshikazu Itabe, Izumi Yamada, Naoki Matayoshi, Dai Matsushima, Sha Weiming, Takeshi Yamazaki, and Toshiki Iwasaki, 2008: Dual-Doppler lidar observation of horizontal convective rolls and near-surface streaks, GEOPHYSICAL RESEARCH LETTERS, VOL. 35.
- [5] Ryoko Oda, Hironori Iwai, Yasuhiro Murayama, Shoken Ishii, Kohei Mizutani, Toshikazu Itabe, Nobumitsu Tsunematsu, Izumi Yamada, Naoki Matayoshi, Dai Matsushima, Weiming Sha. Takeshi Yamazaki and Toshiki Iwasaki: DOPPLER LIDAR OBSERVATIONS OF THE COHERENT STRUCTURES IN THE INTERNAL BOUNDARY LAYER

# APPLICATION OF VIRTUAL REALITY (VR) PANORAMA FOR TOWNSCAPE MONITORING IN THE WORLD HERITAGE SITE OF LUANG PRABANG, LAO P.D.R.

Student Number: 11M18189    Name: Kenta YOKOI    Supervisor: Shinobu YAMAGUCHI, Jun-ichi TAKADA

ラオス、世界遺産地域ルアンパバーンにおける町並み景観モニタリングのための VR パノラマの応用

横井 健太

本研究は、ラオス国の世界遺産地域ルアンパバーンにおける町並み景観の変化をモニタリングのための町並み景観表現技術を試行導入し評価すると同時に、その技術を用いたモニタリング手法の確立を目的とする。町並み景観表現技術の比較検討の結果、VR(バーチャルリアリティ)パノラマを用いた方法が最適であると判断された。そこで VR パノラマ技術を活用した Street-View(ストリートビュー)と名付けたバーチャルツアーを提案し、現地ルアンパバーンにおいて試行導入を行なった。有用性と持続可能性の側面から評価を行った結果、導入した VR パノラマを用いた方法は町並み景観のモニタリングに有効活用できることが判明した。同時に、作成方法に関する研修を適切に行うことで持続的な活用が可能であることが示唆された。

## 1. Introduction

Luang Prabang of Lao P.D.R. was inscribed in the list of World Heritage Site in 1995. Since its inscription, the heritage site has faced dramatic increase of tourists, changing along with rapid tourism development. The UNESCO/ICOMOS monitoring mission noted that if “the Lao traditional heritage continues its steady decline, the Town of Luang Prabang would be heading toward a situation that would justify World Heritage in Danger Listing” [1].

The Department of World Heritage Luang Prabang (DPL) has a responsibility to monitor and manage townscape, in Luang Prabang. Tokyo Tech has been collaborating with DPL in introducing applicable ICT tools for effective management of heritage site since 2003. Local needs assessment identified that there are needs to introduce townscape visualization technology for monitoring and to establish a townscape monitoring procedure from a long-term viewpoint.

Responding to the needs assessment, this research aims to introduce and evaluate applicable and sustainable townscape visualization technology in Luang Prabang. It also aims to establish a townscape monitoring procedure using selected townscape visualization technology.

## 2. Selection of townscape visualization technology

Based on a field survey on existing technologies in DPL, comparative analysis on applicable technologies was conducted between Virtual Reality (VR) panorama and two types of 3D computer graphics, namely 3D modeling and 3D measurement.

VR panorama is panoramic images providing a realistic visualization to all angles from static viewpoints. It establishes a virtual scene through real photos. It can display spherical panoramas format, which refers to 360° in the horizontal direction and 180° in the vertical direction [2]. This technology is becoming quite popular by Google Street View [3].

3D modeling is 3D models created by computer graphics in virtual reality environment. Buildings and exist urban space can be visualized and stored in a computer. Townscape simulation is available with feature of moving view point and editing 3D model [4].

3D measurement is 3D models created by laser range sensor such as air-borne laser-profiler or laser range sensor [5] [6]. It is possible to create precise 3D models and large quantities at one time. However, equipment cost and

maintenance knowledge are required.

As a result, considering feasibility and sustainability, VR panorama was identified as the most applicable technology in Luang Prabang. There are three major reasons for this selection. First, immersive scene can be experienced as a virtual tour. This virtual tour is developed from multiple VR panoramas. Immersion affects understanding and image sharing of the townscape changes. Second, VR panorama requires less knowledge and training. Since VR panorama can be produced by digital single-lens reflex (SLR) camera which is used by DPL staff members daily, it takes less time to master creating skills. If producing VR panorama was easy for staff members, more staff members can join monitoring work using VR panorama. Third, its equipment for VR panorama involves relatively low cost compared to 3D computer graphics. This is important particularly for its feasibility and sustainability.

## 3. Overview of research

Fig. 1 shows the overview of this research, which consists of five steps.

First, survey on current townscape monitoring method was conducted to clarify the monitoring issues. Interviews were conducted at Authorization Unit, Urban Planning Unit as well as with local ICT team. In addition, the author observed fieldwork of Authorization Unit and Urban Planning Unit.

Second, Street-View prototype which is one kind of virtual tour composed by multiple VR panoramas was introduced. This step was composed of four activities: 1) selection of pilot site; 2) comparative analysis for technology of VR panorama; 3) training for creation of Street-View; and 4) development of the prototype.

Third, the townscape monitoring procedure using the prototype was developed. To establish the effective townscape monitoring procedure, it is necessary to share the important townscape elements to preserve unique townscape of Luang Prabang among DPL staff members. Therefore, important townscape elements were extracted using the prototype. Extracted townscape elements were used to lay out indicators for monitoring.

Forth, the case trials and the interviews were conducted to evaluate the prototype as monitoring tool. Case trial is one of evaluation method to identify the advantages and issues of the produced Street-View prototype. Participants were asked to perform the tasks



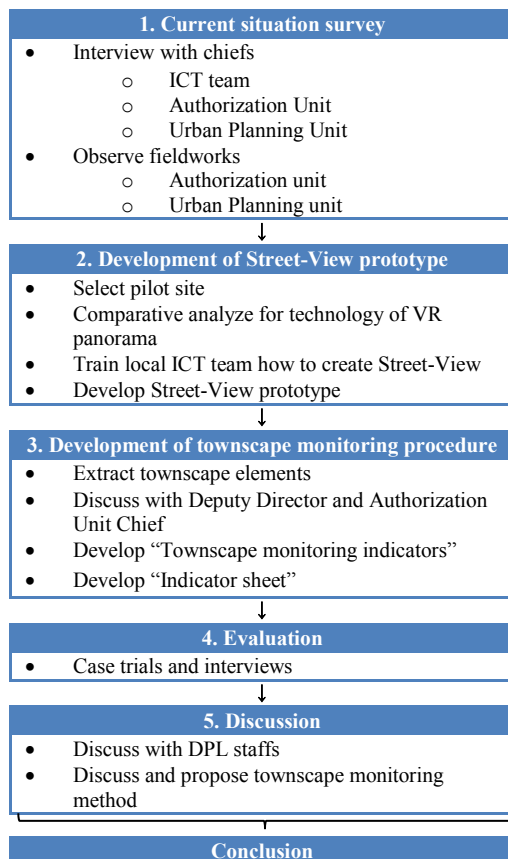


Figure 1 Overview of research  
Source: created by author, 2012

related to townscape monitoring with the prototype and the author observed its process.

Fifth, based on the process of the prototype development and evaluation results, townscape monitoring procedure was discussed.

#### 4. Analysis on current townscape monitoring method

The issues of current townscape monitoring method in DPL could be summarized in the following four points. First, DPL does not have comprehensive townscape monitoring method. Each unit conducts different field survey to monitor townscape independently. Second, the townscape elements required to preserve the unique townscape of Luang Prabang are not shared among DPL staff members. Points of focus are different for each unit and not shared between DPL staff members. Third, there are differences in the level of understanding of the heritage preservation master plan (PSMV). The PSMV is a document that provides comprehensive guideline to regulate building construction among staffs. Understanding of the PSMV content is vital for monitoring. Forth, there is lack of staff members. All units have multiple tasks at one time and all unit chiefs complained about lack of staff members. This issue is important to be considered to develop effective townscape monitoring procedure.

#### 5. Development of Street-View prototype

The author and local staff members developed a prototype of Street-View, which enables users to take virtual tour in order to examine its usability and sustainability. Multiple

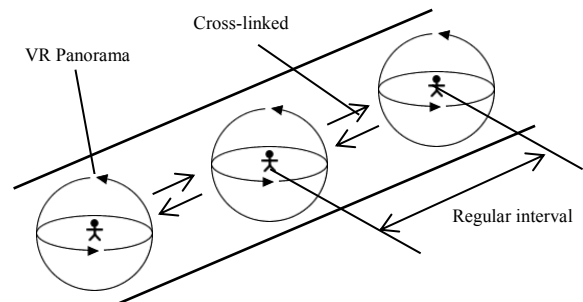


Figure 2 Concept of Street-View  
Source: created by author, 2012

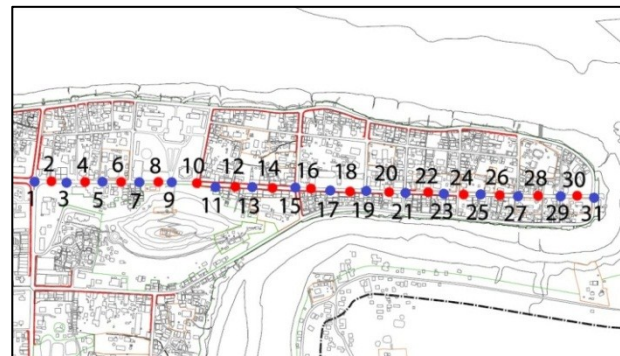


Figure 3 Shooting locations of the Street-View prototype  
Source: Heritage Preservation and Development Master Plan, 2001, p.12

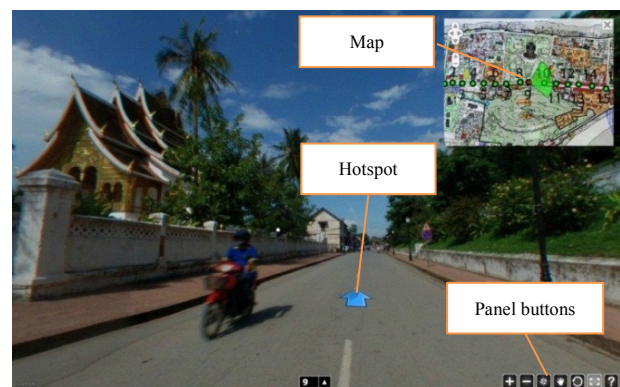


Figure 4 Interface of the Street-View prototype  
Source: the Street-View prototype, created by local ICT team and author, Luang Prabang, 2012

VR panoramas created at a few meters intervals are cross-linked each other (Fig. 2).

The main road in the core heritage zone (1.5 km) was selected for pilot site, since this area has many types of architectures and plans to improve for better townscape (Fig. 3). A total number of 31 VR panorama photos were taken at 50 meter intervals, covering 1.5 km of the main road.

Development of the prototype consists of three steps: 1) shooting four directions of photos with fish-eye lens and digital SLR camera; 2) stitching by software; and 3) authoring by software. Hugin was used for stitching [7]. SaladoPlayer, SaladoConverter and SaladoConfigurator were used for authoring [8] [9] [10]. All software used were free open source software. Training on how to create Street-View was conducted for local DPL staff members.

Before developing the prototype, important functions were discussed. Showing map to navigate desired VR panorama was identified as one of the functions needed to monitor townscape, and thus, the following functions were



equipped: 1) control zoom in/out with mouse, panel button and keyboard; 2) control viewing direction with mouse, panel button and keyboard; 3) select desired spot from map; and 4) move to next spot with hotspot.

Fig. 4 shows interface of the prototype. Map of the PSMV was used in the prototype. In this map, preservation level of buildings and regulations of land use are shown by colors and symbols. These information are important for monitoring.

## 6. Development of townscape monitoring procedure

### 6.1. Creating “Townscape monitoring indicators”

Using Street-View prototype, the important townscape elements were extracted together with the Deputy Director and Authorization Unit Chief. The townscape elements are considered as indicators for townscape monitoring.

First, Authorization Unit Chief identified the important townscape elements from every spots by examining the prototype, following rules and regulations described in the PSMV. Then, the townscape monitoring indicators were created through discussions. The “townscape monitoring indicators” provides 12 types of townscape elements which should be checked when monitoring with Street-View. The indicators are classified into five categories: 1) prescription on buildings and spaces; 2) plantations; 3) appearance of buildings; 4) parking situation; and 5) service by networks.

### 6.2. Creating “Indicator sheet”

Following identification of townscape monitoring indicators, the concrete indicator sheets were created for every spots in the Street-View prototype.

Fig. 5 shows an example of spot No. 1. This spot is the biggest traffic intersection and 13 kinds of indicators were identified. This sheet has equirectangular image of the spot, a list of indicators, a map of the area and dates that photos were taken. Map in the PSMV was used, following the Street-View prototype. The map shows, preservation level of buildings and regulations of land use by colors and symbols.

### 6.3. Townscape monitoring procedure with indicators and Street-View

Townscape monitoring procedure using the indicators and Street-View was established. This procedure has three major steps as bellow:

- 1) Check indicators and regulations
  - 1-1. Check indicators at the desired spot to monitor using the “Indicator sheet.”
  - 1-2. Check where the regulation is described in the PSMV using the “Townscape monitoring indicators” sheet.
  - 1-3. Check regulations referring to the PSMV.
- 2) Check townscape using Street-View
  - 2-1. Open the spot using Street-View.
  - 2-2. Check the situation through the visualized townscape.
- 3) Evaluate the townscape
 

Compare the visualized townscape in Street-View and the PSMV regulations to evaluate the townscape of the selected spot. If there are problems, think about a plan or direction to modify the issue.

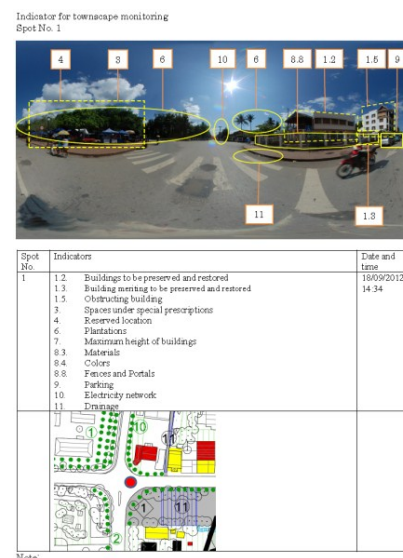


Figure 5 Indicator Sheet on spot No. 1

Source: Indicator sheet, created by author, Luang Prabang, 2012

By using the procedures illustrated above, if the monitors encounter the gap between the conditions shown in Street-View and the PSMV, such gaps can be submitted for discussion at DPL.

## 7. Evaluation analysis

To evaluate the Street-View prototype as a townscape monitoring tool, case trials and interviews were conducted. Further, the townscape monitoring procedure was also examined through evaluations.

Case trial is an evaluation method to identify the advantages and points of improvement of the prototype. Participants were asked to perform the tasks of monitoring with the prototype and the author observed its process. Four tasks to check following important indicators were prepared: 1) prescription of buildings; 2) external aspect; 3) parking; and 4) electricity network. In addition, interviews were conducted after case trials to supplement case trials observation. Five users were selected from each unit in DPL: two members from Authorization Unit; two from Urban Planning Unit; and one from local ICT team.

### 7.1. Positive findings of Street-View prototype

Based on the case trial and interview results, four positive findings of Street-View prototype were identified.

First, user-friendly operation enables users with different experiences and backgrounds to use the Street-View. Participants were able to understand the prototype's operation after a brief explanation of the prototype given before the case trial and accomplished their tasks without difficulty. User-friendly operation is important for different people to participate in townscape monitoring work, especially in circumstances when human resources are limited. This advantage allows the Street-View to overcome the problem of a lack of human resource in DPL.

Second, Street-View makes it possible to share townscape information among DPL and contribute to analyze townscape changes. Street-View can store data of visualized townscape information. By comparing the stored data and PSMV, people can evaluate and analyze the townscape. Furthermore, stored data enables DPL staff

members to formulate a common understanding of townscape information. In the future, a chronological analysis of townscape changes would be possible by accumulating data using Street-View.

Third, Street-View can be utilized as a communication tool for relevant organizations and the local residents. It was suggested in interviews that the Street-View is useful to explain the need to preserve sites with images of good quality and to build a consensus among relevant organizations and the local residents. The Street-View's actual usage as a communication tool should be investigated in the future.

Forth, Street-View meets the need for townscape monitoring through its major functions. The major functions of Street-View are as follows: 1) it can control viewing direction; 2) it enables to zoom in/out; and 3) it can provide virtual tours using hotspot links. The case trial and interviews made it clear that these major functions work effectively for townscape monitoring.

## 7.2. Points of improvement of Street-View

Four aspects of Street-View prototype were identified for further improvement.

First, blind spots reduce the utility value of the Street-View because they hide information that users want to see. There are two factors that cause blind spots. The first is unexpected obstacles, such as cars and motor bikes, coming into the image when taking photos. The second is the fact that the Street-View is unable to capture the buildings and other objects as they exist between shooting intervals. The former factor can be solved by placing extra attention on unexpected obstacles, while the latter can be solved by shortening photograph intervals; however, this takes longer for shooting and stitching.

Second, low resolution images reduce the utility value of Street-View more than expected. The prototype includes several low resolution images and it was difficult to confirm details even with zooming function for particular objects and places. This is due to human error in failing to check the resolution of an image when taking photos. More training on photo taking with specific objectives for townscape monitoring would help solve this problem.

Third, map function of the prototype was found difficult to check building attributes. The prototype has a map function with two objectives. The first is to move to the desired spot for monitoring. The second is to check a building's attributes as defined by the PSMV. The first objective functions effectively. However, the second objective was not achieved because the prototype has a small map size, preventing the users from checking the detailed information on the maps. To utilize the map function effectively, it is necessary to improve it with a proper size and better quality resolution.

Forth, despite user-friendly characteristics, interviews revealed that the prototype does not have a specific user guide. According to Nielsen [11], a user guide can reduce the burden of memorizing how to use a system from an interface usability aspect.

## 7.3. Analysis of townscape monitoring procedure

The monitoring steps illustrated in 6.3 were used in the case trials. The results of the case trials and interviews

identified several issues regarding the townscape monitoring procedure.

First, the indicator sheet should be accompanied with explanation for the users to fully understand its procedure. It is important that what and how to be monitored for each monitoring spot are clearly shared among staff members. Therefore, the indicator sheet should contain descriptions of the indicators at each spot and detailed the monitoring procedures for those spots. Second, understanding level of the PSMV should be promoted. Indicators for monitoring are based on the rules and regulations identified in PSMV. Street-View cannot be utilized effectively without solid knowledge of such rules and regulations. Third, training on townscape monitoring procedures is necessary. Participants were given a brief training on how to use the townscape monitoring indicators, and it was found useful. For implementing full monitoring of the townscape changes, extended training for the users would become vital.

## 7.4. Sustainability of Street-View as monitoring tool

Sustainability of Street-View was discussed from the aspects of required skills and equipment costs. As for the required skills, without advanced technical background, it was found easy for staff members to create Street-View as long as trainings were well-planned and properly conducted. As for the equipment costs, it does not require costly equipment to create/operate Street-View. For these reasons, it can be said that Street-View has a high level of sustainability in Luang Prabang.

## 8. Conclusion

This research developed a townscape monitoring tool using Street-View prototype, which composed by multiple VR panoramas as a townscape visualization technology. Further, townscape monitoring procedure was developed. Evaluation revealed that Street-View can be utilized to monitor townscape changes and further to share important information. Several improvements to avoid blind spots and low resolution of photo were discussed for further improvement. Street-View could be utilized in the future for townscape monitoring in Luang Prabang as long as trainings are well-planned and properly conducted.

## References

- [1] UNESCO, ICOMOS, "Reactive Monitoring Mission to the Town of Luang Prabang World Heritage Property Lao People's Democratic Republic", 2007
- [2] C Deng, et al., "Integration of Web2.0, Panorama Virtual Reality and Geological Information System", Fourth International Conference on Computer Sciences and Convergence Information Technology, pp. 1625-1628, 2009
- [3] Google Maps Street View, <http://google.com/streetview/>. (accessed on Oct. 21, 2012)
- [4] K Ono, et. al., "3DCG Reconstitution and Virtual Reality of UNESCO World Heritage in Danger: the Citadel of Bam", Progress in Informatics, No. 5, pp. 99-136, 2008
- [5] K Yano, et. al., "Virtual Kyoto: 4D GIS Comprising Spatial and Temporal Dimensions", Journal of Geography, 117(2), pp. 464-478, 2008
- [6] K Ikeuchi, et. al., "Flying Laser Range Sensor for Large-Scale Site-Modeling and Its Applications in Bayon Digital Archival Project", International Journal of Computer Vision, 78, 2-3, pp. 207-222, 2008
- [7] Hugin - Panorama photo snitcher, Online, Available: <http://hugin.sourceforge.net/> (accessed on Jan. 14, 2013)
- [8] SaladoPlayer, Online, Available: <http://panozona.com/wiki/SaladoPlayer> (accessed on Dec. 18, 2012)
- [9] SaladoConverter, Online, Available: <http://panozona.com/wiki/SaladoConvertorn> (accessed on Dec. 18, 2012)
- [10] SaladoConfigurator, Online, Available: <http://panozona.com/wiki/SaladoConfigurator> (accessed on Dec. 18, 2012)
- [11] J Nielsen, "Usability engineering", Morgan Kaufman, 1993

# Equilibrium extraction of light rare earth metals with PC-88A as extractant

Student Number: 11M18195 Name: Naoto YOSHIMURA Supervisor: Ryuichi EGASHIRA

## PC-88Aを抽出剤とした軽希土類金属の平衡抽出

吉村 直人

軽希土類金属としてランタン及びセリウム，抽出剤としてPC-88A，希釈剤としてSolvesso150または灯油を用い，金属濃度、原料水溶液相中の $pH$ を変化させて液液平衡抽出を測定した。両金属イオンは溶媒相中に抽出され，ランタンに比較してセリウムの抽出率は高く，溶媒抽出によりセリウムとランタンを分離できることを確認した。水溶液相中の $pH$ の増加および抽出溶媒相中の未反応の抽出剤濃度の増加とともに，金属の抽出溶媒相への分配比は増加した。Solvesso150に比較して灯油を溶媒とした場合，両金属の分配比は大きかったが，分離係数は同程度であった。抽出溶媒相中の未反応抽出剤濃度が高い条件を除いて抽出平衡は報告されている反応式に従った。

### 1. Introduction

Rare earth (RE) metals which possess physically and chemically specific properties are applied in many fields of advanced technology such as magnets, ceramics, electronics, nuclear technology and so on. [1] It is difficult to separate RE metals, since RE metals has the similar chemical nature because of same electric configuration of outermost husks, and all RE metals generally form trivalent cations.

In recent years, demand of RE metals is increasing with development of a high-tech industry. However, supply of RE metals depends strongly on limited area, it is difficult to maintain a stable RE metals supply and price of RE metals are increasing. On the other hand, RE metal deposits are very common, but mineral deposits of RE metals in another area have not been exploited. To maintain a stable RE metals supply, in the present, the Japanese government pushed exploitation of mineral deposits of RE metals in another area and establishment of enrichment plant of RE metals is estimated.

Solvent extraction is presently one of the major techniques on industrial scale for the separation of RE metals. 2-ethylhexyl phosphonic acid mono-2-ethylhexyl ester (PC-88A) is an acidic organophosphorus extractant and has been widely used in solvent extraction of lanthanides industry for the separation and purification of the metal ions.

In separation process of RE metals, most of the RE metals are separated by solvent extraction and only cerium (Ce) is recovered by precipitation. The extraction equilibrium of Ce is not fully studied relative to other RE metals.

A number of fundamental studies of RE solvent extraction have been carried out under low metal concentrations and relatively low extractant concentration. However, practical metal extraction on a commercial scale is usually conducted under high concentrations of metal extractant. There are not many studies on extraction equilibrium analysis of RE metals in high metal concentration and high extractant concentration. Nakamura used lanthanum (La) hydroxide,  $La(OH)_3$ , as a solute and measured that the

effect of extractant concentration on extraction equilibrium. [2] Mori et al. reported that in the region of high extractant concentration, the extraction reaction was quite different from those in the region of relatively low extractant concentration. [3]

In this study, La and Ce were selected from the RE metals. La is neighboring element of Ce in periodic table and well-studied elements in solvent extraction of RE metals. The extraction equilibrium of La and Ce with PC-88A were studied under various conditions.

### 2. Experimental

**Table 1** shows the experimental conditions of solvent extraction of La and Ce by PC-88A.  $La(NO_3)_3$ ,  $La(OH)_3$  and  $Ce(NO_3)_3$  were used as sources of metal ions. Solvesso150 or kerosene was used as a diluent. Solvesso150 is one of the petroleum fractions and contains a high proportion of aromatic hydrocarbons. Kerosene is one of the petroleum fractions and contains a high proportion of alkane. To adjust the  $pH$ , solutions of NaOH and  $HNO_3$  were added to the extraction system. The initial concentrations of metal and extractant were changed.

Same volumes (20ml) of the organic and aqueous solution were poured into a 50ml conical flask with screw cop, and stirred with magnetic stirrer for 24h at  $298 \pm 3K$  to attain equilibrium. The two phases were then separated by a separating funnel and RE metal concentrations of the aqueous solutions were analyzed by ICP-AES. The metal complex concentration of organic solutions was calculated by material balance. The  $pH$  values of the aqueous solutions were measured by  $pH$  meter. In this study, the effect of ionic strength of the aqueous solutions on the extraction equilibrium was not considered.

### 3. Results and Discussion

#### 3.1 Precipitation of solid phase and oxidization of Ce

**Figure 1** shows the photographs of the organic and aqueous solutions in separating funnels. When  $La(OH)_3$  was used with relatively high metal

Table 1 Experimental condition of solvent extraction of La and Ce by PC-88A

Aqueous feed phase		Aqueous solution of	
		La(NO <sub>3</sub> ) <sub>3</sub> , La(OH) <sub>3</sub> , Ce(NO <sub>3</sub> ) <sub>3</sub>	
Volume of aqueous feed phase	$V_{aq} [m^3]$		$2.0 \times 10^{-5}$
Concentration of metal in aqueous feed phase	$[M^{3+}]_0 [kmol \cdot m^{-3}]$		$2.5 \times 10^{-4} - 0.215$
Initial pH (Adjusting by HNO <sub>3</sub> or NaOH)	$pH_0 [-]$		1 – 13
Organic solvent phase PC-88A diluted by Solvesso150 or kerosene			
Volume of organic solvent phase	$V_{org} [m^3]$		$2.0 \times 10^{-5}$
Concentration of PC-88A in organic solvent phase	$[(RH)_2]_0 [kmol \cdot m^{-3}]$		0.06-0.5
Stirring time	$t [h]$		24
Temperature	$T [K]$		$298 \pm 3$

concentration, the solid particles were precipitated in the organic phase to be turbid. [4] When La(NO<sub>3</sub>)<sub>3</sub> or Ce(NO<sub>3</sub>)<sub>3</sub> was used, the solid phase didn't appeared in all cases. When NaOH solution was used to adjust pH in cases with Ce(NO<sub>3</sub>)<sub>3</sub>, the color of both phase changed from colorless to yellow. Since the colors of the solutions containing trivalent and tetravalent Ce are colorless and yellow, respectively, increasing pH made Ce oxidized from trivalent to tetravalent. To prevent oxidization of trivalent Ce, NaOH solution was added to extraction system at contact of solvent phase and aqueous phase. Therefore, it was considered that quantity of oxidized Ce was small and tetravalent Ce wasn't considered.

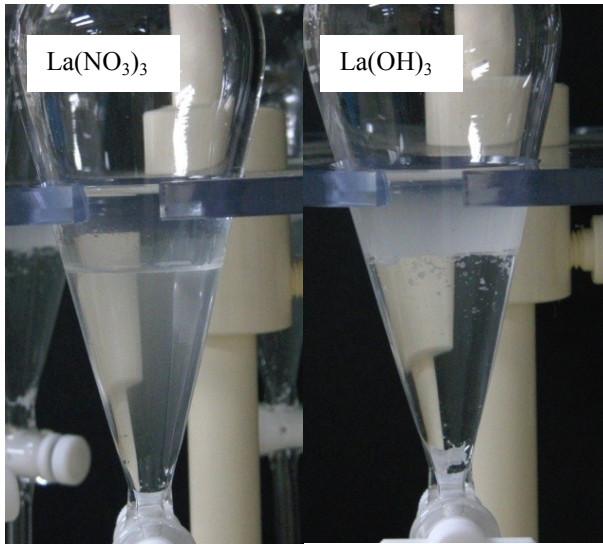
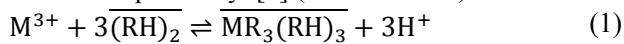


Fig. 1 Photographs of the organic and aqueous solutions in separating funnel

### 3.2 Distribution ratio

In previous studies, the cation exchange reaction has been reported by: [5] (M= RE metal)



$$K_1 = \frac{[MR_3(RH)_3][H^+]^3}{[M^{3+}][(RH)_2]^3} \quad (2)$$

Distribution ratio,  $D$ , is defined by:

$$D = \frac{[MR_3(RH)_3]}{[M^{3+}]} \quad (3)$$

Figures 2 and 3 show that the effect of pH on  $D$  of La and Ce, respectively. RE metals were extracted to the solvent phase and  $D$  of Ce was higher than that of La. Ion radius decreases with an increase of atomic number in lanthanide, and the metal ion of smaller ion radius is easy to make a metal complex because of increase of charge density in the ion[6]. Then Ce was more preferably extracted than La.  $D$  of RE metal increased with pH.

$D$  was larger with kerosene than that with Solvesso150.  $D$  with La(NO<sub>3</sub>)<sub>3</sub> was approximately equal to  $D$  with La(OH)<sub>3</sub> except for the case that solid phase was precipitated. When the system contained both of Ce and La,  $D$  with binary metal system was approximately equal to that with single metal system.

Solute	Diluent	
M(NO <sub>3</sub> ) <sub>3</sub>	Solvesso150	▲
M(NO <sub>3</sub> ) <sub>3</sub>	Kerosene	◆
M(OH) <sub>3</sub>	Solvesso150	▲
La(NO <sub>3</sub> ) <sub>3</sub> + Ce(NO <sub>3</sub> ) <sub>3</sub>	Solvesso150	▲

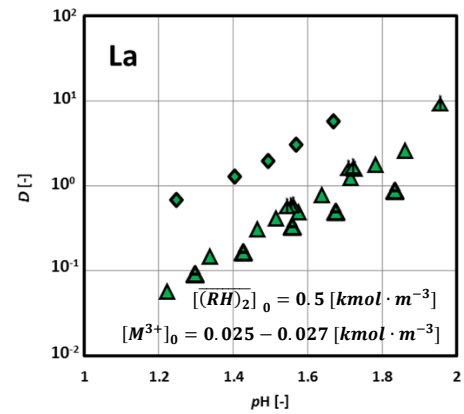


Fig. 2 Effect of pH on the distribution ratio of La

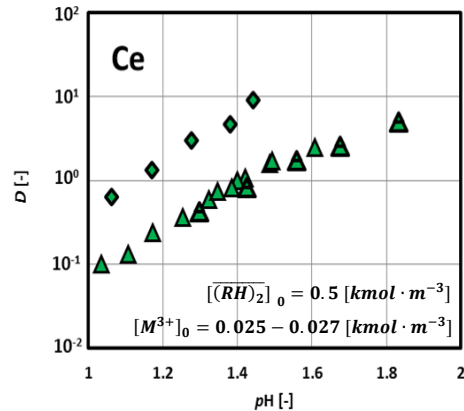


Fig. 3 Effect of pH on the distribution ratio of Ce

From Eq. (2) and Eq. (3),  $D$  is expressed by:

$$D = K_1 \frac{[(RH)_2]^3}{[H^+]^3} \quad (4)$$

Figures 4 and 5 show that the effects of pH on  $D$ s of La and Ce, respectively.  $D$  decreased with an increase in initial metal concentration. With the results in which the initial extractant concentrations were fixed as  $0.5 kmol \cdot m^{-3}$ , the unreacted extractant concentration

decreased with the initial metal concentration at same pH value. Accordingly  $D$  increased with the unreacted extractant concentration, as expressed in Eq.(4).

Solute	$[M^{3+}]_0$ [kmol·m <sup>-3</sup> ]	
$M(NO_3)_3$	$2.5 \times 10^{-4}$	▲
$M(NO_3)_3$	0.005	▲
$M(NO_3)_3$	0.027	▲
$M(NO_3)_3$	0.055	▲
$M(NO_3)_3$	0.11	▲
$M(NO_3)_3$	0.215	▲
$M(OH)_3$	0.025	▲
$La(NO_3)_3 + Ce(NO_3)_3$	0.027(respectively)	▲

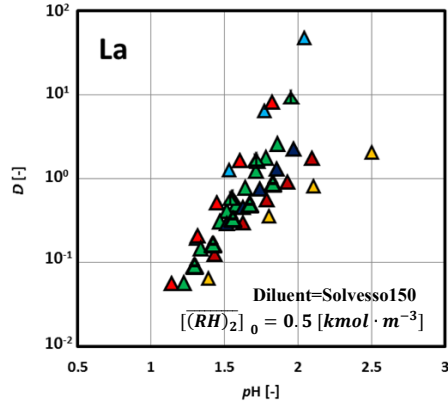


Fig. 4 Effect of pH on the distribution ratio of La

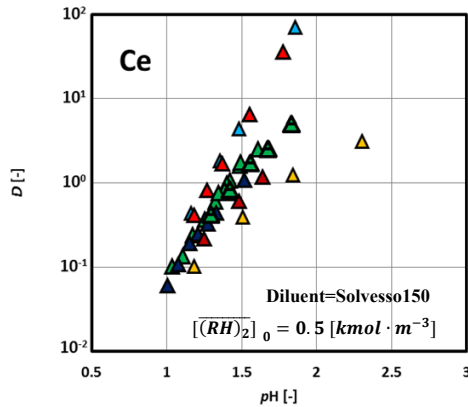


Fig. 5 Effect of pH on the distribution ratio of Ce

### 3.3 Effect of Na on the extraction of La and Ce

PC-88A makes metal complexes with wide variety of metals. The effect of sodium (Na) on the extraction of La and Ce were investigated. The distribution ratio of sodium,  $D$  of Na, is defined by:

$$D = \frac{[NaR(RH)]}{[Na^+]} \quad (5)$$

Figure 6 shows that the effect of pH on  $D$  of Na. Sodium formed metal complexes with PC-88A in the pH range more than 5[7]. The extraction of La and Ce were measured in the pH range from 1 to 2.5.  $D$  of Na is very small in the pH range, and the effects of Na on the extraction of La and Ce might to be small.

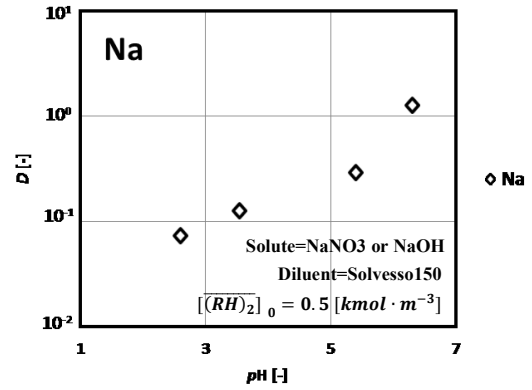


Fig. 6 Effect of pH on the distribution ratio of Na

### 3.4 Effect of $[(HR)_2]$ on $D \cdot [H^+]^3$

Eq. (2) is expressed as below:

$$D \cdot [H^+]^3 = K_1 \cdot [(RH)_2]^3 \quad (6)$$

If the extraction reaction should follow the reaction of Eq. (1),  $D \cdot [H^+]^3$  is proportional to the third power of unreacted extractant concentration. Figures 7 and 8 show that the effect of unreacted extractant concentration on  $D \cdot [H^+]^3$  of La and Ce, respectively. Plots in relatively low unreacted extractant concentration agreed with the line whose slope was 3, but the plots in high unreacted extractant concentration were deviated from the line. This indicated that the extraction reaction should not follow the reaction of Eq. (1) and the additional reaction might occur. It has been reported that in the higher range of extractant concentration, the reaction should require the dimeric species of extractant more than 3 to form complex in the organic phase[3]. In this study, the extraction reaction was not fully clarified in high extractant concentration region.

Solute	$[M^{3+}]_0$ [kmol·m <sup>-3</sup> ]	$[(RH)_2]_0$ [kmol·m <sup>-3</sup> ]	
$M(NO_3)_3$	$2.5 \times 10^{-4}$	0.5	▲
$M(NO_3)_3$	0.005	0.5	▲
$M(NO_3)_3$	0.027	0.5	▲
$M(NO_3)_3$	0.055	0.5	▲
$M(NO_3)_3$	0.11	0.5	▲
$M(NO_3)_3$	0.215	0.5	▲
$M(OH)_3$	0.025	0.5	▲
$La(NO_3)_3 + Ce(NO_3)_3$	0.027(respectively)	0.5	▲
$M(NO_3)_3$	0.055	0.06, 0.08, 0.1, 0.3	■

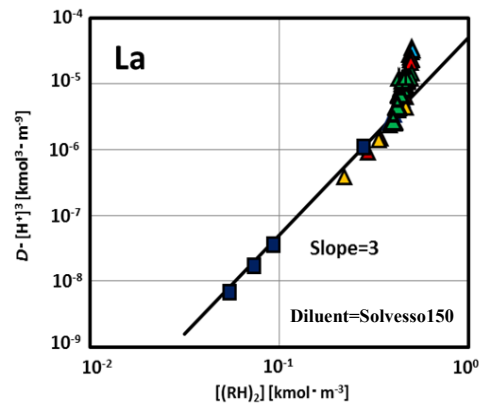


Fig. 7 Effect of  $[(HR)_2]$  on  $D \cdot [H^+]^3$  of La



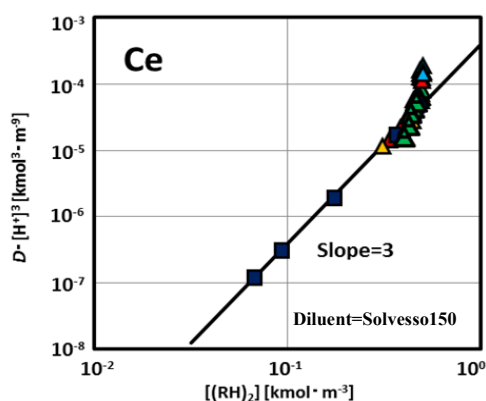


Fig. 8 Effect of  $[(\text{RH})_2]$  on  $D \cdot [\text{H}^+]^3$  of Ce

### 3.5 Extraction equilibrium constant

Table 2 shows the extraction equilibrium constants of La and Ce.  $K_1$  could be obtained by the intercepts of the line whose slopes were 3 in Fig. 7 and Fig. 8.  $K_1$  of Ce was larger than that of La.  $K_1$  with kerosene was larger than that of Solvesso150.

Table 2  $K_1$  of La and Ce

Diluent	La	Ce
Solvesso150	$5.0 \times 10^{-5}$	$4.0 \times 10^{-4}$
Kerosene	$4.7 \times 10^{-4}$	$3.5 \times 10^{-3}$

### 3.6 Separation Factor

Separation Factor,  $\beta$ , is defined by:

$$\beta = \frac{D_{\text{Ce}}}{D_{\text{La}}} = \frac{K_{1,\text{Ce}}}{K_{1,\text{La}}} \quad (7)$$

Table 3 shows the separation factor.  $\beta$  is calculated by using  $K_1$  of La and Ce.  $\beta$  with Solvesso150 was approximately equal to that with kerosene.

Table 3 Separation factor,  $\beta$

Diluent	Separation factor, $\beta$
Solvesso150	7.94
Kerosene	7.59

## 4 Conclusion

Rare earth metals were extracted to the solvent phase and cerium was more preferable extracted than lanthanum. The distribution ratio increased with  $pH$  and unreacted extract concentration.

Effect of difference of diluent on the distribution ratio was observed, but effect of difference of diluent on the separation factor was not observed.

Effect of difference of anion ion of solute on the distribution ratio was not observed.

In the distribution ratio of both rare earth metals, the distribution ratio with binary metal system was approximately equal to distribution ratio with single metal system.

The extraction equilibrium was followed the reaction reported in previous studies except in high extractant concentration.

## Acknowledgement

PC-88A was supplied by daihachi chemical

industry corporation. .

## Nomenclature

$\beta$	=separation factor	[-]
$D$	=distribution ratio	[-]
$(\text{RH})_2$	=dimeric species of extractant	[-]
[ ]	=molarity of the species in the bracket	[kmol · m <sup>-3</sup> ]
$K_1$	=extraction equilibrium constant	[-]
<Subscripts>		
0	=aqueous or organic feed solution	
aq	=aqueous phase	
org	=organic phase	
M	=Rare earth metal	
Na	=Sodium	
La	=Lanthanum	
Ce	=Cerium	
<Superscripts>		
—	=organic phase species	

## References

- [1] S.Radhika,B.Nagaphani Kumar,M.Lakshmi Kantam, B Ramachandra Reddy, Liquid-Liquid extraction and separation possibilities of heavy and light rare-earths from phosphoric acid solutions with acidic organophosphorus reagents, Separation and Purification Technology, 75(2010)295-302
- [2] Kazuma Nakamura, Effect of operating condition on solvent extraction of La with PC-88A, Bachelor Thesis, Tokyo Tech (2012)
- [3] Yasushige Mori, Hitoshi Ohya, Haruhiko Ono, Wataru Eguchi ' Extraction equilibrium of Ce(III), Pr(III) and Nd(III) with acidic organophosphorus extractants' Journal of Chemical Engineering of Japan Vol.21 No.1 (1988) 86-91
- [4] Yoshiyuki Hirashima, Hideaki Koderu, Jiro Shiokawa, Extraction of Lanthanoids with Bis(2-ethylhexyl) Hydrogenphosphate, The Chemical Society of Japan 4(1982) 627-631
- [5] Fu Mian-xin, Sui Zhi-tong, Mikiya Tanaka, Equilibrium analysis of solvent extraction of yttrium and europium from hydrochloric acid with P<sub>507</sub>, Transactions of Nonferrous Metals Society of China 21(2011) 2093-2098
- [6] KazukoMatsumoto 'kidoruigensonokagaku' Asakurasyoten (2008) 53-57
- [7] Annual report of National Institute of Advanced Industrial Science and Technology (2008) 557-558

# Optimal Design and Control of a Buck Converter Used for Energy Harvesting

Student Number: 11M18203 Name: Jiawei WANG Supervisor : Kunio TAKAHASHI

## エネルギーハーベスティング用降圧コンバータの最適な設計及び制御方法

王 佳偉

エネルギーハーベスティングには、エネルギー効率の観点からキャパシタが蓄電デバイスとして検討されている。キャパシタを電源として使用する場合、一定電圧を供給するためには降圧コンバータが必要である。本論文では、線形近似回路を用いて降圧コンバータの電流挙動、効率について解析し、回路と制御パラメータの決め方を示した。理論的な検討に基づいて、キャパシタに蓄えた電力で照明用 LED の点灯する検証実験を行った。

### 1 Introduction

Recently, Energy Harvesting has been widely noticed in the world. Energy Harvesting is the technology of accumulating and storing some energy which is not used surrounding us for later use. In our lab, the energy which is too small to be used directly is defined as tiny electric energy. And in order to charge the tiny electric energy into the capacitor efficiently, how to design and control a boost converter has been studied [1],[2].

When a capacitor is used as power source, a buck converter is necessary. In this case, unlike conventional buck converter, the output voltage is constant and the input voltage is variable. There are also some studies about buck converter with variable input [3], [4]. But in their studies, energy efficiency is not their main purpose. In the energy harvesting, energy efficiency is very important.

In this paper, how to design and control a buck converter when the capacitor is used as a power source is studied. In section 2, a model circuit is used to analyze current behavior and the energy efficiency for the buck converter. In section 3, a method of determining the circuit and controlling parameters is introduced. In section 4, experiment results are shown and in section 5 conclusions are presented.

### 2 Theoretical analysis of buck converter

In the design of buck converter, an analytic solution is useful. Here, an equivalent circuit as figure1(b) is used to analyze the current behavior of buck converter.

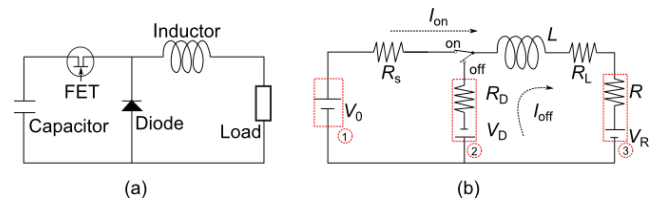


Figure 1 Buck converter and equivalent circuit

Buck converter consists of three components: FET, diode, inductor. The FET is controlled by PWM regulation, and  $T$  is the switching period. Duty ratio  $d = T_{on}/(T_{on} + T_{off}) = T_{on}/T$ , where  $T_{on}$  is the time for which the FET is on, and  $T_{off}$  is the time for which the FET is off. So the circuit's current behavior can be analyzed by considering two time intervals,  $T_{on}$  and  $T_{off}$ . The assumptions made for the analysis is:

- ① The capacitance is large enough, and the voltage of the capacitor can be regarded as constant in one switching period,  $T$ .
- ② Diode's forward voltage can be considered as  $v_f = V_D + R_D i$
- ③ Load has no imaginary part of impedance.  
(In the case of LED,  $v_f = V_R + R i$ )

According to load, the output current and max forward current can be considered as load parameters. And duty ratio and switching period can be considered as control parameters.

With the Kirchoff's voltage law, we can set up equations as:

$$V_0 - V_R = I_{on}R_{on} + L \frac{dI_{on}}{dt}$$

$$L \frac{dI_{off}}{dt} - (V_D + V_R) = I_{off}R_{off}$$

Where,  $R_{on} = R_s + R_L + R$ , and  $R_{off} = R_D + R_L + R$ . With the condition of continuous current and the initial condition, the solution of equations can be obtained.

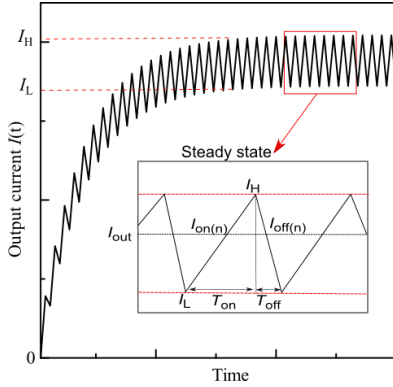


Figure 2 Output current of buck converter

At the steady state, the peak output current is described as  $I_H$  and  $I_L$ , the average output current is described as  $I_{out}$ .

$$I_H = \frac{A(e^{-\tilde{T}_{on}} - 1) - B e^{-\tilde{T}_{on}}(e^{-\tilde{r}\tilde{T}_{off}} - 1)}{(e^{-\tilde{T}_{on}} - \tilde{r}\tilde{T}_{off}) - 1}$$

$$I_L = \frac{A e^{-\tilde{r}\tilde{T}_{off}}(e^{-\tilde{T}_{on}} - 1) - B(e^{-\tilde{r}\tilde{T}_{off}} - 1)}{(e^{-\tilde{T}_{on}} - \tilde{r}\tilde{T}_{off}) - 1}$$

and

$$I_{out} = \frac{1}{T} \left\{ \int_{(n-1)T}^{(n-1)T+T_{on}} I_{on(n)} dt + \int_{(n-1)T+T_{on}}^{nT} I_{off(n)} dt \right\}$$

$$= \frac{1}{\tilde{T}} \left\{ (I_H - A)(1 - e^{-\tilde{T}_{on}}) + \frac{1}{\tilde{r}} (I_L + B)(1 - e^{-\tilde{r}\tilde{T}_{off}}) + A\tilde{T}_{on} - B\tilde{r}\tilde{T}_{off} \right\}$$

At here,

$$\tilde{r} = \frac{R_{off}}{R_{on}}; \tilde{T} = \frac{R_{on}}{L} T$$

$$\tilde{T}_{on} = \frac{R_{on}}{L} T_{on} = d\tilde{T}; \tilde{T}_{off} = \frac{R_{on}}{L} T_{off} = (1-d)\tilde{T}$$

$$A = \frac{V_0 - V_R}{R_{on}}; B = \frac{(V_D + V_R)}{R_{off}}$$

In this paper, the energy efficiency of the buck converter is defined for one switching period at steady state:

$$\eta = \frac{P_{on} + P_{off}}{P_{in}}$$

Where  $P_{on}$  and  $P_{off}$  is the energy consumption in resistance  $R$  when FET is on/off,  $P_{in}$  is the energy introduced from the capacitor to the buck converter for one switching period. With the analytic solution of the output current, energy efficiency  $\eta$  can be calculated. With this solution and the example specifications as figure 3, relationship between efficiency and switching frequency can be plotted like figure 4.

Inductor : $L=1[\text{mH}]$	$R_L = 0.39[\Omega]$
MOS FET : $R_s = 78[\text{m}\Omega]$	$V_{gs} = 5.0[\text{V}]$
Diode : $V_D = 0.3[\text{V}]$	$R_D = 0.2[\Omega]$

Figure 3 Example specifications for buck converter

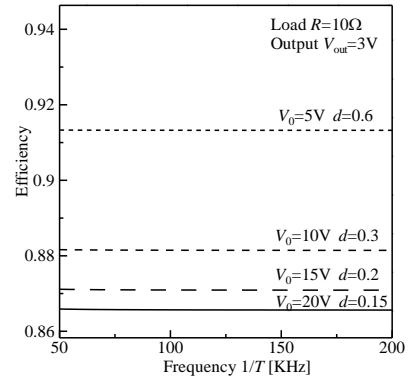


Figure 4 Relationship between energy efficiency and switching frequency

When the output and input voltage of the buck converter is given, the duty ratio can be determined. So the relationship between energy efficiency and switching frequency should only be considered.

From the figure 4, when input and output is given, the energy efficiency will be constant.

### 3 The method to determine control and circuit parameters

### 3-1 Duty ratio's determination

With the solution of current at steady state and the example specifications, the relationship between average output current and control parameters can be plotted as figure 5.

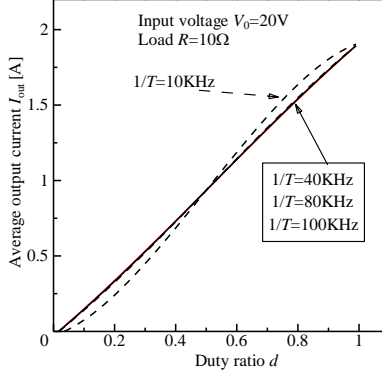


Figure 5 Relationship between output current and control parameters

From the figure 5, at some switching frequency area, the average output current can be obtained only by input voltage and duty ratio. And this switching frequency area is required for buck converter. So the duty ratio can be calculated as the following formula:

$$d = \frac{I_{out} + B\tilde{r}}{A + B\tilde{r}}$$

### 3-2 Switching frequency's determination

In this section, how to determine the switching frequency for buck converter is introduced. The output current and the peak output current of load  $R$  is given, the allowable range of ripple can be determined. As figure 6, The ripple current for buck converter can be defined as  $\Delta I = I_H - I_{out}$ .

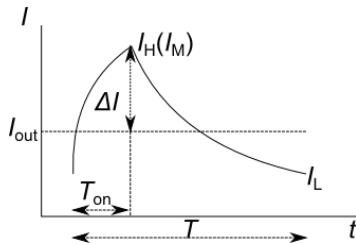


Figure 6 Output and ripple current

With the analytic solution of output current for buck converter, the ripple current can be calculated as

$$\Delta I = I_H - \frac{1}{T} \left\{ (I_H - A)(1 - e^{-\tilde{r}T_{on}}) + \frac{1}{\tilde{r}} (I_L + B)(1 - e^{-\tilde{r}T_{off}}) \right\} + Ad - B\tilde{r}(1 - d) = f(d, T)$$

With this solution and the example specifications, the relationship between ripple current and switching frequency is showed as figure 7.

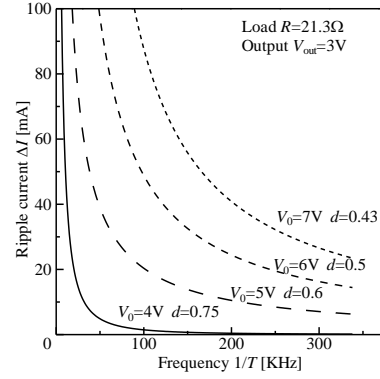


Figure 7 Relationship between ripple current and frequency

According to the output ripple, the necessary switching frequency range can be obtained with this result. In the definition of energy, the switching is not considered. But the relationship between switching loss and switching frequency is clear [2]. In the switching range calculated by allowable ripple current, in order to reduce switching loss, a lower switching frequency is should be selected.

### 3-3 Inductor's choosing

There are two modes of output current for buck converter: continuous mode and discontinuous mode. In this paper, continuous mode is only considered. The critical condition for continuous mode is that the current of inductor is zero ( $I_L = 0$ ).

When FET, inductor, diode are ideal parts, the energy loss for them can be neglected. So the output and input voltage can be calculated as

$$I_H - I_L = \frac{(V_0 - V_{out})}{L} T_{on} = \frac{V_{out}}{L} T_{off}$$

And

$$\frac{V_{out}}{V_0} = \frac{T_{on}}{T_{on} + T_{off}} = d$$

According to the critical condition, in order to have the output at continuous mode, the output current should satisfy the following conditions:

$$I_{out} \geq \frac{1}{2} \frac{(V_0 - V_{out})}{L} T_{on} \left( \text{or } \frac{V_{out}}{L} T_{off} \right)$$

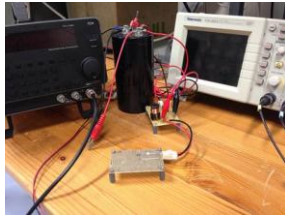
With the relationship between input and output, the critical condition can be calculated as

$$\frac{L}{T} \geq \frac{1}{8} \frac{V_0}{I_{out}}$$

When input voltage and output current is given, With this formula, inductor can be determined considering with the limit of switching frequency.

#### 4 Experiment result and discussion

In the experiment, A capacitor power source for LED lighting is used. With the dynamic input voltage of capacitor, a constant output current for LED lighting is obtained.



Inductor : Panasonic ELC18B102L	
$L : 1[\text{mH}]$	$R_L : 0.39[\Omega]$
MOS FET : TOSHIBA TPC 6006-H	
$R_s : 78[\text{m}\Omega]$	$V_{gs} : 9.0[\text{V}]$
Diode : TOSHIBA CMS16	
$V_D : 0.3[\text{V}]$	$R_D : 0.2[\Omega]$
Capacitor : BHC ALS30A224NP040	
$C : 0.22[\text{F}]$	
LED : SMLZ14WBECW1	
$V_F : 3.2[\text{V}]$	$I_F : 20[\text{mA}]$
Gate Driver : NF WF 1943	
Voltage Measure : GRATHTEC GL900	
AD/DA converter : DA12-16 (PCI)	

Figure 8 Experimental specifications for experiment

With the experimental specifications as figure 8, the voltage for capacitor is from 5V to 4V, and output current  $I_{out} = 9\text{mA}$ , switching frequency  $F = 110\text{KHz}$ , the experiment for LED lighting is conducted, And the result is obtained as figure 9.

From the result of the experiment, a constant output voltage is obtained with a dynamic input voltage. And the output voltage is consisted with the theoretical value. But the output current is different from the theoretical value. At here, LED's voltage is also considered with a linear approximation as diode. in the case of LED, in order to use this linear approximation, the

operating point for LED should be considered. For the next step, the condition for using this linear approximation should be clarified.

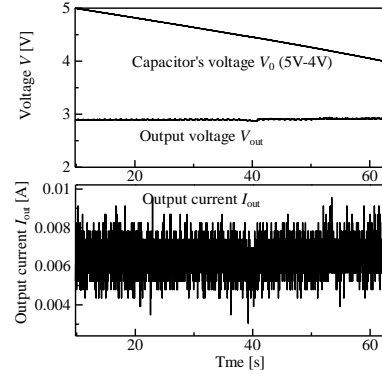


Figure 9 Result of the LED's lighting experiment

In the modeling of circuit, turn on/off delay time for FET is very short comparing to the switching period, so it's not considered. But there is an effect on the experiment result. For the next step, how does the voltage change at the delay time for FET should be considered.

#### 5 Conclusion

In this paper, the electric behavior for buck converter is analyzed with a model circuit. With the analytic solution, how to settle circuit and control parameters is introduced. At last, a capacitor power source is used for LED lighting successfully. For the next step, LED's I-V characteristic and changeable switching frequency circuit should be considered.

#### References

- [1] Keisuke Otome, "Effects of usage conditions on energy efficiency of boost switching regulator"
- [2] Masanori Tanaka, "Optimization of circuit and control parameters of a Boost Converter for Energy Harvesting".
- [3] Marcelo Gradella Villalva, "Dynamic analysis of the input-controlled buck converter fed by a photovoltaic array", Revisra Control& Automacao /Vol.19 no.14/Outubro, Novembro e Dezembro 2008
- [4] M.G.Villalva, "Input-controlled buck converter for photovoltaic applications: modeling and design", PEMD 2008. 4th IET Conference on, pp.505-509



# Preparation of acidic activated carbon from Bagasse Fly Ash

Student Number: 11M18210 Name: Zhaoxia GAN Supervisor: Hirofumi HINODE

バガスフライアッシュを用いた酸性活性炭の製造

甘 釗霞

本研究では、バガスの燃焼灰（バガスフライアッシュ：BFA）の有効利用を目的とし、吸着剤として広く利用されている活性炭の製造を研究した。BFAに酸処理と熱処理を同時に行うワンステップ処理を施し、酸性活性炭の製造を行った。製造した活性炭の重金属吸着実験を行い、吸着性能について検討した。その結果、製造した活性炭が $\text{Pb}^{2+}$ および $\text{Cd}^{2+}$ に対して吸着容量はそれぞれ30.12mg/gと18.66mg/gであり、吸着剤としての利用が期待できる。

## 1. Introduction

Bagasse is a valuable solid fuel to be combusted in steam boilers. In developing countries, most of the industries take this advantage and leave minimal excess of bagasse during normal milling seasons. However, the ashes from the combustion process in the form of fly ash (BFA) have not yet being commercially utilized causing disposal problems.

In terms of BFA, the supply is steady as long as sugar industries still use bagasse for fueling their steam boiler. A sugar industry emits approximately 5.5 kg of fly ash per metric ton of cane processed in the flue gases from the bagasse combustion. In the case of Indonesia with around 2.5 million tons of annual production of cane, 13,750 tons of BFA per year is produced nationwide [1].

Some researchers already made an attempt to utilize it as adsorbents by direct usage with minimal pretreatment. It is very rare that BFA is being upgraded to become advanced material such as high porosity activated carbon before being utilized. Previous study [1] showed that BFA can be converted into high surface area activated carbon by  $\text{CO}_2$  and KOH activation. The conversion of BFA into activated carbon with much higher surface area could improve the adsorption capacity of the material.

In this study, BFA was upgraded using  $\text{H}_2\text{SO}_4$  chemical activation to produce acidic activated carbons. The use of activated carbon to adsorb organic compounds has been widely known and practiced. However, it is also generally known that activated carbon showed only a minimal

adsorption capacity towards heavy metals. Here, the potential of using the produced activated carbon as adsorbent for heavy metals was studied by applying the activated carbon to the adsorption of two model pollutants,  $\text{Pb}^{2+}$  and  $\text{Cd}^{2+}$ .

## 2. Experimental

### 2.1 Preparation of activated carbon from BFA

BFA was obtained from PT Madukismo, a sugar company in Yogyakarta province, Indonesia. The methodology of one step treatment (acid treatment and thermal treatment) is shown in Figure 1. The apparatus of thermal treatment is shown in Figure 2. Before being used for activated carbon precursor, the fly ash has been sieved to obtain particle size from 0.7 to 1.4 mm and underwent chemical impregnation using sulfuric acid with certain weight ratios  $\text{H}_2\text{SO}_4\text{:BFA} = 1, 2, 3$  or 4 prior to heat treatments between 400 and 600°C. The acid treatment was done at room temperature and then subjected to heat treatment by 15°C/min of heating rate in a horizontal tubular furnace (ISUZU, EPKR-12K) under continuous nitrogen flow of 150 ml/min. After reaching final temperature, the condition was maintained for 1 hour before cooling to room temperature. After activation, all samples were subjected to washing by deionized water until neutral pH.

The samples were labeled as STxRy for the activated samples. Small letter x indicates activation temperature in hundreds (°C) while y states the weight ratio of  $\text{H}_2\text{SO}_4\text{/BFA}$ .

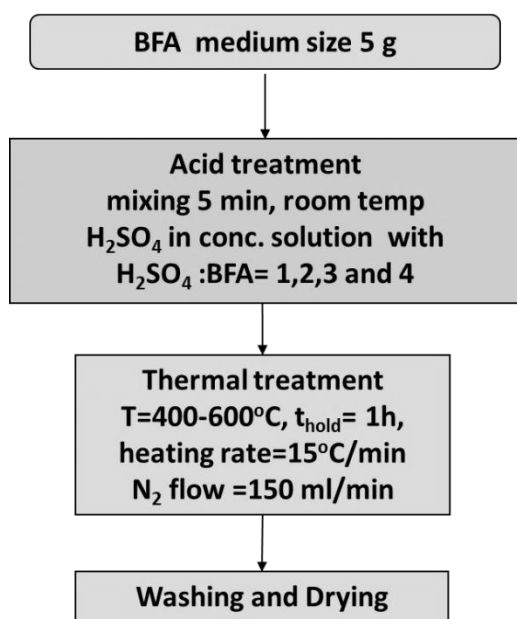


**Fig.1 Methodology of one step treatment (acid treatment and thermal treatment)**

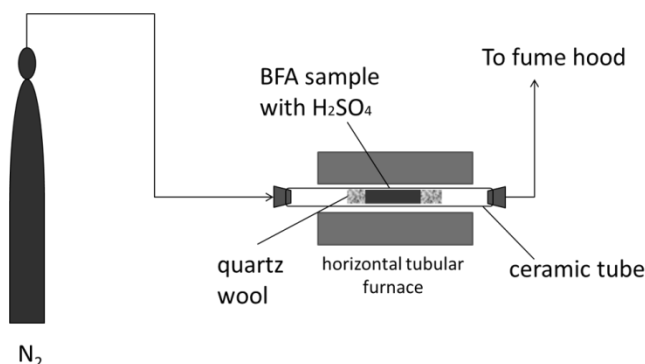


**Fig.2 Apparatus of thermal treatment**

## 2.2 Characterization

The samples textural properties were characterized using nitrogen adsorption at 77K by Autosorb 1 from Quantachrome. Surface area was calculated using BET method, while micropore volume ( $V_{mic}$ ) has been determined using DR method. Then, mesopore volume ( $V_{mes}$ ) was calculated by subtraction of total volume ( $V_{tot}$ ) with micropore volume ( $V_{mic}$ ).

The chemical property analyses were done by measuring point of zero charge  $pH_{ZPC}$ . The method of determining  $pH_{ZPC}$  was based on the method that was proposed by Noh and Schwarz [2].

## 2.3 Adsorption in model solution

The activated carbon prepared from BFA was used as an adsorbent in adsorption runs. Adsorption runs were conducted by 0.05 g of adsorbent and 50 ml of  $Pb^{2+}$  or  $Cd^{2+}$  aqueous solution with the concentration of 10-50 mg/l in flask. This concentration range was selected for easy comparison to results from other studies [6]. The flask was put in a constant temperature ( $30 \pm 1^\circ C$ ) shaker bath with 100 rpm for 12 hours. After reaching adsorption equilibrium, the mixture was filtered and the filtrate was analyzed by ICP. Table 1 shows the conditions of adsorption experiment.

**Table 1 Adsorption experimental conditions**

Mass of solutions [ml]	50
Initial concentration of solutions [mg/l]	10~50
Adsorbent [-]	activated carbon from BFA
Weight of adsorbent [g]	0.05
pH [-]	$Pb^{2+}$ : $5.0 \pm 0.2$ $Cd^{2+}$ : $6.0 \pm 0.2$
Temperature [ $^\circ C$ ]	$30 \pm 1^\circ C$

## 3. Results and discussion

### 3.1 Yield of activated carbon in one step treatment

The yield of activated carbon obtained in one step treatment (activated carbon/BFA weight ratio) was about 0.5.

### 3.2 Activated carbon characterization

Table 2 shows the characterization of activated carbons. Chemical activated carbon samples show a general trend of enhancement of porosity by increasing activation temperature and chemical ratio. Surface areas of the activated samples, which represent the total porosity, have a positive correlation with  $V_{mic}$  data, but it is not always in line with  $V_{mes}$ . Thus, the total surface area of the samples is mostly determined by the surface area in micropores range.

**Table 2 Characteristics of activated carbons**

Sample	$S_{BET} (m^2/g)$	$V_{mic} (cc/g)$	$V_{mes} (cc/g)$	$V_{tot} (cc/g)$
BFA	296.1	0.1267	0.0229	0.1497
ST5R1	482.8	0.2047	0.0173	0.2220
ST5R2	509.5	0.2169	0.0188	0.2357
ST5R3	541.8	0.2319	0.0163	0.2483
ST5R4	556.5	0.2381	0.0188	0.2569
ST4R1	458.6	0.1955	0.0154	0.2109
ST6R1	518.6	0.2207	0.0182	0.2389

The acidity of activated carbon was determined by pH<sub>ZPC</sub> measurement. Table 3 provides the results of pH measurement. The pH<sub>ZPC</sub> of all samples decreased after modification with H<sub>2</sub>SO<sub>4</sub> at different thermal temperatures. At the same thermal temperature, the activated carbon with higher weight ratio of H<sub>2</sub>SO<sub>4</sub>/BFA has lower pH<sub>ZPC</sub>. Lower value of pH<sub>ZPC</sub> means stronger acidity of the sample.

**Table 3 The acidity of solid**

sample	pH <sub>ZPC</sub>
BFA	8.48
ST5R1	5.64
ST5R2	4.86
ST5R3	4.84
ST5R4	4.59
ST4R1	3.76
ST6R1	5.44

### 3.3 Removal ratio r

The removal ratio  $r$  was obtained by,

$$r = \frac{V(c_0 - c_e)}{Vc_0}$$

where  $C_0$  and  $C_e$  are the initial and equilibrium liquid phase concentrations. The  $r$  of Pb<sup>2+</sup> and Cd<sup>2+</sup> in aqueous solutions are shown in Figure 3 and Figure 4.

The maximum  $r$  of Pb<sup>2+</sup> on ST5R4 was about 100%. The maximum  $r$  of Cd<sup>2+</sup> on activated carbon ST5R4 was about 25%. The acidic activated carbon could adsorb both Pb<sup>2+</sup> and Cd<sup>2+</sup>. The difference in the amount adsorbed could be attributed to the difference in the size of hydrated form of each ion, that is, Pb<sup>2+</sup> which has bigger ionic size is less strongly hydrated (smaller hydrated form) compared to Cd<sup>2+</sup> (bigger hydrated form) [3].

### 3.4 Adsorption isotherms

Langmuir adsorption isotherm is most widely used model for the adsorption. According to Langmuir theory, it has been assumed that adsorption occurs at a specific homogenous site within adsorbent, each site is occupied only a adsorbate molecule, all sites are equivalent and there are no interactions between adsorbate molecules. The non-linear form of Langmuir isotherm model can be represented by

$$q_e = \frac{q_{\max} K C_e}{1 + K C_e}$$

where  $C_e$  (mg/L) is the equilibrium concentration of the adsorbate,  $q_e$  (mg/g) is the amount adsorbed per unit weight of adsorbent at equilibrium,  $q_{\max}$  (mg/g) and  $K_L$  (m<sup>3</sup>/mg) are the Langmuir constants related to maximum adsorption capacity and the affinity of binding sites or bonding energy for adsorption processes, respectively [4].

#### 3.4.1 Adsorption of Pb<sup>2+</sup> with different C<sub>0</sub>

Figure 5 shows the comparison of adsorption equilibrium of Pb<sup>2+</sup> on several adsorbents with different weight ratio of H<sub>2</sub>SO<sub>4</sub>/BFA ratio. Table 4 shows Langmuir constants. All the isotherms of Langmuir model fit the experimental data (coefficient of determination R<sup>2</sup>>0.96) meaning that the adsorption process in this study is based on monolayer coverage of Pb<sup>2+</sup> on the surface of activated carbon. The activated carbon samples prepared with higher weight ratio of H<sub>2</sub>SO<sub>4</sub>/BFA have higher adsorption capacities towards Pb<sup>2+</sup>.

#### 3.4.2 Adsorption of Cd<sup>2+</sup> with different C<sub>0</sub>

Figure 6 shows the comparison of adsorption equilibrium of Cd<sup>2+</sup> on several adsorbents with different weight ratio of H<sub>2</sub>SO<sub>4</sub>/BFA ratio. Table 5 shows Langmuir constants. All the isotherms of Langmuir model fit the experimental data (coefficient of determination R<sup>2</sup>>0.95) meaning that the adsorption process in this study is based on monolayer coverage of Cd<sup>2+</sup> on the surface of activated carbon. The activated carbon samples prepared with higher weight ratio of H<sub>2</sub>SO<sub>4</sub>/BFA have higher adsorption capacities towards Cd<sup>2+</sup>.

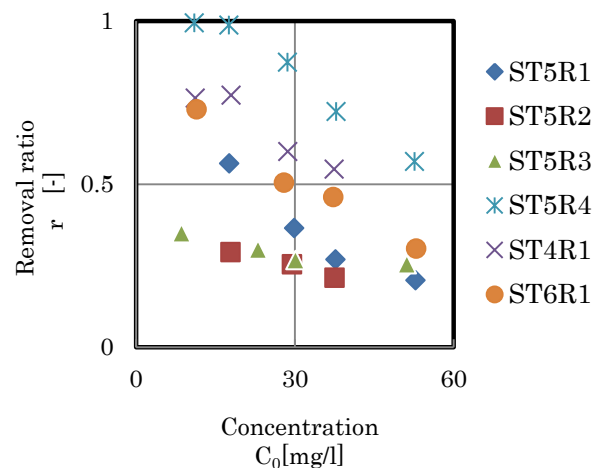


**Fig.3 r of Pb<sup>2+</sup> with different C<sub>0</sub>**

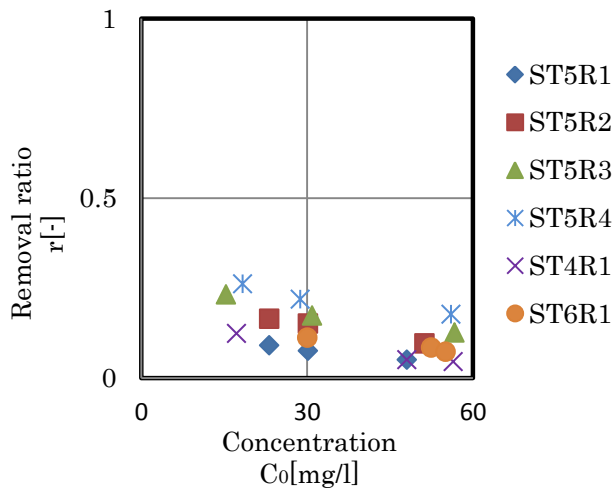


Fig.4 r of Cd<sup>2+</sup> with different C<sub>0</sub>

Table 4 Langmuir constants of Pb<sup>2+</sup>

Pb <sup>2+</sup>	q <sub>max</sub> [mg/g]	K <sub>L</sub> [m <sup>3</sup> /mg]
ST5R1	10.87	1.32
ST5R2	13.40	0.05
ST5R3	19.80	0.03
ST5R4	30.12	2.27

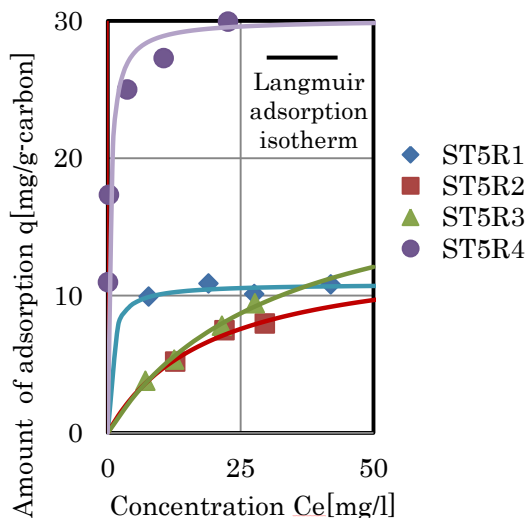


Fig.5 Comparison of adsorption equilibrium of Pb<sup>2+</sup> on several adsorbents of different chemical weight of H<sub>2</sub>SO<sub>4</sub>/BFA ratio

Table 5 Langmuir constants of Cd<sup>2+</sup>

Cd <sup>2+</sup>	q <sub>max</sub> [mg/g]	K <sub>L</sub> [m <sup>3</sup> /mg]
ST5R1	2.81	0.15
ST5R2	5.99	0.10
ST5R3	10.63	0.04
ST5R4	18.66	0.02

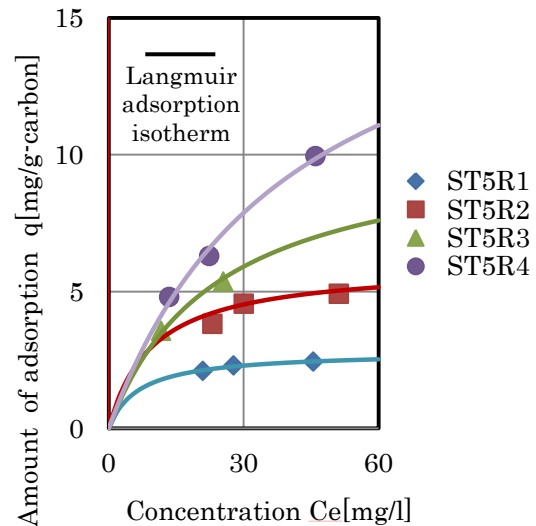


Fig.6 Comparison of adsorption equilibrium of Cd<sup>2+</sup> on several adsorbents of different chemical weight of H<sub>2</sub>SO<sub>4</sub>/BFA ratio

#### 4. Conclusion

BFA was successfully converted into activated carbon with yield of about 0.5. The acidity of prepared activated carbons was confirmed by the measurement of pH<sub>ZPC</sub>. The porosity of prepared activated carbon increased with increasing activation temperature and weight ratio of H<sub>2</sub>SO<sub>4</sub>/BFA. BFA activated carbon showed adsorption ability towards Pb<sup>2+</sup> and Cd<sup>2+</sup>. The activated carbon samples of higher weight ratio of H<sub>2</sub>SO<sub>4</sub>/BFA showed higher adsorption capacities. The maximum adsorption capacity of Pb<sup>2+</sup> and Cd<sup>2+</sup> on ST5R4 obtained from linear Langmuir model is 30.12 mg/g and 18.66 mg/g.

The maximum adsorption capacity of activated carbon prepared from BFA in this study is comparable to other adsorbents (about 5 to 30 mg/g). Therefore, the activated carbon prepared from BFA in this study is applicable for the removal of heavy metal pollutants in the water.

#### References

- [1] Chandra Wahyu Purnomo, Chris Salim, Hirofumi Hinode, Preparation and characterization of activated carbon from bagasse fly ash, Journal of Analytical and Applied Pyrolysis, Volume 91, Issue 1, May 2011, Pages 257-262
- [2] J.S. Noh, J.A. Schwarz, J. Colloid Interface Sci.130, (1990)
- [3] U. Adie Gilbert, I. Unuabonah Emmanuel, A. Adeyemo Adebajo, G. Adeyemi Olalere, Biosorptive removal of Pb<sup>2+</sup> and Cd<sup>2+</sup> onto novel biosorbent: Defatted Carica papaya seeds, Biomass and bioenergy 35 (2011)
- [4] A. Ozer, Removal of Pb(II) ions from aqueous solutions by sulphuric acid-treated wheat bran, Journal of Hazardous Material 141 (2007)
- [5] Bian Jiaxing, "Preparation of solid acid catalysts from Bagasse Fly Ash", Tokyo Institute of Technology (2011)
- [6] H.Trevino-Cordero, L.G.Juárez-Aguilar, D.I.Mendoza-Castillo, V. Hernández-Montoya, A. Bonilla-Petriciolet, M.A. Montes-Morán, Synthesis and adsorption properties of activated carbons from biomass of Prunus domestica and Jacaranda mimosifolia for the removal of heavy metals and dyes from water Industrial Crops and Products 42 (2013) 315–323

# Bioethanol concentration process using solvent extraction

Student Number: 11M18226 Name: Haihao HU Supervisor: Ryuichi EGASHIRA

## 溶媒抽出を用いたバイオエタノール濃縮プロセス

胡 海昊

エタノール水溶液を原料とし、キシレンおよびアルデヒド（フルフラールおよびベンズアルデヒド）を溶媒として回分平衡抽出を行った。水に比較してエタノールは選択的に溶媒相側に抽出され、エタノールが濃縮されることを確認した。比較的高いエタノールの分離の選択性を有しかつ分配係数の低い溶媒であるキシレンにアルデヒドを混合することにより、若干の選択性の低下のみで分配係数が向上した。また液液抽出と蒸留を組み合わせたプロセスを想定し、エタノール-水系の共沸点よりも低い範囲におけるエタノール濃縮を計算により検討した。製品中エタノール濃度の増加と共に所要エネルギーは増加し、また製品中エタノール濃度が高い範囲では蒸留のみに比較して液液抽出および蒸留を組み合わせた場合の所要エネルギーは小さかった。

### 1. Introduction

Bioethanol is considered to be the most promising fuel of the future since it is obtained from renewable sources, and is environmental friendly. The need of bioethanol is increasing quickly in recent year. However the conventional processes tend to be uneconomic because commodity ethanol is cheap in spite of the great difficulty in the separation of ethanol and water, because the ethanol-water system forms azeotropic mixture at 96 % of ethanol concentration.

The technology of bioethanol concentration has long been studied. The typical method of purification is distillation, which requires much energy for ethanol recovery and dehydration. Many ethanol recovery methods have been proposed to replace the distillation method, such as membrane separation<sup>[4]</sup>, adsorption<sup>[4]</sup> and supercritical fluid extraction<sup>[5]</sup>, etc. The solvent extraction technique is regarded as one of the prospective concentration methods.

In this study, batch equilibrium extraction of ethanol was conducted, and the concentration process using solvent extraction was simulated based on the experimental results.

### 2. Batch Extraction

#### 2.1 Solvent Selection

A large number of organic solvents have been examined to measure the extraction of ethanol<sup>[2]</sup>. The properties of water and ethanol are quite similar, making solvent selection more complicated. Many factors should be considered to choose favorable solvents for ethanol extraction, such as distribution coefficient of ethanol, separation selectivity of ethanol over water, availability, solvent toxicity, chemical stability

(thermal stability) and rapid phase separation. The first 2 factors are considered as the most important criteria.

Bioethanol is very cheap and common. Therefore, the solvent should be cheap, common and highly available. These considerations suggested that the favorable solvent would be a hydrocarbon. In the case of the solvent of hydrocarbon, such as, xylene, the distribution coefficient of ethanol was low and the separation selectivity to water was relatively high<sup>[1]</sup>. Among the xylene isomers, m-xylene was considered to be most favorable because of the poor commercial potential in industry and not expensive, so m-xylene was selected. On the other hand, aldehyde had relatively high solvency for ethanol. In this study, we focus on aldehydes of furfural and benzaldehyde, which are used as an extraction solvent for refining lube oil and as a raw material of chemical synthetic substance, respectively. And the effects of the mixed solvents on the ethanol concentration were also discussed.

#### 2.2 Experimental

Table 1 shows the experimental conditions for batch extraction. The specified amounts of the feed and solvent phases were contacted and shaken with each other in conical flasks with screw cap in isothermal bath for 24 h at 298 K to equilibrate. After the equilibration, the raffinate and extract were separated by a separating funnel. The respective liquid phases were analyzed by gas chromatography (GC17A, Shimadzu Ltd.) with a 30m× 0.25mm i.d. capillary column and a flame ionization detector, in which the column temperature was maintained at 333K for the initial 5min, and then increased at 5K/min up to 373K. A Karl Fischer titration (758 KFD Titrino Metrohm



Ltd.) was used with dehydrated methanol of HYDRANAL methanol and titration solution of HYDRANAL composite 5, purchased from Sigma-Aldrich Ltd., to measure the water concentration of each solution.

Table 1 Experimental conditions for LLE	
Feed system	Aqueous solution of ethanol(50g) Furfural <sup>[2]</sup> m-Xylene Benzaldehyde m-Xylene, Benzaldehyde(1:1) m-Xylene, Furfural(1:1,7:3,9:1)
$X_{F,EtOH}$	0.1~0.7
S/F ratio	1
Time	24h
Temperature	298±1K

## 2.3 Results and Discussion

**Figure 1** shows the liquid-liquid phase diagram in water-ethanol-solvent system. The heterogeneous region was wider with the solvent of m-xylene than those with the other solvents<sup>[1][2]</sup>. And it was the smallest in the case of furfural solvent, that is to say, furfural dissolved ethanol most<sup>[2]</sup>.

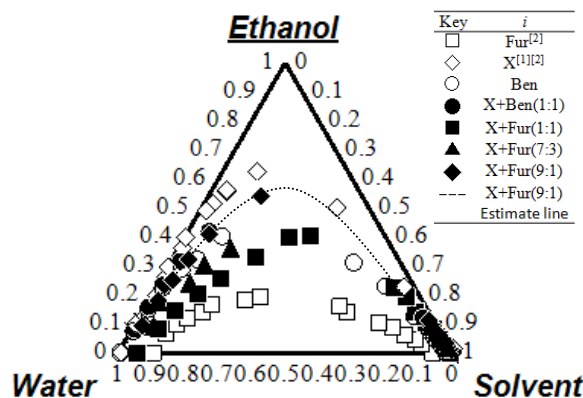


Fig.1 LLE for water-ethanol-solvent system

The ethanol concentrations in the extract phase on solvent-free basis were plotted against the feed ethanol concentrations in **Figure 2**. The concentration of ethanol in the extract phase on solvent-free basis was higher than the ethanol concentration in feed for all runs, namely, ethanol was concentrated by extraction. Although the ethanol was concentrated to relatively high concentration especially in the cases with m-xylene and the mixed solvents of m-xylene-furfural, the concentrations of ethanol in the extract phase based on the solvent-free basis

were lower than that in the azeotropic mixture of ethanol-water system.

The ethanol distribution coefficient and separation selectivity at equilibrium were defined as follows:

$$m_i = y_i / x_i$$

$$\beta_{EtOH,W} = m_{EtOH} / m_W$$

where  $y_i$  and  $x_i$  are the concentrations of component  $i$  in the organic and aqueous phases at liquid-liquid equilibrium.

**Figure 3** shows the relation between the ethanol distribution coefficient and separation selectivity. The selectivity decreased with increasing distribution coefficient in all solvents. The m-xylene solvent<sup>[1][2]</sup> showed a low distribution coefficient, because ethanol has low solubility in m-xylene solvent. However ethanol could be partitioned more easily into the m-xylene phase than the water, so the separation selectivity was very high for m-xylene solvent. The solvent m-xylene-benzaldehyde maintained the separation selectivity and significantly improved the ethanol distribution coefficient. However, benzaldehyde is easily oxidized to benzoic acid, and it is required to care about extraction operation. Comparing with m-xylene-benzaldehyde mixed solvent, the selectivity with m-xylene-furfural mixed solvent was in the same range and the distribution coefficient was higher. Therefore the aldehydes of furfural and benzaldehyde enhanced the ethanol distribution coefficient. And the distribution coefficient increased by greater furfural content, but the heterogeneous region and the ethanol separation selectivity reduced. The addition of only a small amount of furfural significantly improved the distribution coefficient and maintained the separation selectivity.

However, the favorable solvent for concentration process should be selected depending on the process design and specifications.

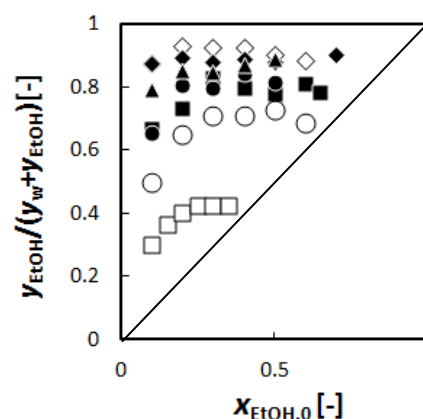


Fig.2 The ethanol concentrations in the extract phase on solvent-free basis at various feed ethanol concentrations.

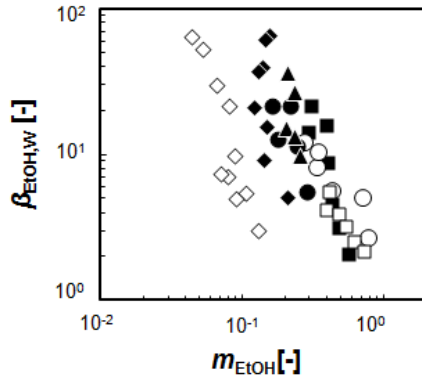


Fig.3 Relation between ethanol distribution coefficient and separation selectivity

Finally the experimental results calculated by the Non-Random Two Liquid (NRTL) model, which is an activity coefficient estimation model can be applied to non-ideal solution.

The NRTL equation and interaction parameters were defined as follows:

$$\ln(\gamma_i) = \frac{\sum_{j=1}^m \tau_{ji} G_{ji} x_j}{\sum_{l=1}^m G_{li} x_l} + \sum_{l=1}^m \frac{x_l G_{lj}}{\sum_{l=1}^m G_{lj} x_l} (\tau_{ij} -$$

$$n=1 \text{ m x n } \tau_{nj} G_{nj} l=1 \text{ m } G_{lj} x_l$$

$$G_{ij} = \exp(-\alpha_{ij} \tau_{ij})$$

where  $\alpha_{ij}$  was the nonrandom parameter,  $\tau_{ij}$  was the interaction parameter. For all components,  $\alpha_{ij}$  was fixed as 0.3.

Table3 shows the NRTL parameters obtained by fitting the measured relationship for ethanol+water+m-xylene+furfural system. Calculation result is shown in **Figure 1** as dashed line.

Table2 NRTL Parameters ( $\alpha_{ij} = 0.3$ )

i	j	$\tau_{ij}$	$\tau_{ji}$
Water	Ethanol	207.8	284.5
Water	m-Xylene	1527.2	3073.6
Water	Furfural	-3565.9	-2915.4
Ethanol	m-Xylene	261.3	808.8
Ethanol	Furfural	1119.6	-355.6
m-Xylene	Furfural	2849.2	456.3

### 3. Liquid-liquid extraction process

#### 3.1 Process

In this study, the concentration process should be focused to recover ethanol the azeotropic mixture of ethanol-water system.

The combination of extraction and distillation was studied to evaluate the recovery of ethanol. Process flow diagram is shown in **Figure 4**. In this process, bioethanol feed F is supplied into

multistage extraction column and contracted with solvent S. The extract phase E is obtained from the top of the extraction column and sent into distillation column 1 to recover solvent. And the distillate D is sent into the distillation column 2 to concentrate ethanol to a high level. The raffinate phase R which comes out at bottom of the extraction column also sent into the distillation column 2 to recover ethanol.

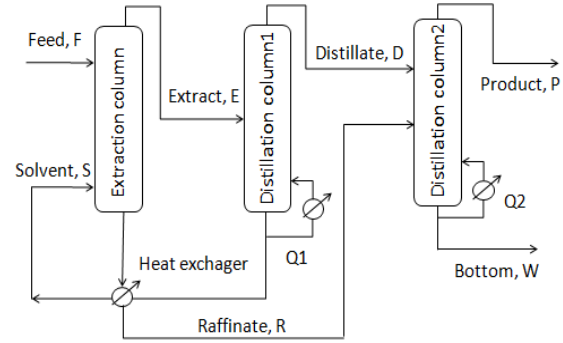


Fig.4 Process flow diagram of ethanol recovery by combination of extraction and distillation

#### 3.2 Process calculation conditions

Aspen Hysys simulator (Aspen Japan, Inc.) was used to simulate extraction process based on the experimental results, which were calculated by the Non-Random Two Liquid (NRTL) model. Table 4 shows calculation conditions of process. The S/F ratio was fixed at 0 to 1. If the S/F ratio equal 0, it means that this process consists only of the distillation column2. The feed temperature was 298K, the operation pressure was one atm, and the pressure drop was zero in all runs.

Table4 Calculation conditions of Process

Feed system	Aqueous solution of ethanol
Solvent system	m-Xylene
	Furfural
	m-Xylene,Furfural (9:1)
Feed, F	1000 kg/h
$x_{F,EtOH}$	0.1
S/F Ratio	0~1
Extraction Column Stages	3
Distillation Column 1 Stages	10
Distillation Column 2 Stages	20
Total Specification	$x_{p,EtOH}=0.85\sim0.95$ $Y_{p,Eth}=0.98$
Specification (Distillation Column 1)	$x_{p,EtOH}=0.6\sim0.75$ $Y_{p,Eth}=0.99$
Specification (Distillation Column 2)	$x_{p,EtOH}=0.85\sim0.95$ $Y_{p,Eth}=0.99$

### 3.3 Results and Discussion

**Figure 6** and **Figure 7** show the effects of S/F ratio on the energy requirements in different distillation column and in different solvents, respectively. The energy requirements in distillation for Process in **Figure 6** and **Figure 7** were estimated under the same specifications ( $x_{p,EtOH}=0.92$ ,  $Y_{p,EtOH}=0.98$ ).

In **Figure 6**, the calculation results show the increase in S/F ratio resulted in the increase of energy requirements of distillation column1 for all cases. As much as solvents increased, energy requirement for recover solvent became large. On the hand, the energy requirements of distillation column2 decreased with increasing S/F ratio in case of furfural solvent only. In **Figure 7**, the calculation results show that furfural required lower energy requirements than the other solvents. And comparing with the case of S/F=0(Distillation column2 only), the required energy with furfural was also lower, if the S/F ratio was lower than 0.8.

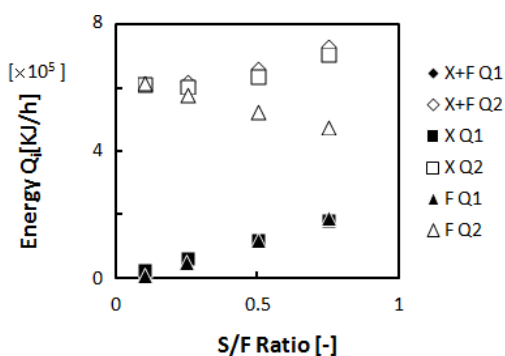


Fig.6 Effects of S/F Ratio on energy requirements in different distillation column.

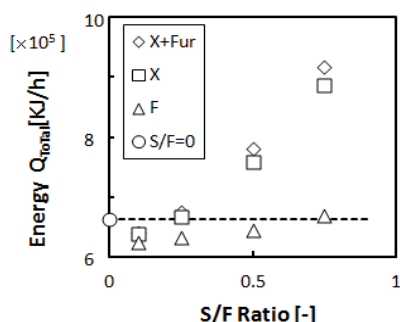


Fig.7 Effects of S/F Ratio on total energy requirements in different solvent.

**Figure 8** shows the effects of ethanol concentration in product on energy requirements. The calculation of the energy requirements in Figure 6 was done under same specification ( $x_{p,EtOH}=0.85\sim0.95$ ,  $Y_{p,EtOH}=0.98$ ).

Energy requirements increases with increasing concentration of ethanol, and it was found that the increase of energy requirements in the case of S/F=0 was particularly noticeable. In the range exceeding 92% of ethanol concentration in product, the solvent extraction process could reduce energy requirements significantly, and could save energy for about 43% to the maximum.

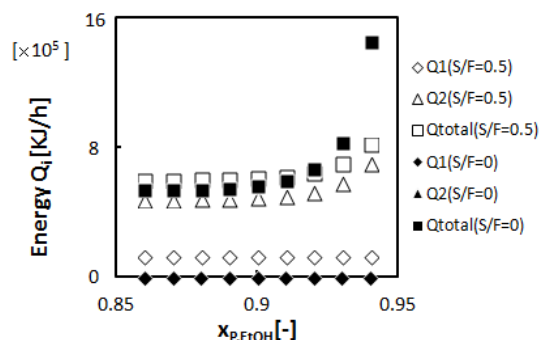


Fig.8 Effects of ethanol concentrations in product on energy requirements

### 4 Conclusion

Firstly, Ethanol could be concentrated by extraction, and the distribution coefficient of ethanol could be improved by the addition of aldehyde, to the solvent of m-xylene, with little decrease of the selectivity.

Secondly, simulation of the ethanol concentration process shows the extraction process using furfural solvent is required lower energy than distillation process.

The results above confirmed the feasibility of bioethanol concentration process by solvent extraction.

### Nomenclatures

$m$ : distribution coefficient,  $y_i$ : mass fraction in extract,  $x_i$ : mass fraction in raffinate,  $\beta$ : separation selectivity

EtOH: ethanol, W: water, Fur: furfural, X: m-xylene, Ben: Benzaldehyde,

<Subscript>0: initial, R: raffinate, E: extract, D: distillate, P: product, W: bottom,

### References

- [1] Habaki,H.,et.,J.of JPI, vol53,(3),135-143 (2010)
- [2] Hu.H., Habaki.H., Egashira.R.,SCEJ 43th Autumn Meeting,J123
- [3] Daniel R. Arenson, A. Steen Kertes, C. Judson King, Ind.Eng.Chem. vol 29,607-613(1990)
- [4] Richare D. Offeman.,et. Separation and Purification Technology.vol72, 180-185(2010)
- [5] A.K.Frolkova V.M.Raeva Theoretical Foundations of Chemical Engineering,Vol.44(2010),No.4,545-556
- [6] Horizoe.H J.of JPI, vol53,(12),31-34 (2007)

# Image based real-time vehicle classification for ETC

Student Number: 11M18232 Name: Cong Geng Supervisor: Yukihiro Yamashita

ETCのための画像に基づくリアルタイム車両認識システム

コウソウ

従来の電波通信に基づくETC(Electronic Toll Collection 電子料金収受システム)は、高価であるため、開発途上国における普及が進んでいない。本論文では、この問題を解決するために、車両画像情報の統計的学習に基づくETCを提案する。その一環として、車両を自動分類できる試行ライブラリを構築した。まず、背景差分法で車両を背景から分離する。次に、車種分類に有用な画像情報を輪郭検出により獲得する。そして、学習データで訓練された統計モデルによって入力データの分類結果を出力する。さらに、コンパクトデジタルカメラと市販のパソコンで実験を行い、安いコストで車両分類を実現できることを検証した。最後に、結論および将来の課題を述べる。

## 1 Introduction

As a part of the Intelligent Transport Systems (ITS), ETC has been widely introduced in over 40 countries. ETC has achieved a considerably high utilization rate in developed countries and brought about remarkable benefits in both economy and environment.

However, due to the expensive starting cost of facilities and equipments, ETC has a comparatively slow spreading speed in developing countries. Inspired by the idea of number-plate automatic reading software using video camera, I proposed an image based toll collection system. In my work, a trial vehicle classification library has been built on a normal notebook PC. It shows the possibility of realtime vehicle classification and the potential of the image based ETC on such cheap facilities.

## 2 Related work

### 2.1 Field work

To know how is ETC being used in developing countries, I conducted a questionnaire on 25 toll gate staffs and an interview to a toll gate manager in Shandong province, China. According to the results of the questionnaire and the interview, the utilization rate of ETC in Shandong province is still low due to the high cost of existing systems.

Most staffs want spread use of ETC because they feel the working condition in toll gate is suffering because of exposure to emission gas and physical exhaustion.

### 2.2 Related researches

Traffic related research, such as traffic surveillance and number-plate recognition has always been one of the most focused fields. Morida et al. and Mohamed et al. have implemented a background subtraction method based on luminance accumulation of pixels [1] [2]. In their work, background is assumed to be the area with comparatively gradual luminance changing from frame to frame, while the foreground is assumed to be the area with drastic changing. In my work, I adopt the above method to erase the background area since it has a computational advantage among others such as optical flow based method [3], and block matching method [4].

As for the step of Feature extraction, Chang et al. implemented a component labeling algorithm [5]. In their work, each component is labeled using a tracing technique. This method is based on the principle that a component is fully determined by its contours, just as a polygon is fully determined by its vertices. This algorithm requires only one pass over the image, which is faster than any other traditional component-labeling algorithms.

### 3 Proposed solution

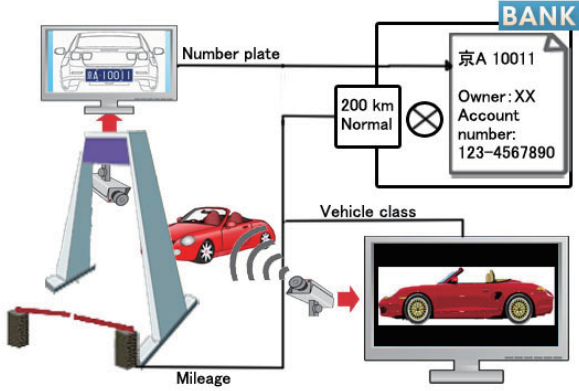


Figure 1: Image-recognition based ETC

The Figure 1 shows the proposed image-recognition based ETC. The bank or credit card company has the vehicle owner's deposit information which is bonding to their numberplate. At the toll station, two video camera is set up to take the photo: one high-resolution camera is in the front to take the scene with the numberplate. The other one is at off the road to take the side view of a passing vehicle. Both number plate and vehicle class are recognized and sent to the bank, then the toll fee is charged automatically. A numberplate reading library and a vehicle classification library are necessary to fulfill this transaction. Many numberplate reading libraries have been introduced into practice use, such as the "Intrada ALPR" library by Q-Free in Norway and the N-system by NEC in Japan. Thus, we can get it from the market. Because vehicle classification library is barely available on the market, so we tried to build a trial library for this task.

## 4 Algorithms

Object recognition using statistical method is a three-stage process which involves pre-processing and feature extraction and classifying in a video sequence. Through the pre-processing, the background and noise are removed, and the objects are localized in the input. Then these objects are described by a set of meaningful values (feature descriptors) in the feature extraction step. Finally the classification requires building a knowledge base of all classes against which an input object is matched.

### 4.1 Pre-processing

#### 4.1.1 Background subtraction

$I(x, y, t)$  refers to the luminance of pixel  $P(x, y)$  in the frame  $t$  of an image sequence. The luminance of background pixel can be modeled by

$$I(x, y, T) = \bar{I}(x, y) + \sigma(x, y) \sin(2\pi\omega t) + k\zeta \quad (1)$$

in which  $\bar{I}(x, y)$  and  $\sigma(x, y)$  (abbreviated into  $\bar{I}$  and  $\sigma$ ) refer to the average luminance and vibration at  $P(x, y)$  up to frame  $t$ .  $\omega$  indicates the frequency of luminance, the bound  $\zeta$  depends on the camera and  $k$  is a coefficient of  $(-1 \leq k \leq 1)$ .

Thus, while the luminance  $I(x, y, t)$  satisfies

$$\bar{I} - \sigma - \zeta \leq I(x, y, t) \leq \bar{I} + \sigma + \zeta, \quad (2)$$

$P(x, y)$  is assigned to a background pixel and being separated from foreground pixels.

As the frames go on,  $\bar{I}$  and  $\sigma$  of the background area are updated by

$$\bar{I}' = (n-1)/n \times \bar{I} + 1/n \times I, \quad (3)$$

$$\sigma' = (n-1)/n \times \sigma + 1/n \times \sqrt{2 \times (I - \bar{I})^2} \quad (4)$$

For the foreground area, the average luminance  $\bar{I}$  is kept and only the vibration  $\sigma$  is updated by

$$\bar{I}' = \bar{I}, \quad (5)$$

$$\sigma' = (m-1)/m \times \sigma + 1/m \times \sqrt{2 \times (I - \bar{I})^2} \quad (6)$$

in which  $m$  and  $n$  ( $n \leq m$ ) refer to the updating parameters.

#### 4.1.2 Smoothing filter

In the pre-processing, smoothing filter is applied to blur the image and leave noise pixels out. In my work, I applied the Gaussian filter to the original image to fulfill the noise reduction. For a 2-D image, Gaussian distribution is defined by the following function:

$$G(x, y) = \frac{1}{2\pi\alpha^2} e^{-\frac{x^2+y^2}{2\alpha^2}} \quad (7)$$

in which  $x$  and  $y$  refers to the distance in 2-D coordinates and  $\alpha$  indicates the standard deviation. The closer the distance from the center pixel is, the more weight on the neighboring pixel is. This operation makes luminance of pixels become related to their neighbors. Therefore, the gap of luminance between pixels is reduced and the input image becomes smoother.



## 4.2 Feature extraction

### 4.2.1 Blob labeling

Blob labeling is to label the connected pixels as an aggregated blob on a binary image. The blob labeling also has two phases: contour detection and contour tracing.

First, a scanner scans the binary image pixel by pixel from the top to the bottom, from the left to the right. When the scanner detects the first foreground pixel, called initial point, the contour tracing is conducted. In the step of tracing, a contour tracer traces the following connected foreground pixels by a prearranged direction (from 0 to 7) shown in Fig 3.

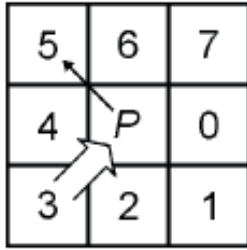


Figure 2: Tracing order

With the previous pixel which is positioned in number  $d$ , the next tracing position is set to  $d + 2$ . For example, since P in Fig 3 follows pixel 3, the next trace position should be pixel 5. It is not necessary to trace pixel 4 since in previous step, if 4 is a foreground pixel, it should have been traced before P. With this trick we can run the algorithm faster than the others. When the tracer came back to the initial point, the tracer start from the first step again, to scan a possible inner contour of this blob or of other blobs and trace them if necessary. By doing this again and over again, I obtained pixel-level information such as area and perimeter of the blob.

### 4.2.2 Feature selecting

After the blob labeling has been done, I have to extract features appropriate for the task of vehicle classification. As our purpose is to classify vehicles by their size, I decided to extract following features from blobs.

1. Number of pixels: indicates the 'size' of the blob on camera.
2. Aspect ratio: calculated by  $length/height$ ,

3. Weight distribution in an  $N \times N$  rectangle partition: First, the entire blob is separated into  $N \times N$  rectangles. Then the weight of distribution of the blob is calculated by  $N \times N$  rectangle partition.(Fig 4)

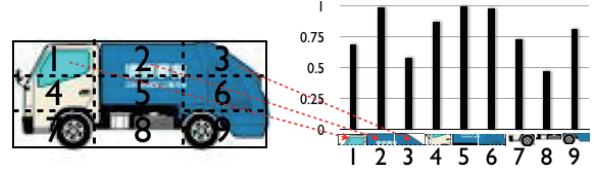


Figure 3: distribute weight of  $3 \times 3$  partition

## 4.3 Classifying

### 4.3.1 Criterion of classification

The criterion of classification of a vehicle has a great variety from country to country, from state to state. To make the trial library fit the general case of on the road, I have set up the task to 3-class and 4-class classifications. The vehicle classification chart is shown in Fig 5













3-Class	4-Class	Description	Samples
I	I	•Motor •Keijidousya	 
	II	•Sedan •Minivan •SUV •Coupe •Wagon •Mini truck	     
II	III	•Middle truck •Van	 
III	IV	•Bus •Truck	 

Figure 4: Vehicle classification

### 4.3.2 Classifier

A number of classifiers are examined to deal with my data. They are NaiveBayes, J48 decision tree, Multilayer perceptron and Logistic. These classifier are often used in machine learning and pattern recognition.

## 5 Experiment

### 5.1 Implementation

The dataset consists video data of 346 vehicles. The video was took on the E6 expressway, near to

Trondheim, Norway. The video format is AVI, with size of 320×240, 30 fps. A Canon compact digital camera, IXY 910 IS, is used to take the video. The whole program is implemented on a Macbook PC, with 2.4GHz Intel Core 2 Duo CPU and 4GB memory. Above hardware cost less than one-thousand dollar.

The code is implemented with C++ on Eclipse ver. 3.7, an open source integrated development environment provided by IBM. I conducted the above image-processing using OpenCV ver. 2.2, an open source library for computer vision mainly provided by Intel. The training and test of data were accomplished on Weka ver 3-6-8, an open source data mining tool.

## 5.2 Results

I separated the video data to a training set with 225 vehicles and a testing set with 121 vehicles. Table 1 shows the accuracy of adaptation on both 3-class and 4-class models trained by different classifiers. The Decision tree achieved the best performance

Table 1: Accuracy of trained model

Classifier name	3-class	4-class
NaiveBayes	80.2%	76.4%
Decision tree	84.3%	81.0%
Multilayer Perceptron	82.6%	82.6%
Logistic	78.5%	79.3%

in the vehicle classification task. Here, it's detailed results are shown in Tables 2 and 3.

According to Table 3, 4-class classification has

Table 2: Details of 3-class classification

Class	Accuracy	F-Measure	ROC Area
I	84.8%	0.912	0.924
II	72.2%	0.578	0.724
III	100%	0.846	0.982

Table 3: Details of 4-class classification

Class	Accuracy	F-Measure	ROC Area
I	46.2%	0.545	0.803
II	88.6%	0.881	0.831
III	83.3%	0.732	0.885
IV	82.6%	0.900	0.994

a difficulty on discriminating a minicar and a normal passenger vehicle. In fact, a minicar is distinguished only by the measure of displacement volume. It does not have much difference with a normal passenger vehicle in their looking.

## 6 Conclusion&Future work

This trial library has proved that the image-based vehicle classification achieved about 80% accuracy under simple 3-class and 4-class classifications. The affordability gives a strong advantage to the utilization in developing countries. However, the disadvantage of the image based system contains the shortage in accuracy and the need for regular cleaning of lens. Thus, it could be seen as a cheaper option to fulfill non-stop toll gate for developing countries which have abundant labor to do manual operations such as re-labeling and regular cleaning of lens.

The future includes: to improve the accuracy of the vehicle classification by using more refined feature and classifier, to combine with numberplate reading library and to convince the authorities to take a pilot test.

## References

- [1] S.Morida, K.Yamazawa. "Networked Remote Surveillance System Using Omnidirectional Image Sensors" (D-II), Vol. J88-D-II, pp. 864-875, May 2005 (in Japanese).
- [2] Shahrizat Shaik Mohamed, Nooritawati Md Tahir, Ramli Adnan , "Background Modelling and Background Subtraction", CSPA 2010 , pp 1-6, May 2005.
- [3] M.S. Kemouche, "A Gaussian Mixture Based Optical Flow Modeling for Object Detection", ICDP2009 3rd International Conference, pp 1-6, 2009.
- [4] Wu-Chih Hu, "Adaptive Template Block-based Block Matching for Object Tracking", ISDA '08. 8th International Conference, pp 61-64, Nov 2008.
- [5] Fu Chang, Chun-Jen Chen, Chi-Jen Lu. "A Linear-Time Component-Labeling Algorithm Using Contour Tracing Technique", Computer Vision and Image Understanding vol 93, pp 206-220, 2004.

# Outdoor Experiments on Human Bio-Meteorology at the Hottest City Tajimi

## Using a New Wearable Measurement System

Student number: 11M18255      Name: Rui SHI      Supervisor: Manabu KANDA

人体装着型計測システムを用いた，多治見市における夏季の熱環境・生理評価実験

石 蕊

人の動線に沿って連続的に変化する温熱環境とそれによる人体生理への影響を評価する目的で，日本で一番熱い町の1つである岐阜県多治見市において夏季の熱環境・生理評価実験を行った．実験には，気象因子（気温，湿度，風速，長波及び短波放射）と生理因子（表面皮膚温度，深部体温，脈拍，運動量，温熱感）を同時計測できる人体装着型温熱生理計測システムを用いた．都市の街区内の詳細な温熱・生理データの可視化を行い，熱環境と人体生理応答の関係，そして過渡現象における急激な熱環境変化に対する人体生理の応答特性を明らかにした．

### 1. Introduction

In recent years, the number of people suffering from heat stroke has increased due to extreme hot weather caused by urban heat island. To prevent heat stroke and evaluate its risk, the detailed understanding of thermal environment in human living spaces and how it's effect to human health are needed.

Knowledge about the relationship between thermal environment and health has been obtained but mostly from laboratory experiments [1]. On the other hand, outdoor experiments [2] focusing on the thermal environment and thermal sensation are plenty, but the measurement of physiological factors are still very limited. Comparing with laboratory, actual urban micro climate, such as air temperature, radiation, wind speed and etc. are largely fluctuating. The evaluation of its impact on human physiology is important.

However, it is not easy to measure thermal environment in urban areas with conventional meteorological sensors due to their heavy and bulky characteristics. To overcome the problem, a compact and portable measurement system (Figure 1) was developed, which can measure both meteorological (air temperature, humidity, long and short wave radiation, wind velocity) and physiological (skin temperature, tympanic (core) temperature, pulsation, rate of acceleration, thermal sensation) parameters. Using this measurement system, two observations along subjects' pathways were conducted in the summer of 2011 and 2012, at Tajimi City, Gifu Prefecture, which is one of the hottest cities in Japan.

### 2. Wearable Measurement System

The compact wearable measurement system, which can measure both meteorological and physiological indices (Table 1), will be explained in this section.

#### 2.1 Meteorological part

All indices relative to thermal environment were measured. Here, wind velocity, short & long wave radiation were measured using three compact globe thermometers with different properties [3]. Those three variables are identified from the heat balance equations of globe thermometers. The sensors for ambient temperature and relative humidity were installed in the radiation shield to reduce the radiation effect. Details are shown in Figure 1(1).

#### 2.2 Physiological part

Subject's physiological responses to thermal environment were also measured. Average skin temperature was estimated from Hardy& Dubois's 7 points method [4]. The other sensor for pulse rate, body motion, and thermal sensation can be seen in Figure 1(2).

### 3. Observation Outline

#### 3.1 2011 year's observation

The first observation was focused on the thermal environment in the urban living spaces. 26 subjects wore the measurement system while walking around the parking lot, commercial area, highly-reflective painted area, biotope area, and green spots (route in Figure 2), from August 22-24, 2011. Three observations (morning 8-10, noon 12:30-14:30, evening 16-18) were held each day. The examinees were classified three groups according age bracket; 30-40's subjects conducted the experiment on first day, 20's on second day, and 50-70's on third day.

#### 3.2 2012 year's observation

The second observation was focused on the transient phenomena, e.g., abrupt changes of environments (hot to cool) and changes of exercise states (walking to rest). 4 subjects held the observation followed the procedures shown in the Figure 3, on September 5-6, 2012.

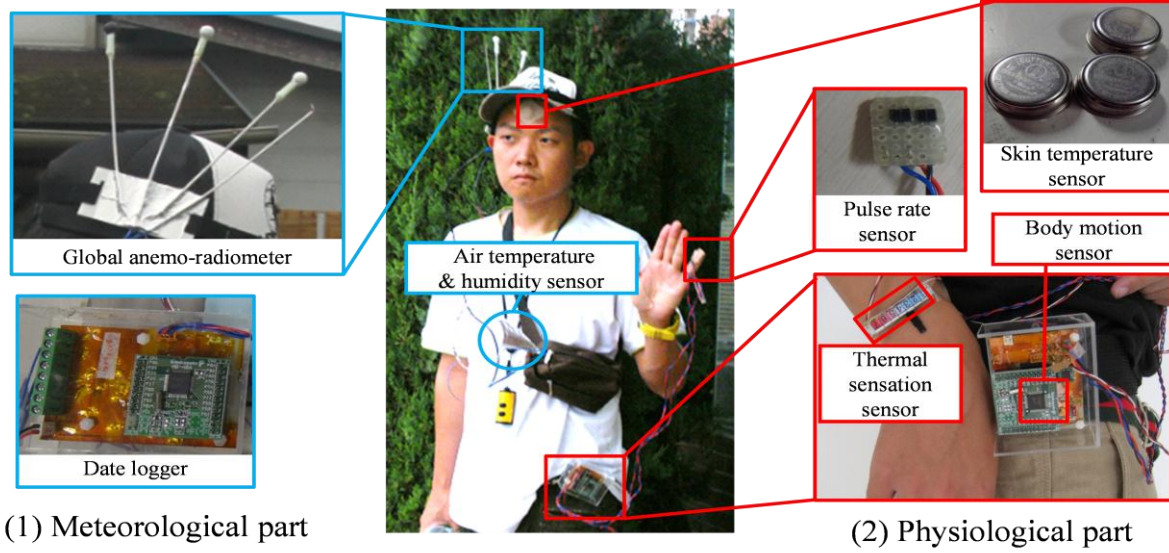


Figure 1. The compact measurement system.

Table 1. Measurement items used in the observation

Meteorological Part			Physiological Part		
Variable	Instrumentation	Accuracy	Variable	Instrumentation	Accuracy
Air temperature (Ta)	K type, Thermocouple	$\pm 0.2$ K	Skin temperature (T <sub>skin</sub> )	Thermochron, SL type, KN Laboratories	$\pm 0.7$ K
Relative humidity (RH)	SHT75, Sensirion	$\pm 1.8$ %	Core temperature (T <sub>core</sub> )	MC-510, Omron (2011) LT-200, Gram (2012)	$\pm 0.1$ K
Wind velocity	Global anemo-radiometer	$0.32 \text{ ms}^{-1}$	Pulse rate (PR)	Handmade	N/A
Short wave radiation(S)		$21.8 \text{ Wm}^{-2}$	Body motion	KXM52-1050, Kionixinc	N/A
Long wave radiation (L)		$10.9 \text{ Wm}^{-2}$	Thermal sensation	Handmade	N/A

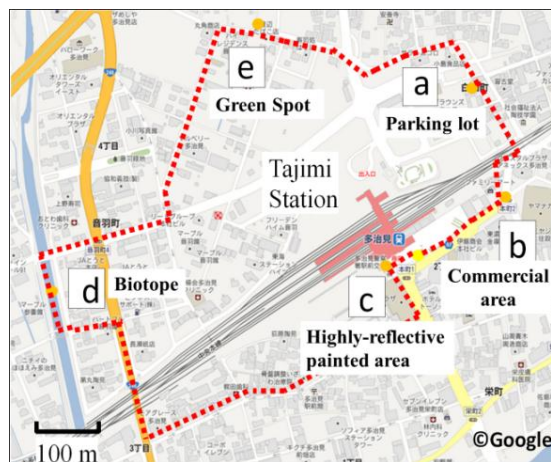


Figure 2. Observational route map

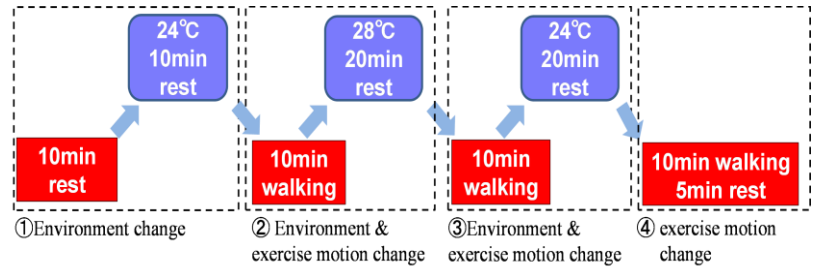


Figure 3. Detailed observation procedures in 2012.

## 4. Results and Discussion

### 4.1 Thermal environmental & physiological map

The detailed thermal environmental and physiological maps were visualized along subjects' pathways. Figure 4[a] shows that the urban canyons have higher temperature about  $3^{\circ}\text{C}$  than the nearest



AMeDAS point (Automated Meteorological Data Acquisition System) of JMA (Japan Meteorological Agency); only biotope and green area (white circle area) are cooler than AMeDAS data. Though the observational area was not too large, just about 700 square meters, data showed spatially heterogeneity. This locality may cause the difficulty of evaluation of micro climate using AMeDAS data. From Figure 4[b], high-temperature area (red circle area) corresponded well with short wave radiation. Figure 4[c] shows SET\* [5], which is an index of heat stress, [d] shows subject's skin temperature(Tskin). They are correlating well each other. The relation between these two will be discussed later.

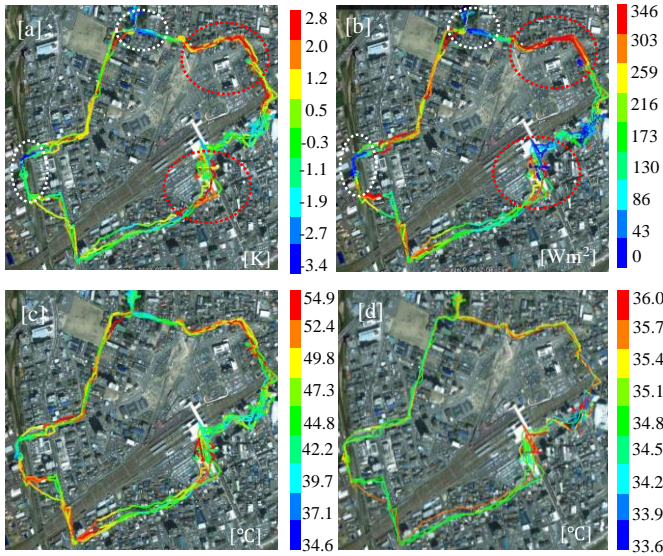


Figure 4. Thermal environment map on the morning of August 24<sup>th</sup>, [a]Ta anomaly from Tajimi city AMeDAS, [b] short wave radiation, [c]SET\*, [d]subject's Tskin

## 4.2 Physiology during transient phenomena

### 1) Analysis of time series data

Here we focused on the relation between wind velocity and body motion in the first observation. Figure 5 shows that wind velocity has the similar behavior with body motion. Such cases were confirmed in 20 out of 26 subjects. Wind velocity in the urban canyon was generally weak, and the subjects' movements could increase relative wind velocity.

From the second observation: when the environment abruptly changed (from outdoor to air-conditional indoor), in response to the cold environment, a drop in Tskin, Tcore and pulse rate can be seen from Figure 6. This decrease is caused by physiological vasoconstriction. Furthermore subject's metabolism is relatively constant for the environments change, which can be seen by the data of METS from 10:25 to 10:50.

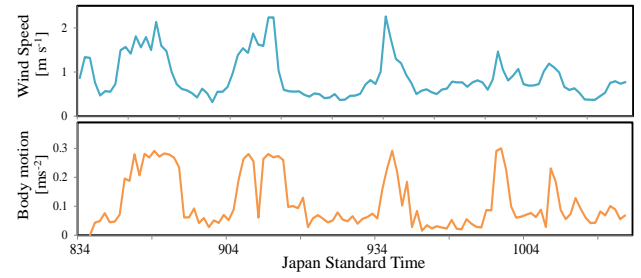


Figure 5. One of time series chart of 2011's observation

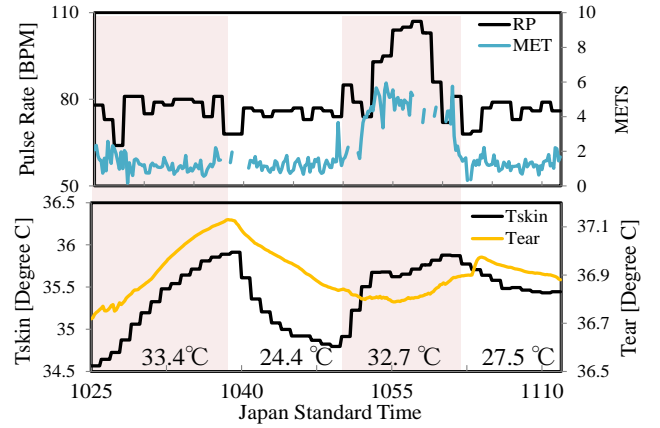


Figure 6. A part of ID3's thermal physiology time series chart of 2012. Enclosure pinky area means outdoor.

### 2) Time constant of human skin temperature

Tskin fell immediately by the abrupt change of environment (hot to cold), and then gradually approached constant. In order to characterize subject's responses for the abrupt change, time constant was estimated by following equation:

$$T_{sk} = \left( T_0 + \frac{b}{a} \right) \exp(at/\tau) - \frac{b}{a} \quad (1)$$

Where  $T_0$  is initial value,  $T_0 + a/b$  is the amplitude of the change in Tskin,  $-b/a$  indicates the steady value.  $\tau$  is a time constant, which gives the time required to reach a 63% responses for  $T_0 + a/b$ . Linear approximation was used to obtain a and b. The average time constant of Tskin is 2.57 [min], for 33.4 °C outdoor to 24.5 °C indoor. This value is comparable as Nagano's experiment (2.39 [min]) [6]. Time constant of Tskin is influenced by age and subjects' sweat rate (Figure is not shown).

### 3) Time delay of core temperature

When the environment abruptly changed, a time delay was found in subjects' core temperatures (Figure 6). The average time delay is 17.4 [sec], when abrupt environment changed from 33.4 °C to 24.5 °C. Furthermore, the time delay became longer when the change of subjects' motion accompanied by the change of environment. For the case into 24.5 °C indoor is 39.9 [sec], while into 28.0 °C indoor more than 167.4 [sec].



### 4.3 Thermal effects to the human physiology

Here the relationship between thermal environment and human physiology was focused. Figure 7 shows the relation between hourly sweat rate and SET\*. Here hourly sweat rate means sweating per unit surface area per unit observation time. Figure 8 shows SET\* has an influence on average T<sub>skin</sub>. Hourly sweat rate and T<sub>skin</sub> corresponds with SET\*, however the plots have dispersion. Factors causing the dispersion are the differences of gender and BMI (body mass index).

First, considering the difference of gender, male shows a tendency to a large hourly sweat rate than female. Furthermore, the T<sub>skin</sub> of female are higher than the male. It can be considered that because of low hourly sweat rate of female, efficient heat dissipation by the heat of vaporization is difficult, as result leading to a high T<sub>skin</sub> for female.

Second, the result of BMI differences goes well with common intuition that obesity subjects are more sweating than others. Due to the fat, a heat-insulating layer formed between capillary and the atmosphere, sensible heat dissipation is reduced. As in the case of gender, sweatier obese subjects have confirmed a significant decrease in T<sub>skin</sub>.

Finally, significant effect to age difference was not confirmed by this observation. One possible reason is that 50s or older have a regular exercise habit.

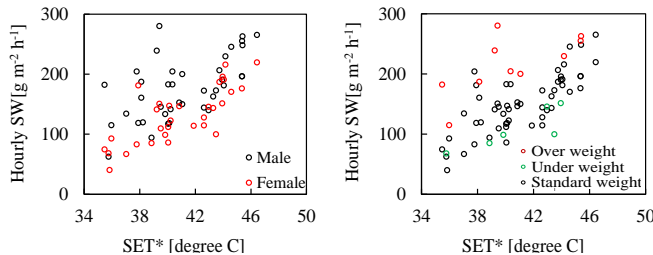


Figure 7. Relation between hourly sweat rate and SET\*.

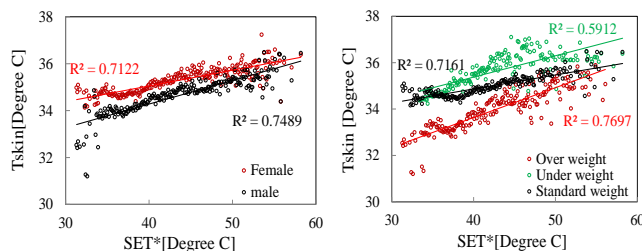


Figure 8. Relation between T<sub>skin</sub> and SET\*.

## 5. Conclusion

The conclusions of this study are summarized as follows:

- 1) The detailed thermal environmental and physiological maps were visualized along subjects' pathways, which can detect localized hot and cool spots and their impacts for human health.
- 2) The close relation between subjects' movements

and conductive heat loss from their bodies was found. Within urban canyons, since wind velocity was low, subjects' movements enhanced the convective heat exchange.

3) For abrupt changes of environments from 33.4°C outside to 24.5°C indoor, the average time constant of human skin temperature is 2.57 minutes, which is influenced by age and subjects' sweat rate.

4) A time delay was found in subjects' core temperatures when the environment abruptly changed, when temperature gap is smaller, the time delay was found to be longer. Furthermore, the time delay was longer when abrupt environment change is accompanied by changes in the subjects' motion.

5) Sweat rate had a correlation with the thermal load (SET\*). Some of deviations for their relation were explainable from the gender and BMI differences; male subjects generally sweated more than female ones; overweight persons sweated more than normal and underweight subjects. The subject with larger amount of sweating showed lower skin temperature due to the evaporative cooling.

## References

- [1] Niimi Y., Matsukawa T., Sugiyama Y., Shamsuzzaman A.S.M., Ito H., Sobue G., Mano T.: Effect of Heat Stress on Muscle Sympathetic Nerve Activity in Humans, *Journal of the Autonomic Nervous System*, pp. 61-67, 1997.
- [2] Kanda M., Kinouchi T., Kobayashi H.: Application of New Outdoor Thermal Sensation Index to Evaluation of Thermal Environment Around River, *Annual Journal of Hydraulic Engineering*, Vol.40, pp.237-242, 1996. (In Japanese)
- [3] Nakayoshi M., Shi R., Kanda M.: Development of Radio-anemometer Using Three-compact Globe Thermometers, *Annual Journal of Hydraulic Engineering*, Vol.55, pp.349-354, 2011. (In Japanese)
- [4] Hardy J. D., DuBois E. F.: The Technique of Measuring Radiation and Convection, *Journal of Nutrition*, Vol.15, pp.461-475. 1938.
- [5] Gagge, A. P.: An Effective temperature scale based on a simple model of human physiological regulatory response, *ASHRAE Transactions* 77(1), pp. 247-262, 1971.
- [6] Nagano K., Takaki A., Hirakawa M., Tochihara Y.: Effects of ambient temperature steps on thermal comfort requirements, *International Journal of Biometeorology*, Vol. 50 (1), pp.33-9, 2005.

# Distributed Video Coding By Selective Line Pruning and multi-frame based Interpolation

Student Number: 11M18261 Name: Phan Tuan Tai Supervisor: Yukihiko Yamashita

## 選択的なライン抽出とマルチフレーム補間を利用した Distributed Video Coding ファン トウアン タイ

Distributed Video Coding (DVC) は、符号化器では予測などを行わず、計算量が少ない手法で画像を符号化し、復号器では誤り訂正の技術を用いて復号器で予測した画像を補正するという特徴を持っている。そこで本論文では、符号化器において選択的なライン抽出による空間的間引きを行い、復号器においてマルチフレーム補間により元の大きさの画像に復元することによって、DVC の符号化効率を向上することを提案する。さらに、提案手法を実装し、計算機実験によりその有効性を確認する。

## 1 Introduction

Distributed source coding (DSC) is based on two results of information theory: the theorems by Slepian and Wolf [1] and by Wyner and Ziv [2] for lossless and lossy codings of correlated source, respectively. Even though, DVC algorithms do not outperform conventional video coding schemes in rate-distortion performance at present, DVC is a promising tool for creating reversed complexity codecs for power-constrained devices. Currently, in conventional digital video coding standards, the encoder typically has high complexity mainly due to motion estimation for finding the best inter picture prediction. On the other hand, DVC enables to reversed complexity codecs, i.e., a simple encoder and a complex decoder.

The common application of DVC is transform-domain Wyner-Ziv (TDWZ) codec [3], where key frames are encoded by the intra mode and Wyner-Ziv (WZ) frames (non-key frames) are inserted between key frames. The decoder uses the key frames for motion estimation to create an estimation frame of the WZ frames. Then WZ frames are corrected by error correcting codecs with using a low-density parity-check (LDPC) code. However, the decoder would require a large amount of computation due to motion estimation.

Moreover, a mixed resolution framework was applied to DVC [4] (MR-DVC), in order to adapt decoder complexity. In MR-DVC, WZ frames are downsampled before encoding. Key frames, which are used for estimating the missing information in WZ frames, are compressed at full resolution. At the decoder, key frames and WZ frames are decoded and WZ frames are interpolated back to their original size. Then, TDWZ decoder further corrects WZ frames by error correcting codecs. The MR-DVC is based on super-resolution framework thus it requires a large amount of parity bits to correct high-frequency region in WZ frames.

In my previous work, I proposed a video coding scheme called selective data pruning based DVC (SDP-DVC) [7] to improve SDP based video coding performance by using an error-correcting system of DVC. In particular, I applied TDWZ coding for residual signals which are differences between the pruned lines by SLP

and their interpolated ones. This method outperforms the conventional DVC for video sequences containing a large number of motions. However, this scheme uses the single-frame based interpolation to reconstruct dropped frames. Therefore, artifacts and flickering effects are visible in the interpolated frame because the temporal correlation between frames of video sequences are ignored.

In this paper, I propose an improved SDP-DVC using the multi-frame based interpolation which is based on the high-order new edge-directed interpolation (NEDI). This scheme uses not only the pixels of current frames but also available pixels in the previous key frame for the interpolation process at the decoder. I utilized motion vectors obtained by the motion estimation for deciding reference pixels in the key frame. This scheme enables to generate interpolated pixels which are taking into account the temporal correlation between frames. This work is regarded as an evolution of work in [7].

The rest of this paper is presented as follows. Section 2 reviews SLP. In Section 3, my proposed DVC by selective line pruning and multi-frame based interpolation is presented. Experimental results are shown in Section 4. Finally, Section 5 concludes the paper.

## 2 Selective Line Pruning and multi-frame based NEDI

### 2.1 Selective Line Pruning

SLP is a simple line-based image downsampling method. It is described as follows: the target columns to be pruned are somehow found in an image, and then they are pruned to reduce the width of the image. The original paper [6] uses a metric based on the mean square error to determine the columns to be pruned.

### 2.2 Multi-frame based NEDI

The NEDI method is based on the idea that the geometric duality between the low-resolution covariance and the high-resolution covariance is useful for interpolating a high-resolution image from its lower resolution

counterpart. This method is originally used for interpolating an image to double the sizes of rows and columns. However, the SLP usually changes aspect ratio of the image. If some columns are pruned, only the horizontal resolution becomes low. To address this issue, the high-order NEDI was proposed to utilize the geometric duality after SLP.

In order to improve the quality of the interpolated image, I try to use the multi-frame based interpolation instead of the single-frame based interpolation in the interpolation process at the decoder. This method can reduce the spatial artifacts since the temporal correlation between frames in the video sequence are also utilized. Not only the quality of the interpolated image is improved, but also I can reduce the bits in the error correction process for improving video coding performance of my scheme. In this paper, I use NEDI-9 with motion estimation (ME) and motion compensation (MC) to gain the best quality of the interpolated image.

NEDI-9 is an extension of NEDI-6 for referencing more pixels between frames in video sequences. Let  $\hat{P}_{h^6}(t)$  be the frame which is interpolated from the low-resolution frame  $I(t)$  by using NEDI-6. Assume that the previous interpolated frame is  $I(t-1)$ . In NEDI-9, ME and MC are applied to align the current block of pixels in  $\hat{P}_{h^6}(t)$  to its matched block in  $I(t-1)$ . Then, six neighboring pixels in  $\hat{P}_{h^6}(t)$  and three pixels in the matched block of  $I(t-1)$  are used to interpolate one high-resolution pixel in the current frame. The interpolated pixel is obtained by taking the weighted average:

$$\begin{aligned} \hat{P}_{h^9}(t, i, j + \frac{1}{2}) &= \sum_{k=-1}^1 \sum_{l=0}^1 h_{3l+k+1}^9 \\ &\quad \times \hat{P}_{h^6}(t, i+k, j+l) \\ &\quad + \sum_{k=-1}^1 h_{7+k}^9 \\ &\quad \times I(t-1, i+k+m_0, j+1+n_0) \\ &= \mathbf{h}^9 \cdot \mathbf{P}_{h^9} \end{aligned} \quad (1)$$

where  $\mathbf{h}^9$  is the vector of ninth-order model parameters,  $\mathbf{P}_{h^9}$  is the vector of 6-spatial neighboring pixels and 3-spatio-temporal neighboring pixels of  $\hat{P}_{h^6}(t, i, j + \frac{1}{2})$ , and  $(m_0, n_0)$  is the motion vector of the current block. The model parameters of NEDI-9 is shown in Fig. 1, where blue circles represent the available pixels in the low resolution frames and black circles represent the pixels need to be interpolated. The first term in equation (1) represents the spatial pixels in NEDI-6 and the second term represents the spatio-temporal pixels in  $I(t-1)$ . The filter-like interpolation of NEDI-9 helps reducing the artifact and flickering effect that appear by the intra frame based interpolation.

### 3 SLP-MFI-DVC

In this section, I present an improvement of my previous SDP-DVC scheme [7] by using NEDI-9 in the in-

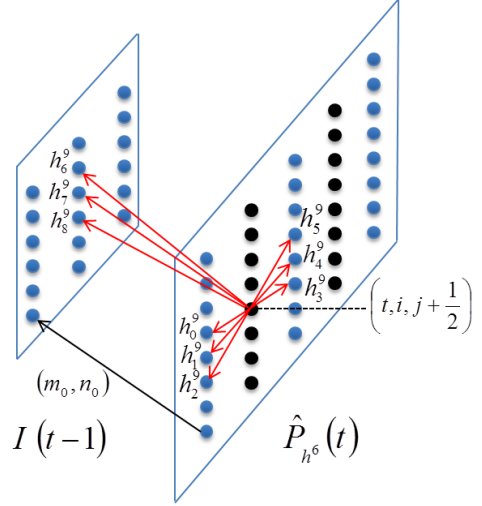


Figure 1: Model parameters of 9th order edge-directed interpolation (NEDI-9).

terpolation process at the decoder. The architecture of new SLP-MFI-DVC is shown in Fig. 2. It is based on the original MR-DVC system [4], but different from the original SDP-DVC, where the motion estimation and motion compensation are performed at the decoder.

#### 3.1 Encoder Architecture

Firstly, all frames are resized by SLP and the resized frames are encoded with H.264/AVC. For all frames within a group of pictures (GOP), the downsampled positions by SLP are the same. In the next step, resized key frames are decoded by a local decoder and interpolated back to their original size by using NEDI-6. Then, the full resolution residues between the interpolated key frames and the corresponding original frames, which are called the spatially scalable residue (SSR) hereafter, are also encoded with H.264. For WZ frames, lines of pixels which locate at the pruned position are extracted by using pruned position indices. After that, residual pruned lines (RPLs) are obtained by taking the difference between the pruned lines of WZ frames and those of the preceding key frames. RPLs are encoded by TDWZ coder and will be used for correcting interpolated lines at the decoder. During the TDWZ encoding, the LDPC-accumulated (LDPCA) codec [8] is used as the error-correcting code since it is suitable for DVC purpose.

#### 3.2 Decoder Architecture

The decoder basically does the reverse operation of the encoder except the interpolation. For the interpolation, the single-frame based NEDI-6 is used for the first key-frame while the multi-frame based NEDI-9 is employed for the following frames in each GOP. The interpolation is performed as follows. First, decoded low-resolution key frames are interpolated to the original size by NEDI-6 interpolation. The interpolated key

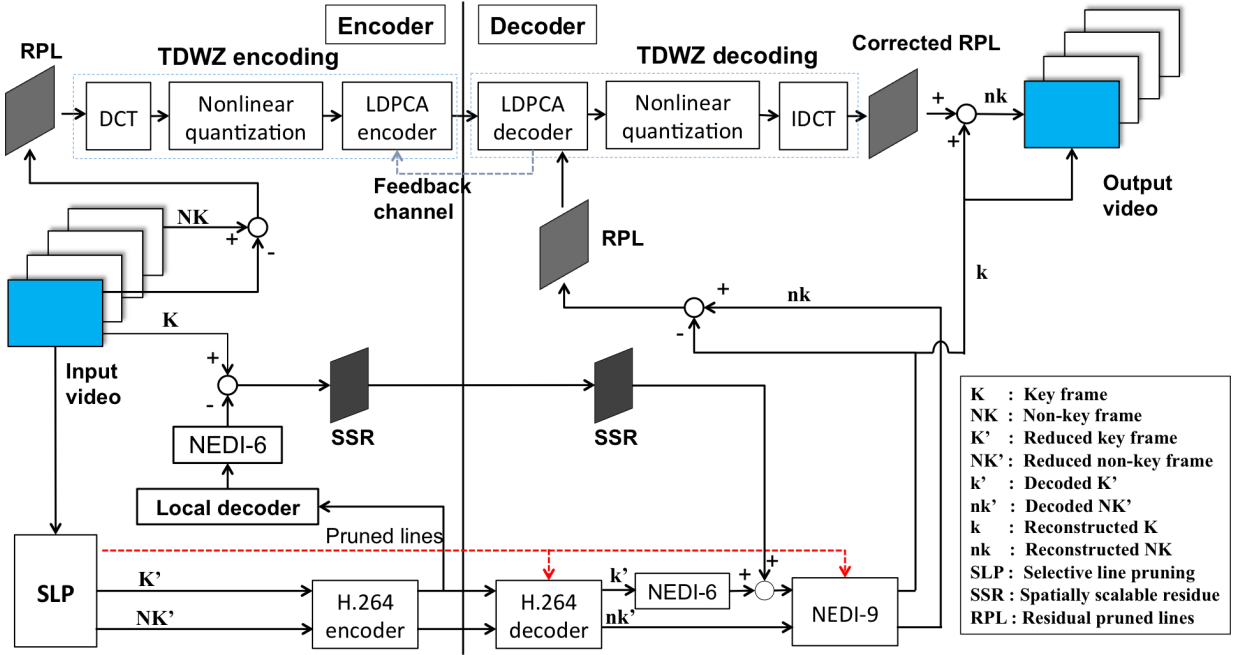


Figure 2: Architecture of proposed SLP-MFI-DVC.

frames are incorporated with SSR to reconstruct full resolution key frames. For the WZ frames, block-based motion estimation and motion compensation are applied to find the most similar block of pixels in the previous full-resolution key frame. Then, NEDI-9 which uses three neighboring pixels in the matching block and six surrounding pixels in the current frame are used to interpolate each pixels in the current block. If the result of the block matching is totally different from the current block, the three spatio-temporal pixels are discarded because the pixels in the matched block are not related. Thus the artifact and flickering effect are reduced from interpolated frames. Moreover, for WZ frames, the temporal residue is calculated to obtain the side information for TDWZ decoder. After TDWZ decoding, the reconstructed WZ frames are obtained by adding the corrected residue to previous reconstructed key frames.

## 4 Experiments

In this section, the experimental results are shown to validate the effectiveness of the new SLP-MFI-DVC method. I used luminance (Y) signal of 150 frames of popular video sequences, *Foreman*, *Hall Monitor*, and *Soccer* with QCIF size and 15fps. As the core codec used in the encoder, I used GOP=4 coding of H.264/AVC.

### 4.1 Effect of using NEDI-9

Fig. 3 shows the PSNR comparison of the interpolation methods between NEDI-6 and NEDI-9. Here, I only compared the PSNR of the WZ frames because key frames are always reconstructed to full resolution.

Comparing to NEDI-6, NEDI-9 achieves higher PSNR for all frames. The interpolated sequence using NEDI-9 also has less flickering artifacts and higher quality consistent in the temporal direction than the single-frame based interpolated sequence using NEDI-6. Especially, for the fast moving sequence, NEDI-9 gained the much larger PSNR than NEDI-6. From this results, I can expect the accuracy of the error correction process is improved and thus the final reconstructed frames have higher PSNR.

### 4.2 Video Coding Performance

The rate-distortion performance of proposed SLP-MFI-DVC is compared with original SDP-DVC, DISCOVER DVC codec [9] at GOP of 4, and H.264/AVC intra coding. In SLP-MFI-DVC, the number of pruned lines in row and column are fixed to 48, which means about a half of pixels in each frame are removed. Besides, I used the same condition with [7] for pruned indices and nonlinear quantization parameters.

Fig. 4 illustrates the R-D curves of various video coding methods. The PSNR and bitrates are calculated for the luminance component of all frames and the PSNR is the average over the sequences. Experimental results show that new SLP-MFI-DVC can outperform original SDP-DVC in all cases. It also outperforms DISCOVER for fast moving sequences, such as *Foreman* and *Soccer*. Moreover, it also shows better performance than H.264/AVC intra coding in *Hall Monitor* sequence. Note that by using multi-frame based interpolation, SLP-MFI-DVC performance gradually reaches to H.264/AVC.

For fast motion video sequences, the conventional DVC usually has problems in frame interpolation, re-

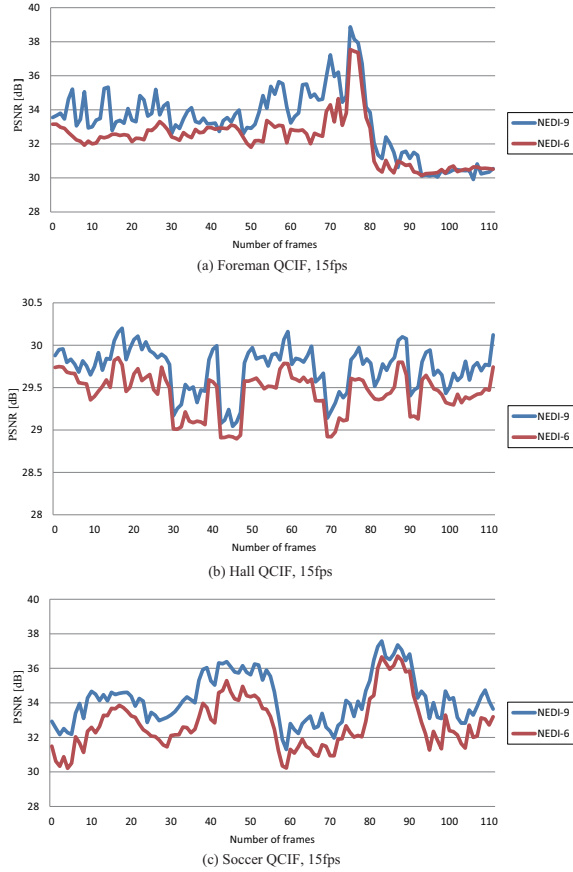


Figure 3: PSNR comparison of the video interpolation methods.

sulting lower performance compared to H.264/AVC. It can be observed in *Foreman* and *Soccer* sequences. In my framework, the multi-frame based interpolation is effective to reduce the artifacts which are occurred by SLP and the multi-frame interpolation process performs better than the single-frame based interpolation.

## 5 Conclusions

In this paper, a new SLP-MFI-DVC using multi-frame based interpolation has been proposed to improve the SDP-DVC video coding performance. The rate-distortion performance of the proposed codec is better than conventional ones and the DISCOVER for videos with relatively many motions. Still, there is a room for improvements in the interpolation. Future work also includes replacing the SLP with other resizing methods such as a fast content aware retargeting.

## 6. References

- [1] D. Slepian and J. Wolf, "Noiseless coding of correlated information sources," *IEEE Trans. Inf. Theory*, vol. 19, no. 4, pp. 471-480, 1973.

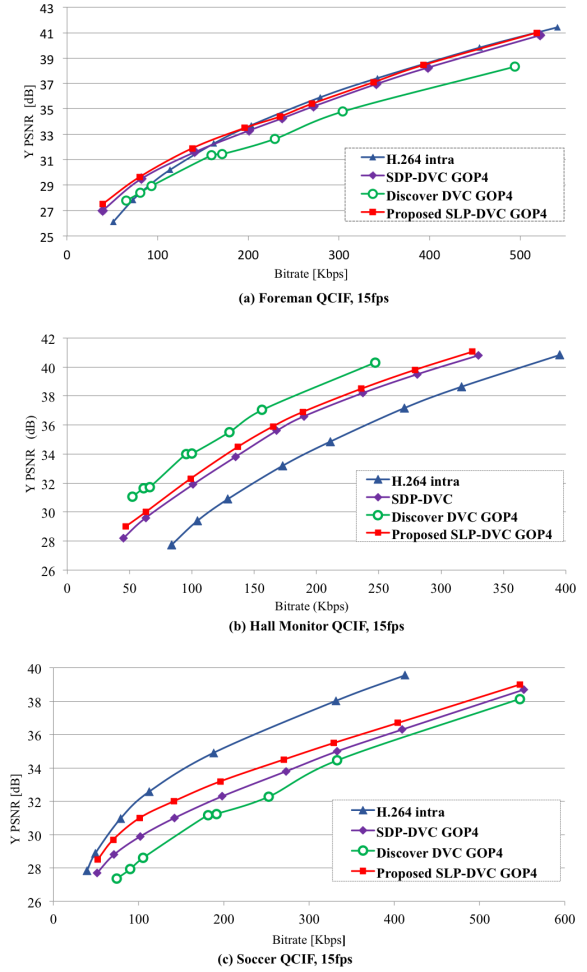


Figure 4: Rate-distortion performance of various coding methods.

- [2] A. Wyner and J. Ziv, "The rate-distortion function for source coding with side information at the decoder," *IEEE Trans. Inf. Theory*, vol. 22, no. 1, pp. 1-10, 1976.
- [3] A. Aaron, S. Rane, E. Setton, and B. Girod, "Transform-domain Wyner-Ziv codec for video," in *Proc. SPIE VCIP'04*, pp. 520-528, 2004.
- [4] B. Macchiavello, F. Brandi, E. Peixoto, R. L. de Queiroz, and D. Mukherjee, "Side-information generation for temporally and spatially scalable Wyner-Ziv codecs," *EURASIP Journal on Image and Video Processing*, vol. 2009, 2009.
- [5] D. Liu, X. Sun, F. Wu, S. Li, and Y. Q. Zhang, "Image compression with edge-based inpainting," *IEEE Trans. Circuits Syst. Video Technol.*, vol. 17, no. 10, pp. 1273-1287, 2007.
- [6] D. T. Võ, J. Solé, P. Yin, C. Gomila, and T. Q. Nguyen, "Selective data pruning-based compression using high-order edge-directed interpolation," *IEEE Trans. Image Process.*, vol. 19, no. 2, pp. 399-409, 2010.
- [7] T. T. Phan, Y. Tanaka, M. Hasegawa, S. Kato, "Mixed-Resolution Wyner-Ziv Video Coding Based on Selective Data Pruning," *MMSP2011*, pp. 2-6, Hangzhou, China, Oct. 17-19, 2011.
- [8] D. Varodayan, A. Aaron, and B. Girod, "Rate-adaptive codes for distributed source coding," *Signal Processing*, vol. 86, no. 11, pp. 3123-3130, 2006.
- [9] X. Artigas, J. Ascenso, M. Dalai, S. Klomp, D. Kubasov, and M. Ouaret, "The DISCOVER codec: architecture, techniques and evaluation," in *Proc. 26th Picture Coding Symposium*, Lisbon, Portugal, Nov. 2007.



# DETERMINANTS OF MOBILE LEARNING ACCEPTANCE IN LUANG PRABANG: TOWARDS WORLD HERITAGE SITE PRESERVATION AWARENESS PROMOTION

Student Number: 11M51436    Name: Yew Siang POONG    Supervisor: Shinobu YAMAGUCHI, Jun-ichi TAKADA

Mobile learning has been gaining attention in international development to promote knowledge among local community. However, little is known about mobile learning acceptance in Luang Prabang, Lao PDR. Through the collaboration with the Department of World Heritage of Luang Prabang, questionnaire survey based on the extended Technology Acceptance Model was administered to 484 students in two local higher education institutions. Besides, face-to-face interview was conducted with eight faculty members to gain understanding on mobile learning implementation perceptions and possibilities. Empirical data shows high degree of intention to use mobile learning, and multiple regression analysis discovered six important mobile learning acceptance factors. Result from this study contributes to knowledge improvement from least developing country perspective and provides valuable guidelines for the development of mobile learning application to promote heritage site preservation awareness in Luang Prabang.

## 1. Introduction and Objective

UNESCO recently issued an urgent call for preservation of Luang Prabang town as a World Heritage Site due to rapid development after Luang Prabang has become a popular tourists spot. Although Lao PDR is identified as a least developed country, mobile subscription rate has shown growing trend and has achieved 65% penetration rate in 2011 [1]. As education is recognized to play an important role in promoting awareness in preservation and protection, this research aims to introduce mobile learning to promote World Heritage Site preservation awareness in World Heritage Site.

Mobile learning is defined as “acquisition of any knowledge and skill through the use of mobile technology, anywhere, anytime that results in an alteration in behavior” [2]. Recently, mobile learning is perceived as a tool to empower people in developing countries in gaining access to information, which would eventually promote sustainable development as well as improving quality of life. This is evidenced from the initiatives of mobile learning application on developing countries by international development agencies, such as UNESCO, World Bank, and Asian Development Bank.

However, in order to ensure sustainable use of ICT implementation, user perception evaluation is vital prior to its implementation, especially in developing countries [3]. Consistent with this view, this research intends to examine mobile phone usage behavior and perceptions of mobile learning to shed light on the actual status of mobile learning readiness among the young generation in Luang Prabang.

## 2. Research Components

### 2.1 Problem statement

The study of mobile learning acceptance has just begun in the recent years. With many literatures focusing on developed countries, there is lack of understanding of end user mobile learning acceptance in least developed countries. Hence, this gives rise to the following research question: what are the factors affecting young adult's intention to adopt mobile learning in Luang Prabang? Following this, three research objectives are developed:

- i. To evaluate current mobile phone ownership profile
- ii. To assess mobile phone usage behavior
- iii. To investigate factors affecting behavioral intention

to use mobile learning

By understanding the acceptance of mobile learning, it is expected that the findings would facilitate the development of effective mobile application to promote World Heritage Site preservation awareness in the future.

### 2.2 Theoretical framework

The original TAM proposes two important antecedents of technology use intention, namely, *perceived usefulness* and *perceived ease of use*. Perceived usefulness is defined as “the degree to which a person believes that using a particular system would enhance his or her job performance” [4, p.320]. Past research has found that intention to use a technology would be enhanced when the technology is believed to provide advantage to the potential users. Also, literature shows that a technology that is easy to use would boost the perception of usefulness, which in turn increases intention to use a technology. This notion is captured by *perceived ease of use*, which is defined as “the degree to which a person believes that using a particular system would be free from effort” [4, p.320]. Therefore, the following hypothesis is developed:

*H1: Perceived usefulness is positively related to behavioral intention to use mobile learning among young adults in Luang Prabang.*

*H2: Perceived ease of use positively affects behavioral intention to use mobile learning among young adults in Luang Prabang, mediated by perceived usefulness.*

Literature indicates that social actors do play an important role in influencing an individual to adopt technology. In particular, the image value of the society of which an individual is active in and the opinion from the close social actor of an individual are the key factors in *social influence* [5]. Nevertheless, social influence does not assert direct effect to intention to use. Rather, social influence increases perceived usefulness of a technology, which in turn influences intention to use [6]. Thus, the following hypothesis is developed:

*H3: Social influence positively affects behavioral intention to use mobile learning among young adults in Luang Prabang, mediated by perceived usefulness.*

Personal innovativeness is defined as “the willingness of an individual to try out any new information technology” [7, p.206]. Research shows that individual

who have high level of personal innovativeness will demonstrate increased curiosity and courage to be the first adopter of new technology. This research intends to test whether there is relationship between personal innovativeness and intention to use mobile learning. Hence, the following hypothesis is developed:

*H4: Personal innovativeness is positively related to behavioral intention to use mobile learning among young adults in Luang Prabang.*

Based on the past findings, *self-efficacy*, which is defined as “people’s judgments of their capabilities to organize and execute courses of action required to attain designated types of performances” [8, p.391], influences an individual’s behavioral intention to use technology. When one has favourable judgment on his/her own capability to handle a technology, intention will be stimulated to use the technology. Therefore, the hypothesis is developed as:

*H5: Self-efficacy is positively related to behavioral intention to use mobile learning among young adults in Luang Prabang*

Motivation theorists have found that individual’s *perceived enjoyment* plays an important role in the process of using technology. Perceived enjoyment is defined as “the extent to which the activity of using the technology is perceived to be enjoyable in its own right, apart from any performance consequences that may be anticipated” [9, p.1113]. Given that mobile learning in this study context is to be used in informal settings, this study proposes the following hypothesis:

*H6: Perceived enjoyment is positively related to behavioral intention to use mobile learning among young adults in Luang Prabang.*

Potential consumers’ affordability has been found to influence purchase in consumer research [10]. *Perceived price* measures young adults’ perception on whether or not the pricing structure offered by telecommunication operators is reasonable for using advanced mobile services [11]. The investigation of perceived price is important to clarify affordability issue since Lao PDR is a lower-middle income economy country. Therefore, the following hypothesis is proposed:

*H7: Perceived price is positively related to behavioral intention to use mobile learning among young adults in Luang Prabang.*

Mathieson, Peacock and Chin [12] argue that an individual may face limited resources in using technology. Although an individual may perceive that he/she has the ability to use technology, *perceived facilitating resources* also plays an important role in use intention. Taylor and Todd assert that “the absence of facilitating resources represents barriers to usage and may inhibit the formation of intention to usage” [13, p. 153]. Given that Lao PDR is a least developed country, this study intends to assess local people’s perception on facilitating resources with respect to the use of mobile learning. Thus, the following hypothesis is proposed:

*H8: Perceived facilitating resources are positively related to behavioral intention to use mobile learning among young adults in Luang Prabang.*

Based on the literature review, the TAM model is

modified to suit the current research context, as shown in Figure 1. There are a total of eight independent variables and one dependent variable. The dependent variable is *behavioral intention to use ML* (ML short for “mobile learning”). Also, two types of relationships are modeled in theoretical framework, namely direct and mediated relationships. In particular, mediated relationship attempts to model the causal chain of an independent-dependent variable relationship, in which deeper insight could be obtained with the inclusion of a mediator variable.

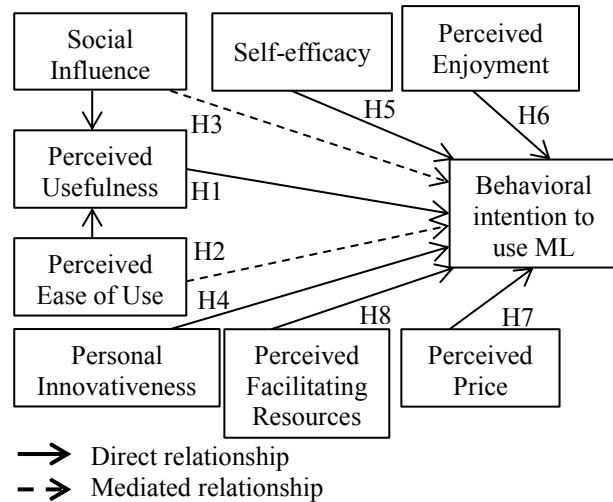


Figure 1: Research model

## 2.3 Methodology

This study adopts questionnaire survey and interview to acquire student perceptions on mobile learning. The questionnaire consists of three sections: 1) collecting of students’ demographic information, 2) investigating mobile phone features and usage by students; and 3) inquiring students’ perceptions towards technology acceptance variables identified in the theoretical framework. The questionnaire was translated into Lao language with the assistance of local DPL staffs and was verified by Souphanouvong University personnel.

A total of 484 questionnaires were distributed to Souphanouvong University (SU) and to Northern Law College (NLC) of Luang Prabang in March 2012. SU is one of the four Lao national universities and NLC is a law-focused college established directly under the Ministry of Justice. There are a total of 4,700 and 4,000 students in SU and NLC respectively. The number of distributed questionnaire compose of about 5% of the total campus population. A total of 443 questionnaires were returned, yielding 91.53% response rate. Finally, 365 questionnaires were considered valid for data analysis.

Descriptive analysis based on frequency result was conducted on demographic and perception questions. Next, inferential analysis using multiple regression was conducted to test the proposed theoretical model. In order to validate mediation effect, mediation procedure based on Baron and Kenny [14] work was performed. Finally, bootstrapping procedure was applied to assess the mediation effect and whether or not the mediation model is statistically significant.

In addition, interviews were conducted with faculty

members of the education institutions to supplement the statistical data. Questions asked include student's mobile usage behavior from adult point of view, mobile learning perceptions and development prospects in general, and implementation suggestions for the development of World Heritage Site preservation awareness mobile application.

### 3. Findings

Male and female respondents comprise of 61.4% (n=224) and 34.5% (n=126) respectively. Fifteen respondents did not state their gender. Majority of the respondents (70.4%, n=257) are in the age around 20 to 24 years old. Mixed distribution is observed in respondents' income demographic, although the highest income category (received >100,000 Lao Kip per month) records the responses (n=97, 26.6%), followed by those who received income less than 19,999 Lao Kip per month (n=81, 22.2%).

#### 3.1 Mobile phone demographic and use behavior

The survey found the following three major characteristics among university students in Luang Prabang:

##### 3.1.1 Most common device owned by student is mobile phone, followed by laptop PC

Given the multiple response options of mobile phone, tablet, laptop personal computer (PC) and desktop PC, a total of 587 (160.8%) cases were reported (n=365). This means respondents own between 1 to 2 devices at the same time. The device that most owned by respondents is mobile phone (n=358), followed by laptop PC (n=188), desktop PC (n=29) and tablet (n=12). The figures conform to the trend of mobile phone ownership in several other developing countries and depict the potential of using mobile phone as a tool to implement innovative ICT application.

##### 3.1.2 Smartphone is popular among university students

Among those who owned a mobile phone (n=358), data analysis shows 177 (49.44%) respondents state that their device is a smartphone. With respect to connectivity options, there are 516 cases reported (144.13% with n=358), depicting one or more connectivity options available in the mobile phone. Specifically, respondents state that their mobile phones have Bluetooth (n=204), 3G (n=149), WiFi (n=76), and infrared (n=15). Internet connectivity wise, 3G-enabled mobile phone appears to be more common than WiFi-enabled mobile phone. The high number of Internet-ready mobile phone owned by the respondents suggests that more varieties of innovative applications could be developed.

##### 3.1.3 Laptop PC is the main device used for digital activities followed by mobile phone, and the school is the common place to access Internet

A multiple response analysis shows that laptop PC is the most used device (1749 cases), followed by mobile phone (1195 cases). Specifically, laptop PC is reported being used mainly for searching information (n=231), learning new knowledge (n=231), e-mail (n=223), watching video (n=220), engaging in social networking

sites (n=203), playing game (n=178), and reading news (n=134). On the other hand, mobile phone is used mainly in chatting (n=230) and listening to music (n=213). Meanwhile, school (n=159, 43.56%) and home (n=119, 32.60%) are the top two places of access to the Internet. Respondents who access to the Internet anywhere using mobile phone comprise of 30.13% (n=110). Analysis shows that Internet access mobility trend is observed among the young adults in Luang Prabang.

### 3.2 Hypotheses testing

Descriptive data analysis on the symmetric agree-disagree 5-point Likert scale revealed high degree of agreement response on *perceived usefulness*, *perceived ease of use*, *perceived enjoyment*, *perceived facilitating resources*, *personal innovativeness*, *social influence* and *intention to use mobile learning*. However, both *self-efficacy* and *perceived price* factors received relatively higher disagreement responses on the scale.

In order to test the hypotheses, three sets of regression models are developed as follows:

$$BI = \gamma + \delta_1 PU + \delta_2 PEOU + \delta_3 PI + \delta_4 SE + \delta_5 PE + \delta_6 PP + \delta_7 PFR \quad (1)$$

$$BI = \alpha_1 + \beta_1 PEOU \quad (2a)$$

$$PU = \alpha_2 + \beta_2 PEOU \quad (2b)$$

$$BI = \alpha_3 + \beta'_1 PEOU + \beta_3 PU \quad (2c)$$

$$BI = \alpha_4 + \beta_4 SI \quad (3a)$$

$$PU = \alpha_5 + \beta_5 SI \quad (3b)$$

$$BI = \alpha_6 + \beta'_4 SI + \beta_6 PU \quad (3c)$$

Equation (1) tests the direct effect of independent to dependent variables (hypothesis 1, 4, 5, 6, 7, and 8). Equation (2) and (3) forms the necessary conditions to test hypothesis 2, and 3 respectively.

Result of the regression model is as shown below:

$$BI = 0.020 + 0.115PU + 0.111PEOU + 0.165PI + 0.369PE + 0.260PFR \quad (4)$$

$$BI = 1.102 + 0.373PEOU \quad (5a)$$

$$PU = 1.396 + 0.292PEOU \quad (5b)$$

$$BI = 0.658 + 0.280PEOU + 0.318PU \quad (5c)$$

$$BI = 1.462 + 0.165SI \quad (6a)$$

$$PU = 1.443 + 0.241SI \quad (6b)$$

$$BI = 0.903 + 0.072SI + 0.388PU \quad (6c)$$

All the hypotheses are supported except *self-efficacy* (H5) and *perceived price* (H7). Result of regression model (4) shows that *perceived enjoyment* is the strongest predictor for *behavioral intention* to use mobile phone for learning, followed by *perceived facilitating resources*. Overall explained variance for regression model (4) is 35.2%. Equation (5) and (6) shows that *perceived ease of use* and *social influence* would enhance *perceived usefulness* of mobile learning, which in turn influence *behavioral intention*. Effect of social influence is reduced significantly after perceived usefulness is included into equation (6a) (see equation (6c) for effect reduction of *SI*). Both the mediation equation (5) and (6) are statistically significant under bootstrap analysis at 95% confidence interval.

### 3.3 Interview results

Feedback from faculty members shows that there is trend of mobile Internet use among students and that

mobile learning is in line with current students' mobile phone use behavior. In addition, the use of mobile learning could increase accessibility to information, given high mobile phone penetration rate in Luang Prabang. With regard to application implementation approach, faculty members commented that mobile learning should be designed in a motivating, interesting, and enjoyable approach so as to be able to attract the young adults to use. In addition, using mobile learning to promote World Heritage Site awareness is thought as an effective approach, given limited accessibility to World Heritage Site information. Faculty members suggest providing hands-on demonstration, assignments, and workshops to promote the application, in addition to media announcement. Well-designed application is also one of the important criteria to promote mobile learning application, according to the interviewees.

Department of World Heritage (DPL) counterpart comments that the introduction of mobile learning application could supplement awareness promotion campaign by providing easy access to heritage information using mobile phone. The development of such application could also contribute to the collection of locally-oriented mobile applications, which is still scarce in number currently.

## 4. Discussion

### 4.1 Data interpretation

Current investigation shows that the determinants of mobile learning use intention among the young adult in Luang Prabang are *perceived usefulness*, *perceived ease of use*, *personal innovativeness*, *perceived enjoyment*, *perceived facilitating resources*, and *social influence*. In addition, relationships between *social influence* and *perceived ease of use* with *behavioral intention to use mobile learning* are mediated by *perceived usefulness*. This result suggests that 1) the effect of social influence on intention to use mobile learning depends largely on how the important social actors convey mobile learning usefulness to the potential users; 2) mobile learning ease of use could enhance usefulness perception, which in turn increase use intention. As oppose to literature, self-efficacy and perceived price did not appear to be the determinant of intention to use mobile learning. Mixed responses on both of the perceptions suggest that some respondents do concern about the skills they possess may not be sufficient for them to use mobile learning. Moreover, there are also relatively high responses of disagreement on the acceptability of mobile pricing structure offered by telecommunication operators to support mobile learning.

### 4.2 Implication for Research and Practice

This study has validated the extended TAM in a least developing country (LDC) context. TAM was originally created in the United States by Davis [4]. However, there are limited studies conducted in Lao PDR using TAM. The finding of this study has filled the gap of understanding mobile learning acceptance in Luang Prabang, which is an imminent research in developing countries.

Practitioners are suggested to look into the enjoyment, usefulness, and ease of use factors while

developing mobile learning application. Also, initiatives to stimulate personal innovativeness among the young adults and engage important social actors of Luang Prabang community in promotion campaign, such as workshops and demonstrations, would be essential to increase mobile learning adoption.

### 4.3 Limitation and future research

As an explorative study, current research draws from student sample, which calls for caution on data generalizability. Future studies with respectable resources could increase the sample size and include different target respondents to achieve a more comprehensive coverage. Empirical testing research are suggested to incorporate additional factors to increase the explanatory power of the current model in this study. In addition, future research could embark on determining the implications of using mobile learning by analyzing user performance on pre- and post- adoption of mobile learning in promoting World Heritage Site preservation awareness. A comparative study between users who adopt mobile learning and those who do not could also be conducted to determine whether mobile learning is an effective solution to promote heritage site preservation awareness in Luang Prabang.

## References

- [1] ICT Development Index. (2011). ITU. Available: <http://www.itu.int/net/pressoffice/backgrounders/general/pdf/5.pdf>
- [2] Geddes, S. J., 2004. Mobile learning in the 21st century: benefit for learners. *Knowledge Tree e-journal: An ejournal of flexible learning in VET*, 30(3), 1 - 13
- [3] Takada, J., Yamaguchi, S., Leong, C. (2008). Geographical Information System (GIS) and Regional Development: Potential Problems and Feasible Solutions. *The Japan Society for International Development, Proceedings of the 19<sup>th</sup> Annual Conference*, 350-353.
- [4] Davis, F. (1989). Perceived usefulness, perceived ease of use, and user acceptance of information technology. *MIS Quarterly*, 13(3), 319-340.
- [5] Fishbein, M., and Ajzen, I. (1975). Belief, attitude, intention, and behavior: An introduction to theory and research. Reading, MA: Addison-Wesley.
- [6] Yuen, A.H.K, and Ma, W.W.K. (2008). Exploring teacher acceptance of e-learning technology. *Asia-Pacific Journal of Teacher Education*, 36(3), 229 – 243.
- [7] Agarwal, R., and Prasad, J. (1998). A conceptual and operational definition of personal innovativeness in the domain of information technology. *Information Systems Research*, 9(2), 204 – 215.
- [8] Bandura, A. (1977). Self-efficacy: Toward a unifying theory of behavioral change. *Psychological Review*, 84(2), 191 – 215.
- [9] Davis, F., Bagozzi, R., and Warshaw, P. (1992). Extrinsic and intrinsic motivation to use computers in the workplace. *Journal of Applied Social Psychology*, 22(14), 1111 – 1132.
- [10] Notani, A.S. (1997). Perceptions of affordability: Their role in predicting purchase intent and purchase. *Journal of Economic Psychology*, 18(5), 525 – 546.
- [11] Liao, C.H., Tsou, C.W., and Shu, Y.C. (2008). The roles of perceived enjoyment and price perception in determining acceptance of multimedia-on-demand. *International Journal of Business and Information*, 3(1), 27 – 52.
- [12] Mathieson, K., Peacock, E., and Chin, W.W. (2001). Extending the Technology Acceptance Model: The influence of perceived user resources. *The DATA BASE for Advances in Information Systems*, 32(3), 86 – 112
- [13] Taylor, S. and Todd, P.A. (1995). Understanding information technology usage: A test of competing models. *Information Systems Research*, 6(2), 144 – 176.
- [14] Baron, R.M., and Kenny, D.A. (1986). The moderator-mediator variable distinction in social psychological research: Conceptual, strategic and statistical consideration. *Journal of Personality and Social Psychology*, 51, 1173 – 1182.